Tampere University

OLLI ORELL

Enriching Mechanical Characterisation Methods of Polymer Composites and Hybrids with Digital Image Correlation

Tampere University Dissertations 976

Tampere University Dissertations 976

OLLI ORELL

Enriching Mechanical Characterisation Methods of Polymer Composites and Hybrids with Digital Image Correlation

ACADEMIC DISSERTATION
To be presented, with the permission of
the Faculty of Engineering and Natural Sciences
of Tampere University,
for public discussion in the auditorium K1702
of the Konetalo, Korkeakoulunkatu 6, Tampere,
on 15th of March 2024, at 12 o'clock.

ACADEMIC DISSERTATION
Tampere University, Faculty of Engineering and Natural Sciences
Finland

Responsible supervisor and Custos	Associate Professor Mikko Kanerva Tampere University Finland	
Supervisor	University Lecturer Jarno Jokinen Tampere University Finland	
Pre-examiners	Associate Professor Sven Bossuyt Aalto University Finland	Associate Professor Enrico Cestino Politecnico di Torino Italy
Opponents	Associate Professor Enrico Cestino Polytecnico di Torino Italy	Dr. Aleksi Laakso Meyer Turku Oy Finland

The originality of this thesis has been checked using the Turnitin OriginalityCheck service.

Copyright ©2024 Olli Orell

Cover design: Roihu Inc.

ISBN 978-952-03-3338-6 (print)
ISBN 978-952-03-3339-3 (pdf)
ISSN 2489-9860 (print)
ISSN 2490-0028 (pdf)
http://urn.fi/URN:ISBN:978-952-03-3339-3

Carbon dioxide emissions from printing Tampere University dissertations have been compensated.

PunaMusta Oy – Yliopistopaino
Joensuu 2024

To Lauri, Toivo and Kerttu

PREFACE

This thesis bases on the research conducted in the Materials Science and Environmental Engineering unit in Tampere University during 2013-2023. The research work was carried out during several research projects funded by different sources, of which to mention FIMECC Breakthrough Materials Doctoral School, Business Finland, Finnish Defence Forces Logistics Command and Jane and Aatos Erkko Foundation.

I am grateful that I had the opportunity to work with extremely interesting research tasks in the research group of Plastics and Elastomer Technology. In the projects I was involved, I was allowed to create, bend, break, and burn the most interesting materials. I want to give my greatest gratitude to my supervisor, Associate Professor Mikko Kanerva for your guidance and invaluable support. The given periodic positive pressure was definitely needed to complete this dissertation. I would also like to thank Professor Jyrki Vuorinen and Associate Professor Essi Sarlin for their contributions.

Naturally the work would not have been possible without the help of all the staff and the talented colleagues in the Laboratory of Materials Science. Even though our research group went through quite a turnover during my rather long personal era there, the enthusiastic and inspiring atmosphere was always maintained. The list would be too long to complete here but especially, Ilari Jönkkäri, Minna Poikelispää, Markus Kakkonen, Pekka Laurikainen, Sarianna Palola, Royson Dsouza, Farzin Javanshour, Pauli Hakala, Nazanin Pournoori and Óscar Rodera García – thank you for all the inspiration and time we shared. Special thanks I want to give to Jarno Jokinen, my closest partner in crime in numerous '15-minute' tasks.

I want to thank my family for their encouragement towards this goal. Also, my long-lasting friends Toni, Lasse, Mikko and Anssi merit special mention for being there from the very beginning of my academic journey.

Finally, Mari, I could not have completed this work without your love, support and patience.

Kangasala, December 2023
Olli Orell

ABSTRACT

Determination of the mechanical properties of materials is largely based on established test methods that aim to generate simple, and typically uniaxial, stress state to the test specimen. If the test specimen behaves homogeneously, the deformation caused by the loading can be measured reliably by common methods. However, as the complexity of the tested material or the geometry of the test specimen increases, the general discrete measuring methods do not necessarily give a true picture of the behaviour of the specimen. This is particularly true for heterogeneous and anisotropic materials whose mechanical response is strongly dependent on the observation point, direction and scale. In these cases, reliable measurements require a more comprehensive examination of deformations, which is typically challenging with traditional discrete measuring methods.

Numerical analysis techniques (such as the finite element method) are increasingly taken advantage of in the identification of material properties, especially when non-uniform stress state is known to occur in the specimen during testing. However, detailed data of the deformed specimen is required in the simulation of the experiments. The measured data must be reliable, as the results of the models are as good as the used raw data.

Digital image correlation (DIC) is an optical method for determining the deformation field from the surface being studied. The objective of this thesis is to improve the reliability and precision of the results produced by the selected experimental test methods using DIC, especially when testing heterogeneous and non-linear–behaving materials. The work is focused on compression tests and methods for determining fracture mechanics properties of polymer coatings and adhesives. The thesis is based on five original scientific publications in which the selected test methods are used to characterise and identify properties of very different materials, including soft hydrogel, fibrous polymer composites, thin polymer coating and adhesive.

In the thesis, the developed method is presented for determining elastic material constants for orthotropic polymer composite using the continuous deformation field provided by DIC with high spatial resolution. DIC was also used to measure the realistic deformation of the soft and transparent compressed hydrogel specimen,

enabling more valid characterisation of the stress-strain relationship of the material. The DIC experiments revealed hidden factors that affected the behaviour of the test specimens in the compression tests. The precision of the test methods was thus improved by the systematic use of DIC, since without the full-field measurements, the factors are difficult to recognise and consider in the analysis of the results.

Generally, the analysis of the fracture mechanics tests is based on the monitoring of the progressive crack growth in the test specimen, which is known to be a major source of uncertainty in the methods. The determination of the crack length is performed typically by visual means, which is challenging, if not impossible, especially in mode II tests where the crack faces do not separate per definition. This thesis presents the developed methods to quantitatively evaluate the crack propagation for the investigated fracture mechanics tests based on the deformation fields provided by the DIC. The presented methodology significantly reduces the uncertainty resulting from the subjective interpretation performed by the operator. Major effort is made to evaluate fracture testing with cyclic loading, i.e. fatigue.

TIIVISTELMÄ

Materiaalien mekaanisten ominaisuuksien määrittäminen perustuu pitkälti vakiintuneisiin testimenetelmiin, joissa koekappaleeseen pyritään kohdistamaan tunnettu yksinkertainen jännitystila. Koekappaleen käyttäytyessä homogeenisesti kuormituksen aiheuttama muodonmuutos voidaan mitata luotettavasti perinteisillä menetelmillä. Testattavan materiaalin sekä koekappaleen muodon tai rakenteen kompleksisuuden kasvaessa yleisesti käytetyt mittausmenetelmät perustuen yksittäisiin tarkastelupisteisiin, eivät kuitenkaan välttämättä anna todellista kuvaa koekappaleen käyttäytymisestä. Tämä pätee erityisesti heterogeenisille ja anisotrooppisille materiaaleille, joiden ominaisuudet riippuvat voimakkaasti tarkastelukohdasta, -suunnasta sekä -mittakaavasta. Näissä tapauksissa mittausten luotettavuutta voidaan parantaa muodonmuutosten kattavammalla tarkastelulla, mikä perinteisillä diskreeteillä mittausmenetelmillä on tyypillisesti haastavaa.

Materiaaliominaisuuksien määrityksessä hyödynnetään yhä yleisemmin numeerisia laskentamenetelmiä (kuten elementtimenetelmää) joiden avulla on mahdollista huomioida muun muassa monimutkaisempien kuormitustilanteiden aiheuttamat vaikutukset koekappaleen käyttäytymisessä. Toimivien mallien ratkaisemiseen tarvitaan kuitenkin yksityiskohtaista mitattua lähtötietoa koekappaleen muodonmuutoksista. Mitatun tiedon tulee olla luotettavaa, sillä tunnetusti malleilla saatavat tulokset ovat korkeintaan yhtä hyviä kuin käytetyt lähtötiedot.

Digitaalinen kuvakorrelaatio (digital image correlation, DIC) on optinen menetelmä, jolla voidaan määrittää muodonmuutoskenttä tutkittavan kappaleen pinnasta. Tässä väitöskirjassa käsitellään DIC:n mahdollistamia menetelmiä, joiden avulla pyritään parantamaan valittujen kokeellisten testimenetelmien tuottamien tulosten soveltuvuutta ja luotettavuutta erityisesti heterogeenisiä ja epälineaarisesti muotoaan muuttavia materiaaleja testattaessa. Työssä keskityttiin puristustestaukseen sekä testimenetelmiin polymeeristen pinnoitteiden ja liimojen murtumismekaanisten ominaisuuksien määrittämiseksi. Työ perustuu viiteen tieteelliseen artikkeliin, joissa tarkasteltuja testimenetelmiä hyödynnettiin määrittämään hyvin erilaisten materiaalien ominaisuuksia – vaihdellen pehmeästä

hydrogeelistä kuitulujitettuihin komposiitteihin sekä ohuisiin, pinnoitteina ja liimoina käytettäviin polymeerimateriaaleihin.

Työn tuloksina esitetään menetelmä ortotrooppisen polymeerikomposiitin elastisten materiaalivakioiden määrittämiseen, jossa hyödynnetään digitaalisella kuvakorrelaatiolla tuotettua korkean paikkaresoluution omaavaa jatkuvaa venymäkenttää. DIC:n avulla voitiin myös tunnistaa hydrogeelin testauksesta tekijöitä, jotka vaikuttavat koekappaleiden ideaalista poikkeavaan käyttäytymiseen puristustesteissä. Ilman toteutettuja full-field-mittauksia nämä tekijät jäävät helposti piileviksi lisäten näin ollen menetelmän epätarkkuutta.

Murtumismekaanisten testien analysointi perustuu testikappaleessa etenevän särön suoraan tai epäsuoraan seurantaan, joka testimenetelmien alkuperäisissä toteutustavoissa suoritetaan tyypillisesti visuaalisesti. Erityisen hankalaa, ellei jopa mahdotonta särön sijainnin määritys perinteisillä mittausmenetelmillä toteutettuna on testeissä, joissa särö ei avaudu vaan etenee leikkautumalla (moodi II -särö). Väitöskirjassa kehitettiin tarkastelluille testimenetelmille soveltuvat menetelmät särön kasvun seuraamiselle perustuen DIC:n tuottamaan muodonmuutoskenttään. Kehitetyt menetelmät vähentävät merkittävästi operaattorin subjektiivisesta tulkinnasta aiheutuvaa epätarkkuutta testien toteutuksessa. Erityisesti tarkasteltiin syklistä, väsyttävää kuormitusta liimatulla koekappaleella.

CONTENTS

ABBREVIATIONS

AM	Additive manufacturing
CBBM	Compliance-based beam method
CCD	Charge-coupled device sensor
CMOS	Complementary metal-oxide-semiconductor sensor
CTOD	Crack-tip opening displacement
CZM	Cohesive zone model
DCB	Double cantilever beam test
DIC	Digital image correlation
ELS	End-loaded split test
ENF	End-notched flexure test
FEA	Finite element analysis
FEMU	Finite element model updating
FOV	Field of view
FPZ	Failure process zone
FRP	Fibre reinforced polymer
IDIC	Integrated digital image correlation
LEFM	Lineal elastic fracture mechanics
NCA	Notched coating adhesion test
ROI	Region of interest
SIF	Stress intensity factor
SLB	Single leg bending test
VCCT	Virtual crack closure technique
VFM	Virtual fields method
VSG	Virtual strain gage
ZNSSD	Zero-mean normalised sum of squared difference

a_e	Equivalent crack length
ε_{true}	Hencky strain
ε_{eng}	Engineering strain
σ_{true}	Cauchy stress

σ_{eng}	Engineering stress
ε_0	Residual strain
ε_c	Critical strain (at debond onset)
ε_y	Strain ahead of crack in the direction Y
E	Elastic modulus
ERR *or* G	Strain energy release rate
$cERR$ *or* G_c	Critical strain energy release rate (or fracture toughness)
γ_{xy}, γ_{12}	Shear strain in xy-plane, and in 12-plane, respectively
L_0	Initial gauge length in strain measurements
L_{VSG}	Size of the virtual strain gauge
L_{window}	Length of the strain window
L_{Step}	Step size
L_{Subset}	Subset size
ν	Poisson's ratio
w	Opening displacement
v	Shear displacement

ORIGINAL PUBLICATIONS

Publication I Jairan Nafar Dastgerdi, Janne T. Koivisto, Olli Orell, Pantea Rava, Jarno Jokinen, Mikko Kanerva & Minna Kellomäki. Comprehensive characterisation of compressive behaviour of hydrogels using a new modelling procedure and redefining compression testing. *Materials Today Communications, Volume 28, September 2021, 102518*

Publication II Olli Orell, Jyrki Vuorinen, Jarno Jokinen, Heikki Kettunen, Jani Turunen, Pertti Hytönen & Mikko Kanerva. Characterization of elastic constants of anisotropic composites in compression using digital image correlation. *Composite Structures, Volume 185 (2018) 176–185*

Publication III Olli Orell, Jarno Jokinen, Marke Kallio, Mikko Kanerva (2021). Revised notched coating adhesion test to account for plasticity and 3D behaviour. *Polymer testing, Volume 102, October 2021, 107319*

Publication IV Jarno Jokinen, Olli Orell, Markus Wallin & Mikko Kanerva. A concept for defining the mixed-mode behaviour of tough epoxy film adhesives by single specimen design, *Journal of Adhesion Science and Technology, Volume 34, 2020 - Issue 18*

Publication V Olli Orell, Jarno Jokinen, Mikko Kanerva. Use of DIC in the characterization of mode II crack propagation in adhesive fatigue testing. *International Journal of Adhesion and Adhesives, Volume 122, February 2023, 103332*

AUTHOR'S CONTRIBUTIONS

Publication I The mechanical testing was carried out by J.T. Koivisto together with the author. The author planned and conducted the DIC measurements and analysed the corresponding results. The author wrote the DIC section and participated in revising and finalising the full manuscript. The publication has also been included in the doctoral thesis by Janne T. Koivisto (Development and Characterization of Gellan Gum Based Hydrogels for Soft Tissue Engineering Applications, 2019).

Publication II The author planned and executed all experiments as well as analysed the consecutive results. The FE analysis was carried out by J. Jokinen. The author prepared the full manuscript excluding the FEA section. The co-authors commented and participated in the finalisation of the manuscript.

Publication III The author performed all specimen fabrication, experimental testing and analysis of the results. J. Jokinen performed the FE analysis and wrote the corresponding section in the manuscript. The author prepared the manuscript that was finalised together with the co-authors.

Publication IV The author performed the experimental testing and planned and executed the analysis of the DIC measurements. The manuscript was written together with J. Jokinen and finalised by the co-authors.

Publication V The author planned and executed all experimental testing and analysis of the results. The author prepared the full manuscript, which was revised and finalised by the co-authors.

1 INTRODUCTION

Materials create the basis for all technologies. The leaps in technological developments are closely related to the progress in material development. The pace in the development is fast – new applications continuously call for better and better functioning materials. New requirements are continuously set, and these requirements can be fulfilled by the development of new materials. Another solution to the requirements is to utilise current materials more efficiently by creating composites, or hybrids, by combining several materials into single system, which performs better than its individual constituents. In addition to the creation of novel technological solutions, the increased awareness of the importance of energy efficiency and the retaining of natural resources loudly call for more efficient methods to replace the already established products and technologies.

The solid development of novel materials also creates the continuous need for various procedures of materials testing. The novel material systems to fulfil the requirements are far more complex than the preceding solutions. For example, different composite materials can offer novel property combinations that are impossible to achieve by (known) monolithic materials. In these composites, behaviour at the macroscale can seem homogeneous but, in reality, the performance is based on the intrinsic heterogeneity at the micro- and nanoscale. On the other hand, hybrid structures, which combine dissimilar materials at the macroscale into a single operating structure (i.e. macrocomposites), can be extremely efficient working solutions. However, property mismatches and component interfaces create new problems, which are often uncharacteristic to more conventional material solutions. All the above-mentioned can be summed up by claiming there is an increased *intrinsic need* for more detailed and tailored material testing, due to the development of the novel and challenging material solutions.

Simultaneously, with the development of new materials, significant progress in analysis methods is going on in terms of how the material data obtained from the experiments is utilised. Numerical analysis methods have already replaced the conventional and established analytic procedures in many areas, enabling more valid and detailed interpretation of the test outcomes. The ideology of multiscale

modelling can vastly improve efficiency in the development of new materials or products [1]. Also, research and development tasks are more and more commonly performed in a virtual way using different kinds of digital twin solutions [2]. However, for the above-mentioned methods to offer the desired outcomes, they require significant amounts of accurate and reliable experimental data. Thus, it can be concluded that development in the analysis and utilisation techniques of the test outcomes creates the *extrinsic need* to acquire more detailed experimental testing data.

The testing for material properties relies, generally, on established procedures and often on standardised methods. Naturally, newly developed experimental techniques continuously evolve, and the basis of this evolution is to improve the reliability, accuracy and efficiency of the testing routines. However, the establishing process takes time. Due to the high speed of the development and the increased scarcity of the novel material solutions, it is evident that the development of the specific testing routines easily lags behind the actual material development. This leads to a situation where the previous test protocols may still be largely used to characterise novel materials or test specimens which were actually not developed to offer the data sought for. For example, an established analytic solution may have originally been derived, for simplicity, to account for a homogeneous two-dimensional problem. However, the same technique can still be routinely used to characterise a novel specimen that can inadvertently encounter significant three-dimensional effects. As a result, remarkable errors in results may appear.

In a simple event, the mechanical testing of materials is straightforward – such as when testing homogenous isotropic materials in uniaxial loading conditions. Conventionally, the measurement of the test response in standard specimens has been performed by discrete means, such as by using extensometers or foil strain gauges to study the deformation of the specimen at previously selected locations. However, with the increased complexity of the tested specimen or in the loading condition of interest, the complexity of the test responses also increases. The defining of the accurate test response with discrete measurements thus becomes more challenging, and this increases the uncertainty of the test outcomes.

In the past two decades, so-called full-field methods to study the *global* deformation responses of the studied objects have been under intensive research. Of the methods, digital image correlation (DIC) [3] in particular has already established its extensive use in a great variety of different applications, including material testing [4], particle movement measurements [5], component-scale testing [6] and fracture mechanics [7], among many others. The possibility of measuring the global deformation of a studied object creates enormous potential to improve the

performance of existing (mechanical) test methods, as summarised as the background of this thesis (Figure 1). The reliability of the established test methods can be improved using the full-field measurement techniques by carefully studying the global behaviour of the specimen or the test fixture. But even more fascinating is that the full-field data enables the development of totally new analysis approaches. These new approaches offer vastly more detailed and accurate material data that is increasingly sought after and that has been impossible to obtain with conventional methods [8]. This potential of DIC will be studied in depth in this thesis.

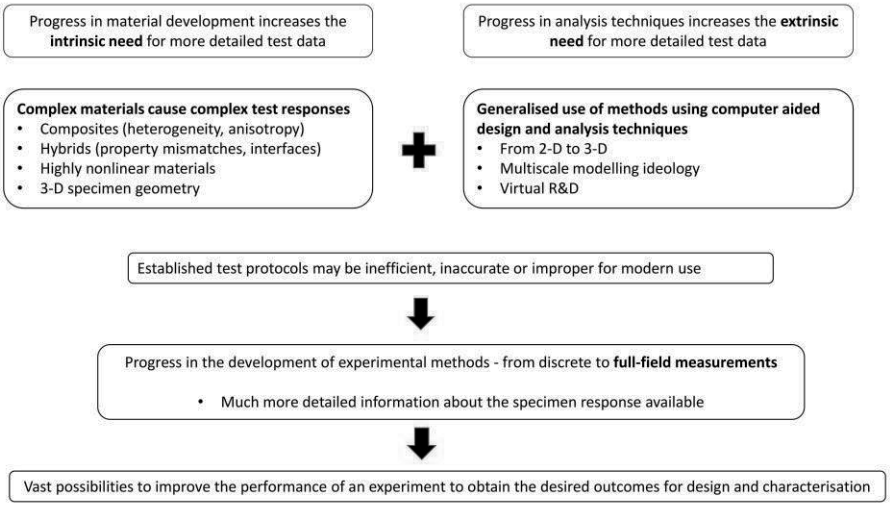

Figure 1. Summary of the motivation aspects, the background, of the thesis.

2 AIMS OF RESEARCH AND HYPOTHESES

In this thesis, the exploitation of 3-D digital image correlation (DIC) is investigated in selected compression and fracture mechanics tests with different polymer-based materials in the specimens. The focus in the work is about how to efficiently utilise the current established subset-based local DIC techniques to get the desired and even new output from the experiments. This focus is expected to result in more detailed data of the specimens' materials and thus extend the scope and improve the precision of the selected test methods. Thus, the aim is to present how DIC measurements can be used in a practical way to further improve the established testing procedures and to offer more precise understanding of the test responses, especially when heterogeneous or nonlinear-behaving materials are investigated with the methods.

The studies of the hypothesis are reflected in two fundamental research questions of this thesis:

- How can the effect of the operator- and specimen-dependent unknown factors in compression and fracture mechanics testing with complex polymer-based test specimens using DIC be minimised?

- How can the high spatial resolution provided with DIC help to improve the mechanical and fracture mechanics test methods for notably anisotropic and heterogeneous materials?

The thesis and its published work are built on four hypotheses:

1. DIC can be used to validate the test response in the unconfined compression of wet hydrogel materials. (Pub I)

2. A set of elastic constants can be solved by enhanced use of small specimen size and DIC for fibrous composite materials. (Pub II)

3. The reliability of the notched coating adhesion test method can be improved by using DIC, even when highly non-linear coating is used. (Pub III)

4. DIC can be used to quantify the local strain state and crack propagation in mode II-dominated quasi-static and fatigue experiments, even for joint specimens with thin bond lines. (Pubs IV and V)

Here, the measured deformation response of an experiment is the base information from which the material properties are eventually determined. One of the main aims in the utilisation of the DIC in the selected material test methods was to minimise the bias to the test results caused by the operator, specimen or testing jig. This was done by systemically examining the 3-D deformation of the specimens to reveal anomalies in the assumed test responses. This enabled us to recognise factors affecting the test results that were difficult, or impossible, to identify without the information provided by DIC. In the traditional process, the specimen deformation is measured either by greatly averaging and contact-requiring (e.g. crosshead traverse or extensometer) or pointwise methods (e.g. strain gauges). In this thesis, new analysis techniques of the investigated test methods were developed that aimed at more applicable and precise characterisation. This was done by first identifying the lacking features that the current techniques possess, and then tackling the recognised problems by developing new analysis approaches based on the measured full-field responses.

This thesis is a compilation dissertation based on five original scientific publications. The structure of the thesis consists of a condensed background theory about DIC (Chapter 3), focusing on its use in material testing with heterogeneous specimens. The experimental methods, and the technique about how the DIC was utilised for acquiring the data, is presented in Chapter 4. The above research questions, in terms of publications I–V, respectively, are discussed in Chapter 5 and the conclusions to the hypotheses will be presented in Chapter 6.

3 BACKGROUND THEORY

3.1 Mechanical and fracture testing of composites, and hybrid materials and structures

Generally speaking, composite is understood as a material system, in which two or more materials are combined during the fabrication process into a single synergistic unit. Composites can be categorised in multiple ways, such as by their constituents' 1) material classes, 2) dimensions or 3) sizes. Hybrid materials are commonly defined as materials incorporating organic and inorganic components (often at the nano- or microscale). Hybrid structures, on the other hand, are defined in this thesis as macrocomposites, in which different materials are combined into a single working unit. Thus, by following these definitions a composite or hybrid material is a continuum, whereas a hybrid structure is comprised of finite blocks of different materials adhered together permanently. In materials, length scales play an evident and important role.

Composites and hybrids offer enhanced performance and flexibility of design over single-constituent materials. However, the increased complexity related to materials complicates the determination of materials' properties and induces challenges in their testing procedures. Certain special features, discussed below, are characteristic of composites and hybrids and have to be considered in testing.

Anisotropy

While excluding the composites with zero-dimensional particulates, composite materials often show anisotropic behaviour. Thus, many of the material properties are dependent on the direction, due to which multiple tests are required to find out the required information for characterising the material behaviour [9]. For example, where the elastic behaviour of isotropic materials (e.g. randomly oriented polycrystalline metals or glass) can be defined by two independent elastic constants, for transversely isotropic material (e.g. unidirectional composite lamina) five independent constants are required. For the orthotropic material model (e.g. wood), the amount of independent elastic constants is already nine. The linear-elastic

compliance matrices clearly present the simplest symmetries of material models, as depicted in Figure 2.

$$S^{(iso)} = \begin{bmatrix} \frac{1}{E} & -\frac{\nu}{E} & -\frac{\nu}{E} & 0 & 0 & 0 \\ -\frac{\nu}{E} & \frac{1}{E} & -\frac{\nu}{E} & 0 & 0 & 0 \\ -\frac{\nu}{E} & -\frac{\nu}{E} & \frac{1}{E} & 0 & 0 & 0 \\ 0 & 0 & 0 & \frac{1+\nu}{E} & 0 & 0 \\ 0 & 0 & 0 & 0 & \frac{1+\nu}{E} & 0 \\ 0 & 0 & 0 & 0 & 0 & \frac{1+\nu}{E} \end{bmatrix} S^{(ortho)} = \begin{bmatrix} \frac{1}{E_1} & -\frac{\nu_{21}}{E_2} & -\frac{\nu_{31}}{E_3} & 0 & 0 & 0 \\ -\frac{\nu_{12}}{E_1} & \frac{1}{E_2} & -\frac{\nu_{32}}{E_3} & 0 & 0 & 0 \\ -\frac{\nu_{13}}{E_1} & -\frac{\nu_{23}}{E_2} & \frac{1}{E_3} & 0 & 0 & 0 \\ 0 & 0 & 0 & \frac{1}{G_{23}} & 0 & 0 \\ 0 & 0 & 0 & 0 & \frac{1}{G_{13}} & 0 \\ 0 & 0 & 0 & 0 & 0 & \frac{1}{G_{12}} \end{bmatrix}$$

Figure 2. The compliance matrices for a) isotropic and b) orthotropic linear elastic materials.

Due to the lack of symmetry and a finally complete anisotropy, many of the test methods developed for isotropic materials are not feasible for composites. In some cases, the test specimen type can be modified for better suitability with anisotropic materials. For example, in the tensile test, the common dogbone specimen cannot be used with unidirectional composite laminates due to the material's relative weakness under (local) shear during tensile loading. For laminates, straight-test coupons can be successfully tested using long adhered end tabs [10]. However, numerous important properties require specific test methods developed specifically for composite materials and new, improved methods are indeed continuously studied.

Heterogeneity

Whereas single-constituent materials are homogeneous, composites and hybrids are strongly heterogeneous by nature. In fibre- or particle-reinforced composite materials, a uniform distribution of the constituents is normally targeted. However, due to the challenges in manufacturing, the actual distribution can be imperfect and practically unknown. The random-alike distribution increases the experimental scatter of the material response and complicates the analysis of the test results.

The combining of different material components into a solid unit inevitably creates internal interfaces and strong property mismatches. Basically, the interfaces in composites create the basis for all the functionality of composites yet increase the complexity in the performance of the materials. The interfaces also make the characterisation methods more challenging. Often, solid adhesion at interfaces, such as between the fibre and matrix, is sought for. Several characterisation methods have been developed to specifically study these features. Essentially, products containing coatings or joints implemented by adhesives can also be considered as hybrids. In such products, especially, a high value of fracture toughness at the interfaces is vital

and various test methods exist to evaluate the fracturing. The heterogeneity also increases the complexity among the failure types of composite and hybrid materials. For instance, in composite laminates, the failure mode can range from the bulk materials' normal failure to the interlaminar shear or the interfacial adhesion failures. Actually, the great fracture toughness of many composites base on the phenomena which occur at interfaces of the constituents. Test methods to characterize the fracture at the interfaces in detail are thus highly valuable. All in all, the use of appropriate testing methods and detailed interpretation of the test responses are essential in order to achieve the desired outcomes from the performed experiments – reliable statistics or properly normalised material constants, for example.

Length dependency

The length scale of the components in heterogeneous materials can range from the nano to the macro level. All the levels of scales have their specific characterisation procedures with their intrinsic challenges. Even though it is essential to understand the mechanical behaviour in the case of each scale, the mechanical testing of composite materials is still mostly performed at the meso or macro scale and, thus, the homogenised properties for the continuum are often determined. However, it is important to acknowledge that the responses of the mechanical tests are usually dictated by the phenomena occurring at a smaller scale in materials. How to select the proper level of homogenisation and how to ensure that the tests are performed using a representative sample of the tested material are essential questions in the testing and analysis of composite and hybrid materials.

3.1.1 Compression tests

In practical applications, materials are normally subjected to complicated loading conditions in which compression plays a significant role. The established compression tests are performed to evaluate the material response under (presumed) uniaxial compression load. In addition to identifying constitutive parameters, compression testing is used regularly in the quality assurance of construction materials, in particular. The elastic constants used to define materials' stress-strain response are generally evaluated with tensile tests. However, the evaluation of compressive properties is especially essential for fibre-reinforced composites because their mechanical properties are known to differ under tension and

compression. For example, Meng et al. reported an average compressive to tensile moduli ratio of 0.9 for unidirectional carbon fibre laminates. The ratio of compressive-to-tensile strengths is even lower, around 0.6–0.7 [11].

Several different standard tests exist for compression, which differ mostly in terms of the technique used to transfer the load to the specimen. Unconfined compression tests are the simplest, where the flat-ended cylindrical or rectangular specimen is loaded using two parallel compression plates. For measuring in-plane compression for sheet- or plate-type samples, the unconfined compression tests are not feasible and specific testing jigs are used that prevent the buckling of the specimen.

In principle, compression tests are simple to carry out but, at the same time, they are prone to test artefacts related to jigs and specimen. The generally assumed uniaxial loading in the specimen is actually difficult to achieve – for example, in the unconfined compression method, contact friction can easily play a strong role. The recorded traverse of the moving crosshead is still a commonly used method for measuring the specimen response in compression. This holds especially when testing materials whose nature restrains the use of foil strain gauges, such as soft elastomers, foams or hydrogels. However, the traverse includes all the compliances caused by the testing apparatus and the used jigs, the effects of which are often unknown. Compression tests include some 3-D effects, although their role is often excluded in the conventional analysis of results. The measuring of the exact specimen deformation during testing is challenging because the detailed 3-D deformation data is difficult to obtain using conventional, discrete measurements. The measurement of specimen deformation directly is an important requirement in the compression testing of novel materials.

3.1.2 Fracture mechanics tests using layered specimens

Adhesively bonded joints are used increasingly in various metal or composite hybrid structures, as they provide low structural weight, great damage tolerance and low manufacturing cost. In the design of adhesively bonded joints, the ability to characterise the crack onset and propagation in the structure is essential to ensure the functionality of the joint. This holds true especially for structures where the highest material performances are required, such as in the aerospace industry [12].

The methods to determine fracture parameters are generally based on linear elastic fracture mechanics (LEFM). LEFM theory is applicable for brittle materials

or when the region of plastic deformation (due to the stress singularity) can be assumed to be small compared to other dimensions of the specimen. In practice, the parameters that are used to characterise the fracture include, for example, stress intensity factor (SIF), critical energy release rate (G_c) and crack-tip opening displacement (CTOD) [13].

G_c, is a generally used parameter to characterise the resistance against fracture for adhesive joints. Specific test methods to determine G_c are employed, such as double-cantilever beam (DCB) [14] for mode I fracture and three-point end-notched flexure (3-ENF) [15], four-point ENF [16] and end loaded split (ELS) [17] for mode II. The methods utilise sandwiched layered specimens that consist of rigid substrate components and a thin layer of the studied adhesive material. An artificial crack is fabricated in the specimen, whose onset and-or propagation in the loaded specimen is studied.

Detection of the initiation (onset) and propagation of the crack in fracture mechanics tests is a well-known challenge. The traditional, and still commonly used, method to determine the crack position is carried out by visually detecting it *in-situ* or from the recorded images afterwards. For mode I (opening) fractures this can normally be performed successfully but is still always a subjective method. On the other hand, in cases where the fracture is dominated by mode II (shear), the visual detection of the crack position can be extremely difficult, or even impossible [15]. The major source of error in the G_c measurements thus lies in the crack length measurements [18]. Alternative strategies have been used to measure the crack length such as strain gauges, distributed optical fibre sensors and acoustic emission techniques. However, the accurate linking of the crack length to the indirect measurements is not straightforward. To overcome the challenges caused by the accurate crack length measurements, various analytical specimen compliance-based approaches have been developed to describe the specimen response with a progressing crack. On the other hand, the direct measurement of the crack length is strongly preferred when, for example, finite element analysis (FEA) is used to simulate the experiment, which is an increasingly utilised technique to solve the values of fracture parameters.

3.2 Digital image correlation

Digital image correlation is a non-contact optical method to acquire full-field deformation data from a studied surface. The idea of utilising digitised optical images

for fast computer-based deformation analysis in experimental mechanics was introduced in the early 1980s by Peters and Ranson [19]. Later, Sutton's team [20], [21] developed the process further and created the basis for the current DIC methods. During the past 30 years, the pace of progress has been fast, both in terms of hardware, especially cameras and the computational capacity of computers, and the fundamental DIC algorithms. A bibliometric study (retrieved using Web of Science™) presented in Figure 3 shows that the use of DIC in scientific publications began to increase rapidly after the mid-2000s and has increased ever since. Nowadays, DIC is already a mature method that has proven its usefulness in different applications in the field of experimental mechanics. This can also be seen in Figure 4, which depicts the diversity of the publication categories for the DIC-related publications.

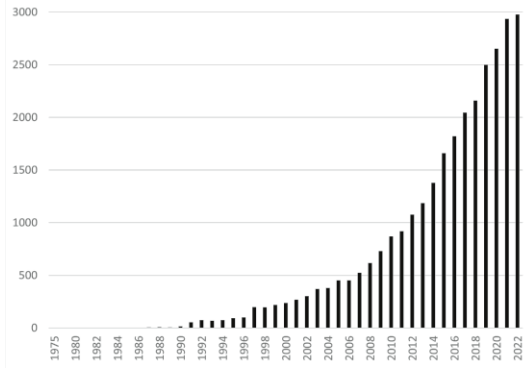

Figure 3. Number of publications per year related to Digital Image Correlation (Source: Web of Science™)

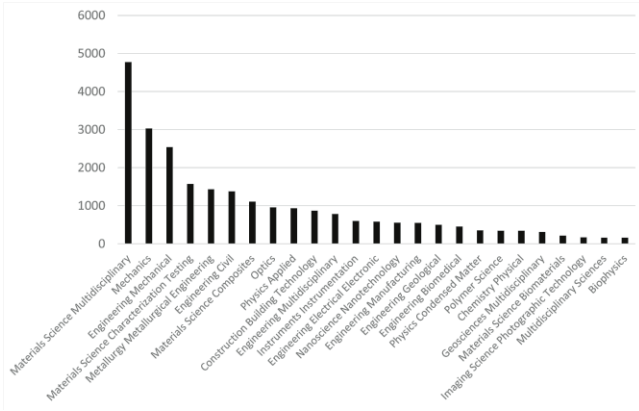

Figure 4. The categories for the Digital Image Correlation containing publications, 1994–2022). (Source: Web of Science™)

Simplified, DIC is based on tracking local motion on discretised surfaces containing a random surface pattern. During the DIC process, the full-field surface displacements are calculated by numerically correlating the deformed surface pattern against the reference pattern ('motion'). 2-D displacement vectors perpendicular to the optical axis of the camera can be measured with one camera system. Simultaneous use of two (or more) cameras enables the determination of surface deformations in 3-D. This method is generally known as the stereo DIC which enables more robust correlation algorithms. Stereo DIC should also always be used when the studied object has non-planar surfaces or out-of-plane deformation is likely to exist during measurement. After the displacement field has been defined, the surface strains can be obtained from the derivative of the determined displacement field. The basic workflow of the DIC measurement process is shown in Figure 5.

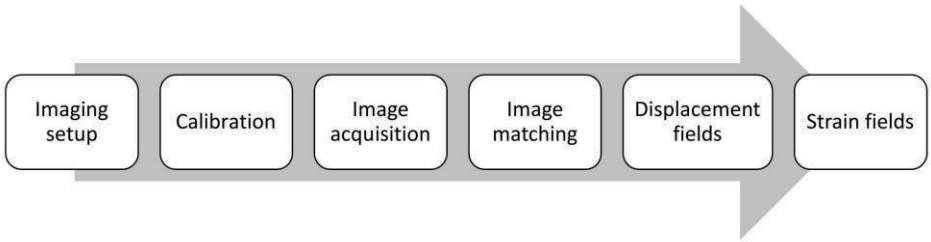

Figure 5. Workflow of the DIC process in general.

Different approaches to DIC exist that can be divided into so-called local and global methods [22]. In the local methods, the acquired images are processed using a battery of smaller regions of the image (called subsets) that include unique features to be distinguishable and whose instantaneous relative locations are computed separately. In local methods the displacement field is thus generally incompatible. However, the implementation of the calculations can be carried out in parallel enabling very fast analysis. The global methods, such as the four-node FE-based DIC [23] and the extended DIC (X-DIC) [24], are generally based on finite element approaches. In these methods, the full region of interest is discretised into elements connected by nodes. By tracing the elements simultaneously, the displacement continuity is guaranteed between neighbouring elements. The global DIC methods have the potential to improve abilities to ensure the accurate matching of smaller details and heterogeneous structures [25]. Also, global techniques can offer more

seamless linking with numerical simulation methods. On the other hand, the convergence of the global methods is slow, and they are computationally significantly more costly.

Recently, new methods to combine the advantages of local and global DIC have been introduced such as the Augmented Lagrangian DIC [26]. However, up to now, the subset-based local DIC is used in most commercial software codes largely due to its high efficiency, and is it still the dominant method in the field of experimental mechanics.

3.2.1 Correlation procedure

The first essential step of the 3-D DIC measurement is the calibration of the camera setup. The purpose of the calibration is to orient and scale the images of the cameras to the physical world positions. A number of different calibration methods [27] exist, but the technique based on the landmark principle is generally implemented in current DIC software [28]. Here, several images of a calibration grid plate are taken by altering its orientation between the views. With the images, the intrinsic and extrinsic calibration parameters of the cameras are defined. The intrinsic calibration parameters include, for example, the focal length, the distortion coefficients, and the centre point of the individual cameras. The extrinsic parameters then define the translation and rotations between the used cameras, which are required for the triangulation procedure enabling studies in 3-D.

In the local DIC methods, a portion of the investigated area in the acquired image, that contains a unique pattern for the pixel intensity in greyscale, is known as a subset. The shape of the subset is typically square, but oblong or round subsets can also be used. In the DIC process, multiple, typically overlapping, subsets are positioned on a grid in the processed image. The distance between two adjacent subsets (in pixels) in the calculation process is called the step size. The basic principle of the DIC is to search for the accurate position of each subset from image to image by the utilised correlation criterion. The searching is carried out by minimising (or maximising) the correlation function that includes the information of the pixel intensities from both the reference and the deformed images. The outcome of the correlation function is thus a measure how accurately the details in the processed subsets correlate with the reference image. The ultimate target of the correlation process is to detect the closest match between the reference and deformed subsets to determine the temporal position of moved subsets in the processed images.

The changes in the illumination affect the recorded greyscale intensities of the speckle pattern that, without compensation, produce fundamental error for the results of the correlation process. Several different correlation criteria exist, such as sum-squared difference (SSD), normalised cross-correlation (NCC), zero-normalised cross-correlation (ZNCC), and zero-mean normalised sum of squared difference (ZNSSD). ZNSSD can efficiently compensate the typical, unavoidable changes in the brightness and contrast during an experiment and is nowadays one of the most regularly exploited criterion in the DIC software packages.

As the studied surface deforms, the subset shape also changes from the original (e.g., square). The shape change of the subset in the correlation process is accommodated with mathematical shape functions. The simplest shape function is the zero-order rotation-free rigid translation. The first-order affine shape functions allow translations, rotation, linear stretching and shearing, and are routinely used in DIC analysis. Higher order shape functions allow non-linear deformation of subsets which is particularly beneficial to curved surfaces. In addition, they can also adapt better to strain gradients occurring inside a subset, which is more likely to occur when the used subset size is large. However, the more complex the shape function, the more computationally expensive they are.

The raw results of stereo DIC process are 3-D points that practically define the locations of each subset's centre in the deformed images. The density of the point grid is defined by the step size in the performed analysis. The displacement vectors are then determined by subtracting the deformed 3-D point cloud from the reference points, as presented schematically in Figure 6. Finally, strains can be calculated by the derivation of the displacement data, which is often the targeted quantity of interest in the DIC measurements. The comprehensive description of the fundamentals of the full DIC process is explained extensively in the current literature [3], [27].

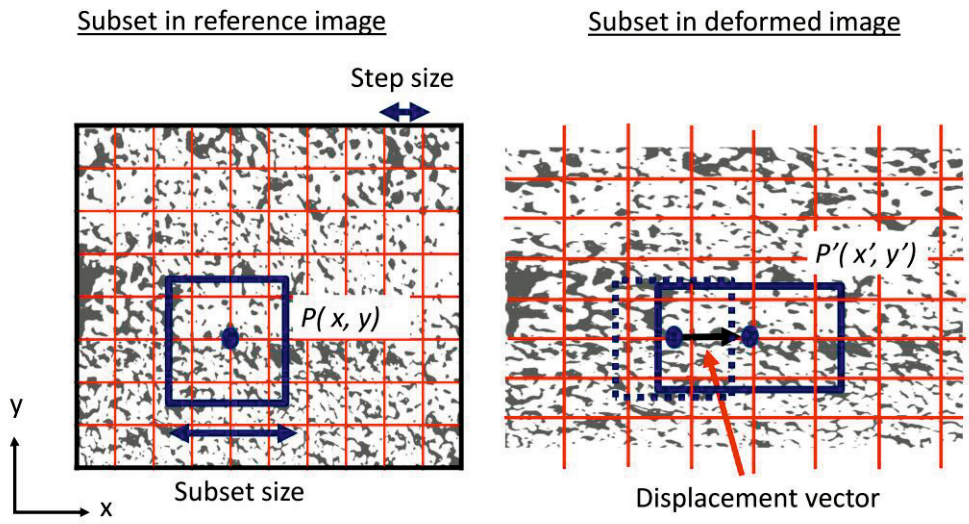

Figure 6. The schematic principle of the DIC.

3.2.2 Requirements for the images and their acquisition

DIC is based on the numerical processing of acquired digital images. Naturally, the most general method for acquiring images is to utilise optical imaging equipment such as that presented in Figure 7. However, DIC is not limited to using optical (white light) imaging and basically any series of images that can provide sufficient contrast patterns can be used. For example, thermal imaging [29], electronic imaging [30] and scanning probe microscopy [31] have been utilised for deformation measurements with the method.

In optical imaging, cameras with a high-resolution charge-coupled device (CCD) or complementary metal-oxide-semiconductor (CMOS) sensors and objectives with minimal lens distortions are typically used. Shooting parameters must be optimised to produce sharp and consistent images for the full imaged region. A high depth of field is often required in the characterisation of 3-D surfaces, calling for the use of a small aperture. At the same time, to minimise the motion blur caused by the moving subject, a fast exposure time is required. In order to decrease the pixel noise of the sensor due to a lack of sufficient lighting, the test setup normally includes powerful extra lights. Good practices for carrying out typical DIC measurements have been described in detail in the guidebook by the International Digital Image Correlation Society (iDIC) [32].

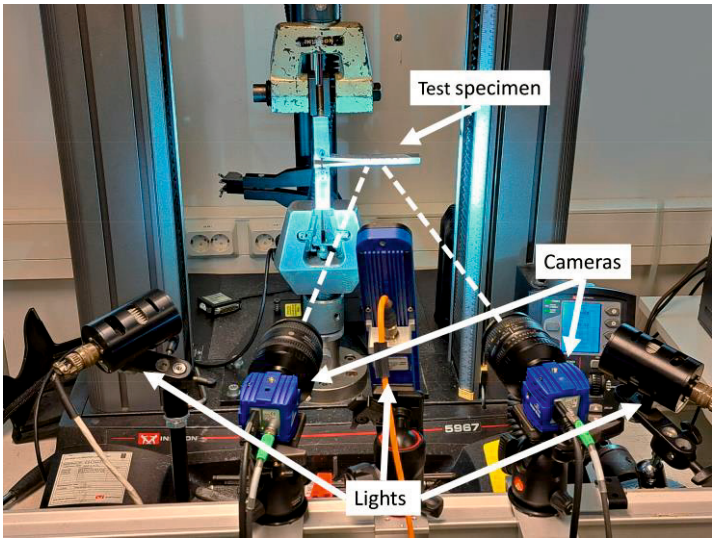

Figure 7. An example of a typical 3-D DIC test setup.

The complete imaging hardware eventually defines the smallest displacement resolution that can be achieved in the experiments. The displacement resolution is proportional to the image resolution (or the mm-to-pixel -ratio), and resolution of 1/30th of a pixel can be often achieved. The actual displacement resolution can range from nanometres (using atomic force or electron microscopy) to hundreds of metres (using e.g. optical satellite images [33]). The temporal resolution of the method is dictated plainly by the achievable image acquiring frequency. For example, the extremely high measuring frequency (>100 000 Hz) that can be obtained with high-speed cameras has enabled the realisation of novel fracture mechanics and vibration measurements.

In the local DIC method, the acquired images are divided into subsets and, during the correlation routine, each subset is processed independently. The requirement for the method is that the subsets include a unique signature, which is guaranteed when the surface has a high-contrast and non-repetitive pattern. A common rule-of-thumb to achieve good results is that a subset should have at least three separate speckles. The size of the subset can be varied when carrying out the correlation routine but the surface pattern, naturally, is defined prior to testing. Also, the diameter of a single speckle should always be more than three pixels to prevent fundamental error due to aliasing caused by undersampling [34]. Thus, the speckle size must always be considered carefully together with the targeted spatial resolution in the planning

phase of the experiments. The fundamental requirement for the pattern is that it must follow the underlying sample as the studied object deforms. In some cases, the natural pattern of the studied surface can be sufficient for performing feasible DIC analysis. Such examples include, for instance, the surfaces of rocks or wood, and the grain boundaries or distributed filler particles at high magnifications in microscale measurements. However, because the quality of the speckle pattern (i.e. size, contrast and distribution) has a great influence on the resulting accuracy of the method [35], normally an optimised random black-and-white pattern is applied to the surface prior to testing. The most common methods for generating the pattern are spraying, stamping and water transfer printing.

3.2.3 Uncertainties in DIC measurements

The accuracy and precision of the displacement measurements with DIC are dependent on the number of factors. Some of the well-recognised factors playing a role for the DIC results are presented in Figure 8. Basically, all the information that the determined values of the analysis are composed of is based on the acquired images. Thus, high contrast images with good resolution are always targeted, and their quality has the most essential importance when considering the results. All factors that can reduce the image quality should be minimised, such as vibrations (both the thermal and the test setup vibrations) and uneven or varying illumination (e.g. glares). The complete error chain for the determined results of a DIC measurement is complex, and the total uncertainty always originates from several sources. The comprehensive analysis of all the errors for stereo DIC is thus very challenging.

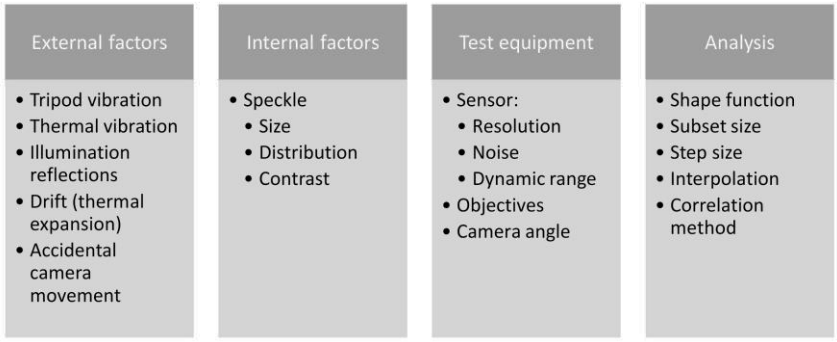

Figure 8. List of parameters affecting the DIC results as a whole.

In engineering applications, often the strain data is sought after instead of the plain displacement information. The spatial resolution (or the density of the measurement point grid) for the displacement is defined by the step size, and the single extracted displacement value represents the displacement of the area dictated by the used subset size. Strain is normally calculated from the determined displacement data over larger area to reduce noise. The area from which the single strain value is computed can be approximated by the size of the Virtual Strain Gauge (VSG) by:

$$L_{VSG} = (L_{Window} - 1) \times L_{step} + L_{subset} \tag{3.1}$$

Here, L_{Window} defines the number of (displacement) data points over which the strain value is determined, and L_{step} and L_{subset} describe the size of the step and the subset (in pixels) in the correlation process. The minimum length of the VSG is thus $L_{step} + L_{subset}$ when the strain is calculated using the adjacent points of the determined displacement field. By increasing the L_{Window} parameter, the VSG size increases (i.e. the locality of the information diminishes) but also the accuracy of strain increases (through statistical averaging) since more data points are used to calculate the quantity. If compared to the displacements, quantifying the accuracy of the determined strain values is more complicated, or even impossible to carry out unambiguously. As strain is derived mathematically from the measured displacements, the measurement noise is strengthened during the process, resulting in uncertainty in the calculated strain always being accentuated.

3.3 Use of DIC in material testing

What is especially characteristic of composites and various hybrids is their strong length dependency in almost all material properties: the ultimate parameters in the macroscale are basically derived from the mesoscale properties and finally from the microscale. For a researcher, this dependency often creates a problem – conventionally one must plan and select the utilised experimental measuring technique strictly according to the aim of the study. A good example relates to the conventional electrical resistance strain gauges used to measure strains. When planning the test setup, one has to decide, in advance, the proper gauge length (averaging length), the number and precise locations of the gauges and their

orientations. However, the load distribution in a hybrid structure is challenging to predict and the gauge installation can be challenging. Typically, (foil) strain gauges are positioned there where the expected strain field has a low gradient (in any direction). The gauge installation is also prone to effects from fixing the gauges (manually) on the surface. In contrast to *local discrete* measuring methods, the above problems can, in many cases, be avoided using full-field techniques to measure the *global* behaviour, for example by using DIC. Full-field methods allow, *after* the well performed measurement, for the making of decisions and running multiple analysis of parameters.

The purposes of the DIC measurements in material testing can be classified into four categories, as described by Pan [27]. The characterisation can be defined as examination of the deformation response of a studied target to external loading, whereas identification aims to determine quantitative material properties by combining the DIC-measured strain data to the known exerted mechanical loading. In cross-validation, the correctness of the FEM analysis or analytic predictions can be verified with the measured experimental fields. Finally, DIC-based measures can also be used in controlled mechanical testing to adjust the measuring devices. In this thesis, DIC is used mostly for characterisation (Publications I–V), but also for identification (Publications I and II) and cross-validation (Publication IV) purposes.

3.3.1 Testing of specimens with non-continuous deformation

DIC is an especially advantageous technique for studying targets with heterogeneous deformation, where the use of conventional single point measuring devices (e.g. extensometers) would easily measure an overly averaged test response. Also, a great number of devices (e.g. displacement sensors or strain gauges) would be required to study the 'heterogeneous' behaviour, or the field of it. Good examples of applications where DIC has been successfully exploited to study local deformation response include adhesively bonded structures and various hybrid joints [12], [13], [36]–[39]. In the studies, the failure mechanisms of the joints (i.e. measuring the local peel and shear deformations) and locations of the strain concentration (hot spots) have been determined, among others. For example, the results have been used in optimising the performance of the adhesively bonded repair patches for composite laminates [40]–[42].

DIC has also been used in the characterisation of thin coatings, which are generally challenging to examine. Both the mechanical properties and interfacial toughness of coatings on rigid substate specimens have been determined [43]–[45].

The mechanical performance of materials fabricated by additive manufacturing (AM) methods deviates in many cases from the behaviour of isotropic materials. The structures are generally at least partly heterogeneous, since they are built of material layers which typically orientate during manufacturing. As a result, in cases where the conventional gauges can be insufficient to describe the complex mechanical behaviour of the materials, DIC has proven its usefulness in the characterisation and identification of AM structures [46]–[48].

Fibre-reinforced composite laminates are well-known owing to their anisotropic behaviour. The bulk behaviour of common composite materials has been extensively characterised using DIC. The method has been used, for instance, in identification of elastic moduli and Poisson's ratios [49]–[51] and also in the characterising of their damaging mechanisms [52]–[54]. The possibility to measure local deformation data is very useful for the interpretation of results in tests like open-hole fracture tests [41] and compression-after-impact tests [55].

Like other full-field characterisation methods, DIC can accurately measure deformation fields with strong gradients, which are challenging to study with discrete physical measuring devices. The method has enabled, for example, experimental mesoscale measurements to study the effect of reinforcement fabrics' weave patterns on the deformation response [4], [56], [57] On the other hand, DIC is still a fuzzy measuring technique by definition because it averages the measured data over its subsets. The deformation gradients or local fragmentation caused by the geometric discontinuities, located for example at the materials' interfaces or cracks, thus cause challenges for the method [27], [58]–[61]. In local DIC, the size of the subset essentially dictates the spatial resolution of the derived displacement field. Decreasing the subset size improves the spatial resolution but simultaneously increases the noise, thus decreasing the accuracy of the measurements [60]. When the subset size approaches the order of the size of heterogeneities in the studied specimen, or when the subsets cannot resolve the localised strain variations, it is evident that the conventional DIC leads to increased local error. This occurs because the regularly used shape functions for the subset deformation cannot characterise the displacement discontinuity occurring inside a subset. Because of this, the very vicinity of the interfaces, or other discontinuities, in the specimen are difficult to study accurately. Also, the effect of the small-scale discontinuities on the analysis

results is difficult to verify, so the resulting strain values in regions containing interfaces can be unreliable.

In order to overcome the discontinuity limitation of the conventional local DIC method hindering the detailed study of interfaces, modified methods have been presented, including the point-wise method [62] and mesh adaptation techniques such as the subset-splitting method [63]–[65]. The point-wise method utilises genetic algorithms to process each pixel separately. It can be used to capture the detailed displacement field in the vicinity of the cracks but is computationally very expensive. The subset-splitting methods are based on 'improving' the shape function of the subset when a discontinuity is detected by dividing the subset into two sections. The methods are rather simple but require further progress to account for regions with multiple cracks or other discontinuities instead of a distinct crack [66]. The global DIC methods can adapt the deformation discontinuities better [25] showing potential use in interface studies but are not included with the recent DIC software packages which base on local method.

A straightforward technique to enable more accurate deformation measurements in the vicinity of a discontinuity with conventional local DIC is to increase the spatial resolution by decreasing the subset size. However, the size of the speckles of the pattern eventually dictates the minimum usable subset size (because single subset should include a minimum of 3–5 individual speckles). An exceptionally fine surface pattern is thus required together with high magnifying imaging setup if the spatial resolution is to be minimised. Feasible methods to fabricate speckle patterns for micro DIC measurements has been introduced by Kammers [67]. For example, detailed micro-scale measurements of polymer composites have been carried out to study the material deformation at single fibre scale. The fine surface pattern was accomplished by applying a nanoscale pattern with submicron alumina particles. The actual measurements, using compression [58] and three-point bending [68] fixtures, were monitored with a scanning electron microscope. It is obvious that the size of the field of view of such measurements (as well as the actual specimen size) is very limited. Studies focusing accurately on the locations near the interfaces require a strongly focused, and thus size-limited, region of interest. Performing focused measurements where a large field of view but still a high spatial resolution is needed or the preferred location to be accurately focused does not remain stationary during a test are thus challenging to carry out. Such tests include, for example, the detailed characterisation of deformation along a thin adhesive bond line or the measuring of a deformation field at the very vicinity of a propagating crack tip.

3.3.2 Use of DIC in fracture mechanics tests

In fracture mechanics tests generally, the crack length and the displacement field of the material around the crack tip is the essential information that is sought from the experiments (in addition to the applied loading). The DIC experiments have been used extensively to study the fracture parameters in various loading modes for bulk material specimens. For example, many studies present how the stress intensity factors have been determined using notched specimens where the displacement fields can be measured accurately around the known crack tip region [69]–[72]. The displacement field data can then, for example, be substituted in analytical relations based on linear elastic fracture mechanics that relate the displacement components to the determined fracture parameters. DIC thus has enabled measuring experimentally fracture parameters that has been challenging to carry out by discrete means due to stress singularity near the crack tip (i.e. very steep gradient).

The fracture mechanics tests of adhesives differ from measurements with bulk materials, since the tests are performed generally using specimens with rigid substrates and thin adhesive bond lines. The experiments normally target measuring the critical value, which is followed by the crack propagation. The established (standard) analysis methods are commonly used, which are often built on linking the measured crack length to the applied loading. The conventional optical methods, to characterise the crack in a specimen, are most typically based on the detection of changes in the contrast in images, due to an onsetting or propagating local discontinuity. To be able to distinguish between the studied regions in the images, various binarisation techniques are used during the image analysis [73]. However, the adhesive-adherend structure is generally very complicated where several local effects occur, such as plasticisation and the non-uniform cracking of the adhesive or the fibre bridging at the interphase, which impede the crack length determination.

DIC-based techniques have been used to overcome the problems in crack length measurements. Many of the crack detection techniques used with DIC are based on the evaluation of the derived strain fields, in which the progressing material discontinuity creates local changes. Again, the (global) deformation response is being measured. The generally used method is to study the opening after or ahead of the crack tip (or the strain perpendicular to the crack surface). Another technique for detecting the crack length is the evaluation of the local decrease in the resulting 'sigma' coefficient of the DIC analysis. The parameter represents the quality of the pixel correlation against the reference image, which can be used to define the crack

front [74]. This is based on the phenomenon where the formed local discontinuity affects the performance of the subset shape function in the DIC analysis, which cannot adapt the strongly heterogeneous deformation inside a subset. However, the strongly heterogeneous deformation at the adherend-adhesive interface in the bi-material specimens has an inevitable consequence on the 'quality' of the DIC results at the adhesive layer. This naturally decreases the uncertainty of the local results and challenges the unambiguous identification of the crack length measurement with the techniques.

Due to the complex geometries of the fracture mechanics specimens used for adhesive joints, the analytical models (calculation methods) can be too demanding to be solved precisely [75]. In recent years, the combined use of DIC and FEA has gained rising popularity for determining adhesive fracture parameters. Virtual crack closure technique [76] (VCCT) together with the direct displacement fields provided by DIC has been used to characterise fracture parameters for adhesive joints. For example, Huo et al. [13] introduced technique to determine the energy release rates of joints effectively, basically with no need of data for specimen geometry, loading or boundary conditions. FEA utilising cohesive zone models (CZM) has been used extensively to model the damage of a homogenised crack tip in adhesive joints. By the defined traction-separation law, the CZM can simulate the non-linear effects (due to nonlinear elastic, micro cracking, fibre bridging, etc.), which takes place generally in structural adhesives in the large failure process zone (FPZ) [77]. The displacement fields provided by DIC experiments have proven to be an excellent tool in the fitting of representative cohesive laws that can be used in characterising the fracture behaviour of materials [12], [78]–[80].

The accurate measurement of the local test responses, instead of the global indirect measurements with derived linkage to the local behaviour, can thus give new insight into the behaviour of the material responses. This has been efficiently utilised in various fracture mechanics studies where the use of DIC is becoming more and more common, and new analysis methods are evolving at a rapid pace.

3.3.3 Inverse analysis methods and DIC

Most studies on experimental mechanics and also the established standard tests have been built on attempts to maintain the response of the tested specimen during a test to be as homogeneous as possible. Naturally, the reason for this has been the

availability of the closed-form solutions covering such responses. With the solutions, one can quantify the unknown constitutive parameters that are used to model the mechanical behaviour [81]. DIC has already become a mature measuring technique and the full-field data it produces can verifiably greatly improve the accuracy and reliability of the established test methods as the specimen response is known more precisely. Currently, the implementation of the full-field method to various experimental characterisation techniques utilising heterogeneously deforming specimens is a hot topic.

Inverse analysis methods based on the use of measured deformation fields for identifying constitutive parameters of heterogeneous and non-linear–behaving materials in particular have been under active research. Here, the set of constitutive parameters are used as input values for numerical models and by finding the result that matches with the experimental deformation field, the sought parameters can be fitted. Two main approaches have been used for solving the inverse problems: the virtual fields method (VFM) and finite element model updating (FEMU). VFM utilises the principle of virtual work to solve the problem [8], [81], [82]. Here the global equilibrium of a structure is expressed using a set of equations from which the constitutive parameters can be obtained when the continuous deformation field of the specimen is known.

FEMU is the most straightforward technique for the inverse identification approaches of constitutive model parameters. It is based on iteratively minimising the gap between experimental and modelled nodal displacements [83], [84]. Basically FEMU is an indirect two-step approach [85], [86]. In the first step, the displacement field is determined experimentally. Then in the second step, the inverse procedure is applied by minimizing the difference between the experimental and FEM-simulated displacement fields and optimizing iteratively the unknown parameters. Recently, new method has been introduced in which the need for computing the displacement field (with DIC) prior to parameter identification has been eliminated. This one-step approach is known as integrated DIC (IDIC) in which the constitutive model is directly related to the experimentally obtained images (from the deformation process of a material) and force measurement [85], [87]. The DIC routine is thus integrated within the identification loop without a separate displacement field determination. The one-step approach contains less systematic errors and has better tolerance against image noise.

The maturing of the full-field measuring techniques has opened up new possibilities to perform the mechanical experiments that so far have been developed based on the use of point sensors. For example, Pierron and Grédiac [8] have

recently named this fully novel philosophy of mechanical experiments the 'Materials testing 2.0' paradigm, which utilises the recent progresses shown in the experimental and computational mechanics. By designing and optimising the experimental test configurations and specimen geometry, desired multi-axial stress states can be obtained within a specimen. Utilising FEMU or VFM together with the experimentally determined full-field displacement data with either local or global DIC, or IDIC with the acquired experimental images, a large set of even complex constitutive parameters can then be identified from a single well-designed experiment. This can make the testing significantly more efficient and reduce the need for performing several separate experiments, especially when identifying constitutive parameters to describe parameters for cohesive zone models [88] or the material behaviour of highly anisotropic and non-linear–behaving materials [84], [89].

4 EXPERIMENTAL METHODS AND MATERIALS

This chapter describes the central experimental methods within the scope of the dissertation. The following subchapters also explain the specific targets for using stereo DIC in different research cases.

4.1 Compression tests for hydrogels

Challenge: How can the validity of a simple unconfined compression test for wet hydrogel specimens be confirmed?

Target for using DIC: *To measure the deformation during compression in terms of shape and quantitative response for transparent and wet hydrogel specimens.*

The compression behaviour of gellan gum hydrogel was studied using displacement controlled unconfined compression testing in Publication I. The hydrogel was cast into cylindrical specimens with a diameter of 12.2 mm and a height of 6.5 mm (Figure 9). The tests were performed with a test instrument (Electroforce BioDynamic 5100, Bose) using 225 N and 22 N load sensors. A range of test parameters were studied to account for the viscoelastic behaviour of the hydrogel material.

Hydrogels contain a large amount of water, typically in the range of 70–95% of their mass. The wet hydrogel specimen against the smooth compression plates shows very low friction. Basically, a low lateral friction is favourable in terms of achieving the uniaxial stress state in the specimen. However, the specimen tends to slide away from the initial position, making testing impossible. Due to this, wetted lint-free cellulose papers were used between the hydrogel specimen and compression plates, enabling the specimen location to stabilise for successful testing.

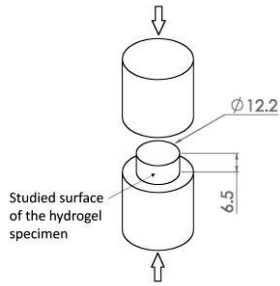

Figure 9. Compressed cylindrical hydrogel specimen.

A stereo DIC setup using 5 Mpix E-lite cameras, 100 mm/F2.8 (Tokina) and a pulsed LED-light was used to study the 3-D deformations. The recording rate ranged from 1 Hz to 8 Hz, depending on the crosshead displacement rate. Naturally, the hydrogel specimens are transparent and mostly water and the common patterning methods of painting could not be used. Here, the random pattern was accomplished by blowing fine carbon powder (Corax N550, Evonik) on the specimen surface just before the specimens were compressed (Figure 10).

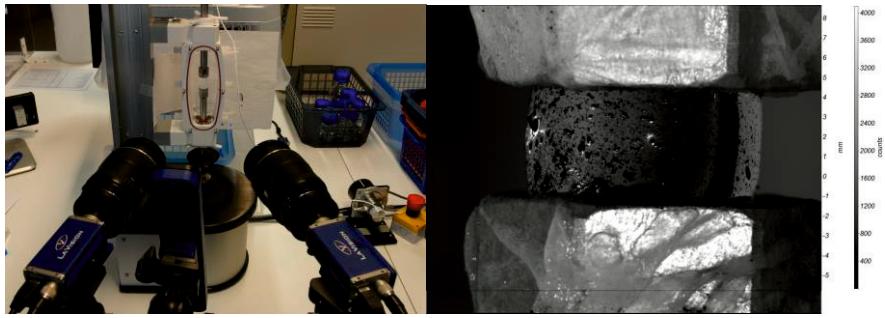

Figure 10. a) The test equipment with the 3D-DIC setup, b) A compressed hydrogel specimen with the applied pattern (Publication I).

The DIC processing (Davis 8.4, LaVision) parameters are listed in Table 1.

Table 1. The processing parameters for DIC in hydrogel compression tests.

Correlation method	Matching criteria	Subset/step size [pix]	Scale factor [pix/mm]	Subset shape function	Interpolation method	VSG size [mm]
Sum-of-differential	ZNSSD*	55/15	125	2nd order	6th order spline	0.68

*Zero-normalised sum of squared differences

4.2 Compression testing for fibre reinforced polymer specimens

Challenge: How can the directional elastic properties from a small volume of anisotropic materials be identified?

Target for using DIC: *To determine accurate strain distribution fields for a small heterogeneous prism specimen under compression.*

Four different fibre reinforced epoxy laminates fabricated either with strip winding (series here coded A, B, C) or resin infusion (series D) methods were studied in Publication II. The laminates (thickness approximately 10 mm) were cut and ground accurately into right-angled prism-shaped specimens (the number of specimens per series, n = 3) having edge lengths of 8 mm to 12 mm.

The compression testing of the specimens was carried out with a servo-hydraulic universal testing machine (Model 8800, Instron). A 50 kN load sensor was used with manually aligned compression plates. The plates were lubricated with silicone oil to minimise the lateral friction forces. The tests were carried out under displacement control (0.5 mm/min) and were stopped at 60 MPa of engineering stress to avoid the plastic deformation (or failure) of the specimen.

Stereo DIC (LaVision) was used to study the deformations of the surface of the prism perpendicular to the loading direction. Prior to testing, a random pattern was applied to the specimen using spraying with black and white alkyd paints. The DIC setup (Figure 11) consisted of two 5 Mpix E-lite cameras with 100 mm F2.8 objectives (Tokina) and pulsed LED lights. The recording frequency was 2 Hz. Davis 8.4 (LaVision) software was used to derive the DIC results and the parameters for the analysis are presented in Table 2.

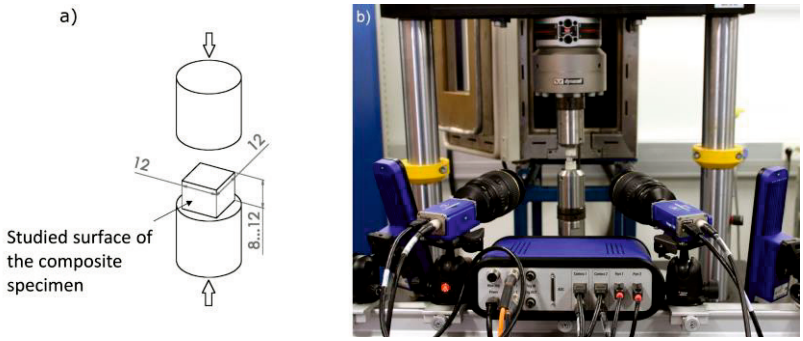

Figure 11. a) A prism specimen under compression, b) the 3-D DIC test setup (modified from Publication II).

Table 2. The processing parameters for DIC in Publication II.

Correlation method	Matching criteria	Subset/step size [pix]	Scale factor [pix/mm]	Subset shape function	Interpolation method	VSG size [mm]
Relative-to-first	ZNSSD*	21/5	66	2nd order	6th order spline	0.47

*Zero-normalised sum of squared differences

Each specimen was tested six times in random order, which means that three different loading directions were used (with reference to the specimen), and the specimen deformation was measured using DIC from the two other directions (faces), as shown in Figure 12. Data obtained in this way enabled us to determine the strain field at the studied surface of the prism and furthermore to derive the compression modulus in the three orthogonal directions of the composite material together with six Poisson's ratios. Additionally, the strain field of the heterogeneous materials could be studied precisely for understanding the length scale effects.

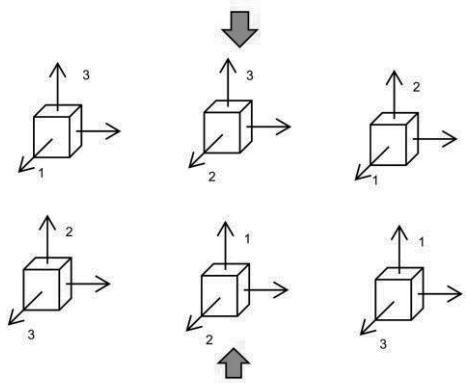

Figure 12. The test sequence of a compressed prism specimen (Publication II).

4.3 Notched coating adhesion test

Challenge: How can the accuracy and efficiency of determining debond for strongly nonlinear coatings be improved?

Target for using DIC: *To quantitatively determine the progress of the coating debond from its substrate.*

The notched coating adhesion (NCA) test is a method for studying the fracture toughness of a coating-substrate interface. The test is performed by a uniaxial tensile load subjected to the test specimen. During the test, coating peels from its substrate. The onset of the coating debond is required in terms of the corresponding specimen strain. The critical strain at the debond onset can further be used to determine the critical energy release rate (G_c). Publication III presented a method based on the stereo DIC to define and determine quantitively the debond progression. In addition to the NCA specimens, DIC was also used to determine Poisson's ratio for the (separate) substrate and thin PAI coating.

In this thesis, the NCA test was used to study the interface between polyamide-imide (PAI) coating (Torlon 4000TF, Solvay) and CuSn10Pb10 substrates. Substrate coupons with the dimensions of 120 mm x 13 mm x 1.6 mm were coated with PAI/dimethylsulfoxide (DMSO) solution using a bar coater (finally 75 μm mean coating thickness), as presented in Figure 13. After the heat treatment of the specimens, a pre-crack transverse to the specimen's longitudinal axis was prepared using a razor blade loaded by a drop-weight impactor.

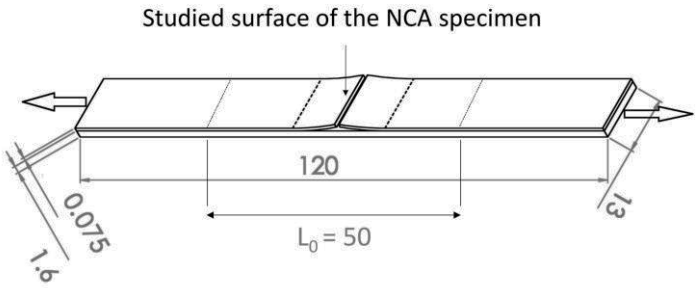

Figure 13. The NCA test specimen dimensions (mm) in the studies of Publication III.

The tensile tests for the NCA specimens were performed using a universal testing machine (Model 5967, Instron) at a test rate of 5 mm/min. A clip-on extensometer (L_0=50 mm) was used to measure the global (engineering) specimen strain. A stereo DIC setup with 5 MP E-lite cameras, 50 mm/F2.8 (Nikon) and pulsed LED lights (Figure 14) were used. The PAI coated surface of the specimen was patterned using black and white spray paints. The average diameter of the speckles was 50–80 μm measured with an optical profilometer (InfiniteFocus G5, Bruker Alicona). The imaging rate was 2 Hz. The processing parameters of the DIC analysis carried out using Davis 8.4 (LaVision) software are presented in Table 3.

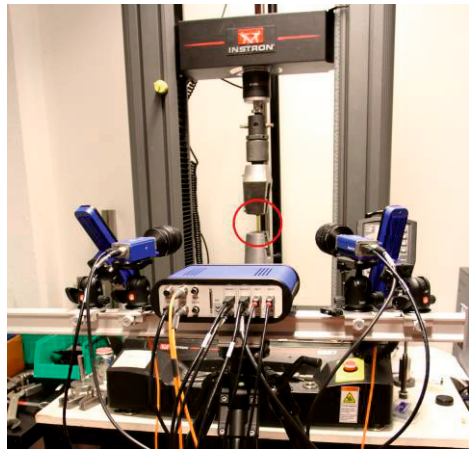

Figure 14. The 3-D DIC setup used with the NCA tests in Publication III.

Table 3. The processing parameters for DIC in the NCA tests.

Correlation method	Matching criteria	Subset/step size [pix]	Scale factor [pix/mm]	Subset shape function	Interpolation method	VSG size [mm]
Relative-to-first	ZNSSD*	33/11	38	Affine	6th order spline	1.45

*Zero-normalised sum of squared differences

4.4 Mixed-mode testing with single leg bending specimen

Challenge: How to experimentally determine normal and shear strains along the adhesive (in bond line) of a bonded test specimen.

Target for using DIC: *To determine the displacement field to provide data for deriving the representative strains of the adhesive layer beyond spatial resolution of the DIC.*

Single leg bending (SLB) specimens were fabricated for studying the mixed-mode fracture behaviour of FM 300-2 (Solvay) epoxy film adhesive in Publication IV. The test specimens presented in Figure 15 consisted of two adhesive plies applied between two thick aluminium alloy (Alumec 89, Uddeholm) plates. A pre-crack was created between the adhesive plies using a thin PTFE foil during manufacture. The adhesive was cured in an oven (120 °C) under a vacuum bag, and finally the plates were water-jet cut into test coupons with a thickness of 17 mm.

The specimens were tested with either of two specimen orientations (here coded test types A and B), which enabled us to achieve two different mixed-mode ratios using the same test specimen geometry as depicted in Figure 15. The specimens were tested using a modified 3-point bending jig enabling the horizontal orientation of the specimen to be maintained for both test types. The tests were performed with a universal testing machine (Model 5967, Instron) using the test rate of 2 mm/min.

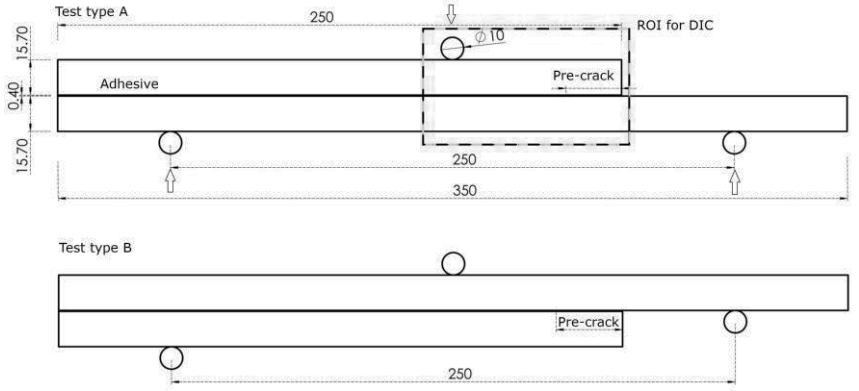

Figure 15. The region of interest (ROI) for DIC and the test types for the single leg bending specimen with dimensions (mm) in Publication IV.

A stereo DIC setup consisting of two 5 MP E-lite cameras, 50 mm/F2.8 (Nikon) and pulsed LED lights was used to study specimen deformation at the region of interest (ROI) shown in Figure 15. Prior to testing, the imaged surface of the specimen was painted with thin white (acryl) spray followed by the creation of the random pattern using black paint and a foam roll.

The recorded images were processed into full-field displacement data using Davis 8.4 (LaVision) software with the parameters presented in Table 4.

Table 4. The processing parameters for DIC in single-leg bending tests in Publication IV.

Correlation method	Matching criteria	Subset/step size [pix]	Scale factor [pix/mm]	Subset shape function	Interpolation method	VSG size [mm]
Relative-to-first	ZNSSD*	25/7	25	Affine	6th order spline	1.56

*Zero-normalised sum of squared differences

4.5 Fatigue testing using the end-notched flexure test

Challenge: How to determine the propagation of the crack in adhesive (in-bond line) of mode II fatigue testing repeatably.

Target for DIC: *To determine the accurate deformation field of the fatigue-tested specimen to provide data for crack growth analysis.*

End-notched flexure (ENF) test specimens were fabricated using aluminium alloy (Alumec 89, Uddeholm) plates and two layers of epoxy film adhesive (FM300-2, Solvay). The pre-crack was fabricated using thin PTFE film with a length of 66% of the half support span. The specimen dimensions are presented in Figure 16.

The fatigue testing (Publication V) with the R-ratio of 0.1 was performed with a servohydraulic universal testing machine (Model 8800, Instron) using sinusoidal loading spectrum shown in Figure 17. The tests were carried out with three different load amplitudes (50%, 60% and 70%) relative to the maximum load measured in a quasistatic ENF test.

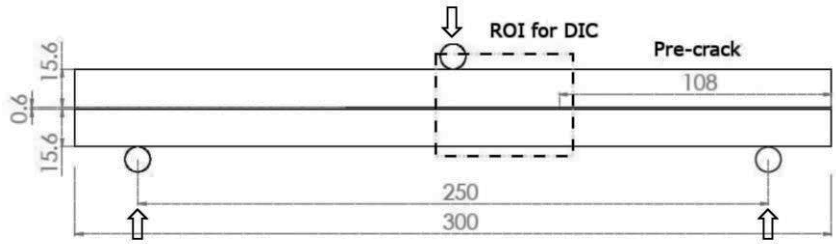

Figure 16. Dimensions of the ENF specimen (mm) and the region of interest (ROI) for DIC in Publication V.

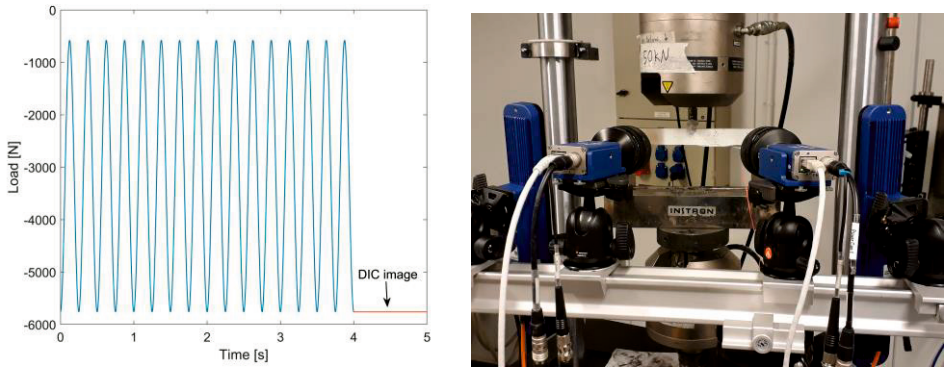

Figure 17. a) The repeating unit of the cyclic loading spectrum. b) The 3-D DIC setup and the test equipment for ENF specimens (Publication V).

The specimen deformation at the defined ROI shown in Figure 16 was studied by synchronising the stereo DIC setup (5 MP E-lite cameras with 50 mm and F2.8 objectives and pulsed LED lights) with the testing machine taking an image pair at every hold step at the maximum load (of the repeated spectrum). Prior to testing, a black-and-white random pattern was applied to the ENF specimen using spray paint and foam roller. Davis 10.1 (LaVision) software was used to process the images into displacement fields using the parameters explained in Table 5.

Table 5. The processing parameters for DIC in ENF tests in Publication V.

Correlation method	Matching criteria	Subset/step size [pix]	Scale factor [pix/mm]	Subset shape function	Interpolation method	VSG size [mm]
Relative-to-first	ZNSSD*	35/11	43	Affine	7th order spline	1.32

*Zero-normalised sum of squared differences

5 RESULTS AND DISCUSSION

This chapter sums up the essential findings in Publications I to V and append the solutions found in the challenges stated in the previous chapter.

5.1 Compression tests

5.1.1 Testing of hydrogel specimens

Gellan gum hydrogel specimens were studied using the unconfined compression test method. Hydrogels possess a strongly nonlinear mechanical stress-strain response due to which their response in compression is also complex. In the literature, the crosshead displacement has been routinely used to determine the estimated (here: engineering) strain of hydrogel specimens [90], [91]. However, measuring the (engineering) strain solely using the stroke of the test device can be considered as a coarse method for soft and highly deforming specimens. To formulate a representative constitutive material model for the strongly nonlinear material applicable to large strains, naturally, the engineering strain and stress measures cannot be used. DIC was used in understanding the valid strain distribution and true specimen cross-section area by studying the intrinsic (i.e. specimen barrelling, local material anomalies) and extrinsic (i.e. uniformity of the specimen/plate contact, specimen sliding) factors affecting the deformation response of the tested specimens.

During compression, the hydrogel specimens tend to move and slide between the smooth compression plates. To prevent this, lint-free cellulose papers were used between the specimen and the plates. On the other hand, the increased contact friction increased the barrelling phenomenon due to the constrained Poisson effect at the contact, as presented in Figure 18. Initial tests revealed that the condition and the application of cellulose paper had a strong effect on the deformation (and stress state respectively). If the same papers were used with several specimens, obviously the friction was altered due to sticking gel, and the specimen deformation was no

longer symmetrical, as depicted in Figure 18. Thus, if such papers are to be used to increase the contact friction in a controlled manner, one has to take great care of their consistent application to achieve deformation and respective symmetric (calculatable) stress distribution.

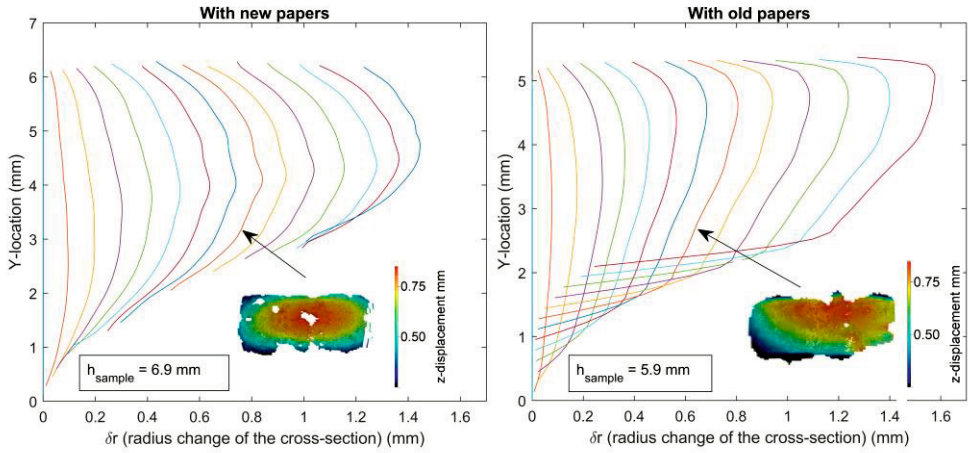

Figure 18. The measured barrelling effect in compressed specimens and the effect of the condition of the papers used to control the contact friction (Publication I).

Figure 19 depicts an example of the axial strain distribution of the compressed hydrogel in which the barrelling deformation was observed to be similar on the upper and lower contact surfaces (to the compression plates). Near the edges the strain field is strongly inhomogeneous, whereas at the central region the strain was considered valid for compressive behaviour. Figure 19 shows the comparison of the axial strains extracted from different locations of the specimen (using ≈ 1.5×1.5 mm^2 artificial strain gauge). The axial strain extracted at the centre of the specimen surface corresponded well with the engineering strain calculated using the crosshead displacement, whereas significant difference was seen when studying regions closer to specimen edges.

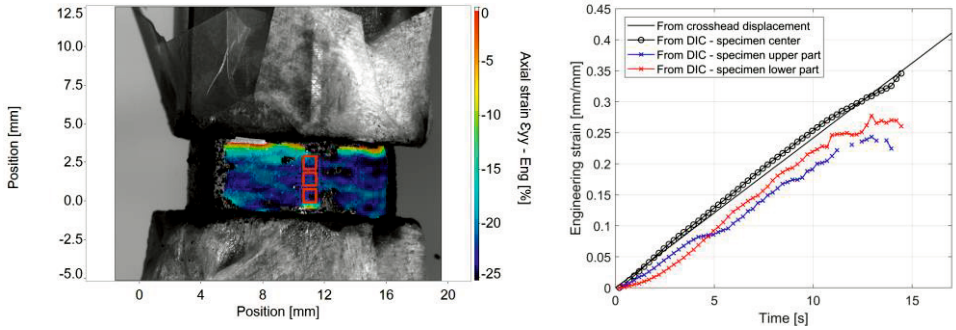

Figure 19. a) The axial strain field in a compressed hydrogel specimen. b) Comparison of the device stroke-based engineering strain and the extracted axial strain from the DIC measurements using different locations at the specimen (unpublished data).

If it was ensured that the specimen deformed approximately symmetrically during the test, the engineering strain determined from the crosshead displacement consistently equalled the local strain at the specimen centre. The true (here, Hencky) strain could then be calculated from the engineering strain using the equation:

$$\varepsilon_{true} = -\ln(1 - \varepsilon_{eng}) \tag{5.1}$$

The experimental true stress at the centre of the specimen was determined by dividing the measured force by the true cross-sectional area. The true area was determined using the measured radius change in the centre of the compressed specimen (Figure 18). The experimental true stress (i.e. assuming constant volume) was then compared with the calculated true (here, Cauchy) stress (based on constant volume):

$$\sigma_{true} = \sigma_{eng}(1 + \varepsilon_{eng}) \tag{5.2}$$

Figure 20 depicts the comparison of the stress-strain curves defined by different means, where it is seen that the experimental true stress accurately follows the calculated Cauchy stress. To conclude, if the plate-specimen friction remains constant and no local material defects are present in the specimen observed to result symmetrical specimen deformation, the simply calculated Cauchy stress and Hencky strain (either from crosshead displacement or from DIC) can be used to estimate the stress state in a valid way for the cylindrical hydrogel specimen. However, it is important to note that Equations 5.1 and 5.2 do not account for boundary conditions and the change in the stress-strain component in the radial direction. In order to

match the absolute stress and strain over the specimen volume, boundary conditions satisfying calculation would be needed with validation to DIC-based barrelling (due to the non-rigid boundary).

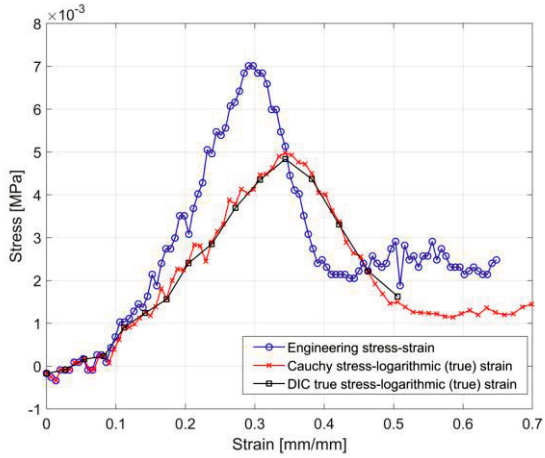

Figure 20. The comparison of different stress-strain definitions (modified from Publication I).

5.1.2 A test method to determine elastic properties of composites under compression

Compression tests were carried out with rectangular prism specimens cut from three strip-wound curved composite laminations with the different weave pattern of the reinforcement fabrics. The elastic constants of the composite material, including three elastic moduli and Poisson's ratios, were determined by loading the specimens in several test orientations as explained in Section 4.2.

Figure 21 depicts the optical and DIC-based axial strain field images of the three different composite materials. The optical images were taken before applying the painted random pattern to the specimens from the same surfaces the strain fields were later acquired from. The strain maps point out the very heterogeneous deformation of the tested specimens and the need to decide upon the proper level of homogenisation. The pseudo images show that the strain maps correspond with the microstructure of the specimens at their surfaces. The high strain regions focus accurately on the resin pockets between the reinforcement fibre bundles, whereas the lowest strains occur over the fibre bundles. For example, along the lines seen in Figure 21, the axial strain fluctuates between -0.002…-0.012 mm/mm, whereas the

average is approximately 0.007 mm/mm (i.e. homogenisation over a frame area of ≈10 × 10 mm²). The strain maps can also reveal the surface or sub-surface flaws in the materials, as presented in Figure 21. In addition, the evenness of the stress distribution, affected by the flatness of the specimen and/or planarity of the compression plates, can be evaluated from the deformation data (strain or displacement). The above-mentioned factors can finally be used to evaluate whether the recorded test response is representative and valid for further analysis of elastic constants. If only contacting discrete strain measuring devices are used, such evaluation is impossible to perform, and the uncertainty (and simultaneously scatter) of the measured results increases.

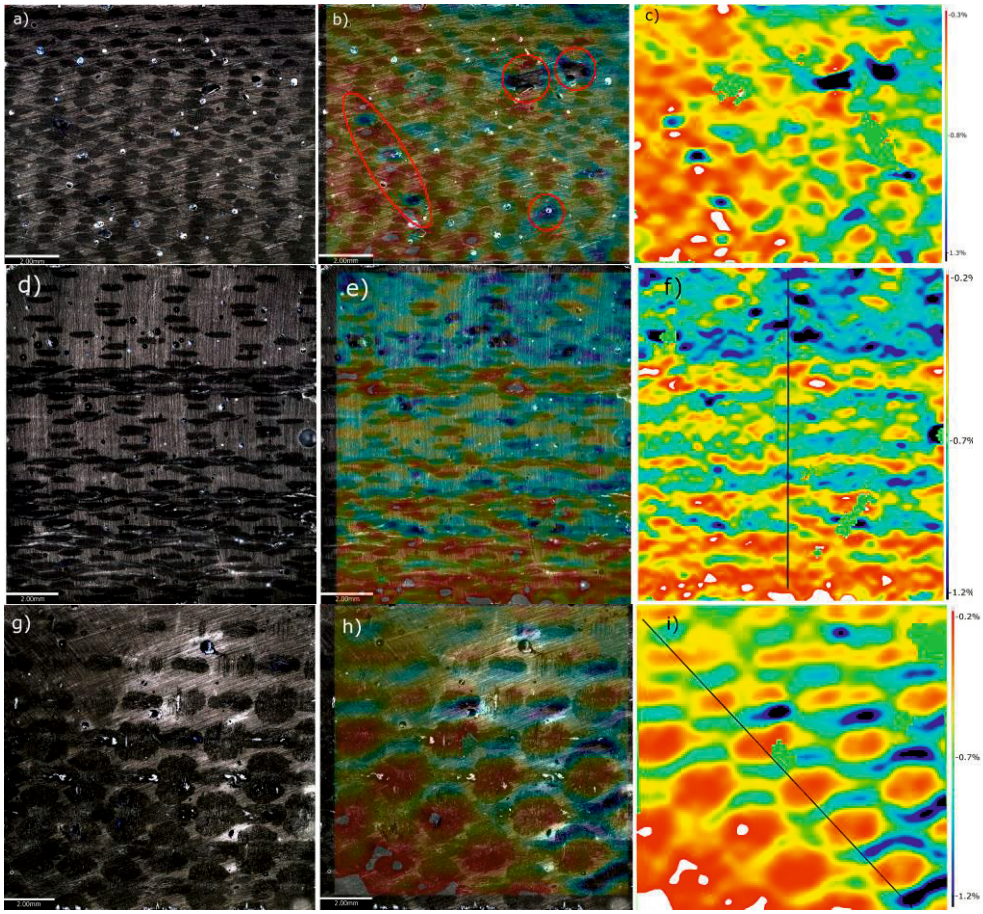

Figure 21. Optical (left), pseudo image (middle) and axial strain (right) of the three compressed composite specimens. The loading direction in the images is vertical (Publication II).

Although the actual material behaviour is fundamentally related to its microstructure, the mechanical properties of materials are still commonly approximated by defining the behaviour using macroscale engineering constants. Here, instead of acknowledging the local heterogeneous fibre-matrix characteristics, the composite material is treated as a homogenised continuum with a generalised material model. For example, the mechanical behaviour of fibrous composites is usually expressed by an orthotropic material model, in which material has three mutually orthogonal symmetry planes, and the behaviour is characterised by nine material constants (E_i, ν_{ij}, and G_{ij}, i = 1…3, j = 1...3).

To determine the elastic constants based on the performed compression tests, representative mean strain values were first determined as the average of the desired strain quantity over the whole specimen surface, excluding 1 mm edge borders. The measured large area, for exporting the strain data, averages the local gradients caused by the woven reinforcements. Thus, apparent strain for the composite specimen is obtained and can be used to determine the homogenised material constants. When the same test specimen was tested using six different test orientations, the three orthogonal Young's moduli and, basically, six Poisson's ratios could be determined. The elastic (compression) moduli were derived as the secant in the engineering stress versus compressive strain curves over the strain range of 0.0005…0.0025 mm/mm. The Poisson's ratios were calculated as areal mean values from the DIC derived field data over the strain range of 0.003…0.006 mm/mm. Figure 22 and Figure 23 depicts examples of the test results. The determined constants of the tested composite materials are presented in Table 6.

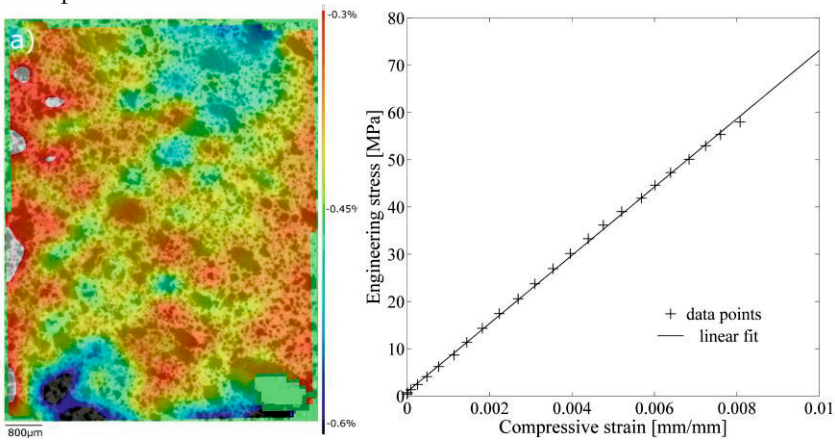

Figure 22. Full-field map for axial strain (ε_2) of the tested composite material B at an engineering stress level of 50 MPa (force per cross-sectional area), and the engineering stress-strain curve (Publication II).

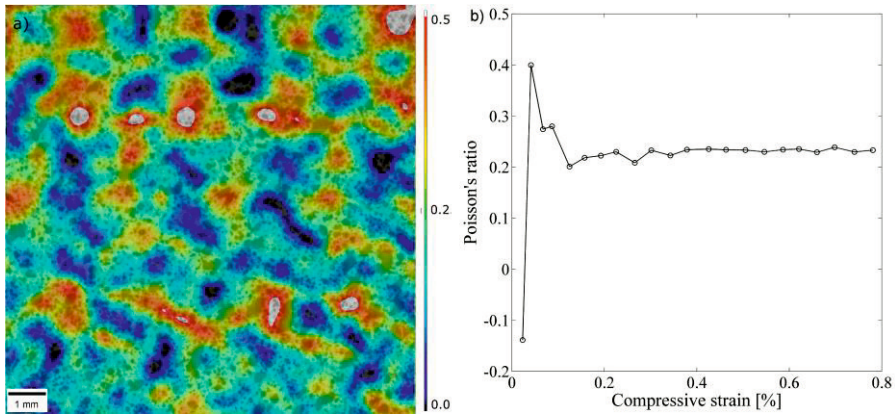

Figure 23. Full-field map for Poisson's ratio (ν_{32}) of the tested composite material C at an engineering stress level of 50 MPa (force per cross-sectional area), and its areal mean value as a function of axial strain (Publication II).

Table 6. Determined engineering constants for the tested composite materials A, B and C in Publication II.

	E_1 [GPa]	E_2 [GPa]	E_3 [GPa]	ν_{12}	ν_{21}	ν_{13}	ν_{31}	ν_{23}	ν_{32}
A	6.8	7.0	6.5	0.34	0.36	0.4	0.38	0.40	0.30
B	15.3	16.8	7.4	0.25	0.19	0.48	0.22	0.46	0.21
C	10.4	11.3	6.1	0.27	0.22	0.48	0.27	0.42	0.23

In orthotropic materials, the moduli and Poisson's ratios are coupled, and the following relationship is fulfilled:

$$\frac{\nu_{ij}}{E_i} = \frac{\nu_{ji}}{E_j} \leftrightarrow \frac{\nu_{ij}}{\nu_{ji}} = \frac{E_i}{E_j} \tag{5.3}$$

where i and j can have values of 1, 2 and 3.

The validity of the orthotropic material behaviour for the tested materials was evaluated by simply plotting the calculated ratios of the Poisson's ratios and the moduli as shown in Figure 24a. For isotropic material, having no orientation dependency, all the calculated ratios (right side of Eq. 5.3) would equal 1. Orthotropic material would result in equal calculated material constant ratios that

always lie on the diagonal line in the figure. Generally, the stronger the orthotropic characteristics, the greater the calculated ratios would be.

The percentage of coupling difference from the theoretical orthogonal behaviour can be calculated as:

$$\Delta_{ij} = 100 \times \left(1 - \frac{\frac{\nu_{ij}}{\nu_{ji}}}{\frac{E_i}{E_j}}\right) \tag{5.4}$$

where *i* and *j* denote the orthogonal directions 1, 2 and 3. Figure 24b shows that for composite materials B and C, the value Δ_{12} is significant. The result suggests that the orthotropic material model is not fully valid for the studied materials. This could have originated from the microstructure of the tested materials where, contrary to unidirectional reinforcement layers, the reinforcement fabrics have significant out-of-plane crimp, inducing the anisotropy [92]. In addition, the winding of laminates over a large cylindrical mandrel will lead to non-zero curvature of reinforcement planes, causing minor deviance between the presumed ply orientation.

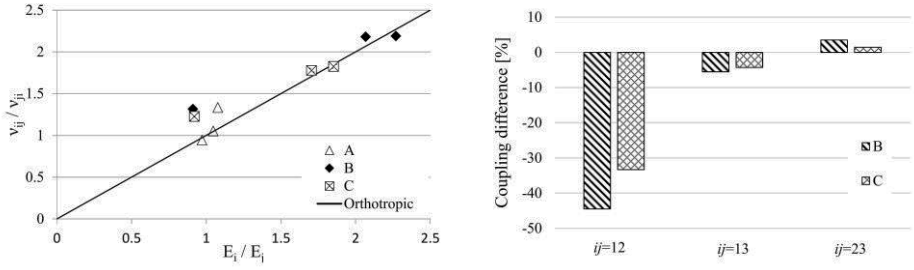

Figure 24. a) Calculated modulus ratios to evaluate material characteristics against the orthotropic behaviour. b) Difference between the theoretical (orthotropic) and measured coupling of the Poisson's ratios and moduli (Publication II).

5.2 Fracture mechanics tests for layered specimens with polymer films

5.2.1 Detection of the debond progression of coating in the NCA test

The NCA test method is based on detecting the critical strain (ε_c) at the onset of the coating debond using a manually pre-cracked coated specimen. As external work is being done to load the specimen, energy is increasingly stored in the deformed coating. As the available strain energy finally exceeds the specific value to cause the crack to propagate, the critical energy release rate to cause the debonding phenomenon (cERR or G_c) can then be calculated using the simplified uniaxial solution [93]:

$$G_c = hE\left[\left(\frac{\varepsilon_0}{1-\nu}\right) + \varepsilon_o\varepsilon_c + \frac{\varepsilon_c^2}{2}\right] \tag{5.5}$$

where h is the thickness, E is the Young's modulus, ε_0 is the residual strain and ν is the Poisson's ratio of the coating.

The accurate detection of the coating debond onset is a challenging task. On the other hand, the onset is the essential parameter the whole method is based on. In addition to the original pure visual detection method, different techniques have been used to study the coating debond, such as acoustic emission [94] and derivatives of strain-time and strain-force curves [95]. However, an imperfect test specimen and material nonlinearities cause unknown factors of scatter in the tests. The coating debond phenomenon can often deviate from the ideal assumed response, which impedes the interpretation of the obtained results.

The full-field deformation data of the NCA specimen was used in the thesis to quantitatively determine the coating debond process. Using the derived DIC-based axial strain, the instantaneous area of the debonded coating was determined throughout the test, as presented in Figure 25. The strain threshold of < 0.005 mm/mm was used to define the local debonded coating and a MATLAB code was written to determine the area of the region. The obtained area was then divided by the specimen width, providing the normalised debond length of the coating in the axial direction (of load). Finally, the debond length was linked to the instantaneous global specimen strain measured with the clip-on extensometer. This arrangement accurately described the debond progression of the coating layer during the test, as depicted in Figure 26. The process flow for determining the critical strain is

summarised in Figure 27. The critical strain thus represents the global axial strain value in the test specimen, which induces the propagation of the coating debond.

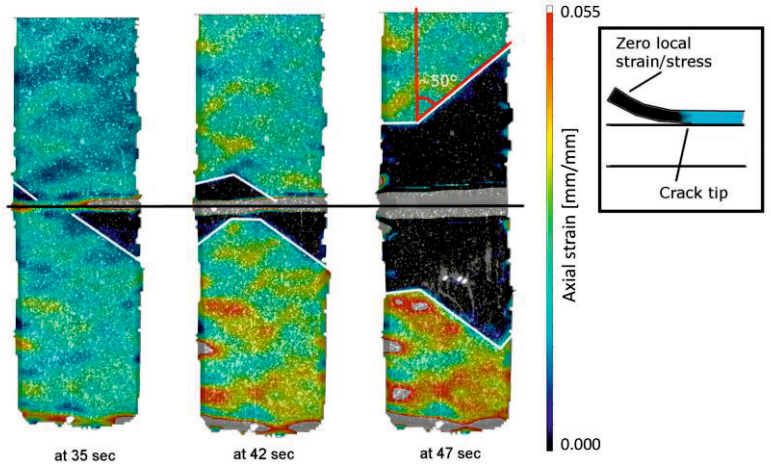

Figure 25. The progress of coating debond in an NCA test. The black region represents the area where the coating has debonded, i.e. where the axial strain of coating is below 0.005 mm/mm (Publication III).

The initial 'stick-slip' phase was characteristic of the tested material system, where the debond propagated a few millimetres by small random steps (during steady loading). After the initiation phase, typically a sudden longer debond(s) was observed. The clip-on extensometer data was also used to derive the strain derivate of stress. The derivate curve in Figure 26 shows evident peaks, which can be linked to the significant sudden progressions of the peeled coating. However, not all the debond steps were strong enough to be detected using the load or extensometer-based results. Thus, the observation suggests that the linking of the measured data to the coating peeling without the full-field data can easily lead to false interpretation of the debond progression in NCA tests.

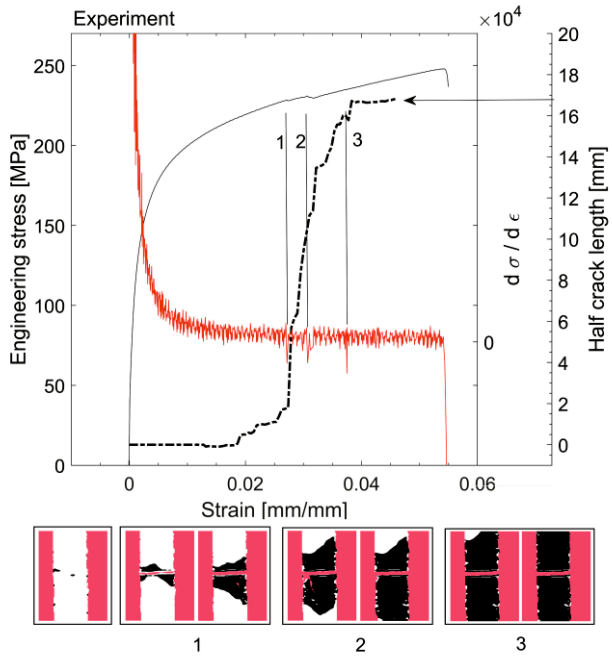

Figure 26. The measured DIC-based instantaneous debond length and the strain derivate of stress (see the stress definition in Publication III) in an NCA test (modified from Publication III).

The DIC-derived half-crack (or debond) length of 8 mm was used to characterise the debond onset of the coating in Publication III. The 8 mm threshold then defined the momentary critical strain value in the developed method. Here, the debond initiation phase was fully developed and the debond showed the high-rate peeling phase in the full test series. In other words, successful peeling was reached instead of coating (tensile) failure or substrate failure.

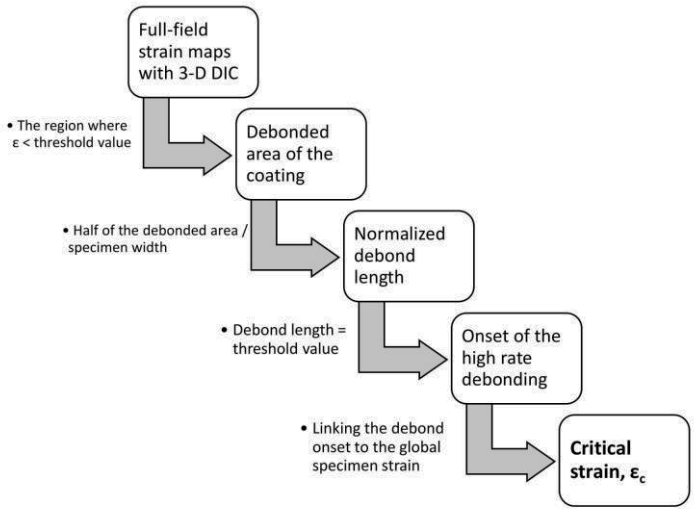

Figure 27. The process flow to derive the critical strain at the debond onset according to the thesis.

Significant variation in strain can occur locally even in a uniaxially loaded macroscopically homogeneous specimen. This is observed for example in Figure 28, which presents the waterfall strain plot provided by the DIC measurements. The curves depict the development of the axial strain exported across the specimen width at a distance of 5 mm from the pre-crack for an NCA specimen. The smoothness of the curves can be largely explained by the averaging size of the VSG (1.45 mm). It is seen that, locally, the strain deviates significantly from the average 'global' strain in the substrate's CuSn10Pb10 material. The local strain gradients are assumed to be induced by the microstructure of the material and have a role in the observed irregular coating debond process. The local variation in turn increases the scatter of the determined critical strain readings at the debond and finally the determined cERR values. However, the use of homogenised (global) strain can be considered a conservative method to represent the critical strain value inducing the debond. The homogenisation fades the local peak strains observed in the test specimen (by DIC), where the debond is presumably initiated (due to the greater available strain energy).

The debond analysis of coating from substrate is naturally a 3-D problem, which is not fully acknowledged with the simplified analytic solution (Equation 5.3). The 3-D effects, as well as the influence of plasticity and the unknown residual stresses in the used material system, in terms of the test response, can be systematically studied with FEA simulations using CZM and non-linear material models. The characteristic parameters of the CZM (e.g. the total G_c and the cohesive strength for the used bilinear traction-separation law and element size) can be fitted so that the

simulation produces similar crack propagation, as observed in the experiments. The experimental crack propagation that is targeted with the simulation can be defined using the DIC-based measured crack onset and growth rate and the shape of the debond patterns (i.e. the angle shown in Figure 25). The fitted CZM can be used for any application and product geometry as long as the manufacture process of coating and substrate are similar, and the finite element mesh is comparable (in density).

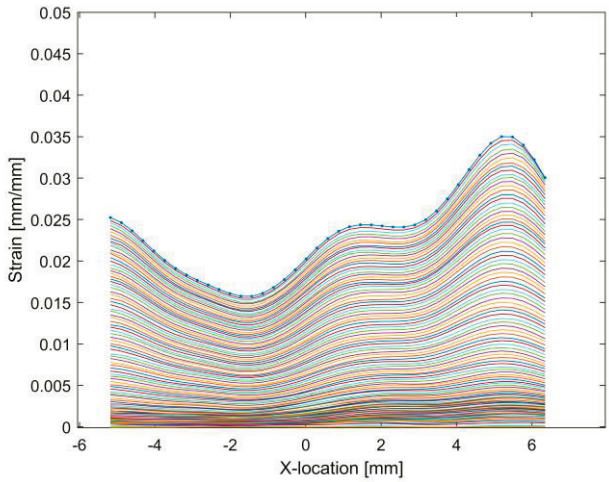

Figure 28. Waterfall plot of the developing axial strain measured across the specimen width at 5 mm from the pre-crack in an NCA test. The dots in the uppermost curve present the spacing of the strain data points. (unpublished data)

5.2.2 Measuring local deformation distributions in thin adhesive layer

Adhesive joints are the most efficient when designed to carry shear loading [96]. However, instead of the pure shear deformation, some peeling, or opening, of the adhered surfaces typically occurs in real applications, especially at the edges of the joints. In an adhesive joint where pure shear stress is having an effect, the failure tends to happen by fracture mode II. In mixed-mode loading, on the other hand, the failure is due to the interaction of modes I and II, which can have synergetic effects compared to single-mode loading. In Publication IV, a new mixed-mode test concept was developed based on the single leg bending test specimen. This concept offers two different mixed-mode ratios by changing the loading direction of the

specimen (Figure 29). Using the results, a mixed-mode failure criterion for the adhesive could be determined.

Experimental determination of the opening and shear deformation at the adhesive is conventionally based on discrete measurements by using, for example, extensometers [97] and crack gauges [98] at the previously decided locations in the test specimens. The extensometers can be used to accurately measure the crack tip opening or shear displacement, but the result is purely local (point-to-point displacement measured). No information is obtained in terms of how the thin adhesive layer deforms outside the measurement point. Also, the detecting of both the opening and the shear deformation of the adherends simultaneously using physical devices is very challenging. In the experiments, where the crack propagates in a test specimen, crack gauges can be used to detect the crack tip location based on the breakage of the physical conductive strands due to increased localised deformation in the specimen. However, again no information is obtained if the breakage is due to the shear or opening deformation of the adhesive.

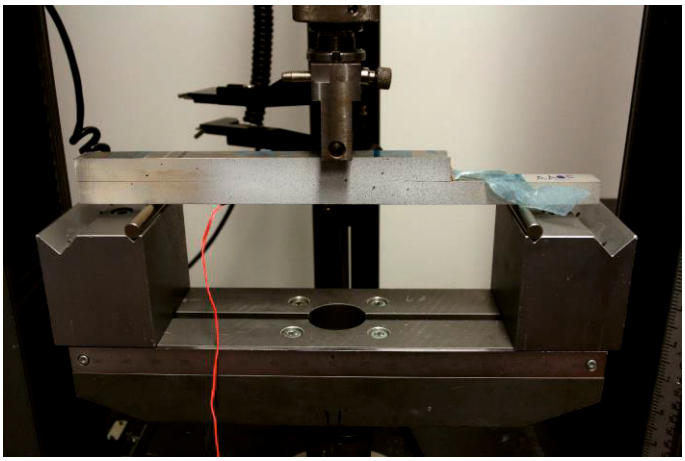

Figure 29. Mixed-mode fracture testing using the SLB specimen in type A loading configuration (Publication IV).

A method based on the DIC was developed to experimentally determine the continuous deformation distributions along the thin adhesive line. Due to the large region of interest relative to the low thickness of the adhesive layer, as depicted in Figure 15, the spatial resolution of the used DIC setup was significantly too low for the characterisation of the strains directly on the adhesive layer. In other words, the virtual strain gauge size was greater than the thickness of the adhesive layer. To

overcome this restriction and to allow the determination of the continuous opening and shear strain distributions in the adhesive, the method was developed based on the measured deformation field of the rigid (aluminium alloy) substrates.

The developed approach is based on the idea of determining the displacement vectors of both adherends along the specimen length (x-direction) at three constant distances measured from the adhesive midline. As the displacements are measured purely from the adherend, the high strain gradient originated at the adhesive-adherend interface does not interfere with the DIC analysis. Points A_n, B_n and C_n presented for the upper adherend in Figure 30 show the unloaded stage. As the specimen is loaded, the bending causes the points to move to locations A'_n, B'_n and C'_n. Considering the Euler-Bernoulli beam theory, the lines P_n and P'_n can be fitted, and the points Q_n and Q'_n at the interface between the adhesive and adherend can be determined. As the same process is repeated with the lower adherend, finally, after some mathematical manipulation given in Publication IV, the local shear (v) and opening (w) displacements along the adhesive can be derived using the determined locations of points Q'_n and R'_n. As the initial thickness of the adhesive layer is also known, the engineering shear (γ_{xy}) and opening (ε_y) strains can be calculated. As the calculation process is repeated at every X-coordinate location from the extracted displacement field, the strain distribution along the whole adhesive layer can be determined.

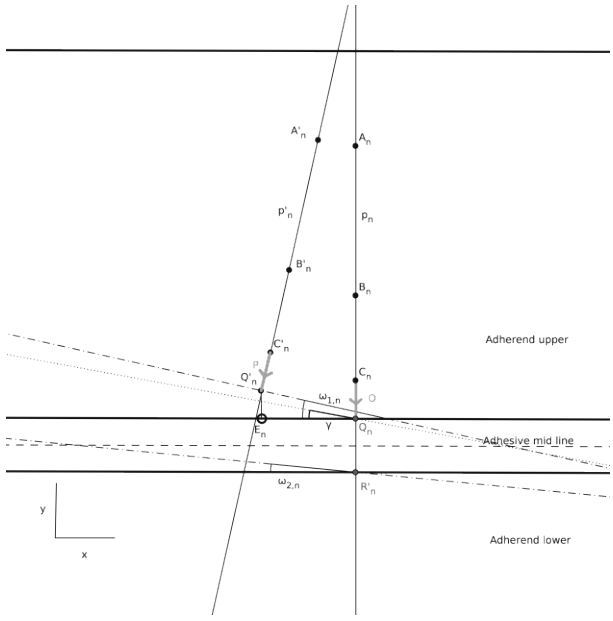

Figure 30. Schematic illustration of the control points used in the DIC data reduction scheme for determining deformation in adhesive (Publication IV).

The SLB tests were simulated by creating a FE model (Abaqus/Standard 2017, Dassault Systemes) using 3-D solid elements. Two element layers were used to model the adhesive. A further purpose of the numerical analysis was to analyse the ERR of the measurements with the VCCT to define the mixed-mode fracture criterion for the adhesive. The comparison of the shear (γ_{xy}) and opening (ε_y) strains between the FE and DIC results at the onset of the crack propagation are presented in Figure 31. It can be seen that there is a good correlation between the determined shear strains along the adhesive. On the other hand, the experimental opening strains in the adhesive are significantly greater than the numerically obtained values. The difference could not be explained by any features related to the used elements (type or size) or the material model in the FE analysis.

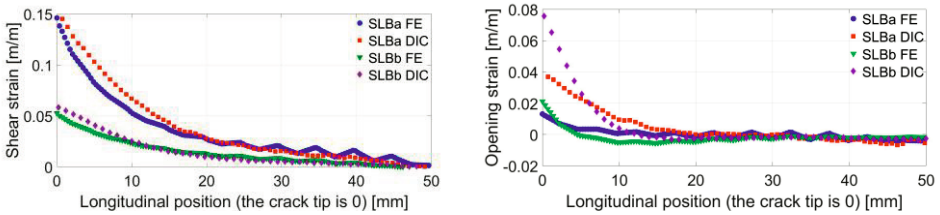

Figure 31. a) Shear (γ_{xy}) and b) opening (ε_y) strains in the adhesive for the SLB specimens at the crack onset (Publication IV).

A plausible explanation for the observed difference was found when the fracture surfaces of the tested specimens were studied. Figure 32 depicts the profilometer image (by using InfiniteFocus G5, Bruker Alicona) of the SLB specimen's fracture surface near the pre-crack tip region. During the specimen manufacturing, the thin foil used to create the pre-crack had wrinkled, presumably due to thermal expansion/shrinking, which formed the ridged topography in the pre-crack region. In these ridges, the wrinkle peak-to-peak amplitude of more than 100 μm was measured. Whereas the modelled specimen had perfectly smooth contact surfaces allowing horizontal sliding, in the experiments the wrinkled pre-crack interface induced external opening loading at the crack tip zone. Basically, the fraction of the mode I loading was higher than assumed in the tests, which has to be considered in the further analysis of the similar experiments. Also, the fabrication process of the pre-cracks using the applied thin PTFE foil needs more careful implementation in order to consistently achieve smooth pre-crack surfaces.

The developed method to determine the strain distributions of an adhesive layer basing purely on the measured deformation fields of the deformed adherends,

instead of the direct measurement from the adhesive, proved to be efficient. With the introduced technique, the spatial resolution of the used DIC setup does not dictate the minimum adhesive thickness for successful strain measurements. The continuous strain distributions can thus be derived even from very thin adhesive layers, well beyond the VSG size of the DIC calculations.

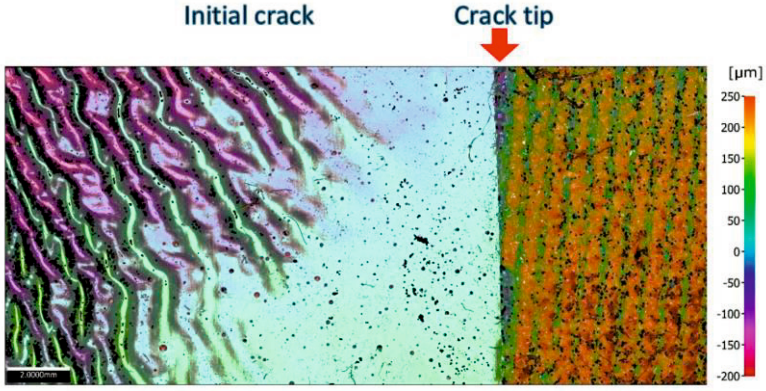

Figure 32. The profilometer image of the surface topography in the pre-crack tip region (Publication IV).

5.2.3 Evaluation of crack propagation in ENF fatigue test for adhesives

Adhesive joints are advantageous over conventional joining technologies, especially due to their fatigue characteristics [99]. The three-point ENF technique was used here to carry out the fatigue testing for the epoxy film adhesive. The test method was selected due to its simplicity for specimen fabrication and the testing jig, and the prior experience obtained with static testing.

In fracture tests where the mode I fracture dominates, the crack opens and can be rather easily examined, even visually. In the mode II dominating fracture, on the contrary, the detection of the propagating crack due to the shear deformation has been recognised as a challenging or sometimes impossible task [100],[101]. The task is even more complicated due to the fact that, generally, the crack does not form the well-defined tip but is characterised by a larger fracture process (FPZ) zone [97], [102]. The FPZ is understood as the non-negligible region in front of the distinct crack tip, where the adhesive has already undergone some softening damage. The damage can include, for example, plasticity, microcracking, microvoiding and crack-branching [103]. The challenges in the reliable crack length determination have been overcome largely with the use of various numerical post-processing methods, which

are mostly based on the measured compliance of the specimen. From the changes in the specimen's compliance, the so-called equivalent crack length (a_e) for the ENF specimen can be determined according to the compliance-based beam method (CBBM), as described by de Moura [104]. The value of a_e can finally be used to determine the fracture toughness (G_{IIC}) of the joint. Even though a_e in theory takes the FPZ into account, it is not the identical measure for the actual size of the damaged region in adhesive. Publication V presented a method to study the development of the plasticised (or damaged) region of the adhesive using DIC.

The full-field displacement field of the fatigue tested specimen was acquired as presented in section 4.5. Even though the opening (peeling) of the joint in this almost purely mode II loaded specimen is not intuitive, small deformation occurs. This opening is presumed to originate mostly due to formed microcracks, which increase the volume of the adhesive as well as the contact surface roughness/waviness in the split region of the ENF specimen encountering the shear-induced sliding. The vertical displacement was extracted from the derived DIC field data along the lines above and below the adhesive from the adherends, as depicted in Figure 33. The minimum distance of the picked displacement values from the adhesive midline was always more than half of the adhesive thickness plus half of the used subset size. This ensured that the local displacement values were extracted outside the region where the high local deformation gradient due to the adhesive-adherend interface emerges.

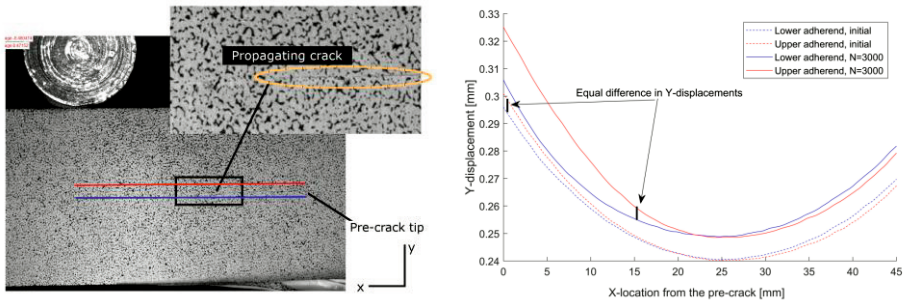

Figure 33. The tested ENF specimen with the applied DIC pattern. a) The lines along which the vertical displacement data was collected. b) The basis of the crack length determination method (Publication V).

From the results, the opening displacement difference of the adherends was determined at the pre-crack tip location. The initial displacement difference at the known pre-crack tip location (at the maximum loading from the first cycle) was used as the threshold value to define the crack location, or the length of the damaged

region. Using a MATLAB script, a similar threshold value was then sought from the sequential curve pairs obtained as the fatigue test proceeded (Figure 33). Figure 34 presents an example of the test result in which the smooth progression of the measured opening separations between the adherends is shown.

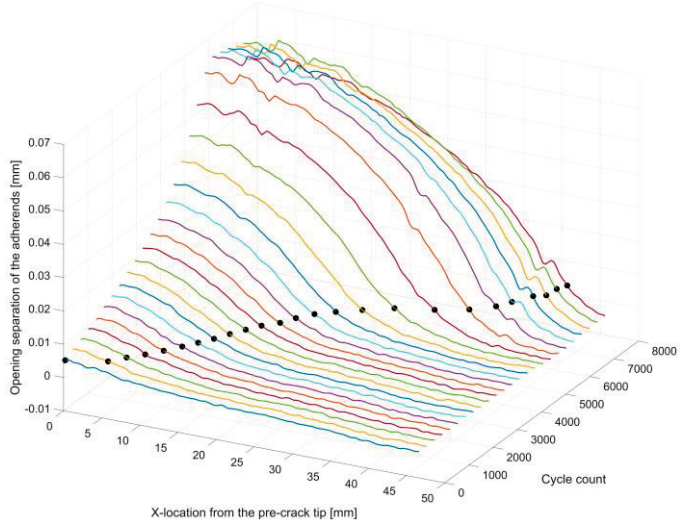

Figure 34. The progress of the opening separation curves along the adhesive, where the black dots present the location of the instantaneous crack length based on the similarity to the initial threshold value (Publication V).

In addition to the DIC-based method, the crack propagation was determined by purely visual means and analytically using the CBBM method. The visual detection of the crack length or the damaged material was difficult, but weak inclined cracks in the adhesive could be detected by detailed inspection of the recorded images representing the crack length, as shown in Figure 35. The DIC-based method corresponds well with the visual observations. On the other hand, the difference between the results provided by the CBBM method is significant.

The penetrating fluid method to evaluate the cracked regions in the specimens was used with the test specimens, the cycling of which was stopped well before the crack had propagated near the central loading pin. The colouring presented in Figure 36 indicates that two distinct regions were revealed. The length of the dark-coloured region corresponded well with crack length obtained with the CBBM method, whereas the pink region matches the result obtained with the DIC-based method (Table 7.

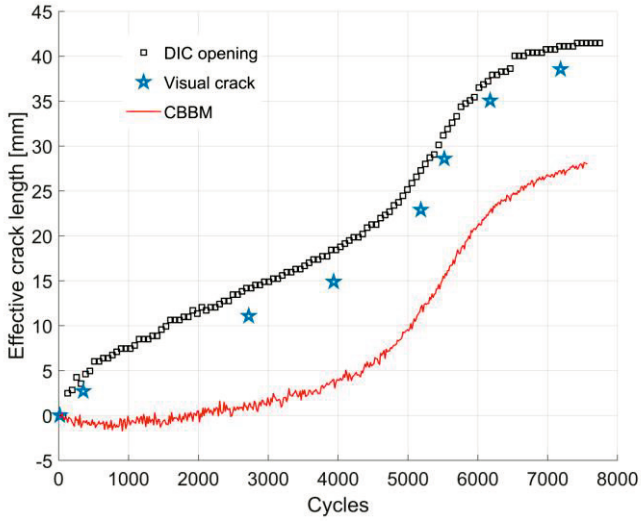

Figure 35. The comparison of the three crack length determination methods (modified from Publication V).

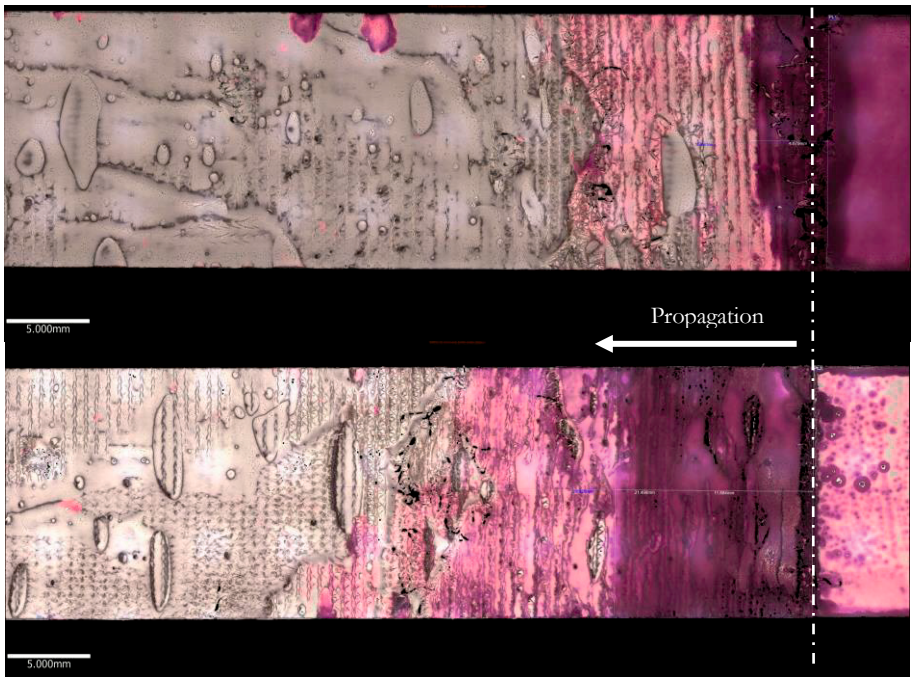

Figure 36. The fracture surface of the separated fatigue specimens after the penetrating fluid treatment from the test, which was stopped after 1500 cycles (upper) and 2000 cycles (lower) (Publication V).

Table 7. The determined crack lengths using the different methods in Publication V.

Specimen	Penetrating fluid, purple (crack) area [mm]	Penetrating fluid, pink (FPZ) area [mm]	Effective crack length (CBBM) a_e [mm]	DIC, opening-based [mm]
Stopped after 1500 cycles	4-5	17	3.5	19
Stopped after 2000 cycles	11-13	22-32	10	30

The DIC method based on the detection of the slight opening of stiff adherends was shown to be suited to quantitatively measuring the length of the damaged region in the ENF tests. Basically, this damage contains the region where the first microcracks develop, but which globally does not have a significant effect on the load-bearing ability (under bending) of the specimen. However, as the cycling continues, finally the microcracks coalesce and form a continuous crack, which is detected as the increased compliance of the test specimen. The schematic presentation of the presumed process of the crack propagation is depicted in Figure 37.

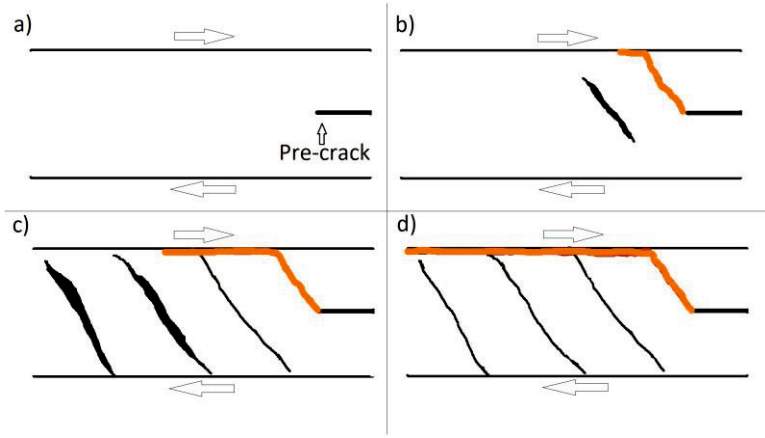

Figure 37. Schematic presentation of the observed propagation of the crack in the adhesive layer as the test proceeds (a-d). First, the inclined repeating microcracks develop, and eventually they coalesce near the upper adhesive-adherend interface. The orange colour indicates the continuous crack.

The results suggest that the microcracked adhesive region does not affect the instantaneous rigidity of the similarly bent specimen. However, as the formation of such damaged adhesive in real applications due to fatigue can also be assumed to exist, the micro-damaged region can actually play a significant role when the loading spectrum is more complex. For example, as the direction of the loading is changed from a mode II- to mode I-favoured failure type, the microcracked region is assumed to perform differently (is very weak). In addition, the environmental ageing can be assumed to have more critical effects on the microcracked region compared to the virgin material. The influence of the damaged region ahead of the distinct crack in thin adhesive layers thus remains an interesting topic for further research.

6 SUMMARY AND RESEARCH HYPOTHESES REVISITED

The use and popularity of DIC methods have increased greatly over the last two decades, and DIC has already become a matured tool in experimental studies in mechanical testing of materials and structures. Although the potential of the methods is acknowledged and tested widely, conventional methods for carrying out the deformation measurements are still largely used. This is due to the established testing procedures and standards, but also because of their simplicity and known precision. Nevertheless, the broad change from the conventional discrete measurement techniques of deformation to the optical full-field methods continues, and the exploitation of the systematic use of DIC in material testing will indubitably increase in future at a rapid pace.

In this thesis, the deformation of highly different varied materials and specimens, ranging from extremely soft hydrogels to rigid fibre-reinforced polymers and bi-layer test specimens, was examined using DIC in the selected compression and fracture mechanics testing methods. The acquired full-field deformation data using the contactless experimental method enabled thorough investigations of the test specimen response. The novel scientific contributions of the thesis rely on the introduced and demonstrated enhancements achieved by the systematic use of the DIC on the selected material test methods, which are used regularly within the material science community.

The inclusion of the DIC in the established test methods was shown to improve their applicability, especially for non-linear and heterogeneous materials. Instead of measuring the specimen deformation by pointwise methods, the available full-field deformation data enabled the characterisation of the local specimen response with adjustable spatial resolution. This allows us to characterise materials and identify their properties using desired level of homogenisation. The use of DIC also reduces the number of unknown factors in the analysis of the test results, which cause operator-, specimen- or testing jig-related bias to the results that decrease the precision of the methods. Examples of the significant factors that were revealed and identified by the DIC measurements include sub-surface voids and uneven surfaces in test specimens, tilted testing jigs, and varying contact friction on the test surfaces.

The available full-field data enabled us to obtain accurate and detailed information from the multi-material test specimens, which was utilised to develop novel strategies to analyse the test outcomes. The data was used to create operator-independent methods to evaluate crack propagation in the selected, mode II-dominated fracture mechanics tests with bi-material test specimens.

Generally, the more detailed raw data provided by the DIC can be exploited in improving the performance of computer-aided modelling and simulation. The simulations based on numerical analysis can be used to expand the current characterisation methods to better understand the material behaviour and to enable the use of more accurate and efficient techniques in virtual research and development of industrial components.

1. *DIC can be used to validate the test response in the unconfined compression of hydrogel materials (Publication I)*

The mechanical testing of hydrogels is challenging due to their intrinsic nature as being extremely soft, watery and transparent materials. Of the regular test types, compression testing is the most commonly used method due to the simple test specimen geometry and loading fixtures (two anvils). The materials show strong non-linear stress-strain behaviour and very strong rate dependency, and various procedures have been utilised to perform the compression tests. The specimen deformation has often been measured solely using the traverse of the crosshead from the test apparatus, because contacting devices cannot be used due to the softness of the materials. However, the possible imperfect specimen geometry, or slightly inclined compression plate fixtures, can easily cause test artefacts on such measured data. Also, the friction between the soft specimen and compression plate surface cause significant barrelling of the specimen (uneven Poisson effect). The determination of the true deformation of the compressed test specimen is thus of great importance in determining the valid material characteristics, like Young's modulus, strength, and relaxation constants.

The stereo DIC method was used to measure the true deformation of the compressed hydrogel cylinder. The random speckle pattern was generated on the transparent material specimen by applying fine carbon black powder on the surface of the wet specimen. The measured 3-D deformations enabled the determination of the true instantaneous geometry of the specimen, which allowed the true stress at the centre of the compressed cylinder to be defined. Moreover, the measured 3-D

deformation results revealed the importance of the constant contact friction at both compression plates for inducing symmetrical specimen deformation to obtain a repeatable test response.

2. *A set of elastic constants can be solved by enhanced use of small specimen size and DIC for fibrous composite materials (Publication II)*

Standard test specimens cannot always be practically fabricated, or include the correct effects of certain manufacturing methods, but still the accurate material properties need to be known, for example, in applying realistic material models used for simulations. This holds especially true for polymer composite materials whose final properties can be strongly dependent on the selected manufacturing method. For example, if the final product will be a curved component manufactured with the strip winding technique, it is practically impossible to fabricate standard material test specimens using the same fabrication process with the same fabrication-based effects. Changing the manufacturing method would have unknown effects, for instance, on the reinforcement orientation and fibre volume content of the composite material, thus affecting the determined material properties.

A method was introduced based on a series of compression tests using a cut prism specimen of a proper size to apply an actual sample of a manufacturing method of composite. The DIC is used to determine the full-field strain data at the surface of the compressed specimen. The local strain mapping provided by the DIC allows the study of the intrinsic heterogeneity of the composite specimen caused by reinforcements, and the definition of the representative region for deriving valid strain data in the studied specimens. With the introduced method, three direction-dependent elastic moduli, including the out-of-plane modulus, and six Poisson's ratios can be determined from a single small test specimen.

3. *The reliability of the notched coating adhesion test method can be improved by using DIC, even when a highly non-linear coating is used (Publication III)*

The established NCA fracture test method for determining the fracture toughness of a coating-substrate interface is based on the detection of the onset of the coating debond during the experiment. In the literature, an analytic 2-D solution was derived to determine the critical energy release rate using the critical strain at the mixed-

mode debond onset. A known challenge in the NCA test is carrying out the detection of the debond of the coating objectively. The conventional method is based on pure visual observation, where the operator undoubtedly has a significant role in defining the 'accurate' onset. Also, several indirect means have been used based on linking the debond onset to the changes in the measured force or specimen deformation. Unambiguous direct linking of the observations is, however, challenging and can lead to high scatter in the final results. The challenges with conventional methods increase further as the heterogeneity and the non-linearity of the tested materials increase.

A method was developed to quantitatively determine the propagation of the coating debond. The technique is based on measuring the full-field strain data of the coating using DIC. From the results, the instantaneous debond length can be determined and linked to the global specimen strain. The process eliminates the operator-based subjective effects on the determination of the critical strain at the coating debond. In addition, the determined instantaneous debond length and the debond shape based on the DIC measurements offer essential raw data that can be used in defining numerical solutions for the problem based on the CZM, for example. The simulations based on CZM or VCCT also take the 3-D effects into account, which can have severe effects on specimen behaviour, especially when non-ideal test specimens are used (e.g. with in various sizes).

4. *DIC can be used to quantify the local strain state and crack propagation in mode II-dominated quasi-static and fatigue experiments, even for joint specimens with thin bond lines (Publications IV and V)*

The extensive characterisation of adhesives requires several different tests to be performed. In addition to the bulk mechanical properties of the material systems, the fracture toughness characteristics are the most essential information required in the design of modern adhesive joints. Different test methods exist to determine the property values under mode I (opening) or mode II (shear). Naturally, in real applications, most cases consist of a combination of the modes, due to which also mixed-mode tests are carried out to enable the formulation of more accurate fracture criterions.

Many of the original test methods are based on the detecting of the crack tip at the test specimen and following its propagation as the test progresses. In mode I-type tests, the crack opens and its width increases, which makes its experimental detection easier. However, in mode II (dominated) tests, the crack propagates under

out-of-plane shear, making its accurate visual detection challenging, and sometimes practically impossible. Due to this, different specimen compliance-based strategies have been introduced to avoid the requirement for the direct crack propagation measurements. However, a variety of different approaches exist, and their outcomes are not always comparable, due to different presumptions and operator selections in the analysis of data.

Nowadays, the fracture mechanics characteristics are determined regularly using numerical analysis methods by simulating the test specimen response related to the experiment in question (inverse methods). For fitting the models to simulate the observed specimen behaviour, the precise crack tip location, however, should be known. Moreover, the local deformation along the adhesive layer, if known, could be used to improve the fit of the models.

A technique based on DIC was introduced and demonstrated to experimentally determine the local opening ('mode I') and shear ('mode II') deformation along the thin adhesive layer in joint specimens, as conventionally used in ENF and SLB tests. The method is based on measuring the accurate deformation of the rather rigid substrates, which then enables the derivation of the local deformation along the actual adhesive layer. With the introduced method, local strain values from the very thin adhesive layers, even beyond the direct spatial resolution of the used DIC setup, can be determined.

Also, a method was developed based on the local crack opening deformation data provided by the DIC at the adhesive bond line, which can be used to monitor the progression of the damaged adhesive zone in cyclic-loaded mode II tests. The results showed that the size of the fracture process zone ahead the distinct crack tip in the fatigue-degraded specimens is significant and not constant over the test time. This finding underlines the need to carefully consider the development of the process zone within the analysis method of fatigue test data.

7 REFERENCES

[1] J. Llorca *et al.*, "Multiscale modeling of composite materials: A roadmap towards virtual testing," *Adv. Mater.*, vol. 23, no. 44, pp. 5130–5147, 2011, doi: 10.1002/adma.201101683.

[2] F. Tao, J. Cheng, Q. Qi, M. Zhang, H. Zhang, and F. Sui, "Digital twin-driven product design, manufacturing and service with big data," *Int. J. Adv. Manuf. Technol.*, vol. 94, no. 9–12, pp. 3563–3576, 2018, doi: 10.1007/s00170-017-0233-1.

[3] M. A. Sutton, J. J. Orteu, and H. Schreier, *Image correlation for shape, motion and deformation measurements: Basic concepts, theory and applications*. Boston, MA: Springer US, 2009. doi: 10.1007/978-0-387-78747-3.

[4] G. Anzelotti, G. Nicoletto, and E. Riva, "Mesomechanic strain analysis of twill-weave composite lamina under unidirectional in-plane tension," *Compos. Part Appl. Sci. Manuf.*, vol. 39, no. 8, pp. 1294–1301, 2008, doi: 10.1016/j.compositesa.2008.01.006.

[5] H. Ghaednia, O. Cermik, D. B. Marghitu, and K. Kardel, "Collision measurements using digital image correlation techniques," *Int. J. Mech. Sci.*, vol. 131–132, pp. 836–846, 2017, doi: 10.1016/j.ijmecsci.2017.07.025.

[6] R. Janeliukstis and X. Chen, "Review of digital image correlation application to large-scale composite structure testing," *Compos. Struct.*, vol. 271, p. 114143, 2021, doi: 10.1016/j.compstruct.2021.114143.

[7] G. Sun, X. Liu, G. Zheng, Z. Gong, and Q. Li, "On fracture characteristics of adhesive joints with dissimilar materials – An experimental study using digital image correlation (DIC) technique," *Compos. Struct.*, vol. 201, pp. 1056–1075, 2018, doi: 10.1016/j.compstruct.2018.06.018.

[8] F. Pierron and M. Grédiac, "Towards Material Testing 2.0. A review of test design for identification of constitutive parameters from full-field measurements," *Strain*, vol. 57, no. 1, pp. 1–22, 2021, doi: 10.1111/str.12370.

[9] J. N. Reddy, *Mechanics of Laminated Composite Plates and Shells*. CRC Press, 2003. doi: 10.1201/b12409.

[10] International Organization for Standardization, "ISO 527 - Part 4: Test conditions for isotropic and orthotropic fibre-reinforced plastic composites," 1997.

[11] M. Meng, H. R. Le, M. J. Rizvi, and S. M. Grove, "The effects of unequal compressive/tensile moduli of composites," *Compos. Struct.*, vol. 126, pp. 207–215, 2015, doi: 10.1016/j.compstruct.2015.02.064.

[12] D. Girolamo *et al.*, "Characterization of adhesive fracture properties by digital image correlation," *Proc. SAMPE Long Beach CA*, 2013.

[13] X. Huo, Q. Luo, Q. Li, and G. Sun, "Measurement of fracture parameters based upon digital image correlation and virtual crack closure techniques," *Compos. Part B Eng.*, vol. 224, p. 109157, 2021, doi: 10.1016/j.compositesb.2021.109157.

[14] International Organization for Standardization, "ISO 25217 Adhesives – Determination of the mode 1 adhesive fracture energy of structural adhesive joints using double cantilever beam and tapered double cantilever beam specimens," 2009.

[15] M. V. Fernández, M. F. S. F. De Moura, L. F. M. Da Silva, and A. T. Marques, "Characterization of composite bonded joints under pure mode II fatigue loading," *Compos. Struct.*, vol. 95, pp. 222–226, 2013, doi: 10.1016/j.compstruct.2012.07.031.

[16] C. Schuecker and B. D. Davidson, "Effect of friction on the perceived mode II delamination toughness from three- and four-point bend end-notched flexure tests," in *ASTM Special Technical Publication, Issue 1383*, 2000, pp. 334–344.

[17] B. R. K. Blackman, A. J. Kinloch, and M. Paraschi, "The determination of the mode II adhesive fracture resistance, GIIC, of structural adhesive joints: An effective crack length approach," *Eng. Fract. Mech.*, vol. 72, no. 6 SPEC. ISS., pp. 877–897, 2005, doi: 10.1016/j.engfracmech.2004.08.007.

[18] F. Sun and B. R. K. Blackman, "Using digital image correlation to automate the measurement of crack length and fracture energy in the mode I testing of

structural adhesive joints," *Eng. Fract. Mech.*, vol. 255, p. 107957, 2021, doi: 10.1016/j.engfracmech.2021.107957.

[19] W. H. Peters and W. F. Ranson, "Digital Imaging Techniques In Experimental Stress Analysis," *Opt. Eng.*, vol. 21, no. 3, p. 213427, 1982, doi: 10.1117/12.7972925.

[20] M. A. Sutton, M. Cheng, W. H. Peters, Y. J. Chao, and S. R. McNeill, "Application of an optimized digital correlation method to planar deformation analysis," *Image Vis. Comput.*, vol. 4, no. 3, pp. 143–150, 1986, doi: https://doi.org/10.1016/0262-8856(86)90057-0.

[21] M. A. Sutton, W. J. Wolters, W. H. Peters, W. F. Ranson, and S. R. McNeill, "Determination of displacements using an improved digital correlation method," *Image Vis. Comput.*, vol. 1, no. 3, pp. 133–139, 1983, doi: https://doi.org/10.1016/0262-8856(83)90064-1.

[22] F. Hild and S. Roux, "Comparison of Local and Global Approaches to Digital Image Correlation," *Exp. Mech.*, vol. 52, no. 9, pp. 1503–1519, 2012, doi: 10.1007/s11340-012-9603-7.

[23] G. Besnard, F. Hild, and S. Roux, "'Finite-element' displacement fields analysis from digital images: Application to Portevin-Le Châtelier bands," *Exp. Mech.*, vol. 46, no. 6, pp. 789–803, 2006, doi: 10.1007/s11340-006-9824-8.

[24] J. Réthoré, S. Roux, and F. Hild, "From pictures to extended finite elements: extended digital image correlation (X-DIC)," *Comptes Rendus - Mec.*, vol. 335, no. 3, pp. 131–137, 2007, doi: 10.1016/j.crme.2007.02.003.

[25] B. Wang and B. Pan, "Subset-based local vs. finite element-based global digital image correlation: A comparison study," *Theor. Appl. Mech. Lett.*, vol. 6, no. 5, pp. 200–208, 2016, doi: 10.1016/j.taml.2016.08.003.

[26] J. Yang and K. Bhattacharya, "Augmented Lagrangian Digital Image Correlation," *Exp. Mech.*, vol. 59, no. 2, pp. 187–205, Feb. 2019, doi: 10.1007/s11340-018-00457-0.

[27] B. Pan, "Digital image correlation for surface deformation measurement: Historical developments, recent advances and future goals," *Meas. Sci. Technol.*, vol. 29, no. 8, 2018, doi: 10.1088/1361-6501/aac55b.

[28] Z. Zhang, "A flexible new technique for camera calibration," *IEEE Trans. Pattern Anal. Mach. Intell.*, vol. 22, no. 11, pp. 1330–1334, 2000, doi: 10.1109/34.888718.

[29] A. Maynadier, M. Poncelet, K. Lavernhe-Taillard, and S. Roux, "One-shot Measurement of Thermal and Kinematic Fields: InfraRed Image Correlation (IRIC)," *Exp. Mech.*, vol. 52, no. 3, pp. 241–255, 2012, doi: 10.1007/s11340-011-9483-2.

[30] X. Wang *et al.*, "Nanoscale Deformation Analysis With High-Resolution Transmission Electron Microscopy and Digital Image Correlation," *J. Appl. Mech.*, vol. 82, no. 12, p. 121001, 2015, doi: 10.1115/1.4031332.

[31] X. Li, W. Xu, M. A. Sutton, and M. Mello, "*In Situ* Nanoscale In-Plane Deformation Studies of Ultrathin Polymeric Films During Tensile Deformation Using Atomic Force Microscopy and Digital Image Correlation Techniques," *IEEE Trans. Nanotechnol.*, vol. 6, no. 1, pp. 4–12, 2007, doi: 10.1109/TNANO.2006.888527.

[32] E. M. C. Jones and M. A. Iadicola, "A Good Practices Guide for Digital Image Correlation," *Int. Digit. Image Correl. Soc.*, p. 94, 2018, doi: 10.32720/idics/gpg.ed1.

[33] L. Guerriero, D. Di Martire, D. Calcaterra, and M. Francioni, "Digital Image Correlation of Google Earth Images for Earth's Surface Displacement Estimation," *Remote Sens.*, vol. 12, no. 21, p. 3518, 2020, doi: 10.3390/rs12213518.

[34] P. L. Reu, W. Sweatt, T. Miller, and D. Fleming, "Camera System Resolution and its Influence on Digital Image Correlation," *Exp. Mech.*, vol. 55, no. 1, pp. 9–25, 2015, doi: 10.1007/s11340-014-9886-y.

[35] D. Lecompte *et al.*, "Quality assessment of speckle patterns for digital image correlation," *Opt. Lasers Eng.*, vol. 44, no. 11, pp. 1132–1145, 2006, doi: 10.1016/j.optlaseng.2005.10.004.

[36] X. Wang, J. Ahn, C. Kaboglu, L. Yu, and B. R. K. Blackman, "Characterisation of composite-titanium alloy hybrid joints using digital image correlation," *Compos. Struct.*, vol. 140, pp. 702–711, 2016, doi: 10.1016/j.compstruct.2015.12.023.

[37] J. Kim, P. Lopez-Cruz, M. Heidari-Rarani, L. Lessard, and J. Laliberté, "An experimental study on the mechanical behaviour of bonded and hybrid bonded-bolted composite joints using digital image correlation (DIC) technique," *Compos. Struct.*, vol. 276, p. 114544, 2021, doi: 10.1016/j.compstruct.2021.114544.

[38] F. Ramezani, M. R. Ayatollahi, A. Akhavan-Safar, and L. F. M. da Silva, "A comprehensive experimental study on bi-adhesive single lap joints using DIC technique," *Int. J. Adhes. Adhes.*, vol. 102, p. 102674, 2020, doi: 10.1016/j.ijadhadh.2020.102674.

[39] M. Mehrabian and R. Boukhili, "Full-field through-the-thickness strain distribution study of hybrid multi-bolted/bonded single-lap composite joints using digital image correlation," *Compos. Part Appl. Sci. Manuf.*, vol. 163, p. 107242, 2022, doi: 10.1016/j.compositesa.2022.107242.

[40] M. Kashfuddoja and M. Ramji, "Whole-field strain analysis and damage assessment of adhesively bonded patch repair of CFRP laminates using 3D-DIC and FEA," *Compos. Part B Eng.*, vol. 53, pp. 46–61, 2013, doi: 10.1016/j.compositesb.2013.04.030.

[41] M. A. Caminero, M. Lopez-Pedrosa, C. Pinna, and C. Soutis, "Damage monitoring and analysis of composite laminates with an open hole and adhesively bonded repairs using digital image correlation," *Compos. Part B Eng.*, vol. 53, pp. 76–91, 2013, doi: 10.1016/j.compositesb.2013.04.050.

[42] M. Kashfuddoja and M. Ramji, "Assessment of local strain field in adhesive layer of an unsymmetrically repaired CFRP panel using digital image correlation," *Int. J. Adhes. Adhes.*, vol. 57, pp. 57–69, 2015, doi: 10.1016/j.ijadhadh.2014.10.005.

[43] D. J. Wu, W. G. Mao, Y. C. Zhou, and C. Lu, "Digital image correlation approach to cracking and decohesion in a brittle coating/ductile substrate system," *Appl. Surf. Sci.*, vol. 257, no. 14, pp. 6040–6043, 2011, doi: 10.1016/j.apsusc.2011.01.119.

[44] M. Zhou *et al.*, "In-situ and real-time tests on the damage evolution and fracture of thermal barrier coatings under tension: A coupled acoustic emission and digital image correlation method," *Surf. Coat. Technol.*, vol. 240, pp. 40–47, 2014, doi: 10.1016/j.surfcoat.2013.12.010.

[45] C. Eberl, D. S. Gianola, and K. J. Hemker, "Mechanical Characterization of Coatings Using Microbeam Bending and Digital Image Correlation

Techniques," *Exp. Mech.*, vol. 50, no. 1, pp. 85–97, 2010, doi: 10.1007/s11340-008-9187-4.

[46] A. Pellegrini, M. E. Palmieri, and M. G. Guerra, "Evaluation of anisotropic mechanical behaviour of 316L parts realized by metal fused filament fabrication using digital image correlation," *Int. J. Adv. Manuf. Technol.*, vol. 120, no. 11–12, pp. 7951–7965, 2022, doi: 10.1007/s00170-022-09303-z.

[47] J. Marae Djouda *et al.*, "Experimental approach for microscale mechanical characterization of polymeric structured materials obtained by additive manufacturing," *Polym. Test.*, vol. 89, p. 106634, 2020, doi: 10.1016/j.polymertesting.2020.106634.

[48] S. Abid, H. Nouri, S. Guessasma, S. Belhabib, and H. Ben Daly, "Digital image correlation to reveal mechanical anisotropy in 3D printing of polymers," *Philos. Mag.*, vol. 103, no. 3, pp. 223–239, 2023, doi: 10.1080/14786435.2022.2140217.

[49] D. Xu, C. Cerbu, H. Wang, and I. C. Rosca, "Analysis of the hybrid composite materials reinforced with natural fibers considering digital image correlation (DIC) measurements," *Mech. Mater.*, vol. 135, pp. 46–56, 2019, doi: 10.1016/j.mechmat.2019.05.001.

[50] M. Kashfuddoja, R. G. R. Prasath, and M. Ramji, "Study on experimental characterization of carbon fiber reinforced polymer panel using digital image correlation: A sensitivity analysis," *Opt. Lasers Eng.*, vol. 62, pp. 17–30, 2014, doi: 10.1016/j.optlaseng.2014.04.019.

[51] T. Brynk, R. M. Molak, M. Janiszewska, and Z. Pakiela, "Digital Image Correlation measurements as a tool of composites deformation description," *Comput. Mater. Sci.*, vol. 64, pp. 157–161, 2012, doi: 10.1016/j.commatsci.2012.04.034.

[52] M. Tekieli, S. De Santis, G. de Felice, A. Kwiecień, and F. Roscini, "Application of Digital Image Correlation to composite reinforcements testing," *Compos. Struct.*, vol. 160, pp. 670–688, 2017, doi: 10.1016/j.compstruct.2016.10.096.

[53] I. E. Tabrizi *et al.*, "Determining tab material for tensile test of CFRP laminates with combined usage of digital image correlation and acoustic emission techniques," *Compos. Part Appl. Sci. Manuf.*, vol. 127, p. 105623, 2019, doi: 10.1016/j.compositesa.2019.105623.

[54] A. Djabali, L. Toubal, R. Zitoune, and S. Rechak, "An experimental investigation of the mechanical behavior and damage of thick laminated carbon/epoxy composite," *Compos. Struct.*, vol. 184, pp. 178–190, 2018, doi: 10.1016/j.compstruct.2017.09.069.

[55] C. Barile, C. Casavola, and G. Pappalettera, "Digital Image Correlation Comparison of Damaged and Undamaged Aeronautical CFRPs During Compression Tests," *Materials*, vol. 12, no. 2, p. 249, 2019, doi: 10.3390/ma12020249.

[56] A. Perrier, D. S. de Vasconcellos, F. Touchard, L. Chocinski-Arnault, and D. Mellier, "Full-Field Measurement at the Weave Scale in Hemp/Epoxy Composite Using Digital Image Correlation," *Polym. Polym. Compos.*, vol. 23, no. 9, pp. 589–600, 2015, doi: 10.1177/096739111502300901.

[57] M. S. Kiasat and M. R. Sangtabi, "Effects of fiber bundle size and weave density on stiffness degradation and final failure of fabric laminates," *Compos. Sci. Technol.*, vol. 111, pp. 23–31, 2015, doi: 10.1016/j.compscitech.2015.02.016.

[58] L. P. Canal, C. González, J. M. Molina-Aldareguía, J. Segurado, and J. Llorca, "Application of digital image correlation at the microscale in fiber-reinforced composites," *Compos. Part Appl. Sci. Manuf.*, vol. 43, no. 10, pp. 1630–1638, 2012, doi: 10.1016/j.compositesa.2011.07.014.

[59] B. Pan, Z. Wang, and Z. Lu, "Genuine full-field deformation measurement of an object with complex shape using reliability-guided digital image correlation," *Opt. Express*, vol. 18, no. 2, p. 1011, 2010, doi: 10.1364/oe.18.001011.

[60] Y. Wang, P. Lava, S. Coppieters, M. De Strycker, P. Van Houtte, and D. Debruyne, "Investigation of the uncertainty of DIC under heterogeneous strain states with numerical tests," *Strain*, vol. 48, no. 6, pp. 453–462, 2012, doi: 10.1111/j.1475-1305.2012.00840.x.

[61] D. Z. Turner, "Peridynamics-Based Digital Image Correlation Algorithm Suitable for Cracks and Other Discontinuities," *J. Eng. Mech.*, vol. 141, no. 2, pp. 1–10, 2015, doi: 10.1061/(asce)em.1943-7889.0000831.

[62] H. Jin and H. A. Bruck, "Pointwise digital image correlation using genetic algorithms," *Exp. Tech.*, vol. 29, no. 1, pp. 36–39, 2005, doi: 10.1111/j.1747-1567.2005.tb00202.x.

[63] J. Poissant and F. Barthelat, "A novel 'subset splitting' procedure for digital image correlation on discontinuous displacement fields," *Exp. Mech.*, vol. 50, no. 3, pp. 353–364, 2010, doi: 10.1007/s11340-009-9220-2.

[64] E. Fagerholt, T. Borvik, and O. S. Hopperstad, "Measuring discontinuous displacement fields in cracked specimens using digital image correlation with mesh adaptation and crack-path optimization," *Opt. Lasers Eng.*, vol. 51, no. 3, pp. 299–310, 2013, doi: 10.1016/j.optlaseng.2012.09.010.

[65] J. Han and B. Pan, "A novel method for measuring discontinuous deformation in digital image correlation based on partition and dividing strategy," *Eng. Fract. Mech.*, vol. 204, pp. 185–197, 2018, doi: 10.1016/j.engfracmech.2018.09.036.

[66] V. Valle, S. Hedan, P. Cosenza, A. L. Fauchille, and M. Berdjane, "Digital Image Correlation Development for the Study of Materials Including Multiple Crossing Cracks," *Exp. Mech.*, vol. 55, no. 2, pp. 379–391, 2015, doi: 10.1007/s11340-014-9948-1.

[67] A. D. Kammers and S. Daly, "Small-scale patterning methods for digital image correlation under scanning electron microscopy," *Meas. Sci. Technol.*, vol. 22, no. 12, p. 125501, 2011, doi: 10.1088/0957-0233/22/12/125501.

[68] M. Mehdikhani, M. Aravand, B. Sabuncuoglu, M. G. Callens, S. V. Lomov, and L. Gorbatikh, "Full-field strain measurements at the micro-scale in fiber-reinforced composites using digital image correlation," *Compos. Struct.*, vol. 140, pp. 192–201, 2016, doi: 10.1016/j.compstruct.2015.12.020.

[69] R. Cappello, G. Pitarresi, J. Xavier, and G. Catalanotti, "Experimental determination of mode I fracture parameters in orthotropic materials by means of Digital Image Correlation," *Theor. Appl. Fract. Mech.*, vol. 108, p. 102663, 2020, doi: 10.1016/j.tafmec.2020.102663.

[70] S. A. Jones and R. A. Tomlinson, "Investigating mixed-mode (I/II) fracture in epoxies using digital image correlation: Composite GIIc performance from resin measurements," *Eng. Fract. Mech.*, vol. 149, pp. 368–374, 2015, doi: 10.1016/j.engfracmech.2015.08.041.

[71] R. Zhang and L. He, "Measurement of mixed-mode stress intensity factors using digital image correlation method," *Opt. Lasers Eng.*, vol. 50, no. 7, pp. 1001–1007, 2012, doi: 10.1016/j.optlaseng.2012.01.009.

[72] M. R. Yadegari Dehnavi, I. Eshraghi, and N. Soltani, "Investigation of fracture parameters of edge V-notches in a polymer material using digital image correlation," *Polym. Test.*, vol. 32, no. 4, pp. 778–784, 2013, doi: 10.1016/j.polymertesting.2013.03.012.

[73] N. Sheerin Sitara, S. Kavitha, and G. Raghuraman, "Review and Analysis of Crack Detection and Classification Techniques based on Crack Types," *Int. J. Appl. Eng. Res.*, vol. 13, no. 8, p. 6056, 2021, doi: 10.37622/IJAER/13.8.2018.6056-6062.

[74] B. R. Murray *et al.*, "Crack Tip Monitoring of Mode I and Mode II Delamination in CF/Epoxies under Static and Dynamic Loading Conditions Using Digital Image Correlation," in *The 18th International Conference on Experimental Mechanics*, MDPI, 2018, p. 389. doi: 10.3390/ICEM18-05225.

[75] J. Jokinen, M. Kanerva, M. Wallin, and O. Saarela, "The simulation of a double cantilever beam test using the virtual crack closure technique with the cohesive zone modelling," *Int. J. Adhes. Adhes.*, vol. 88, pp. 50–58, 2019, doi: 10.1016/j.ijadhadh.2018.10.015.

[76] E. F. Rybicki and M. F. Kanninen, "A finite element calculation of stress intensity factors by a modified crack closure integral," *Eng. Fract. Mech.*, vol. 9, no. 4, pp. 931–938, 1977, doi: https://doi.org/10.1016/0013-7944(77)90013-3.

[77] M. Elices, G. V. Guinea, J. Gómez, and J. Planas, "The cohesive zone model: Advantages, limitations and challenges," *Eng. Fract. Mech.*, vol. 69, no. 2, pp. 137–163, 2001, doi: 10.1016/S0013-7944(01)00083-2.

[78] B. Shen and G. H. Paulino, "Direct Extraction of Cohesive Fracture Properties from Digital Image Correlation: A Hybrid Inverse Technique," *Exp. Mech.*, vol. 51, no. 2, pp. 143–163, 2011, doi: 10.1007/s11340-010-9342-6.

[79] X. Huo, Q. Luo, Q. Li, G. Zheng, and G. Sun, "On characterization of cohesive zone model (CZM) based upon digital image correlation (DIC) method," *Int. J. Mech. Sci.*, vol. 215, p. 106921, 2022, doi: 10.1016/j.ijmecsci.2021.106921.

[80] J. Xavier, M. Oliveira, P. Monteiro, J. J. L. Morais, and M. F. S. F. de Moura, "Direct Evaluation of Cohesive Law in Mode I of Pinus pinaster by Digital Image Correlation," *Exp. Mech.*, vol. 54, no. 5, pp. 829–840, 2014, doi: 10.1007/s11340-013-9838-y.

[81] F. Pierron and M. Grédiac, *The Virtual Fields Method: Extracting Constitutive Mechanical Parameters from Full-field Deformation Measurements*. Springer New York, 2012, doi: 10.1007/978-1-4614-1824-5.

[82] H. Chalal, F. Meraghni, F. Pierron, and M. Grédiac, "Direct identification of the damage behaviour of composite materials using the virtual fields method," *Compos. Part Appl. Sci. Manuf.*, vol. 35, no. 7–8, pp. 841–848, 2004, doi: 10.1016/j.compositesa.2004.01.011.

[83] J.-C. Passieux, F. Bugarin, C. David, J.-N. Périé, and L. Robert, "Multiscale Displacement Field Measurement Using Digital Image Correlation: Application to the Identification of Elastic Properties," *Exp. Mech.*, vol. 55, no. 1, pp. 121–137, 2015, doi: 10.1007/s11340-014-9872-4.

[84] T. He, L. Liu, A. Makeev, and B. Shonkwiler, "Characterization of stress–strain behavior of composites using digital image correlation and finite element analysis," *Compos. Struct.*, vol. 140, pp. 84–93, Apr. 2016, doi: 10.1016/j.compstruct.2015.12.018.

[85] A. P. Ruybalid, J. P. M. Hoefnagels, O. Van Der Sluis, and M. G. D. Geers, "Comparison of the identification performance of conventional FEM updating and integrated DIC," *Int. J. Numer. Methods Eng.*, vol. 106, no. 4, pp. 298–320, Apr. 2016, doi: 10.1002/nme.5127.

[86] S. Roux and F. Hild, "Stress intensity factor measurements from digital image correlation: post-processing and integrated approaches," *Int. J. Fract.*, vol. 140, no. 1–4, pp. 141–157, Jul. 2006, doi: 10.1007/s10704-006-6631-2.

[87] J. Neggers, J. P. M. Hoefnagels, M. G. D. Geers, F. Hild, and S. Roux, "Time-resolved integrated digital image correlation," *Int. J. Numer. Methods Eng.*, vol. 103, no. 3, pp. 157–182, Jul. 2015, doi: 10.1002/nme.4882.

[88] A. P. Ruybalid, J. P. M. Hoefnagels, O. Van Der Sluis, M. P. F. H. L. Van Maris, and M. G. D. Geers, "Mixed-mode cohesive zone parameters from integrated digital image correlation on micrographs only," *Int. J. Solids Struct.*, vol. 156–157, pp. 179–193, Jan. 2019, doi: 10.1016/j.ijsolstr.2018.08.010.

[89] A. Marek, F. M. Davis, J.-H. Kim, and F. Pierron, "Experimental Validation of the Sensitivity-Based Virtual Fields for Identification of Anisotropic Plasticity Models," *Exp. Mech.*, vol. 60, no. 5, pp. 639–664, Jun. 2020, doi: 10.1007/s11340-019-00575-3.

[90] J. A. Stammen, S. Williams, D. N. Ku, and R. E. Guldberg, "Mechanical properties of a novel PVA hydrogel in shear and unconfined compression," *Biomaterials*, vol. 22, no. 8, pp. 799–806, 2001, doi: 10.1016/S0142-9612(00)00242-8.

[91] M. Dehghan-Niri, E. Vasheghani-Farahani, M. Baghaban Eslaminejad, M. Tavakol, and F. Bagheri, "Physicomechanical, rheological and in vitro cytocompatibility properties of the electron beam irradiated blend hydrogels of tyramine conjugated gum tragacanth and poly (vinyl alcohol)," *Mater. Sci. Eng. C*, vol. 114, p. 111073, 2020, doi: 10.1016/j.msec.2020.111073.

[92] F. Stig and S. Hallström, "Influence of crimp on 3D-woven fibre reinforced composites," *Compos. Struct.*, vol. 95, pp. 114–122, 2013, doi: 10.1016/j.compstruct.2012.07.022.

[93] D. A. Dillard, B. Chen, T. N. Chang, and Y. H. Lai, "Analysis of the notched coating adhesion test," *J. Adhes.*, vol. 69, no. 1–2, pp. 99–120, 1999, doi: 10.1080/00218469908015921.

[94] J. Elambasseril and R. N. Ibrahim, "Validity requirements of circumferentially notched tensile specimens for the determination of the interfacial fracture toughness of coatings," *Compos. Part B Eng.*, vol. 43, no. 5, pp. 2415–2422, 2012, doi: 10.1016/j.compositesb.2011.11.038.

[95] M. Kanerva, J. Jokinen, E. Sarlin, and O. Saarela, "Crack propagation under mode II dominance at stainless steel-epoxy interfaces with residual stresses and micro-scale roughness," *Int. J. Solids Struct.*, vol. 50, no. 20–21, pp. 3399–3405, 2013, doi: 10.1016/j.ijsolstr.2013.06.008.

[96] R. D. Adams, *Structural Adhesive Joints in Engineering*. Springer Netherlands, 2012 doi: 10.1007/978-94-009-5616-2

[97] K. Leffler, K. S. Alfredsson, and U. Stigh, "Shear behaviour of adhesive layers," *Int. J. Solids Struct.*, vol. 44, no. 2, pp. 530–545, 2007, doi: 10.1016/j.ijsolstr.2006.04.036.

[98] K. S. Madhusudhana and R. Narasimhan, "Experimental and numerical investigations of mixed mode crack growth resistance of a ductile adhesive joint," *Eng. Fract. Mech.*, vol. 69, no. 7, pp. 865–883, 2002, doi: 10.1016/S0013-7944(01)00110-2.

[99] M. M. Abdel Wahab, "Fatigue in Adhesively Bonded Joints: A Review," *ISRN Mater. Sci.*, vol. 2012, no. c, pp. 1–25, 2012, doi: 10.5402/2012/746308.

[100] B. R. K. Blackman, A. J. Brunner, and J. G. Williams, "Mode II fracture testing of composites: a new look at an old problem," *Eng. Fract. Mech.*, vol. 73, no. 16, pp. 2443–2455, 2006, doi: 10.1016/j.engfracmech.2006.05.022.

[101] M. F. S. F. de Moura, J. P. M. Gonçalves, and M. V. Fernandez, "Fatigue/fracture characterization of composite bonded joints under mode I, mode II and mixed-mode I+II," *Compos. Struct.*, vol. 139, pp. 62–67, 2016, doi: 10.1016/j.compstruct.2015.11.073.

[102] M. Pérez-Galmés, J. Renart, C. Sarrado, A. J. Brunner, and A. Rodríguez-Bellido, "Towards a consensus on mode II adhesive fracture testing: Experimental study," *Theor. Appl. Fract. Mech.*, vol. 98, pp. 210–219, 2018, doi: 10.1016/j.tafmec.2018.09.014.

[103] A. Majano-Majano, A. J. Lara-Bocanegra, J. Xavier, and J. Morais, "Experimental evaluation of mode II fracture properties of Eucalyptus globulus L.," *Materials*, vol. 13, no. 3, pp. 1–13, 2020, doi: 10.3390/ma13030745.

[104] M. F. S. F. de Moura, M. A. L. Silva, A. B. de Morais, and J. J. L. Morais, "Equivalent crack based mode II fracture characterization of wood," *Eng. Fract. Mech.*, vol. 73, no. 8, pp. 978–993, 2006, doi: 10.1016/j.engfracmech.2006.01.004.

PUBLICATIONS

PUBLICATION I

Comprehensive characterisation of the compressive behaviour of hydrogels using a new modelling procedure and redefining compression testing

J. Nafar Dastgerdi, J.T. Koivisto, O. Orell, P. Rava, J. Jokinen, M. Kanerva and M. Kellomäki

Materials Today Communications 28 (2021) 102518
https://doi.org/10.1016/j.mtcomm.2021.102518

Publication reprinted with the permission of the copyright holders.

Materials Today Communications 28 (2021) 102518

Contents lists available at ScienceDirect

Materials Today Communications

journal homepage: www.elsevier.com/locate/mtcomm

Comprehensive characterisation of the compressive behaviour of hydrogels using a new modelling procedure and redefining compression testing

Jairan Nafar Dastgerdi [a,b,*,1], Janne T. Koivisto [c,d,1], Olli Orell [e], Pantea Rava [f], Jarno Jokinen [e], Mikko Kanerva [e], Minna Kellomäki [c]

[a] Department of Aerospace Engineering, Amirkabir University of Technology, 424 Hafez Avenue, Tehran, Iran
[b] Department of Mechanical Engineering, School of Engineering, Aalto University, P.O. Box 14300, 00076, Aalto, Finland
[c] Laboratory of Biomaterials and Tissue Engineering, Faculty of Medicine and Health Technology, Tampere University, Korkeakoulunkatu 3, 33720, Tampere, Finland
[d] Division of Pathology, Department of Laboratory Medicine, Karolinska Institutet, Alfred Nobels allé 8, 14152, Huddinge, Sweden
[e] Materials Science and Environmental Engineering, Faculty of Engineering and Natural Sciences, Tampere University, Korkeakoulunkatu 6, 33720, Tampere, Finland
[f] Department of Industrial and Management Engineering, Amirkabir University of Technology, 424 Hafez Avenue, Tehran, Iran

ARTICLE INFO

Keywords:
Compression testing
Hydrogel
Gellan gum
Mechanical properties
Viscoelastic deformation

ABSTRACT

The aim of tissue engineering is the regeneration of damaged tissue or the production of representative tissue organoids *in vitro*. To achieve this, one approach is to use hydrogels, water-swollen hydrophilic and crosslinked polymer networks, that can accommodate encapsulation of living cells and help the regeneration process. Even though mechanically biomimicking target tissue is important for a favorable cell response, the mechanical characterisation of tissues or hydrogels is not yet a fully defined process with various possible models and methods existing. In this paper, for the first time, a specific procedure and model has been suggested for the discussion of the nonlinear stress-strain relationship in large deformations of hydrogels. Moreover, this approach has comprehensively characterised the compressive material performance of hydrogels in a theoretical framework. To present the performance and utility of the introduced procedure, it is used with two different compositions of bioamine crosslinked gellan gum hydrogel. In addition, a three-dimensional digital image correlation technique has been utilized together with compression testing to measure the actual force and deformation in unconfined compression. The material model parameters were obtained to represent nonlinear stress-strain behaviour and the viscoelastic response (relaxation) of gellan gum hydrogel in compression.

1. Introduction

Hydrogels are three-dimensional (3D), water-filled, crosslinked networks of hydrophilic polymers [1,2]. Similar to the natural extracellular matrix (ECM), hydrogels are soft biomaterials that can contain biofunctionalisation sites for the attachment, migration and differentiation of cells. Moreover, hydrogels are currently being employed and explored for a broad range of medical applications, including cell encapsulation, drug delivery and tissue engineering (TE) [2–5]. In TE, the main goal is to combine a biomaterial, such as a hydrogel, with living cells to produce a piece of tissue *in vitro* that functions the same way as natural tissue *in vivo* [5,6]. The tissue can then be used in either therapeutic clinical applications to replace damaged or malfunctioning tissue [6] or as a model when studying developmental biology, disease modelling or toxicology *in vitro* [7,8].

Biomimicking the ECM mechanically is important in clinical TE as well as during modelling *in vitro*, as cells are known to respond to mechanical cues in their environment via mechanotransduction [8–11]. Thus, a good starting point for rationally designing novel biomaterials for TE is to make their mechanical properties match the target tissue [12]. While recent studies [13–17] have powerfully illustrated the role of mechanics in cell biology, the ECMs in tissues are not just linear elastic, and the high degree of nonlinearity in the stress-strain relationship of ECMs and hydrogels as synthetic ECMs has been proven [18,19]. Hydrogels on their own are complex, hydrophilic polymer networks containing a large amount of water (over 95 %), which makes hydrogels solids with strong fluid-type behaviour. Therefore, an important challenge is to determine how time-dependent and nonlinear mechanics

* Corresponding author at: Department of Aerospace Engineering, Amirkabir University of Technology, 424 Hafez Avenue, Tehran, Iran.
E-mail address: Jairan.nafardastgerdi@aalto.fi (J. Nafar Dastgerdi).
[1] Authors contributed equally.

https://doi.org/10.1016/j.mtcomm.2021.102518
Received 21 March 2021; Received in revised form 3 June 2021; Accepted 4 June 2021
Available online 15 June 2021
2352-4928/© 2021 Elsevier Ltd. All rights reserved.

regulate cell behaviours.

In recent years, an increasing amount of effort has been devoted to the constitutive models of materials to accurately predict the comprehensive 3D stress-strain state [20]. The work-conjugate pair of logarithmic strain and Cauchy stress can even be determined over the large-strain region [21–24]. Numerous measurement techniques and setups, such as compressive (confined and unconfined), tensile, shear, indentation (macro- and micro-) and tests by rheometers, have been applied to validate models. However, the different output data from tests are not directly comparable to each other, especially in the case of anisotropic materials [25]. Furthermore, the test output can hardly ever be directly used to validate a material model – the effects of the shape of the test specimen, the contact to the test machine and the exact 3D deformation can be difficult to simply omit. Only recently has full-field data of the deformation become available. The 3D digital image correlation (3D-DIC) technique has become a widely used method to study full-field displacements and strains in numerous applications [26,27]. For example, in the area of biomechanics, DIC offers new approaches to study the behaviour of soft, sensitive and commonly anisotropic materials in various environments [28].

1.1. Elastic region

The applications of the concepts of the linear theory of elasticity [19, 29] to a highly nonlinear material has led to the inevitable challenge of defining the limit between the elastic and non-elastic regions. Whenever a material, such as a hydrogel, expresses a significant effect by the loading rate (in detail strain rate) on the mechanical response, it will have to be modelled by the time-dependent response to stress [25, 30–32].

The existing literature on hydrogel mechanics is filled extensively with experimental research. Bai et al. [33] compiled a comprehensive list of the published, observed phenomena including solid mechanics, fracture mechanics and fatigue. According to numerous studies, it is rather evident that hydrogel behaviour – including fracture onset, crack propagation and mechanical damage – is strain-rate dependent, and this dependence is a 'function' of the exact chemical composition. Hydrogels can significantly heal after ultimate phenomena (e.g., crack or crease onset), and this feature does not make it any easier to model the ultimate behaviour of hydrogels in a common manner.

The elastic region covers the behaviour where all strain energy stored in the body of the hydrogel (by external loading) can be recovered. Within the recovery of strain energy to another form (mainly potential energy), the body returns to its original state. For typical engineering materials, this type of behaviour occurs at relatively small deformations – within a magnitude of percent strain or less. For hydrogels, the reported 'elastic region', in terms of the percentage of specimen height compressed, ranges up to 10 % [34]. However, hardly ever is the presumed elastic region verified to be elastic in the current literature. Furthermore, the challenges in the test machine's crosshead-integrated sensor data are that it is not directly related to an elastic (nonlinearity) limit such as the true strain or stress level of a material model. The most common test to study the elastic and dissipative ranges of deformation is dynamic mechanical analysis (DMA). For hydrogels, the typical test sequence is run at a constant frequency and low deformation range (≈1% of specimen height) and with a load ratio of 0.1 [35]. Further frequency sweeps (0.1 Hz–100 Hz) are run to determine the complex modulus [36]. Another alternative is small-amplitude oscillatory shear testing [35]. It should be noted, however, that a dynamic stiffness (storage modulus) does not correspond to the quasi-static elastic (Young's) modulus – especially for hydrogels, as noted by Kocen et al. [35].

The elastic region, per experimental actions, is highly dependent on the test speed [37]. Gofman and Buyanov [38] reported an unusual disappearance of hysteresis, yet they did not report permanent deformation. In their tests, hysteresis suggests either stress sign-dependent nonlinear elastic behaviour or relaxation-creep that is able to heal upon a single load cycle. Several studies (e.g., Nakamura et al. [37]) have shown that for constant hydrogel composition and test specimen geometry, an 'overly high' test speed and likewise an 'overly low' test speed leads to simply non-linear behaviour (in force-displacement data). At an 'intermediate' speed, the behaviour tends to involve a linear region, although it might simply form a balance between the relaxation and strain-hardening effects in the specimen. At very low (i.e., 0.05 %/min) test speeds, hydrogels begin to seep the internal solvent [39–45]. Hence, several modelling studies have dealt with poroelasticity and viscoelasticity separately [45–51], while only a few studies have analysed the combined poroviscoelastic models [32,52–54]. These models aim to phenomenologically describe the conformational change of the molecular network and the migration of the incompressible solvent [25,39]. Researchers have suggested that the elastic region of hydrogels could refer to the behaviour where solvent does not have enough time to migrate in a gel and when the poroelastic-type behaviour caused by the 'long-range' motion of (solvent) molecules is negligible [37,55,56].

1.2. Compression testing of hydrogels

Compressive testing has the advantage of being relatively easy to perform in practice by using a universal tester, and the test data (force-displacement curves) are considered to be simple to interpret. Many researchers have interpreted test data as a direct uniaxial response of hydrogel bulk (material). Consequently, the suggested models mostly cover one and two-dimensional forms [52,54,55]. On the other hand, compression testing and the theory (of elastic response) has several challenging issues, such as exact changes of volume, as reported by Zhang et al. [76].

The typical reported crosshead displacement ranges of compression extend up to 60 % of specimen height. Sometimes researchers have indicated the elastic region based on the initial 'instant fit' (tangent) to the engineering stress-strain derived from the crosshead displacement curve [35]. For reliable test data, the first data points are in a way problematic due to the load cell's inaccuracy and noise as well as the effects of non-ideal surface flatness. Some researchers suggested that Young's modulus could be directly calculated as a linear fit along the engineering stress-strain curve (derived from crosshead displacement) between 5% and 10 % strain [34]. However, true stress or strain are hardly ever reported, and engineering stress and averaged strain (namely, applied strain [57] from the crosshead displacement) or even normalized values are reported instead [36]. At these typical high levels of deformation, the test specimen behaviour cannot be presumed to be purely elastic. Therefore, since hydrogels contain mostly water, they are incompressible for any reasonable test procedure. For compressive deformations as high as 15 %–30 %, the test specimen must significantly deform in the lateral direction to preserve the volume (Poisson's ratio ≈0.5). Ideally, when the test machine's (anvil) contact with the hydrogel is frictionless, the Poisson's effect is no longer a problem. However, when the contact friction goes to zero, the side force to slide the specimen out goes to zero. In practice, researchers use thin pieces of paper to increase the friction and to hold the hydrogel test specimen firmly in place [37]. The higher the friction, the more the hydrogel must worm (including local rotation) on contacts with the test machine. Moreover, the shorter (low height to diameter ratio) the test specimen is, the more extensive are the contact-related effects on the test output data. On the other hand, a higher specimen easily bends and can buckle under the compressive load.

Due to the variety of hydrogel chemistry, the complex strain-rate dependence and the viscous-porous behaviour, it is anticipated that completely generalised test guidelines for an 'elastic region' and negligible nonlinearities as well as the contact effects cannot be given. However, a clear procedure should be established to investigate the significance of these 'artifacts' during the compression testing of

hydrogels and to determine the appropriate elastic region per hydrogel. Bai et al. [33] aimed to connect chemists and mechanicians – the next step is to define common, quantitative understanding.

1.3. Prerequisites

The lower bound of the compression test speed is not useful for determining the mechanics of hydrogels because the seeping or vaporizing of solvent results in something other than the original hydrogel, even anisotropy (gradients). For the upper bound, viscoelasticity governs hydrogel behaviour up to the deformation rate where the viscous flow or relaxation becomes negligible. It has been suggested that the viscoelastic region resembles reversible crosslinks in hydrogels [30–32]. Combined spring and dashpot modellings are common for viscoelastic models in general. When these elements are connected in series, they are referred to as a Maxwell model, whereas a connection made in parallel is referred to as a Kelvin–Voigt model. In addition, specialised combinations are used for specific loadings and materials [58]. To determine the precise material constants for viscoelastic behaviour, further testing is required, yet this testing can be performed by applying compression. In summary, a reasonable procedure for the compression testing of hydrogels to determine compression (Young's) modulus must contain the following elements:

I Tests run at several test speeds (strain rates)
II Tests run over a displacement range without observable permanent damage (e.g., crease [57])
III Accurate analysis of linearity per test speed using fitted viscoelastic models
IV An iterative scheme for estimating the significance of viscous effects over a truncated displacement range with selected acceptable error
V Finite element analysis to estimate the significance of test artifacts at test machine-hydrogel contact with DIC comparison
VI Correcting for relaxation to resolve the value of modulus

The hydrogel type chosen in this study for the characterisation of mechanical behaviour, the testing of a new mechanical model and the characterising approach is gellan gum (GG) [59], a bacterial polysaccharide with high potential for TE applications and 3D cell culturing [60–62]. The bioamine crosslinking of GG [60] and the chemical crosslinking of oxidized GG with hydrazide-modified hyaluronic acid [61] and hydrazide-modified gelatin [62] via hydrazone reaction, have been reported by some authors to be potential methods for the production of biocompatible hydrogel for soft TE applications. When using the bioamine GG in neuronal cell culture, it was noted that the neural cells prefer a surprisingly high elastic modulus (≈23 kPa) compared with our reference measurements with brain tissue (≈7−10 kPa) and common published results (<1 kPa) [9,60]. A possible reason for this discrepancy is the inadequacy of the mechanical model and the test procedures. Therefore, an extensive analysis of the compression testing for hydrogels is presented to determine the appropriate elastic region in the following study.

2. Experimental

2.1. Preparation of hydrogel

Gellan gum (GG, Gelzan™, low acyl, Mw 1 000 g/mol), spermine tetrahydrochloride (SPM) and sucrose were obtained from Sigma-Aldrich (St. Louis, MO, USA) with the highest level of purity available. The hydrogel solutions were prepared as previously stated and followed the same protocol as used in cell culture experiments [60]. In brief, 10 % (w/w) sucrose in deionized water was used as solvent; GG was dissolved at 5 mg/mL and SPM at 0.35 mg/mL and at 0.175 mg/mL. After dissolution, all solutions were sterile filtered at 60 °C with a 0.8/0.2 μm Acrodisc® syringe filter (PALL Corporation, Port Washington, NY, USA). To produce a compression sample, solutions were heated to 37 °C in a water bath. The SPM crosslinker was combined with GG at a volume ratio of 4:25 and mixed with a magnetic stirrer as described in [63], and cast into self-made cylindrical moulds with an approximate height of 6.5 mm and a cross-sectional diameter of 12.2 mm. The specimens for testing were incubated overnight in a humid atmosphere at 37 °C and tested the following day. In this study, two different SPM crosslinker concentrations, 1.1 % and 0.6 % (w/w of polymer), were tested. These concentrations, chosen based on our previous study [60], were found to be mechanically biomimicking to soft tissue and suitable for 3D cell culture applications.

2.2. Compression testing

Unconfined compression testing was performed with a Bose Electroforce BioDynamic 5100 machine using WinTest 4.1 software and 225 N load cell (TA Instruments, Eden Prairie, MN, USA). Due to the softness of 0.6 % SPM hydrogel, the load cell was changed to 22 N (TA Instruments), and digital filtration at 1 Hz was used to reduce the noise in the load signal. The compression test parameters (displacement rate, starting point, friction) were varied to gain a complete view of the hydrogel's viscoelastic response, and a part of the individual tests were analysed using a 3D-DIC setup as described in the following section. All tests were performed on wet hydrogels at room temperature. In addition, a wetted piece of lint-free cellulose paper (Cellulose wadding, Katrin, Espoo, Finland) was used on both compression plate surfaces to increase the friction between the hydrogel and the test machine boundary as well as to prevent sample slippage. The exact dimensions (diameter, height) of each sample were measured with callipers before testing. The standard test parameters were the same as in [60,63], compressing the sample at different displacement rates until reaching 65 % displacement of the original sample height (causing fracture). In this study, 10 mm/min and 1 mm/min displacement rates were examined to observe the rate dependency of the hydrogel compression.

2.3. Digital image correlation

The 3D-DIC technique [27] using lenses with a focal length of 100 mm was used to study the surface deformations during the compression tests of the hydrogel samples (Fig. 1). Using this technique, the unique features of the sample surface are recorded simultaneously by two cameras (5 Mpix Imager E-Lite, LaVision, Germany).

From the recorded images, the full-field surface deformation map was obtained by tracking the movement of the surface divided into small subsets. The unique surface pattern required for the carrying out of the experiments was accomplished by blowing fine carbon black powder (Corax® N550, Evonik, Germany) on the naturally transparent, moist sample.

The lighting of the sample was performed using two synchronized pulsed led lights operated directly via DIC software (Davis 8.4, LaVision). To achieve a constant and flat light throughout the sample, the reflections caused by the curved, wet and transparent sample needed to be optimised and balanced. The recording rate of the 3D-DIC measurements ranged from 1 Hz to 8 Hz, depending on the total time per each compression test. The scale factor of the images was 8 μm/pix, and the root mean square (RMS) fit of the calibration was 0.4 pix.

The deformation analysis was performed using Davis 8.4 software. The used subset and step sizes were 55 pix × 55 pix and 15 pix, respectively. To ease the tracking process against, e.g., an artificially changing pattern due to seeping water on the surface or changing reflections due to curvature changes of the sample surface, the applied correlation mode in the analysis was the sum of differential images instead of the more conventionally used mode (i.e., relative to the first image). In addition to the qualitative examinations of the sample deformations, axial surface strains and radial surface displacements were

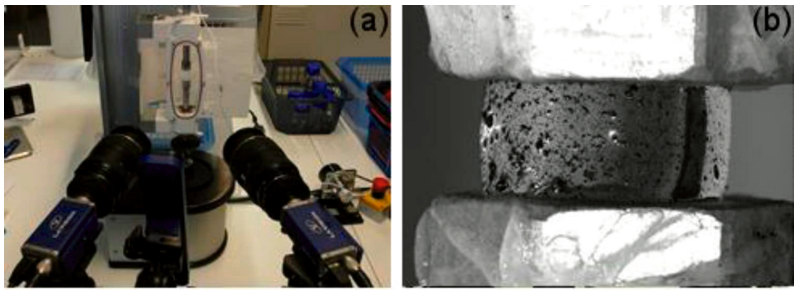

Fig. 1. (a) 3D-DIC test set up, (b) an image taken of a sample with carbon black speckle pattern.

calculated from the correlation results.

3. Theory/Calculations

3.1. Determination of stress and strain

Due to the finite but complex deformation [81] of the test specimens, logarithmic strain (ε^n), and Cauchy stress (σ^c) are employed in this study. The logarithmic strain possesses certain intrinsic properties that show its favoured position among all strain measures [22,81]. In the uniaxial case, to start with, the Cauchy stress takes the following form:

$$\sigma^c = \frac{N}{A}, \tag{1}$$

where (N) is the applied force, and (A) is the true, current cross-sectional area.

The logarithmic strain is defined as follows:

$$\varepsilon^n := \int_{l_0}^{l} \frac{dl}{l} = \ln\frac{l}{l_0}, \tag{2}$$

where (l_0) and (l) are the initial and current gauge length of the sample, respectively. Here, the positive directions are defined so that the strain for tensile deformation is positive and, likewise, stress for tensile loading is positive. After mathematical manipulations, the logarithmic strain and the Cauchy stress are obtained in terms of engineering strain (ε^{eng}) and engineering stress (σ^{eng}) as follows:

$$\varepsilon^n = \ln(1 + \varepsilon^{eng}), \tag{3}$$

and

$$\sigma^c = \sigma^{eng}(1 + \varepsilon^{eng}). \tag{4}$$

3.2. Uniaxial approximation for the analysis of linear region

A mathematical model has been presented to characterise the presumed nonlinear (elastic) mechanical behaviour of hydrogels covering the possible toe region followed by a continuous elastic behaviour [58,64]:

$$\sigma = \begin{cases} A\,(e^{B\varepsilon} - 1) & \forall \varepsilon \le p \\ E\,(\varepsilon - p) + q & \forall \varepsilon \succ p \end{cases} \tag{5}$$

where (σ) is the stress and (ε) is the strain. This nonlinear fitting simultaneously applies the modulus (E), transition strain (p) and transition stress (q) where the transition point is defined as the end of the initial toe region (if a toe region is observed). At the transition point, the stress-strain curve shifts from strain-stiffening to strain-softening.

To maintain the elastic modulus (E), the slope of the linear portion was defined as the slope of the stress-strain curve at the transition point (p,q) between the two portions. Thus, this equation can be fully defined by three parameters: p and the constants A and B. Using the MATLAB function *fmincon*, the parameter values (A, B and p) are simultaneously optimised to minimise the mean square error. It should be noted that the optimisation here is performed on the entire selected data, simultaneously fitting the exponential section and the linear section, and that the location of the transition point is a continuous variable included in the optimisation process. This approach maintains continuity at the transition between the exponential and linear portions of the stress-strain curve.

3.3. Relaxation test and data analysis

In general terms, a viscoelastic material shows the behaviour of both an elastic solid ($\sigma = E\varepsilon$) and a viscous liquid ($\sigma = \eta\dot{\varepsilon}$) at the same time when subjected to a stress or strain. A commonly used test to measure the viscoelastic properties of hydrogels is the stress relaxation test. In this test, a constant strain (ε_0) is targeted by applying 'constant' crosshead displacement, and the reaction force at the test machine is recorded over time. Within the terminology of statistical mechanics, relaxation means an irreversible process in contradistinction to the time-reversible process of Newtonian mechanics. It is the change of a system from one physical state to another, involving the dissipation of energy. Relaxation is generally described by the following function:

$$\sigma(t) = \sigma_\infty + \sigma_0 G(t), \tag{6}$$

where (σ_∞) and (σ_0) are material constants, and $G(t)$ is the normalized relaxation function [65,66].

The best known relaxation function is the simple exponential decay function:

$$G(t) = \exp(-\frac{t}{\tau}), \tag{7}$$

where (τ) is the relaxation time. This parameter determines the rate of decrease of the relaxation function. It is well known that Eq. (7) is the solution of the linear first order equation:

$$G(t) = -\frac{1}{\tau}(\sigma(t) - \sigma_\infty). \tag{8}$$

It means that the rate (of approximation) of the parameter to the equilibrium state is proportional to its shift from the equilibrium state. Wide-ranging experimental information leads to the conclusion that pure exponential relaxation is rarely found in nature [67]. To describe the relaxation that does not obey the simple exponential law, the empirical stretched exponential law or the Kohlrausch-Williams-Watts (KWW) function has been widely applied [68,69]:

$$G(t) = \exp(-\frac{t}{\tau})^\beta, \tag{9}$$

Where β is an empirical exponent ($0 \le \beta \le 1$). The β term in the KWW

stretched-exponential characterises the degree of non-exponentiality of the relaxation function.

The main difference between exponential decay and KWW-type relaxations is the nonlinear dissipation of energy. A non-linear behaviour in the stress relaxation response of the hydrogels has been predicted using KWW-type relaxation.

The time dependent relaxation modulus of the material is defined as:

$$E_{rel}(t) = \frac{\sigma(t)}{\varepsilon_0}. \tag{10}$$

At the beginning of a stress relaxation test, the test specimen is loaded suddenly and, by definition, so fast that only elastic deformation can take place (i.e., a test rate to iterate per hydrogel chemistry). It is convenient to set the zero-reference for time to this moment. Therefore, the strain is given at $t = 0$ as ε_0 can be calculated by presuming Hooke's law as follows:

$$\varepsilon_0 = \frac{\sigma_c^{11}}{E} \; where \; \sigma_c^{11} = \frac{N}{A}. \tag{11}$$

Similar to the above, in Eq. (11), the variable N is the measured force and A is the current cross-sectional area of the sample. E is the linear region modulus (for a selected or truncated single linear portion model of the elastic region). Finite element implementations can be made by using a series expansion of the relaxation modulus (see Section 3.3).

3.4. Test artifacts, 3-D effects and strain rate effects for test data truncation

The effects of the true 3D stress-strain field, the contact with the test machine, and possible specimen inhomogeneity must be in details analysed. Here, ABAQUS (Standard and Explicit) code was used for the simulations in an axisymmetric space. The test machine surfaces were modelled as analytical rigid. As a starting point, the bulk hydrogel specimen (height 6.5 mm, radius 6.1 mm) was connected in a rigid manner (i.e., tie constraint) to the machine. Then, elastic moduli of 15.36 kPa and 1.719 kPa were studied one by one (based on Fig. 10b), and a Poisson's ratio of 0.48 (nearly incompressible) was applied. The bulk hydrogel was meshed using the fully-integrated biquadratic quadrilateral elements (CAX8). As a possible explanation for the formation of a toe region in some experiments (shown by force-displacement data), anisotropic elastic behaviour was studied as an alternative – the engineering constants are derived in the Appendix A. Similarly, an inhomogeneous hydrogel specimen was considered by modelling a 'skin' (100 μm by partition), forming the free surface of hydrogel having the higher modulus of the two above values. The formation of skin in reality could follow the vaporisation of solvent on the specimen's free surfaces. Furthermore, a membrane-like skin (a type of behaviour) was studied by using quadratic membrane elements (MAX2) with a given thickness of 10 μm (modulus 15.36 kPa, Poisson's ratio of 0). The interface between the membrane-like skin and hydrogel bulk was a frictionless non-penetrating contact formulation. For both skin simulation cases, an upper limit of 6 kPa was defined and followed by an ideal-plastic behaviour.

For a rigid machine-hydrogel contact, it was observed that the hydrogel specimen reached stresses beyond any reasonable strength at the very beginning of a compression test. Therefore, at the contact near the free edge of the specimen (termed a 'corner'), the hydrogel must either slide, worm and/or flow locally (via plastic or viscous flow). An enhanced contact was studied as an alternative by applying a penalty-based contact with a friction coefficient of 0.2. Additionally, a slight rounding (radius 0.5 mm) of the specimen corner was considered. For an artifact of the specimen's geometry, a convex top (5°) of the hydrogel specimen and related behaviour, i.e., non-flat contact to the test machine, was studied. The mentioned simulations were run by launching an enforced displacement in the direction of the symmetry axis (i.e., compression).

The dynamic effects and relaxation during compression testing (at displacement rates of 1 mm and 10 mm/min) were simulated using the explicit solver of ABAQUS. Pure linear elastic and viscoelastic material models were incorporated (in details rate-dependent time domain viscoelasticity). The viscoelastic part was inputted by using the relaxation test data, i.e., 600 experimental data points of the fitted $G(t)$ of Eq. (9) to create the Prony series parameters of the relaxation modulus. The elastic deformation was based on elastic modulus (values 15.36 kPa and 1.719 kPa were analysed one by one). The elastic modulus was defined as instantaneous stiffness so that a Maxwell-type coupling with viscous dissipation is essentially produced for the simulated tests. A density of 1000 kg/m^3 was used for the hydrogel. Mass scaling of ×100 was used, and a survey was made to check the effects for up to ×1000 scaling. The quadratic triangle element (CAX6M) was used for the explicit computations. The FEA models included 3656–9452 variables for the different simulation cases.

4. Results and discussion

4.1. Measured behaviour of hydrogel in compression

Fig. 2 shows typical Cauchy stress-logarithmic strain curves of GG hydrogel specimens for two different test speeds. The displacement rate-dependent stress-strain behaviour of the hydrogel samples can be clearly observed in this graph. For a low displacement rate, the stress state relaxes during the test and leads to a lower peak stress level.

DIC has previously been applied to studying the compression behaviour of bioactive-glass- reinforced GG with both visible light and micro-CT imaging, but only to freeze-dried scaffolds [70,71]. To our knowledge, DIC has not previously been used on wet GG hydrogels. Here, visible light DIC has been used during the unconfined compression of wet hydrogels. In Fig. 3a, a full-field strain map of the axial strains in the sample tested with a test speed of 10 mm/min is presented. Near the compression plates, the strain field is strongly uneven, which mostly arises from DIC subset-related issues close to the interface between the rigid (compression plate) and the deforming (specimen) surfaces. Based on the full-field data, the nominal axial strains were calculated using a virtual strain gauge size of 1.5 mm × 1.5 mm located at the centre of the sample (from which a mean strain value was calculated).

In Fig. 3b, the determined DIC strains are compared with the engineering strains calculated from the crosshead displacement data and a good correspondence can be seen. Furthermore, the correspondence indicates that the logarithmic strain calculated from the crosshead displacement data reliably represents the strains at the middle of the specimen. At a timestamp of 14.5 s, the fracture initiates in the

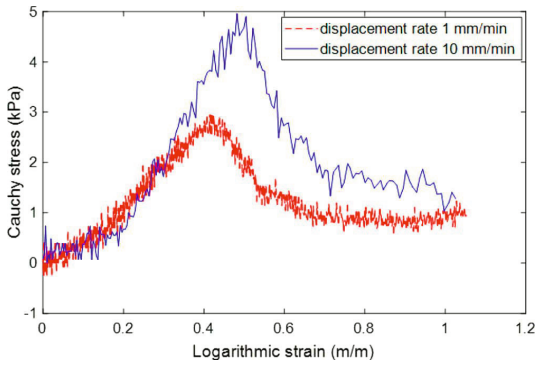

Fig. 2. Typical examples of the Cauchy stress-logarithmic strain curves for the bioamine crosslinked GG hydrogel (1.1 % SPM). Test results at two different displacement rates are given.

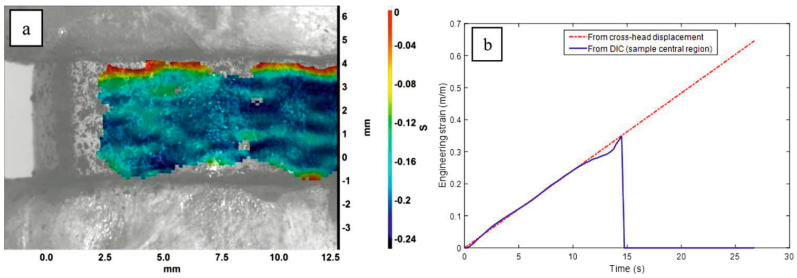

Fig. 3. (a) Strains in the loading direction ε_{yy} at sample surface after 8 s. (b) Comparison of the determined engineering strains. Displacement rate was 10 mm/min.

specimen, which is seen as a sudden load drop in the recorded data and also from the recorded images (Supplementary Video 1). After the specimen fracture (14.5 s), the DIC correlation process fails in post-processing due to the rapidly changing surface pattern, and no further data from the DIC analysis is obtained. Fig. 4 depicts the determined radial surface deformation during a compression test using 3D-DIC measurement. It can be seen that the variation of the cross-sectional area of the specimen is significant. Clearly, simply-defined engineering stress and strain terms cannot illustrate the reality of this hydrogel material. Using 3D-DIC measurement and the radius change of the cross-section, the current cross-sectional area of the specimen and the true stress can be calculated. Thus, by using these data and considering hydrogel as an incompressible material with constant volume after deformation, the true strain can be obtained [72].

The Cauchy stress–logarithmic strain curve obtained by applying experimental data and calculus in Eqs. (3) and (4) is shown in Fig. 5. The engineering stress-strain curve and the true stress-strain curve from the 3D-DIC measurement are illustrated. It can be seen that there is a significant difference between the engineering stress-strain curve and the two other curves (true stress-strain obtained from the 3D-DIC measurement and the Cauchy stress-logarithmic strain curve), whereas there is a good agreement between the true stress-strain curve from the 3D-DIC measurement and the Cauchy stress-logarithmic strain curve. Thus, the Cauchy stress and logarithmic strain have been used in the constitutive law to determine the material properties of hydrogel materials. However, most of the studies in this field have employed the engineering stress-strain curve to determine the mechanical properties of the hydrogels under tension or compression [29,60,73–75].

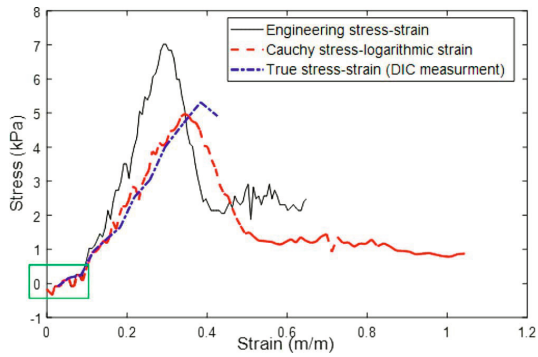

Fig. 5. Engineering stress-strain curve of a hydrogel specimen in comparison with the true stress-strain curve based on 3D-DIC measurement and the calculated Cauchy stress–logarithmic strain curve. The green rectangle highlights early phase of compression, where the strain increases, although the stress remains small. The displacement rate is 10 mm/min.

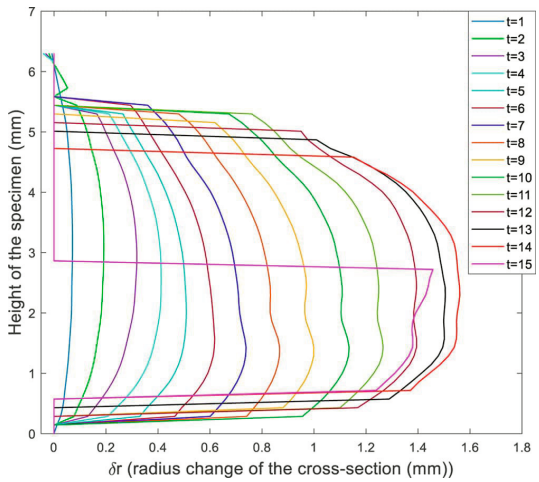

Fig. 4. Radial surface deformation of a typical hydrogel specimen during a compression test. The initial height of the sample is 6.3 mm.

4.2. Frictional contact between hydrogel and anvil

In Fig. 5, it can be seen that at the beginning of loading, the strain increases, although stress takes very small values. This region is highlighted by a green rectangle in Fig. 5. This region forms in the very early phase, and it is necessary to determine whether different boundary conditions could cause this behaviour as an artifact or as an actual material response. Here, various experimental measurement methodologies have been investigated to understand the early deformation phase. Therefore, a specimen was compressed without using a piece of paper between the sample and the compression plate (lowest friction case). In theory, a frictionless boundary would be ideal for compression testing [76].

Fig. 6a–b illustrates the Cauchy stress–logarithmic strain curves of two typical specimens under compression loading with and without the piece of paper when using a 10 mm/min displacement rate. Since the effect of the loading boundary condition was studied for the early phase, the target load level was approximately 50 % of the fracture load level. The testing without the paper was only possible to ~30 % of the displacement range, after which the specimen tended to slip off from between the compression plates due to low friction.

Changing the paper between each specimen helped to keep the contact friction constant between tests, as the pores of the papers from previous tests were probably filled with hydrogel residue. Further varying of the friction between a specimen and the compression plate

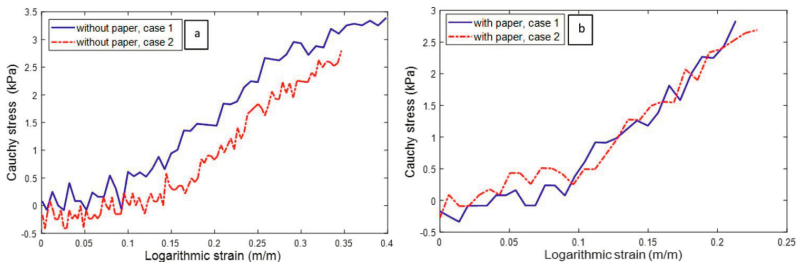

Fig. 6. Cauchy stress–logarithmic strain curves of hydrogel specimens under compression loading (a) without and (b) with pieces of paper placed between the specimens and the test machine (compression plates).

was carried out to study the boundary effect in detail. Fig. 7 shows the effect of the piece of paper at the specimen-machine boundary on the specimen form as the test proceeds. Here, the radial surface deformation along a vertical line on the specimen surface is obtained from the 3D-DIC measurements. The barrelling effect, i.e., the change in the specimen form sideways, is significant due to friction at the interface between the specimen and the compression plate. Moreover, it is also obvious that the simply defined engineering stress and strain cannot illustrate the real behaviour of the hydrogel specimen. The barrelling effect is more significant when new pieces of paper are used, but the deformation is essentially symmetrical. When the paper pieces are used several times for subsequent specimens, the changed friction at the specimen-machine interface, e.g., due to water/residues from the previous specimen or due to the damaged paper, causes the specimen to deform unevenly. Furthermore, when removing the old and installing the new specimen, the pieces of paper may easily fold in front of the specimen and cause obstacles to the optical axis of the cameras. If the whole specimen surface is not visible to both cameras used in the 3D-DIC, the correlation process cannot be carried out for those regions. In Supplementary Videos 2A-B and 3, cases of applying new and old pieces of paper at the sample machine boundary are presented. However, the plain videos cannot fully cover the differences. Fig. 7 provides more information about the boundary effects.

4.3. Threshold load and 'toe region'

The load threshold for defining the test start regarding the material response was examined. The compression was either pre-loaded so that the test machine indicated a 0.06 N pre-load, or the test was started above the hydrogel without any contact with the specimen surface. Only 1.1 % SPM hydrogel was used for this determination of the measurement parameters step. Fig. 8a–b depicts the Cauchy stress-logarithmic strain curves of two typical specimens in cases where the test started with a threshold of 0.06 N pre-load (Fig. 8a) and above the specimen (Fig. 8b). These different pre-loading conditions yield more information about the early phase and the response for low loads and small strains, indicating the existence of the so-called toe region in the stress-strain curve [29, 77].

4.4. Linearity of data and test interpretation

Researchers have reported a non-linear region (toe region) at the beginning of the stress-strain curve of hydrogels [29,60,73,74,78]. In all the tested cases in these studies, the initial resistance of hydrogels against applied load and further deformation with increased load at specific strain has been observed. In this study, it is proposed to characterise the stress-strain behaviour of hydrogels, including an exponential toe region followed continuously by a linear elastic region (fitted per hydrogel composition). A continuous method is introduced to fit both the exponential and linear portions simultaneously, which ensures continuity between regions and the necessary accuracy. To highlight the efficiency and utility of the proposed approach, the performance of this method is compared to the more conventional piecewise method [78]. Fig. 9a–d shows the characterized stress-strain curve of hydrogel compositions with 1.1 % and 0.6 % SPM concentration using the proposed approach and the conventional piecewise method. The values for parameters ABE and q are presented in Fig. 9a and c for 1.1 % and 0.6 % SPM concentration, respectively. To provide a better overview of the performance and efficiency of the proposed approach, the fully linear and nonlinear part of the model have been employed to present the material behaviour of hydrogels, as done by most researchers, applying a single full linear or a single full nonlinear approach (region) to the

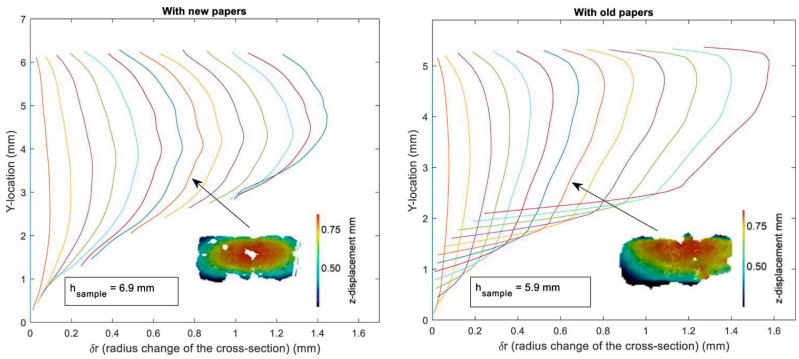

Fig. 7. Radial surface deformation for hydrogel specimen during compression testing and the effect of the pieces of paper placed between the specimen and test machine. The time interval between the curves in each figure is 1 s.

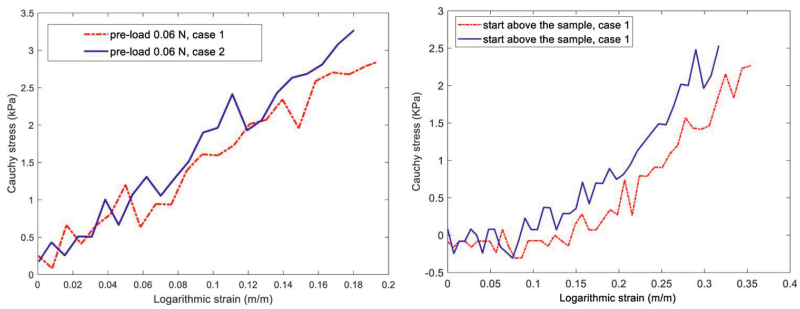

Fig. 8. Cauchy stress-logarithmic strain curve of hydrogel specimens under compression loading (a) with a 0.06 N pre-load and (b) the test is started above the specimen without contact.

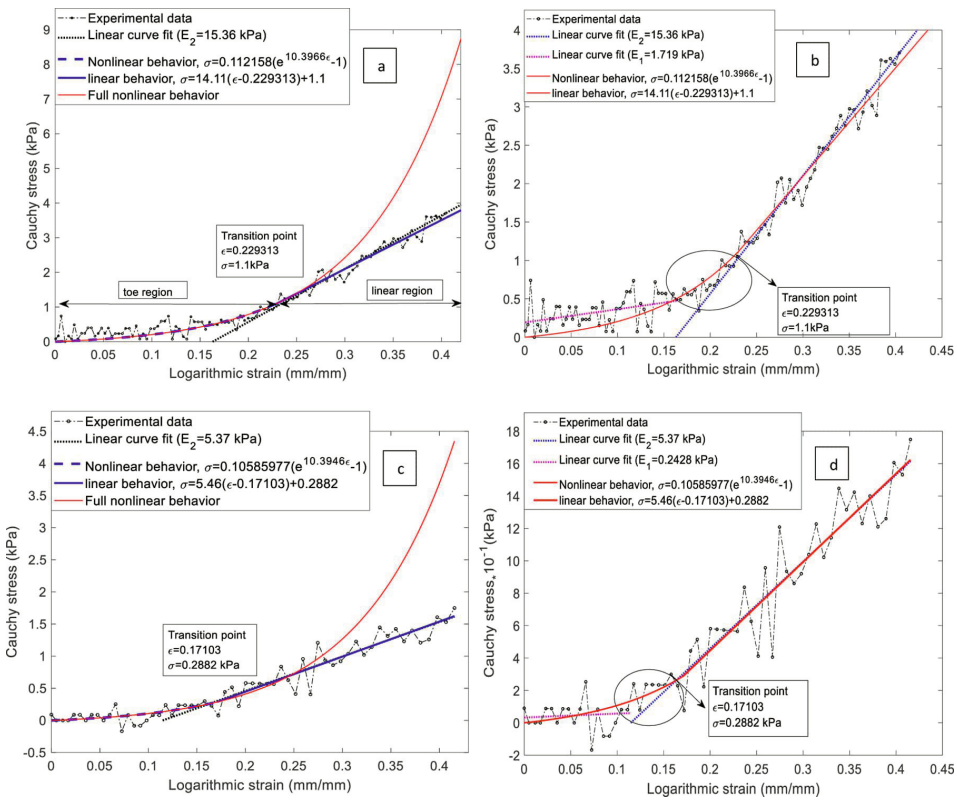

Fig. 9. Determination of the value of the model parameters for (performance of) (a) the proposed continuous method and (b) the piecewise method for 1.1 % SPM concentration, and (c) the proposed continuous method and (b) the piecewise method for 0.6 % SPM concentration. The displacement rate is 10 mm/min.

presented mechanical properties of hydrogels and biological materials [29,60,73,74,78].

In the conventional piecewise method, two different 'elastic moduli' are considered as a model to represent the elastic behaviour of hydrogel by fitting a linear curve to the toe and further elastic region of the stress–strain curve as shown in Fig. 9b and d for 1.1 % and 0.6 % SPM concentration, respectively. The first modulus (E_1) is proposed for the early nonlinear-elastic region (i.e., toe region) and the second modulus (E_2) is considered for the latter linear-elastic region. The strain range of the toe region was calculated by extrapolating the curve tangent of the linear portion of the stress–strain curve during the test to failure to the strain axis. The strain at which the curve crossed the strain axis was taken to be the strain range of the toe region [77]. Using a separate piecewise fitting method for each region, the two curves are independently fitted to a separate set of data points. It can be seen that the application of this method resulted in a discontinuity of 0.7 kPa at the transition between two regions for 1.1 % SPM concentration. The magnitude of this discontinuity is large and clearly apparent for the experimental data used.

Even if the piecewise method developed the exponential curve for

the toe region followed by a linear curve for the elastic region, there will be a discontinuity in the derivative of the stress-strain curve, leading to an inflection at the transition between two sections. Thus, there is no continuity in the performance of the piecewise technique at the transition between the two regions, leading to inaccuracies in the material model. However, the continuous method proposed in this study performs in continuity in both the stress-strain curve and its derivative by simultaneously optimising the curve fit for both regions. The continuous method has provided an improved fit to the data, resulting in a more accurate material model for the hydrogels.

When comparing to soft tissue, the division of the stress-strain curve into the toe region and linear region is due to the elastin fibres of the ECM (carrying the stress initially) which, after a certain amount of strain, transfer the load-bearing to the collagen fibres (which only take the load once they unfold [68,69]). This type of correspondence in terms of having similar toe and elastic regions in the hydrogel's stress-strain curve is a strong indication of the material's biomimicry, which is the desired property. Similarly, as in tissue, the unfolding molecules carry the initial load, and the crosslinks of the GG molecules begin carrying the larger portion of the load once they unfold. The molecular structures of collagen and GG are highly similar to each other, collagen forms a triple helix and GG a double helix, both via Coulombic forces [79,80]. As the ionic crosslinking of GG stabilises the hydrogel network [80], the hydrogen-bonded helices give the materials this biomimicking behaviour. However, at longer strains, GG will exhibit brittle behaviour and fractures at much lower strains than collagen hydrogel or actual soft tissue. This is likely due to weaker bonds when compared to those between peptides in collagen, being only a double and not a triple helix, and missing the small composite enhancement effect of elastin fibres [19,77–79]. Thus, the multi-portion elastic region and its model to describe the hydrogel can be considered biologically relevant and should be used whenever final results indicate this behaviour.

4.5. Stress-relaxation parametrisation

The stress-strain-time relationship, or constitutive law, can be determined by loading a hydrogel specimen at a constant load (referring to creep test) or a constant deformation (referring to stress relaxation test). In this study, the stress relaxation test is applied, and it is defined as a gradual decrease in reaction force (stress) with time under a constant deformation (strain level). At high strain rates, it has been observed for hydrogels that there is a time-dependent deformation and not much water seeps out during a test. Therefore, a viscoelastic material behaviour is proposed initially to approximate the behaviour of hydrogels. Here, a hydrogel specimen is suddenly deformed by compressing the specimen until a predetermined force (stress) level is reached, after which that displacement level is constantly maintained [81]. The load level consideration in this study is approximately 50 % of the fracture load. The engineering stress versus time relation during the proposed relaxation test procedure is depicted in Fig. 10for four typical specimens with 1.1 % SPM concentration.

As explained in Section 3.1 and due to the finite deformation of the test specimens, the Cauchy stress (σ^c) was employed in this study. The Cauchy stress versus time relation during the proposed relaxation stress test procedure for one of typical specimens of 1.1 % and 0.6 % SPM concentration is depicted in Fig. 11a–b, respectively.

The values for the material parameters (τ. β. σ_0, σ_∞) used in the simple decay exponential function and the stretched exponential KWW function, Eq. (6), can be obtained using a curve fitting technique. Fig. 11a–b also shows the data curves for the fitting and experimental reference. Using these values, it is possible to define relaxation modulus, Eq. (10) as a characteristic for stress relaxation behaviour.

In this figure, it can be seen that the stretched exponential KWW function allows a better fit to the stress relaxation behaviour of the tested specimens than when using the simple decay exponential function. In particular, the fit is better for the early stages of relaxation.

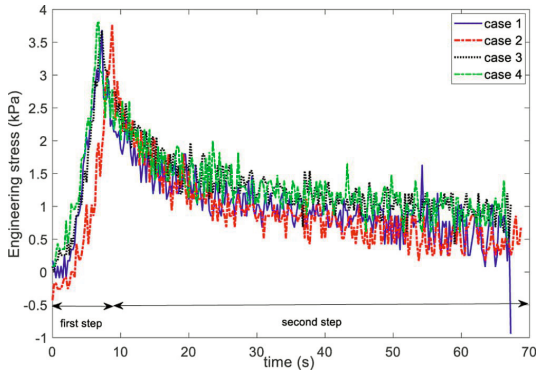

Fig. 10. Engineering stress versus time relation during the stress relaxation test for GG 1.1 % SPM specimen.

Indeed, the KWW function can evaluate the non-linearity of the stress-relaxation behaviour of these hydrogels.

The values determined for the material parameters for two compositions with 1.1 % and 0.6 % SPM concentration are listed in Table 1. From Table 1, it can be seen that the relaxation time values$\tau$are lower for the specimen of 1.1 % SPM concentration in comparison with the other concentration, whereas the empirical exponent value β is higher for the specimen of 0.6 % SPM concentration. The relaxation time is directly related to the material damping properties. In general terms, as τdecreases the internal damping tends to increase and vice versa. As a result, a greater aptitude to dissipate or absorb the energy of mechanical work occurs. The β term in the KWW stretched-exponential characterises the degree of non-exponentially of the relaxation function. Generally, the distribution changes from a broad distribution to a sharp one, increasing β from 0 to 1. Moreover, the relaxation distribution is sharper for the specimen of 0.6 % SPM concentration with a higher value for the empirical exponent.

4.6. Artifacts affecting the modulus determination

The stress-strain behaviour of hydrogel during simulated compression testing with various artifacts is shown in Fig. 12a, and one example case is shown in Supplementary Video 4. The modelled 'artifacts' only produce essentially linear behaviour – the only exception was the model with a non-flat top geometry (specimen's top surface aligned by 5°). The non-linearity produced by the initial partial contact to the specimen's top is merely an insignificant feature when noting the large, modelled alignment here and the highly linear response after the full contact with the (modelled) test machine surface. It should be noted, however, that the produced slope does not fully recover for the aligned specimen when compared to the response of the standard specimen with an ideal geometry. In general, the important detail from the 3D simulations is the local stress concentration at the specimen corner (see Fig. 12a and 'worming' in Supplementary Video 4). The stress concentration requires either slippage or plastic or viscous flow in a real hydrogel specimen. Only at an ideal frictionless boundary, the stress concentration would not occur. Due to the real, finite friction in a practical test environment, entirely elastic compression is impossible to produce especially over a large displacement (strain) range.

The dynamic simulations indicated that (1) the effects of inertia and kinetic energy are not crucial and that (2) immediate relaxation occurs during the compression testing at typical test rates. As presented in Fig. 12b and Supplementary Video 5, linear-elastic behaviour cannot be produced by using the elastic constants fitted directly to the compression (stress-strain) test data due to the instantaneous relaxation. In other words, the experimental test output is not a representation of uniaxial

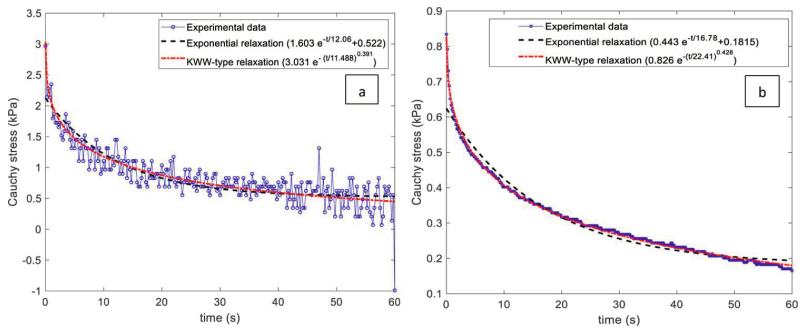

Fig. 11. Cauchy stress versus time relation in the second step of the stress relaxation test of (a) GG 1.1 % SPM specimen and (b) GG 0.6 % SPM specimen held in constant displacement for 60 s with the values for the material parameters (τ, β, σ_0, σ_∞) employed in the simple decay exponential function and the stretched exponential KWW function. ((a) 225 N load cell in experiment and (b) 22 N load cell in experiment and 1 Hz signal noise filtration).

Table 1
Fitted values of the material parameters by simple decay exponential and KWW-type function for different compositions of GG hydrogel.

hydrogel	model	τ	β	σ_0 (kPa)	σ_∞ (kPa)
GG 1.1 % SPM	Simple decay Exponential	12.06	–	1.603	0.522
	KWW	11.48	0.391	3.031	–
GG 0.6 % SPM	Simple decay Exponential	16.78	–	0.433	0.1815
	KWW	22.41	0.428	0.826	–

elastic compression but a simultaneous relaxation and (visco) elastic deformation. Therefore, the modulus values anticipated in Eq. (5) are 'effective' constants for the elastic-dissipative behaviour after the 'first iteration'. For the GG hydrogel considered in this study, a test rate of at least 10 mm/min is necessary for an acceptable error in linearity due to the viscous effects (maximum logarithmic strain in the order of 5 %–10 %). Any higher accuracy can be reached by (1) focusing on the higher rate test data; (2) updating the (quasi) static compression models for the proper deformation region and (3) re-fitting the relaxation model based on the updated elastic region (at the beginning of a relaxation test).

4.7. *Procedure for determining hydrogel modulus in compression*

The following is the suggested procedure for hydrogel compression testing to determine elastic modulus:

- Select a displacement rate-range where no significant leaking of water from the hydrogel specimen or any visible permanent deformation is observed.
- Specimen size should be measured individually for each compression specimen due to possible variations in the hydrogel production (geometry). Specimen height should be low enough to rule out bending and buckling.
- Specimen slippage can be minimised by adding a small piece of wet lint-free cellulose paper on both compression anvils. This increases friction between the hydrogel and machine. Although this makes the measurement easier, it causes the stress field to be clearly non-uniaxial on the edges of the specimen. The paper should be replaced after each test to ensure similar friction for each specimen.
- Care should be taken in adjusting the starting point of the measurement so as not to apply any unknown pre-load that could obscure a possible 'toe' region in the raw test data.
- Compute the Cauchy stress and logarithmic strain as given in Eqs. (3) and (4) and Fig. 5.
- The first estimated stress-strain curve might be characterised by an (exponential) toe region followed by an essentially linear portion. A continuous method introduced here can be used to fit both portions simultaneously. In this event, a stress-strain model can be defined by the three parameters p and the constants A and B (see Eq. (5)) to compare different specimens.
- Perform a relaxation test in compression per hydrogel type. Select a suitable model to fit the constants, such as τ, β, σ_0 of the KWW stretched exponential function.

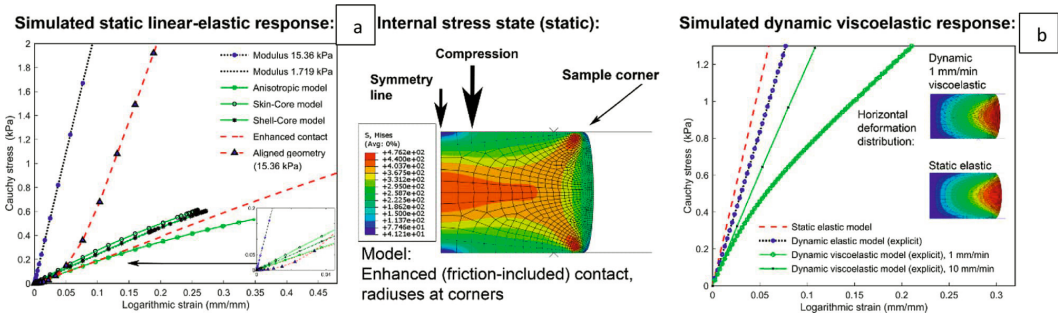

Fig. 12. (a) FEA cases of inherently elastic material with different artifacts of compression testing and material homogeneity. (b) FEA cases of hydrogel compression with a fully elastic model (implicit), a model with dynamic effects considered, and a model with dynamic and viscoelastic (relaxation) behaviour simulated. The stress and strain are calculated from the force and deformation output by using Eqs. (3) and (4).

- Simulate the compression test using a modelling technique (e.g., with FEM implementation) that simultaneously computes the elastic deformation and (rate-dependent) degradation with the parameters (constants) determined by the experiments. Determine the 'elastic region' in terms of proper test rate and level of deformation (strain) with a selected maximum error (e.g., <20 % exaggerated modulus).
- Iterate the above experimental-numerical cycle until the value of modulus (moduli) converge (error convergence depends on the originally selected stress-strain data and their shape).

In future, this method should be used to characterise different hydrogel compositions, produced using different crosslinking methods, to be able to truly compare the elastic behaviour of hydrogels (at a comparable level of accuracy). The time-consuming iteration for the modulus in compression has the advantage that it also results in the characterised dissipative (e.g., viscous) behaviour of the hydrogel specimens.

In this study, the displacement rates (e.g., 1 mm/min and 10 mm/min) significantly affected the measured responses of hydrogel. Based on the relaxation data and FEA, the error in directly measuring the elastic response (by presuming that stress has not relaxed) is 43 % at a maximum of 0 %–8 % (logarithmic) strain data range and a test speed of 10 mm/min. For a test speed of 1 mm/min, the corresponding error is 63 %. In terms of the estimated Young's modulus by least squares fitting, the errors due to relaxation are 21 % (linear fitting's quality $R^2 = 0.9998$) and 50 % (linear fitting's quality $R^2 = 0.9896$) for 10 mm/min and 1 mm/min, respectively, and when compared to the real modulus as it was inputted for FEA of the ideal elastic model. Due to the fast relaxation in the hydrogel of this study, minimising the strain range of Young's modulus fitting does not markedly improve the estimated modulus. It is clear, however, that the 10 mm/min or even higher test speed should be selected here. If the determined relaxation data is presumed to be valid, the true Young's modulus of the GG hydrogel with a 1.1 % SPM concentration is 19.2 kPa. For a 0.6 % SPM content, the true Young's modulus is 6.7 kPa for a similar estimation of relaxation during testing. In these values of true moduli, the 'second' portion of the stress-strain curve is considered, and the 'toe' region is excluded (more characterisation would be needed to validate the lowest force and displacement values).

It should be noted, however, that fast relaxation also affects the estimated stress in the first phase (compression) of the relaxation test. Therefore, the peak stress at the beginning of the relaxation phase is not exactly true when presuming elastic response (i.e., Eq. (11)). Whenever extreme accuracy (in Young's modulus) is necessary, the relaxation data (e.g., relaxation modulus) should be re-iterated (e.g., by FEA capable of simultaneous elastic and viscous/dissipative response). In general, the testing of hydrogels for exact viscous/dissipative behaviour (data) should be further developed in future, e.g., in terms of improved relaxation or creep testing.

5. Conclusions

In this paper, a specific approach to characterise the mechanical compressive response of hydrogels with a proper set of material parameters and analysis is proposed. Hydrogels have a nonlinear and dissipative behaviour when subject to mechanical loading. A continuous method is therefore introduced to fit both the exponential and linear portions of stress-strain data simultaneously, which ensures continuity in the data analysis. The continuous method provides an improved fit to the test data, leading to a precise basis for dividing the data into different behaviour. The data analysis is continued to cover the determining of a stress relaxation response that can be modelled using a KWW-type model. Throughout the testing, the stress and strain values are expressed as Cauchy stress and logarithmic strain and confirmed by 3D-DIC imaging of deformation. Finally, the presumed elastic portions used for determining (Young's) modulus are corrected to exclude the error due to viscous (dissipative) relaxation. To present the performance and utility of the proposed approach, it is applied to two different compositions of bioamine crosslinked gellan gum hydrogel at two displacement test rates. The proposed method should be used in future for a more thorough and representative mechanical characterisation of both TE scaffold materials and target tissues, providing a better understanding of the requirements of manufacturing mechanically biomimicking biomaterials. Here, the approach indicates an error of between 21 % and 50 % when no relaxation is accounted for. After correcting for viscous relaxation, Young's modulus values of ≈19 kPa and ≈7 kPa are determined for 1.1 % and 0.6 % SPM contents, respectively.

Author statement

Jairan Nafar Dastgerdi: Conceptualization, Methodology, Investigation, Writing - Original Draft, Janne T. Koivisto: Conceptualization, Methodology, Investigation, Writing - Review & Editing, Olli Orell: Formal analysis, Validation, Pantea Rava: Formal analysis, Jarno Jokinen: Software, Mikko Kanerva: Visualization, Resources, Writing - Review & Editing, Supervision, Minna Kellomäki: Supervision, Funding acquisition

Declaration of Competing Interest

The authors declare that they have no known competing financial interests or personal relationships that could have appeared to influence the work reported in this paper.

Acknowledgements

J.T. Koivisto and M. Kellomäki would like to thank the Human Spare Parts program of Business Finland and the Center of Excellence – Body on Chip (312409, 326587, 336663) of the Academy of Finlandfor the funding of this research. J.T. Koivisto would also like to acknowledge the support given by the Finnish Cultural Foundation the Pirkanmaa Regional Fund personal grant number 50151501. J. Nafar Dastgerdi, O. Orell and M. Kanerva would like to thank the LuxTurrim5G project grant by Business Finlandand the related subtask (10098/31/2016) about compression testing of polymers and polymer composites carried out by Tampere University of Technology. The authors wish to thank Peter Heath for help with language checking and proof-reading the manuscript. CSC–IT Center for Science (Finland) is acknowledged for computational resources.

Appendix A

The anisotropic behaviour of hydrogels could stem from molecular stretching as a compression sample stretches horizontally. For a cylindrical test sample, the circumferential dimension likewise stretches according to the Poisson's ratios inputted. In the event of instantaneous stretching, the resulting elastic constants can be modelled by using engineering constants per direction. For an axisymmetric space with unit axes (directions) of Z, R, θ (i.e., axial, radial, circumferential), the constants in this study were estimated as follows:

$$E_\theta = 15360 \text{ Pa} \quad \text{(A1)}$$

$$E_z = 1719 \text{ Pa}, \tag{A2}$$

where the stiffer behaviour (15.36 kPa) observed during the experiments is presumed to be due to a high modulus (E_θ) in the circumferential stretching direction of the cylindrical test sample. Likewise, the lower stiffness (the very initial toe region) is presumed to be due to a low modulus (E_z) in the axial direction. The radial direction was presumed to act as the axial direction ($E_z = E_R$) as in orthotropic material.

For hydrogel, being nearly fluid (incompressible), the Poisson's ratios were set as follows:

$$\nu_{ZR} = 0.48 \approx 0.5 \tag{A3}$$

and

$$\nu_{R\theta} = 0.48 \times \frac{E_R}{E_\theta} = 0.05. \tag{A4}$$

To preserve requirements (see e.g., [82]):

$$1 - \nu_{ij}\nu_{ji} \succ 0 \tag{A5}$$

and

$$\left|\nu_{ij}\right| \prec \sqrt{\frac{E_j}{E_i}} \tag{A6}$$

the value of $\nu_{Z\theta}$ was set to 0.03. Therefore, the Poisson's ratios satisfy:

$$1 - \nu_{ZR}\nu_{RZ} - \nu_{R\theta}\nu_{\theta R} - \nu_{Z\theta}\nu_{\theta Z} - 2\nu_{ZR}\nu_{R\theta}\nu_{\theta Z} \succ 0. \tag{A7}$$

The shear moduli were calculated based on the relationship

$$G_{ij} = \frac{E_j}{2(1+\nu_{ij})}. \tag{A8}$$

Thus, that the following values were used in this study:

$G_{Z\theta} = 5.20$ kPa

$G_{ZR} = 0.58$ kPa

$G_{R\theta} = 7.29$ kPa

Appendix B. Supplementary data

Supplementary material related to this article can be found, in the online version, at doi:https://doi.org/10.1016/j.mtcomm.2021.102518.

References

[1] S.J. Buwalda, K.W.M. Boere, P.J. Dijkstra, J. Feijen, T. Vermonden, W.E. Hennink, Hydrogels in a historical perspective: from simple networks to smart materials, J. Control. Release 190 (2014) 254–273, https://doi.org/10.1016/j.jconrel.2014.03.052.

[2] S.H. Aswathy, U. Narendrakumar, I. Manjubala, Commercial hydrogels for biomedical applications, Heliyon 6 (2020) e03719, https://doi.org/10.1016/j.heliyon.2020.e03719.

[3] X. Zhang, P. Huang, G. Jiang, M. Zhang, F. Yu, X. Dong, L. Wang, Y. Chen, W. Zhang, Y. Qi, W. Li, H. Zeng, A novel magnesium ion-incorporating dual-crosslinked hydrogel to improve bone scaffold-mediated osteogenesis and angiogenesis, Mater. Sci. Eng. C. 121 (2021) 111868, https://doi.org/10.1016/j.msec.2021.111868.

[4] J. Li, D.J. Mooney, Designing hydrogels for controlled drug delivery, Nat. Rev. Mater. 1 (2016) 16071, https://doi.org/10.1038/natrevmats.2016.71.

[5] B.G. Chung, K.-H. Lee, A. Khademhosseini, S.-H. Lee, Microfluidic fabrication of microengineered hydrogels and their application in tissue engineering, Lab Chip 12 (2011) 45–59, https://doi.org/10.1039/C1LC20859D.

[6] M.E. Gomes, M. Rodrigues, R.M.A. Domingues, R.L. Reis, Tissue engineering and regenerative medicine: new trends and directions—A year in review, Tissue Eng. Part B Rev. 23 (2017) 211–224, https://doi.org/10.1089/ten.teb.2017.0081.

[7] S. Breslin, L. O'Driscoll, Three-dimensional cell culture: the missing link in drug discovery, Drug Disc. Today 18 (2013) 240–249, https://doi.org/10.1016/j.drudis.2012.10.003.

[8] S.B. Shah, A. Singh, Cellular self-assembly and biomaterials-based organoid models of development and diseases, Acta Biomater. 53 (2017) 29–45, https://doi.org/10.1016/j.actbio.2017.01.075.

[9] A.J. Engler, S. Sen, H.L. Sweeney, D.E. Discher, Matrix elasticity directs stem cell lineage specification, Cell 126 (2006) 677–689, https://doi.org/10.1016/j.cell.2006.06.044.

[10] W.L. Murphy, T.C. McDevitt, A.J. Engler, Materials as stem cell regulators, Nat. Mater. 13 (2014) 547–557, https://doi.org/10.1038/nmat3937.

[11] N.J. Walters, E. Gentleman, Evolving insights in cell-matrix interactions: elucidating how non-soluble properties of the extracellular niche direct stem cell fate, Acta Biomater. 11 (2015) 3–16, https://doi.org/10.1016/j.actbio.2014.09.038.

[12] F. Brandl, F. Sommer, A. Goepferich, Rational design of hydrogels for tissue engineering: impact of physical factors on cell behavior, Biomaterials 28 (2007) 134–146, https://doi.org/10.1016/j.biomaterials.2006.09.017.

[13] F.M. Watt, W.T.S. Huck, Role of the extracellular matrix in regulating stem cell fate, Nat. Rev. Mol. Cell Biol. 14 (2013) 467–473, https://doi.org/10.1038/nrm3620.

[14] S.K. Bhatia, Engineering Biomaterials for Regenerative Medicine: Novel Technologies for Clinical Applications, First ed., Springer, New York, New York, 2012.

[15] A.M. Handorf, Y. Zhou, M.A. Halanski, W.-J. Li, Tissue stiffness dictates development, homeostasis, and disease progression, Organogenesis 11 (2015) 1–15, https://doi.org/10.1080/15476278.2015.1019687.

[16] G. Mattei, A. Ahluwalia, Sample, testing and analysis variables affecting liver mechanical properties: a review, Acta Biomater. 45 (2016) 60–71, https://doi.org/10.1016/j.actbio.2016.08.055.

[17] R.K. Das, V. Gocheva, R. Hammink, O.F. Zouani, A.E. Rowan, Stress-stiffening-mediated stem-cell commitment switch in soft responsive hydrogels, Nat. Mater. 15 (2016) 318–325, https://doi.org/10.1038/nmat4483.

[18] C. Storm, J.J. Pastore, F.C. MacKintosh, T.C. Lubensky, P.A. Janmey, Nonlinear elasticity in biological gels, Nature 435 (2005) 191–194, https://doi.org/10.1038/nature03521.

[19] A.V. Dobrynin, J.-M.Y. Carrillo, Universality in nonlinear elasticity of biological and polymeric networks and gels, Macromolecules 44 (2011) 140–146, https://doi.org/10.1021/ma102154u.

[20] H. Hencky, Über die form des elastizitätsgesetzes bei ideal elastischen stoffen, Z. Technol. Phys. 9 (1928) 215–220.

[21] H. Xiao, O.T. Bruhns, A. Meyers, Explicit dual stress-strain and strain-stress relations of incompressible isotropic hyperelastic solids via deviatoric Hencky strain and Cauchy stress, Acta Mech. 168 (2004) 21–33, https://doi.org/10.1007/s00707-004-0074-5.

[22] H. Xiao, O.T. Bruhns, A. Meyers, Elastoplasticity beyond small deformations, Acta Mech. 182 (2006) 31–111, https://doi.org/10.1007/s00707-005-0282-7.

[23] R. Naghdabadi, M. Yeganeh, A.R. Saidi, Application of corotational rates of the logarithmic strain in constitutive modeling of hardening materials at finite deformations, Int. J. Plast. 21 (2005) 1546–1567, https://doi.org/10.1016/j.ijplas.2004.07.005.

[24] R.C. Lin, U. Schomburg, A novel internal dissipation inequality by isotropy and its implication for inelastic constitutive characterization, Mech. Res. Commun. 30 (2003) 125–133, https://doi.org/10.1016/S0093-6413(02)00349-X.

[25] M.L. Oyen, Mechanical characterisation of hydrogel materials, Int. Mater. Rev. 59 (2014) 44–59, https://doi.org/10.1179/1743280413Y.0000000022.

[26] F. Hild, S. Roux, Digital image correlation: from displacement measurement to identification of elastic properties – a review, Strain 42 (2006) 69–80, https://doi.org/10.1111/j.1475-1305.2006.00258.x.

[27] H. Schreier, J.-J. Orteu, M.A. Sutton, Image Correlation for Shape, Motion and Deformation Measurements, First ed., Springer US, New York, 2009.

[28] M. Palanca, G. Tozzi, L. Cristofolini, The use of digital image correlation in the biomechanical area: a review, Int. Biomech. 3 (2016) 1–21, https://doi.org/10.1080/23335432.2015.1117395.

[29] J.L. Drury, R.G. Dennis, D.J. Mooney, The tensile properties of alginate hydrogels, Biomaterials 25 (2004) 3187–3199, https://doi.org/10.1016/j.biomaterials.2003.10.002.

[30] J.D. Ferry, Viscoelastic Properties of Polymers, Third ed., John Wiley & Sons, New York, 1980.

[31] X. Zhao, N. Huebsch, D.J. Mooney, Z. Suo, Stress-relaxation behavior in gels with ionic and covalent crosslinks, J. Appl. Phys. 107 (2010) 063509, https://doi.org/10.1063/1.3343265.

[32] S.A. Chester, A constitutive model for coupled fluid permeation and large viscoelastic deformation in polymeric gels, Soft Matter 8 (2012) 8223–8233, https://doi.org/10.1039/C2SM25372K.

[33] R. Bai, J. Yang, Z. Suo, Fatigue of hydrogels, Eur. J. Mech. A Solids 74 (2019) 337–370, https://doi.org/10.1016/j.euromechsol.2018.12.001.

[34] A. Bauer, L. Gu, B. Kwee, W.A. Li, M. Dellacherie, A.D. Celiz, D.J. Mooney, Hydrogel substrate stress-relaxation regulates the spreading and proliferation of mouse myoblasts, Acta Biomater. 62 (2017) 82–90, https://doi.org/10.1016/j.actbio.2017.08.041.

[35] R. Kocen, M. Gasik, A. Gantar, S.S. Novak, Viscoelastic behavior of hydrogel-based composites for tissue engineering under mechanical load, Biomed. Mater. 12 (2017) 25004, https://doi.org/10.1088/1748-605x/aa5b00.

[36] O. Chaudhuri, Viscoelastic hydrogels for 3D cell culture, Biomater. Sci. 5 (2017) 1480–1490, https://doi.org/10.1039/C7BM00261K.

[37] K. Nakamura, E. Shinoda, M. Tokita, The influence of compression velocity on strength and structure for gellan gels, Food Hydrocoll. 15 (2001) 247–252, https://doi.org/10.1016/S0268-005X(01)00021-2.

[38] I.V. Gofman, A.L. Buyanov, Unusual effect evidenced at the investigations of the mechanical behavior of composite hydrogels under cyclic compression, J. Mech. Behav. Biomed. Mater. 71 (2017) 238–243, https://doi.org/10.1016/j.jmbbm.2017.03.030.

[39] M.A. Biot, General theory of three-dimensional consolidation, J. Appl. Phys. 12 (1941) 155–164, https://doi.org/10.1063/1.1712886.

[40] W. Hong, X. Zhao, J. Zhou, Z. Suo, A theory of coupled diffusion and large deformation in polymeric gels, J. Mech. Phys. Solids 56 (2008) 1779–1793, https://doi.org/10.1016/j.jmps.2007.11.010.

[41] J. Yoon, S. Cai, Z. Suo, R.C. Hayward, Poroelastic swelling kinetics of thin hydrogel layers: Comparison of theory and experiment, Soft Matter 6 (2010) 6004–6012, https://doi.org/10.1039/C0SM00434K.

[42] Y. Li, T. Tanaka, Kinetics of swelling and shrinking of gels, J. Chem. Phys. 92 (1990) 1365–1371, https://doi.org/10.1063/1.458148.

[43] M. Quesada-Pérez, J. Maroto-Centeno, J. Forcada, R. Hidalgo-Alvarez, Gel swelling theories: the classical formalism and recent approaches, Soft Matter 7 (2011) 10536–10547, https://doi.org/10.1039/C1SM06031G.

[44] S. Cai, Y. Hu, X. Zhao, Z. Suo, Poroelasticity of a covalently crosslinked alginate hydrogel under compression, J. Appl. Phys. 108 (2010) 113514, https://doi.org/10.1063/1.3517146.

[45] W. Hong, Z. Liu, Z. Suo, Inhomogeneous swelling of a gel in equilibrium with a solvent and mechanical load, Int. J. Solids Struct. 46 (2009) 3282–3289, https://doi.org/10.1016/j.ijsolstr.2009.04.022.

[46] S.A. Chester, L. Anand, A coupled theory of fluid permeation and large deformations for elastomeric materials, J. Mech. Phys. Solids 58 (2010) 1879–1906, https://doi.org/10.1016/j.jmps.2010.07.020.

[47] W. Hong, X. Zhao, Z. Suo, Large deformation and electrochemistry of polyelectrolyte gels, J. Mech. Phys. Solids 58 (2010) 558–577, https://doi.org/10.1016/j.jmps.2010.01.005.

[48] M.K. Kang, R. Huang, A variational approach and finite element implementation for swelling of polymeric hydrogels under geometric constraints, J. Appl. Mech. 77 (2010) 61004–61012, https://doi.org/10.1115/1.4001715.

[49] A. Lucantonio, P. Nardinocchi, L. Teresi, Transient analysis of swelling-induced large deformations in polymer gels, J. Mech. Phys. Solids 61 (2013) 205–218, https://doi.org/10.1016/j.jmps.2012.07.010.

[50] J. Zhang, X. Zhao, Z. Suo, H. Jiang, A finite element method for transient analysis of concurrent large deformation and mass transport in gels, J. Appl. Phys. 105 (2009) 93522, https://doi.org/10.1063/1.3106628.

[51] Q.-M. Wang, A.C. Mohan, M.L. Oyen, X.-H. Zhao, Separating viscoelasticity and poroelasticity of gels with different length and time scales, Acta Mech. Sin. 30 (2014) 20–27, https://doi.org/10.1007/s10409-014-0015-z.

[52] Y. Hu, Z. Suo, Viscoelasticity and poroelasticity in elastomeric gels, Acta Mech. Solida Sin. 25 (2012) 441–458, https://doi.org/10.1016/S0894-9166(12)60039-1.

[53] D. Caccavo, G. Lamberti, PoroViscoElastic model to describe hydrogels' behavior, Mater. Sci. Eng. C 76 (2017) 102–113, https://doi.org/10.1016/j.msec.2017.02.155.

[54] X. Zhao, S.J.A. Koh, Z. Suo, Nonequilibrium thermodynamics of dielectric elastomers, Int. J. Appl. Mech. 3 (2011) 203–217, https://doi.org/10.1142/S1758825111000944.

[55] X. Wang, W. Hong, A visco-poroelastic theory for polymeric gels, Proc. Math. Phys. Eng. Sci. 468 (2012) 3824–3841, https://doi.org/10.1098/rspa.2012.0385.

[56] D.T.N. Chen, Q. Wen, P.A. Janmey, J.C. Crocker, A.G. Yodh, Rheology of soft materials, Annu. Rev. Condens. Matter Phys. 1 (2010) 301–322, https://doi.org/10.1146/annurev-conmatphys-070909-104120.

[57] J. Yang, W. Illeperuma, Z. Suo, Inelasticity increases the critical strain for the onset of creases on hydrogels, Extreme Mech. Lett. 40 (2020) 100966, https://doi.org/10.1016/j.eml.2020.100966.

[58] Y.C. Fung, Elasticity of soft tissues in simple elongation, Am. J. Physiol. 213 (1967) 1532–1544, https://doi.org/10.1152/ajplegacy.1967.213.6.1532.

[59] A.H. Bacelar, J. Silva-Correia, J.M. Oliveira, R.L. Reis, Recent progress in gellan gum hydrogels provided by functionalization strategies, J. Mater. Chem. B 4 (2016) 6164–6174, https://doi.org/10.1039/c6tb01488g.

[60] J.T. Koivisto, T. Joki, J.E. Parraga, R. Pääkkönen, L. Ylä-Outinen, L. Salonen, I. Jönkkäri, M. Peltola, T.O. Ihalainen, S. Narkilahti, M. Kellomäki, Bioamine-crosslinked gellan gum hydrogel for neural tissue engineering, Biomed. Mater. 12 (2017) 025014, https://doi.org/10.1088/1748-605X/aa62b0.

[61] J. Karvinen, J.T. Koivisto, I. Jönkkäri, M. Kellomäki, The production of injectable hydrazone crosslinked gellan gum-hyaluronan-hydrogels with tunable mechanical and physical properties, J. Mech. Behav. Biomed. Mater. 71 (2017) 383–391, https://doi.org/10.1016/j.jmbbm.2017.04.006.

[62] J.T. Koivisto, C. Gering, J. Karvinen, R. Maria Cherian, B. Belay, J. Hyttinen, K. Aalto-Setälä, M. Kellomäki, J. Parraga, Mechanically biomimetic gelatin–gellan gum hydrogels for 3D culture of beating human cardiomyocytes, ACS Appl. Mater. Interfaces 11 (2019) 20589–20602, https://doi.org/10.1021/acsami.8b22343.

[63] C. Gering, J.T. Koivisto, J.E. Parraga, M. Kellomäki, Reproducible preparation method of hydrogels for cell culture applications – case study with spermidine crosslinked gellan gum, IFMBE Proc. 65 (2017) 811–814, https://doi.org/10.1007/978-981-10-5122-7_203.

[64] Y.-C. Fung, Biomechanics: Mechanical Properties of Living Tissues, First ed., Springer-Verlag, New York, 1981.

[65] A.Ya. Malkin, Rheology Fundamentals, First ed., ChemTec Publishing, Toronto-Scarborough, 1994.

[66] K.L. Ngai, Relaxation and Diffusion in Complex Systems, First ed., Springer Science & Business Media, New York, 2011.

[67] G.G. Raju, Dielectrics in Electric Fields, First ed., CRC Press, Boca Raton, 2003.

[68] Y. Gueguen, V. Keryvin, T. Rouxel, M. Le Fur, H. Orain, B. Bureau, C. Boussard-Plédel, J.-C. Sangeleboeuf, A relationship between non-exponential stress relaxation and delayed elasticity in the viscoelastic process in amorphous solids: illustration on a chalcogenide glass, Mech. Mater. 85 (2015) 47–56, https://doi.org/10.1016/j.mechmat.2015.02.013.

[69] R.S. Anderssen, S.A. Husain, R.J. Loy, The Kohlrausch function: properties and applications, ANZIAM J. 45 (2004) 800–816, https://doi.org/10.21914/anziamj.v45i0.924.

[70] D. Kytýř, T. Doktor, M. Adorna, M. Neuhauserova, J. Sleichrt, N. Fenclova, A. Gantar, S. Novak, Deformation behavior of gellan gum based scaffold subjected to compression loading, Appl. Mech. Mater. 821 (2016) 665–670, https://doi.org/10.4028/www.scientific.net/AMM.821.665.

[71] D. Kytýř, P. Zlámal, P. Koudelka, T. Fíla, N. Krčmářová, I. Kumpová, D. Vavřík, A. Gantar, S. Novak, Deformation analysis of gellan-gum based bone scaffold using on-the-fly tomography, Mater. Des. 134 (2017) 400–417, https://doi.org/10.1016/j.matdes.2017.08.036.

[72] J. Tang, M.A. Tung, Y. Zeng, Compression strength and deformation of gellan gels formed with mono- and divalent cations, Carbohydr. Polym. 29 (1996) 11–16, https://doi.org/10.1016/0144-8617(95)00124-7.

[73] L. Koivusalo, J. Karvinen, E. Sorsa, I. Jönkkäri, J. Väliaho, P. Kallio, T. Ilmarinen, S. Miettinen, H. Skottman, M. Kellomäki, Hydrazone crosslinked hyaluronan-based hydrogels for therapeutic delivery of adipose stem cells to treat corneal defects, Mater. Sci. Eng. C 85 (2018) 68–78, https://doi.org/10.1016/j.msec.2017.12.013.

[74] M. Dehghan-Niri, E. Vasheghani-Farahani, M. Baghaban Eslaminejad, M. Tavakol, F. Bagheri, Physicomechanical, rheological and in vitro cytocompatibility properties of the electron beam irradiated blend hydrogels of tyramine conjugated gum tragacanth and poly (vinyl alcohol), Mater. Sci. Eng. C 114 (2020) 111073, https://doi.org/10.1016/j.msec.2020.111073.

[75] K. Vuornos, M. Ojansivu, J.T. Koivisto, H. Häkkänen, B. Belay, T. Montonen, H. Huhtala, M. Kääriäinen, L. Hupa, M. Kellomäki, J. Hyttinen, J.A. Ihalainen, S. Miettinen, Bioactive glass ions induce efficient osteogenic differentiation of human adipose stem cells encapsulated in gellan gum and collagen type I

hydrogels, Mater. Sci. Eng. C 99 (2019) 905–918, https://doi.org/10.1016/j.msec.2019.02.035.
[76] Y.R. Zhang, K.J. Xu, Y.L. Bai, L.Q. Tang, Z.Y. Jiang, Y.P. Liu, Z.J. Liu, L.C. Zhou, X. F. Zhou, Features of the volume change and a new constitutive equation of hydrogels under uniaxial compression, J. Mech. Behav. Biomed. Mater. 85 (2018) 181–187, https://doi.org/10.1016/j.jmbbm.2018.06.004.
[77] L.A. Pruitt, A.M. Chakravartula, Mechanics of Biomaterials - Fundamental Principles for Implant Design, First ed., Cambridge University Press, Cambridge, 2011.
[78] E. Gentleman, G.A. Livesay, K.C. Dee, E.A. Nauman, Development of ligament-like structural organization and properties in cell-seeded collagen scaffolds in vitro, Ann. Biomed. Eng. 34 (2006) 726–736, https://doi.org/10.1007/s10439-005-9058-4.
[79] M.D. Shoulders, R.T. Raines, Collagen structure and stability, Annu. Rev. Biochem. 78 (2009) 929–958, https://doi.org/10.1146/annurev.biochem.77.032207.120833.
[80] R. Chandrasekaran, A. Radha, Molecular architectures and functional properties of gellan gum and related polysaccharides, Trends Food Sci. Technol. 6 (1995) 143–148, https://doi.org/10.1016/S0924-2244(00)89022-6.
[81] S. Lee, W.G. Knauss, A note on the determination of relaxation and creep data from ramp tests, Mech. Time Depend. Mater. 4 (2000) 1–7, https://doi.org/10.1023/A:1009827622426.
[82] B.M. Lempriere, Poisson's ratio in orthotropic materials, AIAA J. 6 (1968) 2226–2227, https://doi.org/10.2514/3.4974.

PUBLICATION II

Characterization of elastic constants of anisotropic composites in compression using digital image correlation

O. Orell, J. Vuorinen, J. Jokinen, H. Kettunen, P. Hytönen, J. Turunen and M. Kanerva

Composite Structures 185 (2018) 176–185
https://doi.org/10.1016/j.compstruct.2017.11.008

Publication reprinted with the permission of the copyright holders.

Composite Structures 185 (2018) 176–185

Contents lists available at ScienceDirect

Composite Structures

journal homepage: www.elsevier.com/locate/compstruct

Characterization of elastic constants of anisotropic composites in compression using digital image correlation

Olli Orell[a,*], Jyrki Vuorinen[a], Jarno Jokinen[a], Heikki Kettunen[b], Pertti Hytönen[b], Jani Turunen[b], Mikko Kanerva[a]

[a] Laboratory of Materials Science, Tampere University of Technology, P.O. Box 589, FI-33101 Tampere, Finland
[b] Valmet Technologies Oy, P.O. Box 587, FI-40101 Jyväskylä, Finland

ARTICLE INFO

Keywords:
Laminates
Elastic constants
Digital image correlation
Microstructural analysis

ABSTRACT

Experimental determination of elastic constants of anisotropic composite laminates in all orthogonal directions is generally a complex process. In this paper a simple direct technique to determine a broad set of elastic moduli is presented based on compression testing of a prism sample. Digital image correlation is used to measure the full-field deformations that allow the determination of Young's moduli and all six Poisson's ratios for the three orthogonal directions based on a single sample. Finite element model is used in evaluation of the effect of friction on the measured properties. In addition to quantitative characterization of the material properties, local strain mapping is used in qualitative evaluation of the sample structures.

1. Introduction

To utilize fiber reinforced polymers (FRPs) materials efficiently, it is necessary to have comprehensive knowledge of the material behavior. FRPs are typically transversely isotropic but normally their state of symmetry is orthotropic or in some case fully anisotropic [1,2]. In traditional design of composite structures, the properties of the fabricated materials are routinely estimated and simulated with well-recognized models and theories. Although computer aided calculations are the basis for the design of composites nowadays, experimental testing is still required to confirm the simulations. Also, if the mechanical behavior of a composite structure is to be studied but the exact input data, such as the ply structure or the material properties of the constituents, are unknown, the uncertainty in the simulation results is greatly increased.

Generally, the mechanical testing of FRPs is challenging due to the anisotropic nature, which necessitates numerous tests to be carried out to determine the constants required in describing the mechanical behavior [3,4]. In addition to symmetry-related anisotropy causing orientation-dependent heterogeneity, the microstructure of FRPs is often far from ideal e.g. due to imperfections of manufacturing. These features can cause severe local anomaly differing greatly from the behavior of the global structure. Typically, the tests are carried out using test coupons cut off the laminates fabricated for the purpose. However, it is common for composites that the manufacturing process can have strong influence on the structure, including e.g. reinforcement orientation and volume fraction. In some cases, it can actually be questioned if a simple test coupon correlates with the actual material of the final application or not.

Traditional experimental determination of elastic constants is based on the measured data of the load and the deformations induced in the material. Recently, new indirect determination techniques have also been introduced e.g. based on vibration testing or wave propagation combined with the utilization of genetic algorithms [3–6,8]. In direct measurements extensometers and electrical resistance strain gauges are routinely used in mechanical testing, and they give averaged strains over the set gauge length. However, the distribution of reinforcements in FRPs is normally in the millimeter range or less [7,9]. If local deformations in composites are to be studied, the spatial resolution of the strain gauges and extensometers is thus not high enough. The anisotropic FRPs call for full-field strain measuring techniques, which include for example Moiré interferometry [10], grating shearography [11], Raman spectroscopy [7], and digital image correlation (DIC) [9,12–14]. Especially DIC has recently proven to be efficient technique in the studies of composite structures. In this non-contact measuring technique, strain fields in materials can be studied in conventional manner similar to strain gauges yet simultaneously it allows so called local strain mapping to be carried out offering precise examination of the deformation distribution in a material [7,12,13,15].

Digital image correlation is an optical non-contact method to measure full-field displacements of the studied surface. The technique developed already in 1980s is well-known and has been described by

* Corresponding author.
E-mail address: olli.orell@tut.fi (O. Orell).

https://doi.org/10.1016/j.compstruct.2017.11.008
Received 22 February 2017; Received in revised form 18 September 2017; Accepted 6 November 2017
Available online 07 November 2017
0263-8223/ © 2017 Elsevier Ltd. All rights reserved.

several authors [12,17–19]. In practice, the imaged surface applied with a random speckle pattern is divided into small subsets and the deformations of the surface are computed via algorithms by tracking the spatial shift of the subsets per image to image. As a result, a complete full-field displacement map of the studied surface is obtained, from which desired deformation analysis can be post-processed. The deformations can even be determined at a sub-pixel accuracy and the measuring frequency depends purely on the performance of the cameras used. While 2D deformations can be measured with one camera, 3D deformations require use of two cameras both of measuring the changes of the deformed surface at different angles.

This work presents a technique to experimentally evaluate a broad set of elastic constants. A similar technique was used earlier by Wang [16] in analysis of properties of anisotropic cartilages. With the technique three Young's moduli and six Poisson's ratios can be determined from a single bulk specimen minimizing thus the need of material quantity. The advantages of the presented technique based on mechanical testing and full-field strain measuring with DIC include: 1) several properties can be determined from a single small test coupon if, for example, only limited amount of material is available, 2) the samples can be made from bulk material fabricated with the identical parameters as the final product and 3) measured off-plane properties of the real component are available. In addition, local strain mapping can be used to examine the micro or macro structure of the extracted samples.

2. Experimental

2.1. Materials and sample preparation

Three different fiber reinforced epoxy laminates fabricated with strip winding technique were studied (Table 1). In addition to these, a single laminate was made with vacuum infusion used in the comparative tests of two different compressive testing techniques. The initial height of the laminates ranged from 8 mm to 12 mm, where the nominal thickness of a fabric ply was 0.5 mm for the wound laminates, and 0.2 mm for the vacuum infused laminate. The sample preparation was carried out as follows: 1) cutting of a prism-shaped specimen with edge lengths of 12 mm in laminate 1–2 plane using precision circular saw and 2) grinding of the samples with an in-house built fine mechanical abrasive grinder to achieve highly parallel opposite edges of the prism sample (Fig. 1). The sample height was thus significantly lower than used in the standard compression tests of block samples, for example in ASTM D695 (Compressive properties of rigid plastics). However, the two other dimensions were in the same range. The variation in flatness along the sample surfaces was measured to be in the range of 10–50 μm using optical profilometer (Alicona InfiniteFocus G5). The inclination of the samples was low enough for successful compression testing.

Finally, a random speckle pattern with high contrast was applied on the surfaces of the specimen by spraying with matt alkyd paints. First thin (10–15 μm) constant layer of matt white was applied over which black speckles were applied having average diameter of approximately 150 μm and thickness of 5–10 μm, measured with the optical profilometer.

The reinforcement strip in the material A was aramid fiber mat, and in the materials B and C the strips were uneven-sided woven glass fiber fabrics. The fiber volume fractions were determined using optical microscopy and burn-off technique for the materials containing aramid and glass fibers, respectively. The vacuum infused epoxy laminate (D) consisted of 55 plies of plain weave E-glass fabric.

2.2. Compression testing

Compression testing of the rectangular parallelepiped samples was carried out using a servo-hydraulic universal testing machine (Instron 8800) with a 50 kN load cell and manually aligned compression plates with a low surface roughness (Fig. 2a). Self-aligning compression plates with spherical bearing system was tried first but the simultaneous use with DIC was difficult, and smaller manually aligned compression plates were used instead. The alignment was carried out with the help of rotating thin paper between the plates almost at contact and difference in flatness of less than 30 μm across the compression plates could be assumed. The testing rate and the end criteria for each test were set to 0.5 mm/min and 60 MPa, respectively. In each test linear elastic behavior without any significant plastic deformation was presumed, which was ensured by pre-tests. Silicone oil was used between the compression plates and the sample to decrease the effect of lateral friction.

Each sample (n = 3) was tested six times in a random order so that for each direction of loading (1-2-3) the deformations were measured from the other two directions as shown in Fig. 3. The tests were denoted by I_{jk}, where i is the sample name and indices j and k are the loading direction and the studied surface normal, respectively.

In addition to the compression method of the prisms, combined loading compression (CLC) method (ASTM D 6641) was used for comparative testing for single material. The text fixture was compressed with self-aligning compression plates using Instron 5967 universal testing machine with 30 kN load sensor (Fig. 4) The testing rate was 1.3 mm/min and end criteria was 10 kN. The samples cut from the laminate had dimensions of 12 × 9 × 140 mm where the long direction was the direction 1 in the laminate coordination. The gauge length of the unconstrained portion of the sample was thus 13 mm. Before testing electric resistance strain gauges were glued to gauge area: three-axial rosettes (gauge length 5 mm) in the perpendicular surfaces (surfaces 2 and 3) and a single gauge (5 mm) in the opposite side of the surface 3 to detect possible bending of the sample.

2.3. Digital image correlation analysis

In this study, the deformations were measured with a 3D-DIC system (LaVision) using lenses with a 100 mm focal length and a recording rate of 2 Hz (Fig. 2b). The spatial resolution of the displacement measurement was 15 μm/pixel and the RMS fit of the calibration 0.20 pixel in the first tests with samples A, B and C. In the later tests with material D, the same parameters were 4 μm/pixel and 0.51 pixel. For each measurement, strains were determined both parallel and transverse to loading direction, which enabled the calculation of Poisson's ratios. In addition, the full-field strain maps were used to study local microstructure in the samples.

Table 1
Tested materials. The percentage ratios of reinforcement denote fiber fractions in warp/weft directions.

Sample	Sample size [mm]	Sample height [mm]	Reinforcement (fabric strip)	Matrix	V_f [%]
A	12 × 12	7	Aramid mat	Silica-filled epoxy	8
B	12 × 12	9	Glass fabric (52%/48%)	Epoxy	38
C	12 × 12	10	Glass fabric (50%/50%)	Epoxy	29
D	140 × 12 and 12 × 12	9	Glass fabric (50%/50%)	Epoxy	–

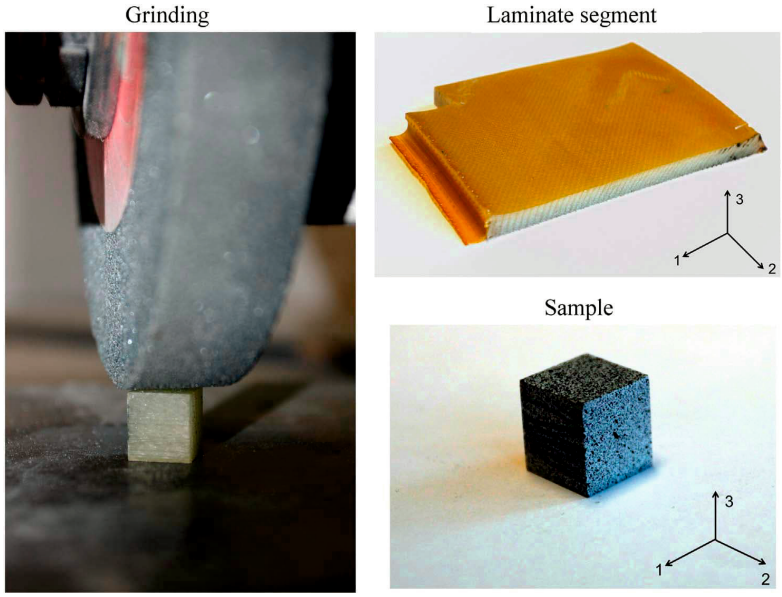

Fig. 1. Specimen preparation and coordinate system, where the strip winding direction is parallel to axis 2.

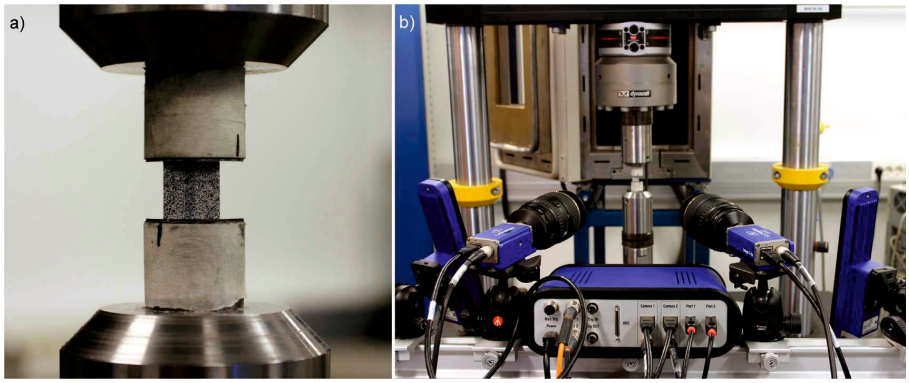

Fig. 2. a) A cubic sample during compression testing b) the 3-D DIC test setup.

2.4. Friction measurements

The static and dynamic friction coefficients between the sample and compression plates were determined with CETR UMT-2 tribometer equipped with 200 N 2-D load sensor (Fig. 5). The tests were carried out with and without lubrication to study the effect of greasing on the friction. A prism compression sample with the painted pattern was glued to aluminium pin, which was loaded against the actual compression plate with force 20 N and moved horizontally 4 mm with the velocity of 1 mm/s. The tests were repeated five times from which averages were calculated.

2.5. Finite element analysis

A finite element model was created for studying the frictional effects. Sample B was chosen as reference, because its properties were expected to be the most oriented. Three-dimensional finite element model was applied using Abaqus/Standard (2016). The model consisted of a ample and two identical rigid parts. The geometry of the sample corresponded sample to the real dimensions (Table 1). The rigid parts were positioned below and above the sample. Surface-to-surface contact was set between the sample and the rigid parts.

Material properties were defined using the Engineering constant option of Abaqus. The option presumes orthotropic relationships. The option applies three Young's moduli, Poisson's ratio (v_{12}, v_{13}, v_{23}) and shear moduli. Young's moduli and Poisson's ratio values were based on experimental results. Shear moduli were approximated based on [26], which provided 3.94 GPa for G_{12} and 4.2 GPa for G_{13} and G_{23}.

Boundary conditions were applied on each part. All translations and rotations of the lower rigid part were restricted. Sample's boundary conditions were applied for restricting the rigid body motion. Horizontal translations were restricted at middle nodal points of the sample upper and lower surface. The sample lower surface edge middle points included restricting boundary conditions parallel to the edge. For the upper rigid part, all translations and rotations excluding vertical translation were restricted. The compression was applied using enforced displacement providing one percent strain in the vertical direction. The sample was meshed using 10,368 solid elements (C3D8).

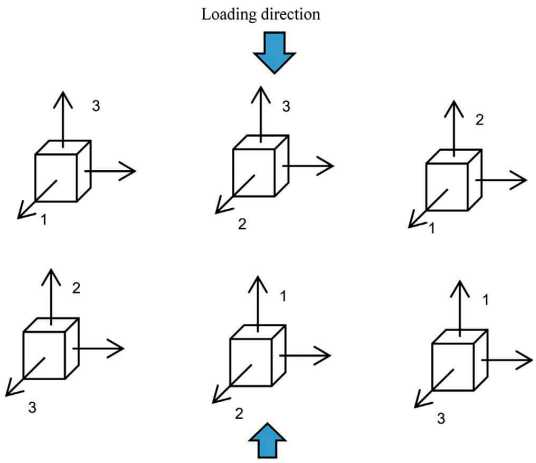

Fig. 3. Test sequence of a prism sample.

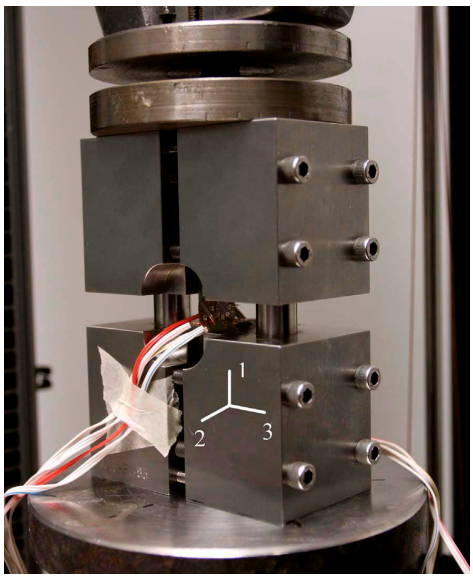

Fig. 4. Combined loading compression test setup.

Typical element dimension in the sample was 0.5 mm, which corresponds 18 × 24 × 24 elements for height, width and length, respectively. Rigid parts were meshed using typical 1 mm element dimension. The finite element mesh of the model is shown in Fig. 6.

The analyses were performed for three different friction coefficients between the sample and the rigid parts. For comparison, a frictionless analysis was computed. When defining a Poisson's ratio value, average strain in the transverse direction to the loading direction was recorded. The strain was evaluated based on average nodal displacements on the surface of interest. Nodal points closer than 1 mm distance from an edge were not included, since they were not included in DIC analyses. For studying six different Poisson's ratio, the specimen was rotated per analysis according to Fig.3.

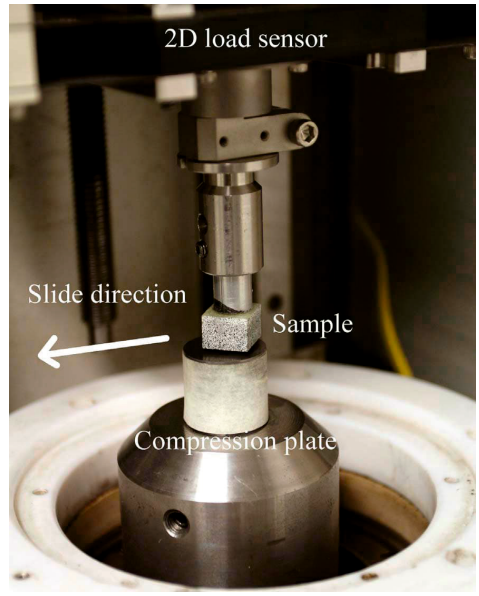

Fig. 5. Measurement of friction coefficients between the coated compression sample and the compression plate.

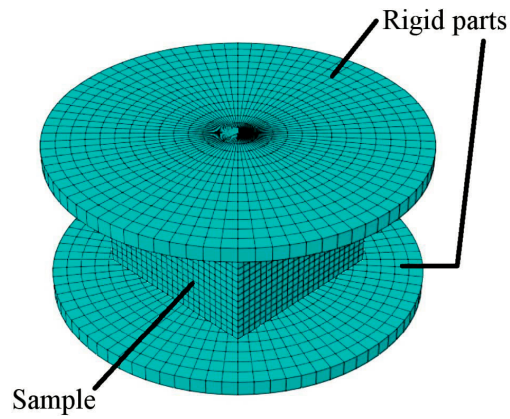

Fig. 6. Finite element model of sample B.

3. Results

Full field strain maps presented in Fig. 7 show the local strains in the loading direction. In many cases distributions are very uneven. This arises mainly due to the intrinsic heterogeneous structure of the fiber-reinforced materials but also due to the lack of perfect parallelism between the contact surfaces causing deviation from a truly uniaxial loading condition. Even though DIC is a fuzzy measuring technique [20] in which average displacements are computed over defined subsets, the spatial resolution of full-field measurements is usually excellent compared to conventional strain measurement techniques. However, there are certain limitations when studying local deformations in heterogeneous materials since the subset size should be smaller than the size of the heterogeneity [20,21]. If there are different materials inside a subset, the averaging process leads to blurred measuring artefacts at the interface regions, which is a fundamental effect of the

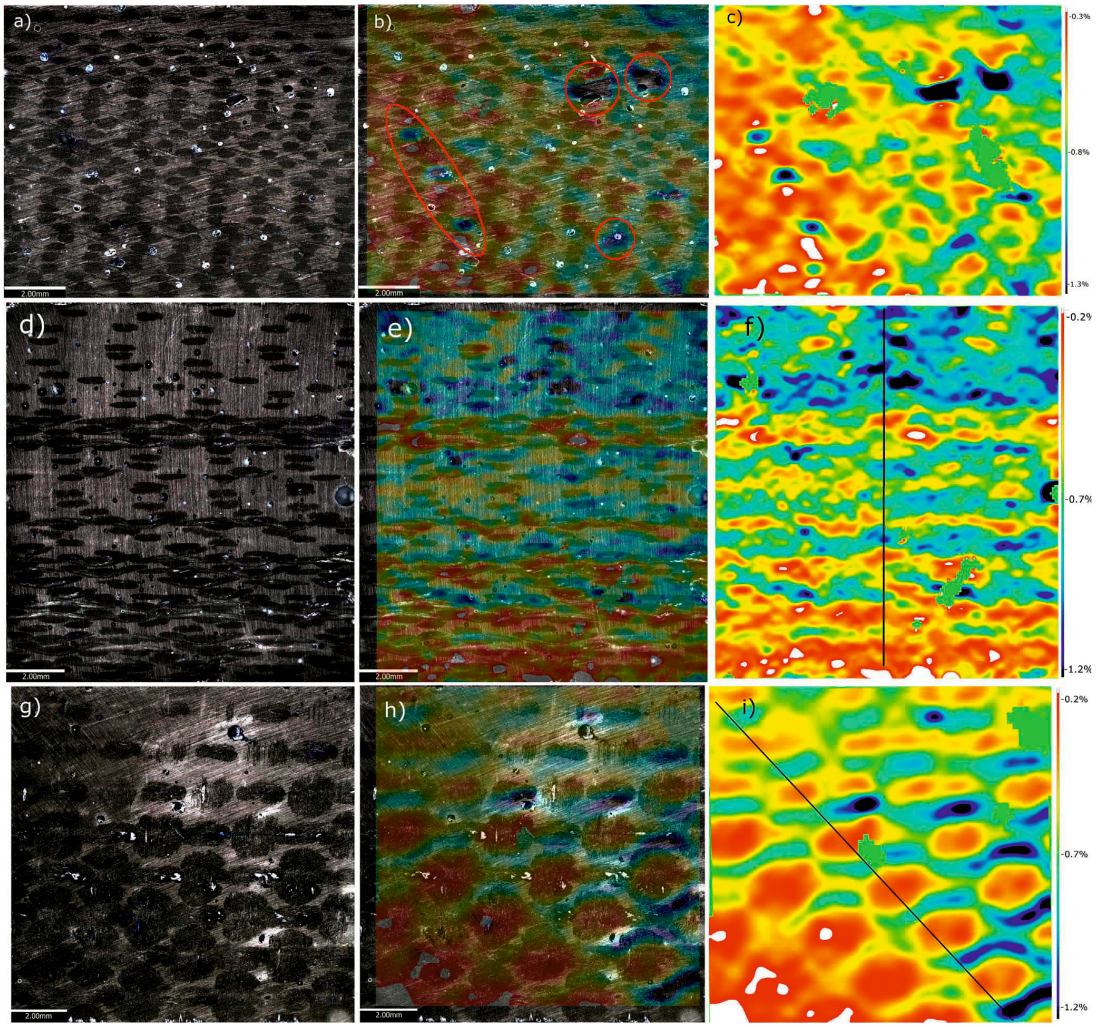

Fig. 7. Left column = optical microscopy, Middle column = pseudo image, Right column = axial strain from DIC measurements. Top row = material B, surface 2; Middle row = material C, surface 1; Bottom row = material B, surface 3.

technique. In a DIC measurement, there are several factors affecting the outcome of the analysis (such as speckle pattern size, subset size and used magnification). Compromises have to be made to obtain large enough study window, sufficient spatial resolution and low noise.

In this study, with the first tests (materials A, B and C) the DIC analysis was given a subset size of 21 pixels with a 5-pixel step size. In the latter test with material D the parameters were 39 pixels and 10 pixel, respectively. These parameters have a strong influence on the computed strain fields, as explained in [22,23]. Different subset and step sizes were studied and the selected parameters presented a good combination of low noise and good spatial resolution of the local strain fields in the measurements.

Engineering constants (i.e. E, ν, G) in macroscale are generally used to define mechanical behavior of FRPs, which simplifies for example the design process of a component and the comparison with conventional monolithic materials. In that case the local material characteristics are disregarded and the structures are treated as a homogeneous continuum with, for example, orthotropic material properties [3]. In this study, the strains were determined over the whole analyzed surface, excluding 1 mm edge borders thus giving a representative mean values for the measured quantities.

3.1. Microstructural observations with local strain mapping

Due to the inhomogeneous microstructure consisting of the reinforcement fiber bundles in polymer matrix, great deformation concentrations and strain gradients are formed in the composite materials under stress. In Fig.7 three optical microscope images are shown for the different polished surfaces of the studied materials (B and C), where the distribution of the glass fiber bundles is clearly visible in the cross sections. The right column of the figure shows the axial strains under compression measured with DIC from the same surfaces. By combining the optical and DIC images a concrete indication of the spatial resolution of the measured strain can be seen. It is seen that the high strain areas under compressive stress locate precisely at the matrix regions in the studied flat surfaces whereas remarkably lower strains are observed

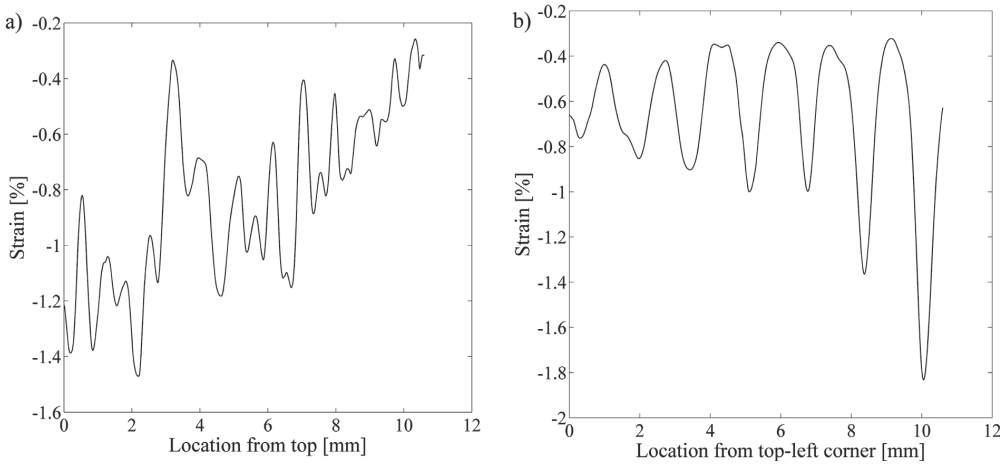

Fig. 8. Axial strain along a) the vertical line in Fig. 7f and b) the diagonal line in Fig. 7i.

at the roving locations, where the reinforcement volume fraction is locally high. In addition to the reinforcement yarn distribution at the studied surface, surface and sub-surface voids can be detected from the full-field strain maps seen as locally increased strain spots shown in Fig. 7b.

Fig. 8a shows the line plot of the axial through-thickness strains (in direction 3) shown in Fig. 7f. The average strain over the studied surface is −0.8% but locally the strain fluctuates between −0.3% at the reinforcements and −1.5% at the matrix rich locations. The decreasing strain from top to bottom of the studied surface can be explained by the reinforcement content gradient at the cut surface. This can arise either due to uneven actual reinforcement distribution in the material or by the small variation in the location of separate plies in through-thickness direction at the cut surface.

The small fluctuations in the axial strain arise from the alternating reinforcement and matrix components of the multilayer laminate at the cross section, from which the ply count of the laminate can be calculated. It should be noticed that whereas the optical image shows the reinforcement distribution only at the cut surface, the deformations under loading at the free surface measured with DIC are partly affected by properties of the material below the studied surface.

Fig. 8b shows the local strains from the diagonal line shown in Fig. 7i which is the in-plane surface of the thick laminate. Here the axial strain fluctuates between −0.3% and −1.8% and the mean strain in the surface is −0.7%. The minimum compressive strain is found in the middle of the warp yarn whereas the maximum compressive strain is located at the resin pockets which form over the space between warp and weft yarns of the fabric.

3.2. Elastic moduli

Elastic moduli of the samples were calculated as a secant modulus from the initial part (appr. $\Delta\varepsilon = 0.0005...0.003$) of the stress-strain curve based on compressive load. An example of the axial strain map at 50 MPa compressive stress and a stress-strain curve for the material are shown in Fig. 9. The curves show no significant plastic deformation confirming the initial assumption that no remarkable irreversible deformation occurs in the samples, which could affect detrimentally the results when the same sample is tested six times.

The measured moduli for each tested material are shown in Fig. 10 and Table 2. The slightly higher E_2 compared to E_1 can be explained with the higher crimp in the fabrics in transverse direction compared to winding direction causing increased off-axis orientation of the reinforcement in direction 1. In addition, the fiber content in material B (52%/48%) was higher in direction 2 increasing the modulus. The high E_3 of material A in terms of its low fiber content is due to the high inorganic filler content of the resin.

3.3. Poisson's ratios

Precise determination of Poisson's ratios of materials is generally challenging: 1) it requires simultaneous measurements of strain in two accurately perpendicular directions, 2) the percentage errors in transverse strain measurements can be large and 3) uniaxial stress state is required. Since the transverse strains are usually lower than the axial strains, Poisson's ratios are normally calculated over a higher strain region than what is used for modulus determination, as recommended, for example by ISO-527 for tensile tests [24]. The strains are usually measured with extensometers or biaxial strain gauges, with whom the misalignment of the measuring devices can have a significant effect on the results. On the other hand, with DIC there are several different factors which can have an effect on the measured strains, such as the quality of the calibration, the used surface pattern and the chosen analysis parameters (subset size, step size, etc.). However, from the full field strain data obtained with 3D-DIC analysis Poisson's ratios can be rather practically determined over the studied surface provided that the strains are high enough considering the resolution of the measurement.

Here, the Poisson's ratios (ν_{yx}) were calculated for each loading orientation as a ratio of transverse strain in the x-direction (transverse to load direction) and axial strain in the y-direction (load direction). Generally, the full-field figures (e.g. Fig. 11a) showed very uneven values of Poisson ratio on the studied surfaces, which is explained by the actual inhomogeneous microstructure of the composite, i.e. caused by the distribution of the fiber bundles in the woven reinforcements. However, when a mean value is calculated over the data, a representative apparent homogenous property can be obtained. In Fig. 11b the apparent ν_{32} of material C is plotted against the axial strain. With the lowest strain values ν_{32} fluctuated presumably due to uneven loading conditions of the samples with the compression plates and the very small transverse strains considering the resolution of the technique. At higher axial strains, the ratio stabilizes and an average value of the Poisson's ratio was determined from the axial strain range of (0.003...0.006). Results of the six Poisson's ratios for the three materials are shown in Fig. 12.

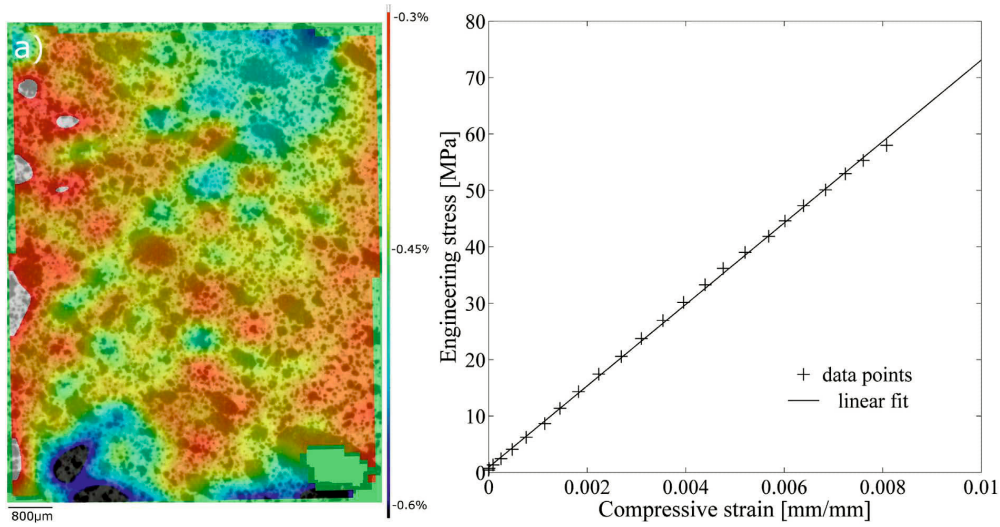

Fig. 9. a) Full-field strain map of the test B_{21} showing compressive strain in direction 2 (vertical in the figure), P = 50 MPa. b) Apparent stress-strain curve of the test B_{21}.

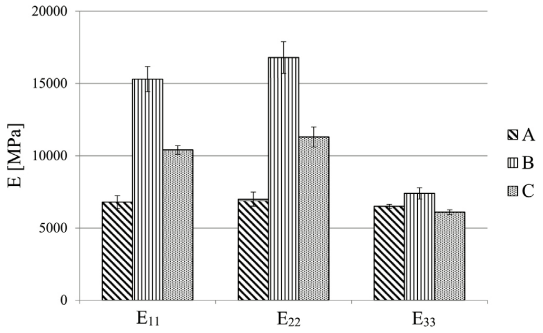

Fig. 10. Determined apparent Young's moduli of the materials.

Table 2
Determined engineering elastic constants for the materials A, B and C.

	E_1 [GPa]	E_2 [GPa]	E_3 [GPa]	ν_{12}	ν_{21}	ν_{13}	ν_{31}	ν_{23}	ν_{32}
A	6.8	7.0	6.5	0.34	0.36	0.4	0.38	0.40	0.30
B	15.3	16.8	7.4	0.25	0.19	0.48	0.22	0.46	0.21
C	10.4	11.3	6.1	0.27	0.22	0.48	0.27	0.42	0.23

3.4. Friction effects

The FEM simulations indicated that the friction between the sample and the compression plates had insignificant effect on the deformation in the loading direction. Thus, the experimentally determined Young's moduli can be considered valid. However, the friction restraining the lateral deformations of the sample at the contact plane has an effect on the Poisson's ratio as shown in Fig. 13. The higher the friction coefficient, the greater the effect (that decreases Poisson's ratio values) on the Poisson's ratios, which gives reasons to use polished and lubricated compression plates in the compression tests.

Actual friction coefficients were determined using real contact surfaces used in the compression tests. On the dry plate the composite sample with the sprayed pattern showed static and dynamic friction coefficients of 0.23 and 0.18, respectively. By lubricating the compression plate with silicone oil the friction coefficients decreased to 0.14 and 0.09, respectively (Fig. 14). Due to the friction effect the measured Poisson's ratios in these tests are thus approximately 3%–7% lower than for compression with zero friction.

3.5. Comparison of the compression methods

To evaluate the robustness and accuracy of the prism compression technique, five samples (140 mm × 12 mm × 9 mm) from laminate D were tested with the combined loading compression method (according to ASTM D 6641) to determine Young's moduli E_1 and Poisson's ratios ν_{12} and ν_{13}. After that, the compression tests using DIC and prism samples (12 mm × 12 mm × 9 mm) made of the same laminate were carried out to determine the same properties.

The results presented in Table 3 show that both methods give good correspondence for modulus E_1, indicating that the axial strain determinations are consistent. The measured Poisson's ratios, on the other hand, show significant difference where the trend is that the combined loading compression gives lower values (−18% and −20%). The higher standard deviation in the values measured with DIC is due to lower strain resolution compared to strain gauges, which is emphasized with the transverse strains being significantly lower. However, the observed difference in Poisson's ratios can largely be explained with the different boundary conditions of the samples in the test methods. In the combined loading compression method the sample is fully constrained in direction 3, and likely also in the direction 2 because the friction between the sample and text fixture is high on purpose. In the prism compression test, on the contrary, the lateral constrains are remarkably lower, in which the friction coefficient was shown to be approximately 0.15. The greater the lateral constrains in the gauge ends the lower the Poisson's strains are during the compression.

4. Discussion

4.1. Sample size and edge effects

In the determination of apparent mechanical properties of anisotropic materials using small samples the question of adequate sample size is of essential importance. Through-thickness properties, especially through-thickness strength, have been determined with parallel-sided

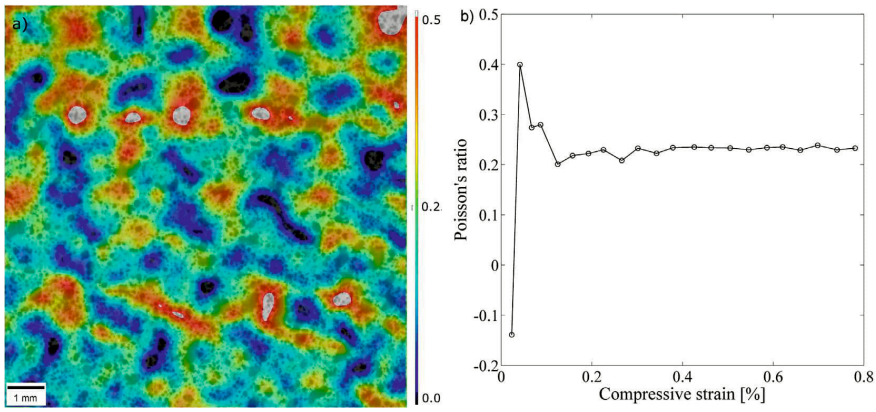

Fig. 11. a) Full-field map for ν_{32} of material C, P = 50 MPa. b) Areal mean value of ν_{32} as a function of strain measured.

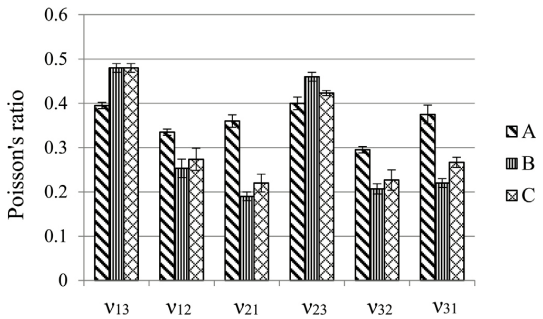

Fig. 12. Determined Poisson's ratios of the materials.

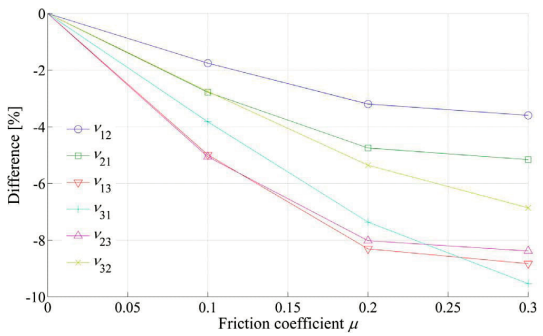

Fig. 13. Simulated effect of the friction between compression plates and sample on Poisson's ratios for sample B.

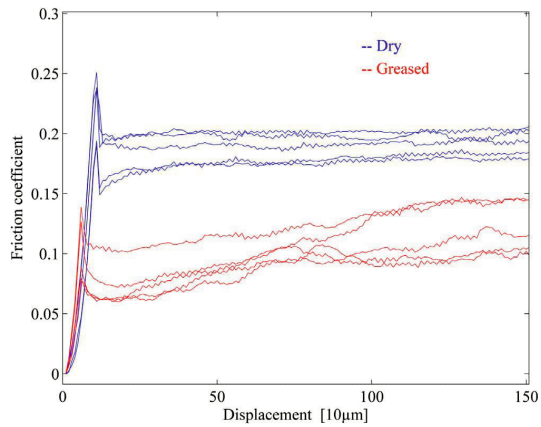

Fig. 14. Measured friction coefficients of the painted compression prism sample against dry and greased compression plate.

Table 3
Measured properties for the laminate D with two different test methods. (n = 5, average values and their standard deviation).

Test	Studied surface	E_1 [GPa]	ν_{12}	ν_{13}
ASTM D 6641 with strain gauges	S2	20.4 (2.8)		0.393 (0.005)
ASTM D 6641 with strain gauges	S3	25.9 (1.9)	0.163 (0.004)	
Prism compression with DIC	S2	21.7 (1.7)		0.476 (0.014)
Prism compression with DIC	S3	26.6 (2.0)	0.205 (0.020)	

prism samples similar to used in this study by several research groups [28–32]. In the studies typical sample edge length has been 10 mm–12 mm, and it has been shown that the compressive stress below the contact plane becomes stable normally after the distance of approximately 10% of their total thickness [30,31].

Although the stress distribution in sample under compression is dependent on the properties of the reinforcement, stacking sequence and global orientation of the sample, in terms of the constant stress state required for successful measurements, the size of the prism samples used in our tests was deemed suitable for testing.

In addition to the stress concentrations close to the compression plates, in laminates adjacent to free edges there exists a narrow region in which large interlaminar normal and shear stresses exist. Several authors [29,33] have commented that the prism specimens are subjected to these free-edge effects but their impact on the measured properties is seldom analyzed in detail. With a comprehensive FE analysis Thompson showed that the edge-effects can be remarkable, but were almost fully dissipated after 1.5 mm from each edge (12 mm) into the centre of sample. [31]

The edge effects are thus always present in laminated materials,

which can have an effect on the experimentally measured strains on the free surfaces causing, for example, inaccuracy in the determined modulus values.

When the determined elastic properties of the same material measured with the two different compression techniques (Table 3) are compared, it is observed that the both give statistically similar values for E_1. However, the modulus determined with the surfaces normal to axis 2 and 3 differed significantly, on the contrary to the initial assumption. The difference is presumed to be affected by two different phenomena. Firstly, the edge effects in the surface 2 are greater than in the surface normal to laminate thickness (surface 3). Secondly, even though the volume fraction of the reinforcement in the small sample is more or less constant, the relative area of the reinforcement in the ground surfaces can differ between the faces of the prism. The strains are measured purely from the surface and, for example, in Fig. 7 it is seen that locally the strains locally fluctuate over the studied surface. This phenomenon is emphasized when woven reinforcements with larger repeating units are used. Kim et al. [29] suggested that the minimum edge length of a sample should be at least twice the repeating unit so that the sample can be considered to be a representative of the structure. When determining strains from the surface, similar assumption can be made, i.e. the gauge length in strain measurement (in the middle area where the compression stress state is not affected by the loaded ends) should at least twice the length of repeating unit of the reinforcement giving a rough guideline for the minimum dimensions of the sample.

4.2. Anisotropy

In essence, the properties of anisotropic materials are dependent on the direction of the material. The elastic behavior of fully anisotropic materials can be described with 21 independent elastic constants. With continuous fiber reinforced composites, often some planes of symmetry exist, which reduces the number of the individual elastic constants. FRPs are typically orthotropic, thus, have three mutually orthogonal planes of symmetry reducing the number of the individual constants to nine [1,2,25].

For linear orthotropic materials, only three Young's moduli and three Poisson's ratios are independent. Thus, the Poisson's ratios and Young's moduli are coupled with the following relationship:

$$\frac{\nu_{ij}}{E_i} = \frac{\nu_{ji}}{E_j} \leftrightarrow \frac{\nu_{ij}}{\nu_{ji}} = \frac{E_i}{E_j} \tag{1}$$

Fig. 15a shows the $\frac{\nu_{ij}}{\nu_{ji}}$ vs $\frac{E_i}{E_j}$ – plot, where the three determined moduli ratios based on the DIC measured values of each material are plotted together with an orthotropic model (the diagonal line). The coupled moduli ratios of material A match amidst point (1,1), indicating that the properties were only slightly dependent on the orientation. The materials B and C, in contrast, show greatly scattered moduli ratios explained by increased anisotropy due to the fabric reinforcements.

The fiber content in the warp and weft directions of the reinforcements used in materials B and C were 52/48 and 50/50, respectively. However, the determined E_1 and E_2 of materials B and C were observed to differ significantly based on Student's *t*-test ($p < .05$) for both materials. The weaving pattern of the reinforcements was uneven-sided, and different in the tested materials. Moreover, during manufacturing the fabric strips are tensioned slightly in the direction 2 causing straightening of the fibers. Thus, the difference in the moduli is considered to result mostly due to the different level of undulation of fibers in the two directions.

The percentage coupling difference (Δ) between theoretical and measured elastic moduli can be calculated by

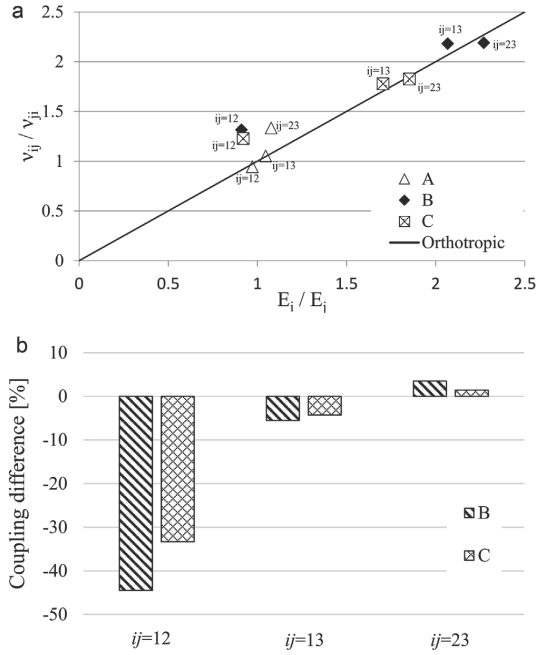

Fig. 15. a) Evaluation of the elastic behavior of the materials (i, j = from 1 to 3). b) Difference between theoretical and measured coupling of Poisson's ratios and Young's moduli.

$$\Delta_{ij} = 100 \times \left(1 - \frac{\frac{\nu_{ij}}{\nu_{ji}}}{\frac{E_i}{E_j}}\right) \tag{2}$$

where *i* and *j* denote the orthogonal directions 1, 2 and 3. The calculated coupling differences for the materials B and C are presented in Fig. 15b, where it is seen that especially Δ_{12} is significant. It is well known that the tensile and compressive moduli of fiber reinforced materials are different, mainly due to the local microbuckling or kinking phenomena of fibers under compression decreasing the compressive modulus [27]. In the compression tests, the axial loading causes compression whereas, due to the Poisson's effect, tensile stresses are generated in the transverse directions. The difference between E_t and E_c, is presumably taking also part, in addition to the edge-effects, into the observed variation of measured values and the theoretical symmetrical elastic behavior, explained by Eq. (1).

5. Conclusions

Digital image correlation is an effective non-contact full-field technique to study surface deformations. In this research we used DIC to determine deformations of cubic samples made of thick polymer composite laminates under compression. By measuring a sample in six different test orientations nine engineering elastic constants, i.e. three Young's modulus and six Poisson's ratios, were determined directly based on the single sample for three different composite materials. The properties are generally arduous to measure and also difficult to simulate, because the out-of-plane properties of the multilayer fabric reinforced composites are often unknown.

For successful compression testing, highly parallel opposite edges of the rectangular cubic sample are required, which complicates the sample manufacturing. However, with the presented technique, the required amount of sample material is at a minimum. This allows a

broad set of elastic material properties in three orthogonal directions to be directly determined, for example, from a piece of material used in a real application. This is a clear benefit if, for example, the microstructure of a composite component is strongly dependent on the fabrication technique, and the manufacturing of conventional test coupons with the same technique is challenging or impossible. A rule of thumb of two repeating units can be used for the absolute minimum edge length for the compression sample. Here, a sample edge length of 12 mm was used.

The measured compressive Young's moduli showed reasonable agreement when considering the microstructure of the materials. The measured elastic moduli were analyzed against an orthotropic material model and the results showed good correspondence with the model. The actual friction coefficients between the tested samples and the compression plates were measured. The effect of friction on the measured properties was analyzed with a finite element model, which indicated that, on the measured Young's moduli, the effect is minimal but resulting in lower values of the Poisson's ratios. The comparison of the Young's moduli and Poisson's ratios in single loading direction measured with the prism compression technique and ASTM D6641 standard test was carried out. The determined Young's moduli were in a good agreement but the Poisson's ratios measured with ASTM D6641 showed lower values. The difference was largely explained with the differences in the constraints between the tests.

In addition to the quantitative determination of the engineering moduli, the full-field strain measuring technique with very good spatial resolution allows local strain mapping of the samples. This can be used in evaluation of the microstructure (e.g. reinforcement distribution, local defects) of the materials, but also to ascertain that the strains are measured from a representative location on the sample surface.

Acknowledgements

The work has been done as a part of the FIMECC Hybrids research program supported by the Tekes - Finnish Funding Agency for Technology and Innovation and the participating companies. The authors would like to thank Tekes for the financial support and Mr. Mika Pihlajamäki and Mr. Tommi Lehtinen for helping with the experiments.

References

[1] Hull D, Clyne TW. An introduction to composite materials. In: Cambridge solid state science series; 1981.
[2] Reddy JN. Mechanics of laminated composite plates and shells: theory and analysis. CRC Press LLC; 2004.
[3] Lasn K, Klauson A, Chati F, Décultot D. Experimental determination of elastic constants of an orthotropic composite plate by using lamb waves. Mech Compos Mater 2011;47(4):435–46.
[4] Lasn K, Echtermeyer AT, Klauson A, Chati F, Décultot D. Comparison of laminate stiffness as measured by three experimental methods. Polym Test 2015;44:143–52.
[5] Vishnuvardhan J, Krishnamurthy CV, Balasubramaniam K. Genetic algorithm reconstruction of orthotropic composite plate elastic constants from a single non-symmetric plane ultrasonic velocity data. Compos Part B 2007;38(2):216–27.
[6] Kersemans M, Paepegem WV, Abeele KWD, Pyl L, Zastavnik F, Sol H, Degrieck J. The Quasi-harmonic ultrasonic polar scan for material characterization: Experiment and numerical modeling. In: The 12th International Conference of the Slovenian Society for Non-Destructive Testing, September 2013.
[7] Potluri P, Young RJ, Rashed K, Manan A, Shyng YT. Meso-scale strain mapping in UD woven composites. Compos Part A: Appl Sci Manuf 2009;40(12):1838–45.
[8] Vuorinen JE, Schwarz RB, McCullouh C. Elastic constants of an aluminum-alumina unidirectional composite. J Acoust Soc Am 2000;108(2):574–9.
[9] Anzelotti G, Nicoletto G, Riva E. Mesomechanic strain analysis of twill-weave composite lamina under unidirectional in-plane tension. Compos Part A 2008;39(8):1294–301.
[10] Kadooka K, Kunoo K, Uda N, Ono K, Nagayasu T. Strain analysis for Moiré interferometry using the two-dimensional continuos wavelet transform. Exp Mech 2003;43(1):45–51.
[11] Lee JR, Molimard J, Vautrin A, Surrel Y. Digital phase-shifting grating shearography for experimental analysis of fabric composites under tension. Compos Part A 2004;35(7–8):849–59.
[12] Ivanov D, Ivanov S, Lomov S, Verpoest I. Strain mapping analysis of textile composites. Opt Lasers Eng 2009;47(3–4):360–70.
[13] Daggumati S, Voet E, Paepegem WVV, Degrieck J, Xu J, Lomov SV, et al. Local strain in a 5-harness satin weave composite under static tension: Part I – experimental analysis. Compos Sci Technol 2011;71(8):1171–9.
[14] Flament C, Salvia M, Berthel B, Crosland G. Local strain and damage measurements on a composite with digital image correlation and acoustic emission. J Compos Mater 2016;50(4):1989–96.
[15] Daggumati S, In-situ local strain measurement in textile composites with embedded optical fibre sensors. In: 5th International conference on Emerging Technologies in Non Destructive Testing (ETNDT-5); 2011.
[16] Wang CC, Chahine NO, Hung CT, Ateshian GA. Optical determination of anisotropic material properties of bovine articular cartilage in compression. J Biomech 2003;36(3):339–53.
[17] Heinz SR, Wiggins JS. Uniaxial compression analysis of glassy polymer networks using digital image correlation. Polym Test 2010;29(8):925–32.
[18] Sánchez-Arévalo FM, Pulos G. Use of digital image correlation to determine the mechanical behavior of materials. Mater Charact 2008;59(11):1572–9.
[19] Jerabek M, Major Z, Lang RW. Strain determination of polymeric materials using digital image correlation. Polym Test 2010;29(3):407–16.
[20] Canal LP, González C, Molina-Aldareguía JM, Segurado J, Llorca J. Application of digital image correlation at the microscale in fiber-reinforced composites. Compos Part A 2012;43(10):1630–8.
[21] Rajan VP, Rossol MN, Zok FW. Optimization of digital image correlation for high-resolution strain mapping of ceramic composites. Exp Mech 2012;52(9):1407–21.
[22] Rossi M, Lava P, Pierron F, Debruyne D, Sasso M. Effect of DIC spatial resolution, noise and interpolation error on identification results with the VFM. Strain 2015;51(3):206–22.
[23] Wang Y, Lava P, Coppieters S, De Strycker M, Van Houtte P, Debruyne D. Investigation of the uncertainty of DIC under heterogeneous strain states with numerical tests. Strain 2012;48(6):453–62.
[24] ISO-527-1:2012, Plastics – determination of tensile properties.
[25] Lempriere BM. Poisson's ratio in orthotropic materials. AIAA J 1968;6(11):2226–7.
[26] Naik NK, Chandra Sekher Y, Meduri S. Damage in woven-fabric composites subjected to low-velocity impact. Compos Sci Technol 2000;60:731–44.
[27] Meng M, Le HR, Rizvi MJ, Grove SM. The effects of unequal compressive/tensile moduli of composites. Compos Struct 2015;126:207–15.
[28] Tagarielli VL, Minisgallo G, McMillan AJ, Petrinic N. The response of a multi-directional composite laminate to through-thickness loading. Compos Sci Technol 2010;70:1950–7.
[29] Kim BC, Park DC, Kim BJ, Lee DG. Through-thickness compressive strength of a carbon/epoxy composite laminate. Compos Struct 2010;92:480–7.
[30] Lee DG, Park DC. Through-thickness compressive strength of carbon-phenolic woven composites. Compos Struct 2005;70:403–12.
[31] Thompson LF. Through-thickness compression testing and theory of carbon fibre composite materials [Ph.D. thesis]: School of Mechanical, Aerospace and Civil Engineering; University of Manchester; 2011.
[32] Guo Y, Post D, Han B. An experimental study of micromechanical behavior and smeared engineering properties. J Compos Mater 1992;26(13):1930–44.
[33] Mespoulet S, Hodgkinson JM, Matthews FL, Hitchings D, Robinson P. Design, development, and implementation of test methods for determination of through thickness properties of laminated composites. Plast Rubber Compos 2000;29(9):496–502.

PUBLICATION III

Revised notched coating adhesion test to account for plasticity and 3D behaviour

O. Orell, J. Jokinen, M. Kallio and M. Kanerva

Polymer Testing 102 (2021) 107319
https://doi.org/10.1016/j.polymertesting.2021.107319

Publication is licensed under a Creative Commons Attribution 4.0 International License CC-BY

Polymer Testing 102 (2021) 107319

Contents lists available at ScienceDirect

Polymer Testing

journal homepage: www.elsevier.com/locate/polytest

Revised notched coating adhesion test to account for plasticity and 3D behaviour

Olli Orell [a,*], Jarno Jokinen [a], Marke Kallio [b], Mikko Kanerva [a]

[a] Tampere University, Faculty of Engineering and Natural Sciences, P.O.B. 589, 33014 Tampere, Finland
[b] Metso Outotec Finland Oy, P.O.B 306, 33101 Tampere, Finland

ARTICLE INFO

Keywords:
Notched coating adhesion
Fracture toughness
Digital image correlation
Polyamide-imide
Virtual crack closure technique
Cohesive zone model

ABSTRACT

Specialized polyamide-imide coating on a CuSn10Pb10 substrate, a material combination utilized often in modern bearing applications, is fabricated using the solvent casting method. The coating adhesion is studied using the well-known notched coating adhesion (NCA) test. Conventionally, the critical strain required to cause the debond propagation is determined by visual observation and indirectly linked to measured strain data to calculate fracture toughness. Here, digital image correlation (DIC) is used to systemically study the coating deformations during testing that enables quantitative determination of the instantaneous debond length. With the introduced method, the critical strain to induce the debond of the coating and the propagation of the debond can be determined for non-elastically behaving specimens reliably. The coating's debond onset is studied with virtual crack closure technique (VCCT) here. The method can take 3D effects into account in detail and provides a sophisticated method to determine the critical energy release rate. Additionally, cohesive zone modelling (CZM) is used to simulate debond progression. Nonlinear stress–strain responses are observed taking place both with the coating and the substrate materials. The results emphasize that the coating plasticity has a remarkable role in the test behaviour which needs to be taken into account in the revised analysis.

1. Introduction

1.1. Modern polymer coatings

Polymeric materials are used as functional coatings in numerous industrial applications. The coating-integrated functionality is typically a requirement by design, such as (1) the aesthetics, (2) environmental resistance and (3) the tribological properties of the parent material, inter alia. One branch of the significant industrial applications, where the polymer coatings are utilized, is the modern bearings.

Current bearing designs require multi-layer components. The polymer overlays in the products often outperform conventional (metal) surfaces, in terms of lower friction coefficients, improved wear resistance and favourable contact pressure distribution upon service loads [1–4]. Modern high-performance polymer coatings are normally strongly filled high-performance polymers based on polyetheretherketone (PEEK), polyimides (PI), polyetherimide (PEI) or polyamide-imides (PAI). The processing of these polymers into functional coatings is typically carried out using different spraying techniques [5], dip or spin coating, or electrodeposition methods [6]. The polymer materials are normally mixed with different compositions of various fillers of which the common are molybdenum disulfide (MoS_2), polytetrafluoroethylene (PTFE) and graphite [3,7]. In addition to the micro-sized fillers, also nanofillers have been shown to offer remarkable positive effects on mechanical and tribological properties. The nanofillers combined with the microsized fillers can have synergistic effect on these properties which can be achieved with already at a very small volume fraction [8].

All in all, the complexity of the coatings increases all the time. The combination of several functionalities in addition to the fundamental requirements of coatings to adhere and withstand the operational environment leads to challenges in design and sizing. For coating adhesion, the most challenging case results due to non-linear coating behaviour, highly ductile substrate behaviour, and brittle and unstable interface debonding. For example, ductile metal substrates, such as leaded bronzes or stainless steels, incur low yield strain level but often also low adhesion with polymer coatings. Environmental factors, such as temperature cycling and corrosive mediums, may have radical detrimental effects on the coating adhesion and cause premature failures.

* Corresponding author.
E-mail address: Olli.Orell@tuni.fi (O. Orell).

https://doi.org/10.1016/j.polymertesting.2021.107319
Received 14 May 2021; Received in revised form 30 June 2021; Accepted 19 August 2021
Available online 28 August 2021
0142-9418/© 2021 The Authors. Published by Elsevier Ltd. This is an open access article under the CC BY license (http://creativecommons.org/licenses/by/4.0/).

1.2. Coating adhesion tests

The fundamental adhesion properties to be used for numerical models and design codes are the fracture toughness and critical (allowable) stress and strain to induce the debond at the interface [9,10]. Multiple different techniques to evaluate adhesion characteristics exist, and the selection of the most reliable method depends on several aspects as explained by Chen et al. [11]. The important factors affecting the selection of the method include, for example, the brittleness of the components, the coating thickness, the residual stresses, and the correspondence of the method to the assumed in-service adhesion failure. Generally, the adhesion testing methods can be roughly divided into sandwich type specimen and bimaterial specimen based methods [12]. The former includes, for example, double cantilever beam (DCB) and four-point bending tests where the coating is sandwiched between stiff substrate beams using strong adhesive layers. The techniques are widely used for quantitative determination of coating adhesion characteristics, but require laborious specimen fabrication and may not be suited for thin coatings which could be affected by the extra gluing process (to add the sandwiching substrate pair). The bimaterial based methods, such as indentation and scratch tests, blister tests and peel tests, are simple to carry out and do not require attaching extra devices or substrates to the studied coating. However, these methods provide typically more qualitative than quantitative information on the adhesion characteristics and are used mostly for comparative studies [13].

The notched coating adhesion (NCA) test is a simple bimaterial adhesion test which has been used for determining the critical energy release rate (ERR) for linear-elastic coating behaviour and insignificant substrate influence [14]. The test method bases on measuring the critical specimen strain occurring at the time of onset of the coating debond. The onset is observed visually during specimen loading. The test has been successfully applied for various polymeric coatings and adhesive films [15–19]. However, even though being simple test to carry out, the method is non-standard and several challenging issues should be taken into account in the analysis of the test results. A deficiency is that the selected specimen geometry may affect the generalized test output. Especially, often the coating thickness is not a real parameter that can be precisely adjusted during the specimen fabrication. The coating thickness in the NCA method, however, is a dominant factor on the level of the critical strain where the debond occurs. Polymer coatings show basically always nonlinear mechanical behaviour. If the critical strains causing the onset of the coating debond are high, the polymer material can already go through significant plastic deformation and related effects. The residual (thermal) strains have also a significant effect on the determined critical ERR values. Overall, the extension of the NCA method to account for three-dimensional (3D) residual stresses, free-edge stresses, coating plasticity, and severe substrate deformation is not straightforward. Especially, if the results to determine the critical ERR are analysed using analytic solutions, as they conventionally are.

1.3. Test specimen monitoring

The technologies for sensing and monitoring test specimens have developed significantly since the NCA method was established. For example, data analysis to detect critical strain, derivatives of strain-time and strain-force curves have been suggested to observe slight changes in the interfacial energy release [18]. Another procedure to observe debond propagation was introduced by Elambasseril et al. who used an acoustic emission technique with circumferentially notched tensile specimens [20]. Optical extensometers have also been used to precisely measure specimen strain and coating debond [17]. The coating's debond onset can, however, be difficult to observe visually due to the lack of coating transparency, reflections, colour changes and minimum opening at the bond line. On the other hand, the variation in the specimen's coating thickness, the imperfect pre-crack and the local substrate inhomogeneities can induce test artefacts. Due to the non-ideal specimen systems, in experiments, the debond onset and propagation may actually not be clearly-defined sudden phenomena complicating even more the determination of the unambiguous critical specimen strain the method greatly bases on.

Digital image correlation (DIC) is a full-field optical method for determining deformations of a studied surface. The displacements are computed after matching the changes in recorded images (per time step) with so-called correlation algorithms. In local DIC, the images are divided into smaller subsets, that include unique features to be distinguishable, and whose instantaneous relative locations can be computed independently from the other subsets. Based on the determined full-field displacement field, local strains over the studied surface can be derived [21–24].

1.4. Research target of current study

In this work, we present a method based on the systematic use of local DIC to study the debond of the coating in the NCA tests. With the technique, one can measure accurately and objectively the debond progression and define precisely the critical specimen strain. Moreover, a procedure to define fracture toughness taking into account 3D deformation and plasticity is developed. The method is demonstrated for a PAI coating on a leaded tin bronze (CuSn10Pb10) substrate, where significant non-linear effects are observed. In addition, the procedure is studied for modelling applications and is based on the combined use of DIC and finite element analysis (FEA) using virtual crack closure technique (VCCT) and cohesive zone model (CZM). VCCT is shown to be able to simulate the cracking onset in detail and provide G_c values where also the 3D effects are taken into account. CZM enables then accurate prediction of the debond progression. In addition, energy quantities provided by the FEA are used to study the overall non-linearity in the behaviour during a test, which emphasize the effects of the coating plasticity. Finally, the feasibility of the different analysis approaches are discussed.

2. Methods

2.1. Case materials and NCA specimen preparation

The NCA specimen used in the study consisted of solvent-cast PAI (Torlon 4000TF provided by Solvay) applied on CuSn10Pb10 substrate. Fine PAI powder was first dried for four hours at 170 °C and then diluted to dimethylsulfoxide (DMSO) with a magnetic stirrer—forming a 15 wt-% solution. The bronze samples were cut from a rectangular block to form test coupons with dimensions of 120 mm × 13 mm × 1.6 mm. The surface treatment of the substrate samples consisted of (1) degreasing with ethanol, (2) blasting the surfaces with Al_2O_3, (3) cleaning in an ultrasonic bath (acetone). After the surface treatment procedure, the samples were stored in a desiccator until the coating was applied.

The coating process was performed by using a bar coater having a wet-film deposition thickness of 20 μm. The process consisted of eight repeated application cycles, where the applied coating was dried at 120 °C in a furnace, for five minutes before each subsequent coating cycle in order to decrease the amount of trapped solvent in the film. Finally, the specimens were heat-treated at 210 °C for 30 min by using a 2 °C/min heating rate. The same process was used to fabricate free PAI films with equal thickness using a glass plate, from which the cured film was finally peeled off for characterisations.

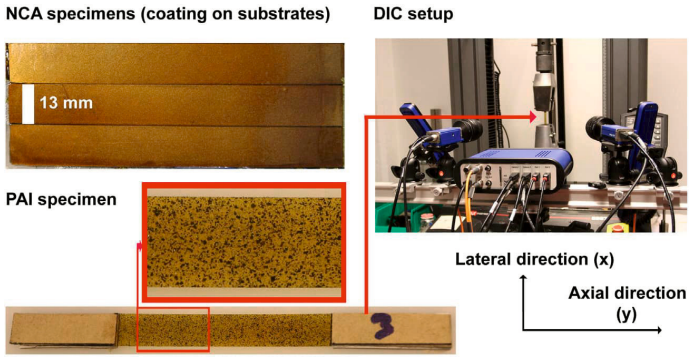

Fig. 1. NCA specimens coated, PAI specimen with the speckle pattern, and the DIC setup for testing.

2.2. NCA test

NCA testing is carried out on uniaxially tensile-loaded specimens until, basically, the strain energy of the adhered coating exceeds the critical value of interfacial adhesion. For an ideal case, the polymer coating falls off, parallel to the loading direction. The thickness of the substrate shall be significantly greater than the coating film to minimize bending. In the event of reversible coating deformation, the critical strain level is determined based on the onset of the unstable propagation of the debond crack front. The test method utilizes manually fabricated pre-cracks, which enables the controlled propagation of the debond during testing. A simplified form for the presumed steady-state debonding was derived by Dillard [14]. Here, the debond length is required to exceed five times the coating thickness to ensure the full release of the strain energy so that the critical ERR is given by:

$$G_{ss} = hE\left[\frac{\epsilon_0^2}{(1-\nu)} + \epsilon_0\hat{\epsilon} + \frac{\hat{\epsilon}^2}{2}\right]. \quad (1)$$

For pre-cracks shorter than five times the coating thickness, the lateral strain remaining must be accounted for to calculate the critical ERR:

$$G_{lc} = hE\frac{(1+\nu)}{2(1-\nu)}\left[\epsilon_0 - \nu\hat{\epsilon} + \hat{\epsilon}\right]^2. \quad (2)$$

In Eqs. (1)–(2), h is the thickness, E is the Young's modulus, ϵ_0 is the residual strain, ν is the Poisson's ratio of the coating and $\hat{\epsilon}$ is the critical strain to be determined by the debond onset.

In this study, the preparation of pre-cracks was carried out with an in-house jig controlling a horizontally-aligned razor blade. The pre-crack load was induced by a drop-weight impactor. A suitable level of impact energy (100 g weight, dropping height 8 cm) was screened out in order to form a constant cut to the coating across the specimen. The testing of the fabricated NCA specimens (Fig. 1) was carried out using a universal testing machine (Model 5967, Instron) at a test rate of 5 mm/min. The specimen deformations were recorded using an axial clip-on extensometer (gauge length 50 mm) and 3D-DIC simultaneously.

2.3. Digital image correlation setup

Commercial stereo-DIC setup (LaVision) was used to study the specimen deformations, in addition to a conventional clip-on extensometer. Especially, the aim in the using DIC was to study locally the debonding phenomenon of the coating during the NCA tests. A two-camera setup (i.e. stereo-DIC) enables calculation of 3D deformation fields whereas one camera systems (2D-DIC) provide only in-plane deformations. The stereo-DIC was preferred because it is not that sensitive on the misalignment errors of the setup and also the out-of-plane coating deformation causes no issues. High-contrast matt black and white speckles were applied by spraying on the specimen surface to generate random pattern for the DIC measurements. The average diameter of the speckles was 50–80 μm measured using an optical profilometer (Alicona, InfiniteFocus G5).

Images were recorded using two 5 MPix (Elite) cameras with objectives having a focal length of 50 mm and by using an aperture of F8. The recording rate was 2 Hz. The scale factor of the used setup was 38 pix/mm and the root mean square error of the calibration was 0.3 pix. The zero-normalized sum of squared difference (ZNSSD) was used as the matching criteria and the affine shape function was used for the subsets. The interpolation method used was 6^{th} order spline. Different analysis parameters were screened with Davis 8.4 software to optimize the spatial resolution and measurement noise. Finally, subset and step sizes of 33 pix and 11 pix were used, respectively, resulting a virtual strain gauge length of 55 pix, or 1.45 mm.

2.4. Numerical analysis and modelling

A finite element model (FEM) representing the NCA specimen was created using Abaqus/Standard 2017 (Simulia). Symmetry was used in the modelling to decrease the analysis time. Crack onset analysis was performed using VCCT that is able to output the momentary ERR for any crack tip opening. The half model of the specimen was used in the VCCT analysis. A crack propagation analysis was performed with a quarter model by applying CZM that is able to simulate non-linear material behaviour and interfacial crack propagation simultaneously. The model length was 60.5 mm (half of specimen) and width 13.6 mm (6.8 mm for the quarter model). The thickness of the substrate and the coating were set in 1.614 mm and 0.076 mm, respectively, representing the measured average dimensions of the fabricated specimens. Elastic and elastic–plastic material models were studied to develop suitable tools for (1) calculating ERR at the debond onset; (2) and predict the propagation of debond. The plasticity in the substrate and coating was modelled using the Johnson–Cook formulation, which takes the form:

$$\sigma^0 = A + B\left(\bar{\varepsilon}^{pl}\right)^n \quad (3)$$

where A, B and n are material parameters [25]. The parameters were fitted based on the tensile testing (Section 3.1). The fitted parameters and other experimentally determined material constants are given in Table 1.

The substrate was meshed using fully-integrated solid elements (C3D8) while the coating was meshed using solid elements with incompatible modes (C3D8I). Both substrate and coating had the same element dimensions. VCCT analysis was observed more efficient in terms of the analysis time when the crack did not propagate (as with the

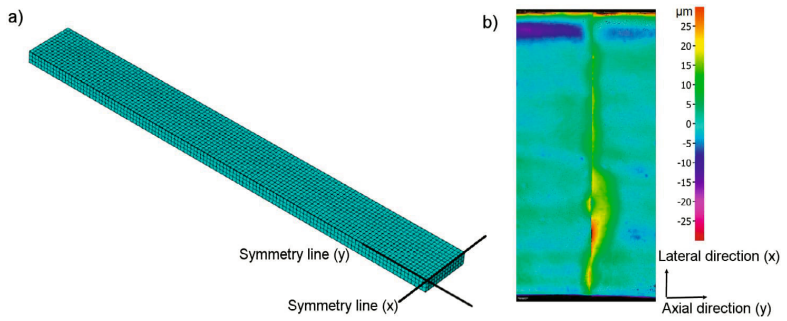

Fig. 2. (a) The quarter FE model when using CZM, and (b) a profilometer image from an NCA specimen and focused at the pre-crack region indicating crack opening (out-of-plane deformation).

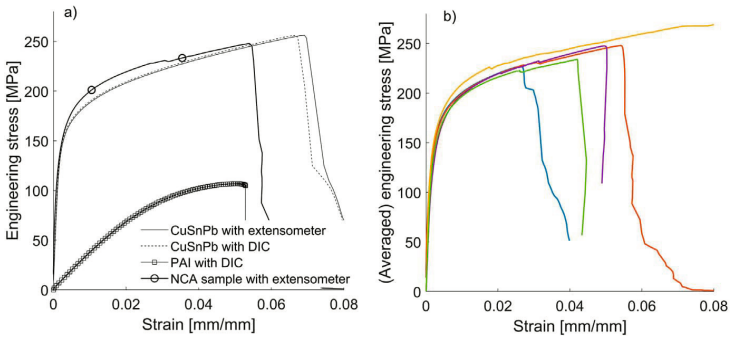

Fig. 3. (a) Typical engineering stress–strain curves of CuSn10Pb10 substrate, PAI coating and NCA specimen (substrate and coating); different measurement techniques applied for the axial strain as defined in the legend. (b) Experimental stress–strain plots of the NCA tests (coated specimens).

Table 1
Fitted parameters and material constants of the coating and the substrate in FE models.

Material	E [GPa]	ν [–]	A [MPa]	B [MPa]	n [–]
PAI	3.7	0.38	67.1	292.4	0.56
CuSn10Pb10	84.5	0.35	106.0	462.6	0.36

CZM model, in contrast). For that reason, the typical element dimension in the VCCT crack model was 0.25 mm whereas in the CZM model the substrate and coating were meshed with 0.5 mm elements. The coating's thickness was less than the applied element dimension. For that reason, the element thickness in the coating was equal to the coating thickness. In addition to the substrate and coating, in the CZM, separate cohesive elements (COH3D8) with the typical dimension of 0.25 mm were attached to the interface. The CZM mesh is illustrated in Fig. 2.

Boundary conditions were attached to both ends of the model. The substrate longitudinal displacement was restricted at the specimen middle for taking account the applied symmetry. The displacements in the lateral direction were restricted at the mid line symmetry plane for this case of symmetry. In the quarter model, the symmetry boundary conditions were set to the entire symmetry plane at the middle (in lateral direction). The CZM model included both residual (thermal) and mechanical loads, which were taken into account in separate computation steps. The first step presented the fabrication based residual (thermal) load where the temperature change of −185 °C degrees was placed on both substrate and coating. The temperature change of −185 °C represented the cooling from the curing of the specimen at 210 °C to room temperature (25 °C). The mechanical loading was then performed using the enforced displacement of 2.5 mm in the specimen loading direction. The displacements in the thickness direction were restricted at this end (simulating the test machine gripping) during the mechanical loading. The rigid body motion during the residual step was limited to only one nodal point in the thickness direction. The VCCT crack model was analysed, as well, for pure mechanical load and including residual (thermal) loading. The residual loading was performed similar to the CZM model. The mechanical loading was based on the experimentally determined critical strain which was converted into a displacement for the VCCT crack model. The VCCT analysis was studied for using elastic material models, whereas CZM analysis was done using both elastic and elastic–plastic material models.

All the models had an initial crack length of 0.5 mm based on the experiments. The VCCT crack model was computed for analysing ERR distributions at the crack onset phase, excluding crack propagation. By definition, VCCT is a fracture mechanics method, which estimates the ERR at the crack tip. The ERR can be extracted from the equation: ERR $= F\delta u/2B\,\delta a$. Here, F is the reaction force, δu is the separation, B and δa are the element width and length, respectively. The ERR evaluation is performed separately for three fracture modes. VCCT assumes linear elastic material behaviour, thus cases including plasticity are not according to the theory.

Material non-linearity was included in the CZM computations. In the first computation ($CZM_{plastic/plastic}$), both bulk material's plasticity were modelled using the Johnson–Cook model. For the second CZM computation ($CZM_{elastic/elastic}$), both bulk materials remained linear elastic (without the Johnson–Cook formulation). The CZM is based on a traction–separation law, which defines the debond damage onset and degradation until full debond. The cohesive stiffness was set to 10^{15} N/m^3 for all three fracture modes. The value fits in the middle

of the range provided by Zou et al. [26]. The debond damage onset was defined using the quadratic stress criterion of the following form:

$$\left(\frac{\sigma_I}{\sigma_{IC}}\right)^2 + \left(\frac{\tau_{II}}{\tau_{IIC}}\right)^2 + \left(\frac{\tau_{III}}{\tau_{IIIC}}\right)^2 = 1 \quad (4)$$

where σ_I, τ_{II} and τ_{III} are the momentary tractions whereas σ_{IC}, τ_{IIC} and τ_{IIIC} represent the critical cohesive strengths of the interface. We assumed equal value for all critical cohesive strengths ($\sigma_{IC} = \tau_{IIC} = \tau_{IIIC}$). After the debond damage onsets, the CZM elements start to degrade. The degradation was defined by using a bi-linear traction–separation law. The fracture mode coupling was defined by the law:

$$f_{CZM} = \frac{G_I + G_{II} + G_{III}}{G_c} \quad (5)$$

where G_c is the total critical ERR. The critical cohesive strengths and total critical ERR were fitted based on the experimental debond onset and propagation. The critical cohesive stresses mainly define the crack onset and it was fitted using the critical strain. The total critical level of ERR defined mainly crack propagation and it was fitted based on the slope of the crack length versus strain data of experiments. The fitting was performed using the CZM model with the elastic–plastic material models. For comparison, the similar parameters were also used in the CZM model with the elastic material models. As the name implies, CZM is not a crack model but homogenization method and its parameters are always dependent on the selected modelling resolution (mesh & details).

3. Results

3.1. Characterization of materials

The representative engineering stress–strain curves for the CuSn10Pb10 substrate, the PAI coating film and the NCA specimen are shown in Fig. 3a. The nominal thicknesses of the CuSn10Pb10 specimens and PAI films were 1.3 mm and 0.075 mm, respectively. No significant differences were observed when the extensometer and DIC-based strains were compared simultaneously from the same specimen. Based on the axial strains, measured either with a clip-on extensometer (CuSn10Pb10) or with the 3D-DIC method (PAI), the Young's modulus (secant modulus) and Poisson's ratios were determined for the material constituents as given in Table 1.

3.2. NCA test results

The stress–strain plots for the NCA tests are depicted in Fig. 3b. The axial (global) strain was measured with the clip-on extensometer and the whole specimen's cross section (substrate + coating) was used to calculate the averaged specimen stress. The test specimens were loaded until substrate fracture. In the stress–strain curves, small kinks can be seen, which have been reported to be linked to the sudden debond effects of the coating during tests [27]. In the derivative curves, the original weak kinks are visible as local well-distinguishable peaks, as seen in Fig. 4.

The axial strain of the specimen was determined also with the DIC locally from the coating surface. Until the coating debond, the strain all over the coating follows the global specimen strain. When the coating is debonded from the substrate, locally the strain in the coating is released and decreases toward zero. A code was developed to record the area of the deformed specimen (in pixels) experiencing the practical zero-strain limit (here $\varepsilon < 0.005$ mm/mm). The code was then run for the whole DIC dataset of the NCA test (recorded images). These regions (in pixels) were defined as debonded and were graphically denoted by (black) colour (Fig. 5). Furthermore, due to the applied axial loading and crack propagation direction overall, the total normalized debond length can be determined by dividing the debonded area by specimen width. This total debond length divided into half (to get the debond length from the pre-crack) is defined as the half crack length in the following.

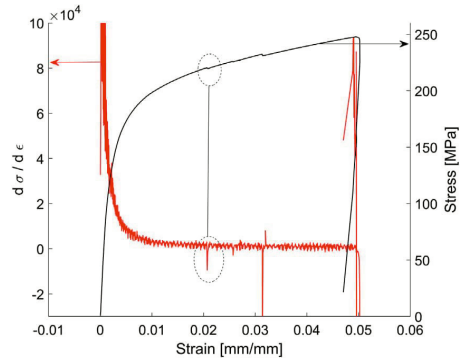

Fig. 4. Experimental strain derivative (of stress, σ) for detecting discontinuities in the stress–strain behaviour of NCA specimens.

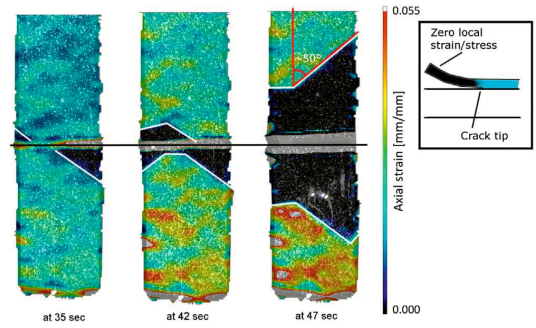

Fig. 5. The experimental progress of coating debond during an NCA test as quantitatively defined using the 3D DIC. The debonded areas of the coating, where the axial strain drops to zero (here ε <0.005), are illustrated in black colour.

Table 2
The experimental coating thickness, axial strain values at the detected discontinuities in the stress data with the corresponding half crack length measured with the DIC method, and the critical elastic strain of the debond onset.

Specimen	Coating thickness	ε at 1st peak	ε at 2nd peak	ε at 3rd peak	Half crack length at 1st peak	Critical elastic strain, $\varepsilon_{crit.el}$
NCA1	70 μm	0.027			2.5 mm	0.022
NCA3	72 μm	0.027	0.031	0.038	1.8 mm	0.024
NCA4	88 μm	0.018	0.023	0.033	4.5 mm	0.024
NCA5	74 μm	0.021	0.026	0.032	0.7 mm	0.020
NCA6	78 μm	0.026			2.3 mm	0.023

The extensometer based strain values corresponding to the peaks in the strain derivative are presented in Table 2. In addition, it shows the half crack lengths of the coatings determined with the DIC method which correspond the first detected strain derivative stress peaks.

3.3. Preliminary FE simulations

The VCCT method with elastic material models was used to study the total ERR (sum of three modes) at the debond onset. An example of the ERR distribution across the specimen width provided by the VCCT model is shown in Fig. 6a. The total ERR distribution shape shows a typical shape where the highest ERR values occur at the edges of the specimen and in the middle the value remains constant.

The ERR at the middle point of the specimen was used to define the representative G_c with the VCCT method. The comparison between the experimental load–strain data and simulated behaviour using CZM and plastic material models (Johnson–Cook) is shown in Fig. 6b. The FE simulation matches well with the experiments in terms of the stress–strain behaviour.

4. Analysis

4.1. New method to determine the critical elastic strain

Instantaneous crack length curves were determined based on the debonded coating areas using the DIC data. Fig. 7 shows the determined half crack length as a function of the global extensometer strain (for a median specimen, as example). Here, the term half crack length is used to define the distance of the debonded coating section from the pre-crack. The curve shows typical observed behaviour for the studied specimens, where, first, the debond propagates several millimetres by small random steps ('stick–slip' phase) after which the crack propagation rate increases suddenly and larger portion of the coating debonds. The first crack propagation steps do not represent the critical strain which would cause the steady-state coating debond in the current material system. Screening was carried out to define a common half crack length at which the debond initiation ('stick slip') phase was over and the debond continued to propagate with high rate. The half crack length of 8 mm was finally defined to present the length, at which in each tested specimens the debond initiation phase was over and the propagation occurred at the 'steady-state' phase. The global critical specimen (extensometer) strain to represent the debond onset was then determined from the combined debond length and global strain data.

In Eq. (1), the critical (onset) ERR (G) is calculated based on the critical strain at the debond onset. Depending greatly on the test specimen materials, the debond may occur at the strain range where the fraction of the plastic deformation in the total strain of the (polymer) coating is already significant. To take this into account, a nonlinear stress–strain dependency of the coating was derived, as used by Nichols et al. [17]. Here, the total strain of the coating is divided into elastic and plastic strain components using a fictitious unloading curve for the loaded coating. Fig. 8 depicts the presentation of the method and the continuous strain component division as a function of the total strain (in the coating). The determined critical elastic strain values ($\varepsilon_{crit,el}$) derived with the method are presented in Table 2.

4.2. Critical energy release rates: comparisons

The G_c values were analytically calculated using Eqs. (1) and (2), in which both the mechanically induced strain and fabrication-based (thermal) residual strains (ε_0, in Eq. (6)) are taken into account. For a thick rigid substrate with thin coating, ε_0 can be estimated using simply the thermal expansion mismatch (i.e. film's thermal stresses do not affect substrate deformation):

$$\varepsilon_0 = \varepsilon_s - \varepsilon_c = (\alpha_s - \alpha_c)\Delta T \tag{6}$$

where subscripts c and s denote coating and substrate materials, respectively, and ΔT is the temperature difference between the highest curing temperature and the room temperature. The α_s value was measured for CuSn10Pb10 (19×10^{-6} °C^{-1}) using a dilatometer (DIL402, Netzsch) and a value of 35×10^{-6} °C^{-1} [28] was used for α_c. Finally, when ΔT = −185 °C, a residual strain of 0.3% was obtained. It should be noted that the shrinkage due to the evaporated solvent was excluded here.

The calculated ('average') G_c values using Eqs. (1) and (2) are presented in Table 3. If the plasticity of the coating is excluded in the result analysis, the calculated G_c is significantly overestimated. The steady-state analytic solution including residual strains matches well the FEM results. However, if residual strains are excluded, the steady-state solution overestimates the critical ERR compared to the FEM result. This indicates that the lateral constraint at the debond tip region should be taken into account in this case. Overall, the comparison confirms that the analytic solution when residual strains are taken into account can be used, especially, to obtain a simple comparative measure for evaluating materials.

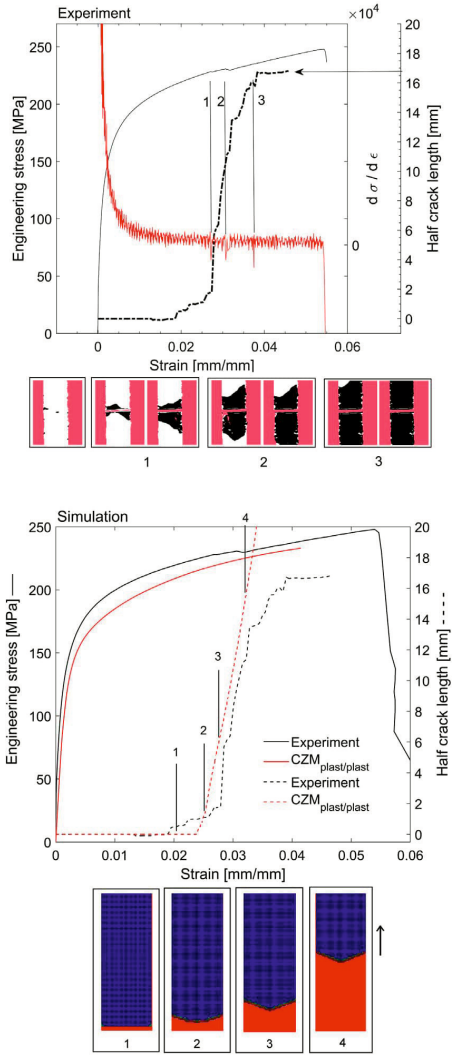

Fig. 7. The experimental and FEM simulated propagation and quantitative instantaneous crack length determined with DIC and according to the $CZM_{plast/plast}$ model.

4.3. Numerical prediction of debond propagation

Fig. 7 depicts an experimental stress–strain curve and its strain derivative, where the peaks originate from the sudden progressions of the debond. However, the experimental results showed that only the most abrupt debond progression steps caused an observable peak in the stress–strain curves whereas, often, the visual debond progression steps caused no detectable signals in the stress–strain data. By plotting

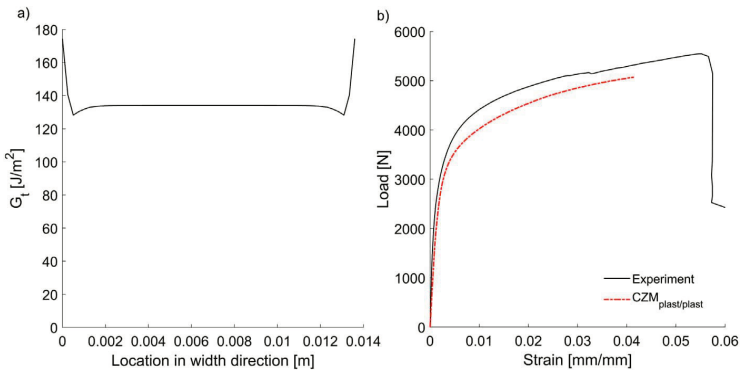

Fig. 6. (a) The FEM local ERR along the specimen width at the crack onset strain of a representative NCA test. (b) Representative experimental and FEM simulated load–strain curves using the CZM with plastic material models for both substrate and coating.

Table 3
Comparison of the determined (critical) ERR values by different methods of critical strain and constraint for a specimen with average properties.

Method	G_c [J/m^2]		G_c [J/m^2]	
	$\epsilon_0 = 0.003$ (residual strain)	Error to 3D FEM [%]	$\epsilon_0 = 0$	Error to 3D FEM [%]
Eq. (1) G_{ss}	95.0* (134.5**)	−1.7* (+0.3**)	71.8* (107.1**)	+12.5* (+13.0**)
Eq. (2) G_{Ic}	90.6* (126.6**)	−6.2* (−5.6**)	61.4* (91.6**)	−3.8* (−3.4**)
3D FEM (VCTT)	96.6* (134.1**)		63.8* (94.8**)	

The values analysed using * the elastic critical strain (i.e. $\epsilon_{crit,el}$) or ** the total critical strain (i.e. ϵ).

the curves together with the half-crack length curve determined from the DIC data, it is seen that the debond has actually already begun to proceed before any effects can be detected from the stress–strain results (by the extensometer). For the case material and fracture toughness of the interface, the debond first occurs at the edges (corners), as can be predicted based on the ERR distribution by the FEM (VCCT).

The fracture parameters of the CZM in FEM simulations can be fitted to produce similar crack propagation to experiments, i.e. showing similar initial onset, stable stress and half crack length slopes. The experimental results in average showed the typical V-shaped debond progression pattern at approximately 50° angle to the loading direction. Here, this accuracy of crack propagation prediction was targeted. Both cohesive strengths (Eq. (4)) and total critical ERR (Eq. (5)) were used for fitting the CZM with plastic material models. The best fit was obtained using 50 J/m^2 and 27.5 MPa as the total critical ERR (G_c) and cohesive strength ($\sigma_{IC} = \tau_{IIC} = \tau_{IIIC}$), respectively. It should be noted that the CZM values do not represent a sharp crack tip but a cohesive zone. As shown in Fig. 7, the correctly fitted CZM produces the targeted V-shape propagation pattern — agreeing with the experiments. The average half crack length in the FE model was defined as the average of crack length at the edge and central nodal lines so that the level of homogenization is comparable. The crack onset of the CZM model occurs slightly later than in the experiment. In the beginning (phase 2 in Fig. 7b), the V-shape debond pattern forms starting from the specimen edges and the slope of the simulated crack length-to-stress curve is nonlinear. Once the crack front has fully formed, the slope remains constant.

4.4. Coupling of plastic deformation and interface damage

The overall non-linearity of the test behaviour was studied using energy quantities provided by the CZM simulations and depicted in Fig. 9. Fig. 9 presents that the substrate becomes nonlinear at the early stage of a test (Knee 1), which was also seen in the experimental stress–strain graph (Fig. 3). Basically the non-linear behaviour of the substrate had no effect on the coating or interfacial energy accumulation. With the plastic material model for the coating, a weak knee (Knee 2) is observed at ≈ 0.012 mm/mm which corresponds exactly the behaviour seen in the curve for the division of the experimental strain into elastic and plastic components (Fig. 8b). Basically, only with the critical strains below this knee point, the linear elastic solutions utilizing the total (global) strain to evaluate G_c can be considered as valid means. The interfacial energy dissipation, i.e. debond process, starts at 0.024 mm/mm strain when the plastic material models are used. The characteristic V-shape debond shape forms as the strain increases and, at 0.026 mm/mm strain (Knee 3) is then fully developed finalizing the debond onset process. In the case of using only elastic material models, the onset of the interfacial energy dissipation occurs earlier in the test.

The coating debond patterns obtained experimentally using the DIC and numerically using the CZM$_{plast/plast}$ model are also shown in Fig. 9 at selected global strains. Basically, up to the onset of the interfacial energy dissipation curve, the debond does not proceed. Beyond that point, the debond initiates from the edges. The determined critical strain, to represent the debond onset in the method, bases on the predefined strain value determined from the experiments, where the debond begins to proceed in a 'steady-state' phase. Here, this was seen with a debond (or half-crack) length of 8 mm, which in the median specimen occurred at a global strain value of appr. 0.03. The results show that the interfacial energy dissipation curve has a rising trend at the defined strain value, and the simulated debond pattern shows a fully developed V-shape. The perfect V-shape is not observed in the experimental results, due to the inhomogeneities in the coating thickness and substrate microstructure.

5. Discussion

What is evident for the specific substrate material (CuSn10Pb10) is that it deforms very inhomogeneously under uniaxial loading. Fig. 10 shows the topographic image of the exposed bronze surface (interface)

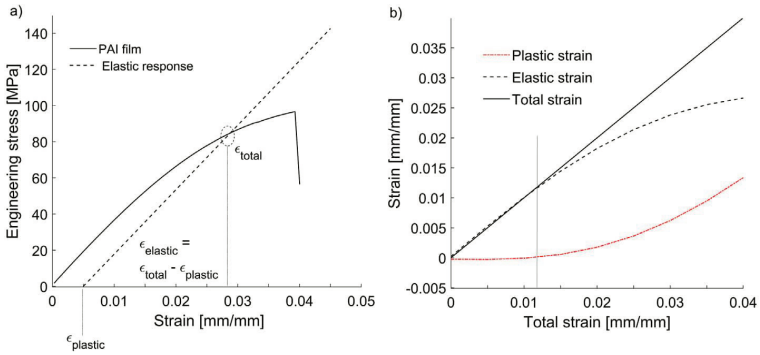

Fig. 8. (a) The engineering stress–strain curve of (separated) PAI film and presentation of the determination of the elastic strain. The slope of the dashed line equals E_{PAI}. Here, the total strain value (ϵ_{total}) is the global critical strain determined in an NCA test. (b) The division of the measured total strain into the elastic and plastic components.

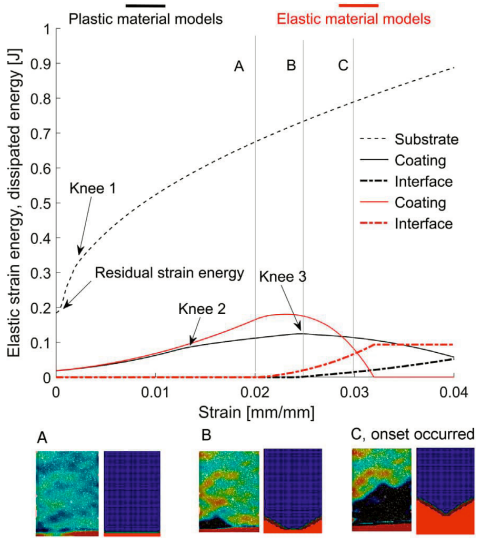

Fig. 9. The energy components from the $CZM_{plast/plast}$ and $CZM_{elast/elast}$ computations in a simulated NCA test. The debond patterns by DIC and $CZM_{plast/plast}$ methods are shown for the selected global strain values.

from the tested NCA specimen (after PAI coating debonded). The initially flat specimen surface shows, after the tensile test, significant local humps due to the inhomogeneous plastic deformation of the substrate. When comparing the final topography of the substrate surface with the full-field strain maps of the NCA specimen during testing, similarities can be observed. This is assumed to originate from the orientation differences of the large grains in the polycrystalline alloy. During deformation of such material, heterogeneous strain fields are developed that can result, for example, visible orange peel or ridging and roping phenomena at the material surface [29]. The changing topography affects the surface roughness of substrate which influences the intensity of the mechanical interlocking of the polymer to the substrate. The microstructure of the material plays an important role on the local mechanical properties (in millimetre scale) of the substrate and, thus also the local substrate strains can differ significantly from the global (average) strain. Furthermore, the polymer coating may possess more severe plastic deformation in the (more strained) discrete areas causing permanent changes in the material properties at the interphase. Overall, the heterogeneous mechanical behaviour at a small scale presumably has an effect on the location where the debond at the coating–substrate interface begins to propagate.

The determined critical strain from the experiments with the proposed method, hence, is a value of a homogenized debond model compared to the real strain at the interfacial crack tip against the alloy surface. The substrate inhomogeneity, as well as the variation in the coating thickness, affect the unsymmetrical crack propagation observed often in the experiments, and thus increases the small-scale scatter (below target accuracy level).

The determined G_c (Eq. (1)) for the studied material system showed a significant scatter: the mean and standard deviation of the experiments with series size of 5 are 96.4 J/m^2 and 17.9 J/m^2, respectively. Anticipated sources for scatter originated from both the thickness measurement of the coating and from the determination of the critical strain. To have a better understanding on their significance in the current system, we first set the critical strain to its average value, and vary only the coating thickness. The same range in G_c (using Eq. (1)) is then achieved with the thickness range of 0.063...0.090 mm (or −18%...+18%). Observable variation was found in the PAI coating thickness over the specimen—probably due to the manual solvent casting method (Table 2). The coating thickness has a linear influence on the calculated ERR which is seen as a significant error source to the experimental results in general. The error between the coating thickness used in the analysis and the real thickness at the crack tip is actually a combination of the variation in the coating thickness in the specimen (due to fabrication method) and the random measurement error of the thin coatings with a micrometre. When considering that the coating thickness is low as an absolute value, the relative error compared to the presumed uniform coating thickness can be significant. Thus, a consistent coating thickness in a specimen is a necessity for the NCA test method and care has to be taken on the precise thickness measurements (and thickness values applied in predictive simulations).

Another study of error was performed where all the error would arise due to the scatter in the determined critical strain, whereas the thickness is set constant (0.076 mm). In this case, the same G_c range is achieved with the critical (extensometer) strain range of 0.025..0.032 mm/mm (or −10%...+16%). Fig. 7 depicts the crack propagation behaviour for the median specimen. Here it is seen, that this strain range would equal the half crack length range of ≈ 1...12 mm. Generally, the instantaneous crack length determination method based on the DIC gives objective quantitative results. The slope of the crack length versus strain is steep (> 1500 mm/(mm/mm)) at the onset when the debond propagates its first greater step, i.e. when the debond initiation phase is over. Thus, at the moment when the predefined half-crack length (in this study 8 mm) is observed, the error on the critical strain (due

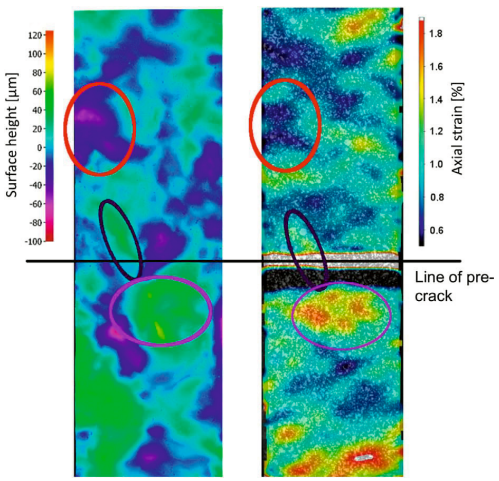

Fig. 10. A comparison of the substrate's surface topography (profilometry) of the CuSn10Pb10 substrate after an NCA test (left) and experimental (DIC) axial strain on the NCA specimen coating (right).

to measurement technique based factors) can be considered minor. However, when carrying out the analysis with the proposed method, the predefined half-crack length at which the critical strain is read has to be ensured to be located in the region where the unstable ('steady-state') debond propagation occurs. This can be done, for example, by plotting the half-crack length curves against strain for each specimen in the same figure. The common minimum half-crack length value can then be defined where all the specimens show similar behaviour with the steep crack length-to-strain slopes.

6. Conclusions

The specimen deformation in the NCA test was studied with the stereo-DIC technique. In experiments, the coating debond rarely behaves ideally challenging the quality of the test outcomes, i.e. statistics and representative values for FE models or other applications. To overcome this, a method based on the DIC was developed to determine quantitatively the instantaneous coating debond length. Furthermore, by combining the debond length data provided by DIC with the clip-on extensometer data, the representative objective critical strain value to correspond with the coating debond onset can be accurately defined.

During the benchmark experiments of this study, significant plastic behaviour occurred both in the substrate and in the coating. The determined critical strain in the polymer coating can be divided into elastic and plastic parts using the stress–strain data obtained for the separate coating film. The elastic critical strain together with the residual (thermal) strain is used as the strain measure to calculate the interfacial fracture toughness with the simplified analytic solution.

The analytic solution method provides an apparent G_c value, which can be used as the measure for comparative material studies. However, basically this applies only on the conditions when the specimen geometries are well reproducible and the critical strain causing the coating debond remains low. The NCA test is actually a 3D problem, which is not considered in the simplified analytic solutions (hand calculations). The 3D effects and plasticity of the materials can be taken into account with the systematic use of DIC and FEA in the execution of NCA testing. The improved methodology for 3D debond predictions is as follows:

- To define the material models, the stress–strain data has to be available for both the polymer coating and the substrate materials up to the strain levels where the coating's debond occurs in the NCA test.
- DIC is needed to provide the instantaneous debond length versus specimen strain curve, which is obtained by determining the debonded area of the coating during loading of the NCA specimen.
- The critical strain at the debond onset is determined from the debond length-to-strain curve at the point, where the debond initiation phase has ended and the high rate debond begins.
- The parameters of the CZM are fit for the improved NCA test so that (1) the simulated debond onset process will occur at the same strain values as resulted in the experiments and (2) the slope in the debond length versus strain curves (during debond propagation) matches between the FEA and DIC.
- As a benchmark case, a bi-material PAI/CuSn10Pb10 system was studied. The G_c at the debond onset was determined using the VCCT method with elastic material models and with the analytic solution. When the residual (thermal) strain was taken into account the methods resulted 96.6 J/m^2 and 95.0 J/m^2 for the median specimen using the VCCT method and the simplified solution, respectively.

CRediT authorship contribution statement

Olli Orell: Conceptualization, Methodology, Investigation, Writing – original draft. **Jarno Jokinen:** Formal analysis, Methodology, Writing – original draft. **Marke Kallio:** Resources, Project administration. **Mikko Kanerva:** Writing – review & editing, Supervision, Project administration.

Declaration of competing interest

The authors declare that they have no known competing financial interests or personal relationships that could have appeared to influence the work reported in this paper.

Data availability

The raw/processed data required to reproduce these findings cannot be shared at this time due to technical or time limitations.

Acknowledgements

The work was done as part of the FIMECC Hybrids research program supported by Tekes - Finnish Funding Agency for Technology and Innovation, Finland and SmartRail2 ecosystem's funding from Business Finland and the participating companies. The authors want to gratefully acknowledge CSC - IT Center for Science Ltd. for the computation services.

References

[1] D.M.C. McCarthy, S.B. Glavatskih, Assessment of polymer composites for hydrodynamic journal-bearing applications, Lubr. Sci. 21 (8) (2009) 331–341, http://dx.doi.org/10.1002/ls.92, arXiv:https://onlinelibrary.wiley.com/doi/pdf/10.1002/ls.92, URL https://onlinelibrary.wiley.com/doi/abs/10.1002/ls.92.

[2] G.F. Simmons, Journal Bearing Design, Lubrication and Operation for Enhanced Performance (Ph.D. thesis), Luleå University of Technology, Sweden, 2013.

[3] W. Grün, I. Gódor, W. Gärtner, W. Eichlseder, Tribological performance of thin overlays for journal bearings, Tribol. Int. 44 (2011) 1271–1280, http://dx.doi.org/10.1016/j.triboint.2010.10.027.

[4] D.W. Gebretsadik, Tribological Characteristics of Some Multi-layered Pb-free Engine Bearing Materials (Ph.D. thesis), Luleå University of Technology, Sweden, 2017.

[5] B. Fotovvati, N. Namdari, A. Dehghanghadikolaei, On coating techniques for surface protection: A review, J. Manuf. Mater. Process. 3 (1) (2019) 28, http://dx.doi.org/10.3390/jmmp3010028.

[6] G. de With, Polymer Coatings: A Guide to Chemistry, Characterization, and Selected Application (2018), Wiley-VCH, Weinheim, 2018.

[7] Z. Zhang, C. Breidt, L. Chang, K. Friedrich, Wear of PEEK composites related to their mechanical performances, Tribol. Int. 37 (3) (2004) 271–277, http://dx.doi.org/10.1016/j.triboint.2003.09.005.

[8] B.J. Briscoe, S.K. Sinha, Tribological applications of polymers and their composites : Past , present and future prospects, Tribol. Interface Eng. Ser. 55 (2008) 1–14, http://dx.doi.org/10.1016/S1572-3364(08)55001-4.

[9] E.R. Chandrathilaka, J.C. Gamage, S. Fawzia, Numerical modelling of bond shear stress slip behavior of CFRP/steel composites cured and tested at elevated temperature, Compos. Struct. 212 (2019) 1–10, http://dx.doi.org/10.1016/j.compstruct.2019.01.002.

[10] M. Heidari-Rarani, M. Sayedain, Finite element modeling strategies for 2D and 3D delamination propagation in composite DCB specimens using VCCT, CZM and XFEM approaches, Theor. Appl. Fract. Mech. 103 (2019) (2019) http://dx.doi.org/10.1016/j.tafmec.2019.102246.

[11] J. Chen, S.J. Bull, Approaches to investigate delamination and interfacial toughness in coated systems: An overview, J. Phys. D: Appl. Phys. 44 (3) (2011) http://dx.doi.org/10.1088/0022-3727/44/3/034001.

[12] Z. Chen, K. Zhou, X. Lu, Y.C. Lam, A review on the mechanical methods for evaluating coating adhesion, Acta Mech. 225 (2) (2014) 431–452, http://dx.doi.org/10.1007/s00707-013-0979-y.

[13] A.A. Volinsky, N.R. Moody, W.W. Gerberich, Interfacial toughness measurements for thin films on substrates, Acta Mater. 50 (3) (2002) 441–466, http://dx.doi.org/10.1016/S1359-6454(01)00354-8.

[14] D.A. Dillard, B. Chen, T.N. Chang, Y.H. Lai, Analysis of the notched coating adhesion test, J. Adhes. 69 (1–2) (1999) 99–120, http://dx.doi.org/10.1080/00218469908015921.

[15] R. Hayes, J. David, A study of critical strain and nanomechanical test methods as predictive tools for coating changes in weathering, Plast. Des. Libr. (2018) 263–281, http://dx.doi.org/10.1016/B978-0-323-49776-3.00015-5.

[16] R.K. Giunta, R.G. Kander, Accelerated aging of polyimide/titanium adhesive bonds using the notched coating adhesion test, Polym. Eng. Sci. 42 (8) (2002) 1789–1797, http://dx.doi.org/10.1002/pen.11070.

[17] M. Nichols, C. Darr, C. Smith, M. Thouless, E. Fischer, Fracture energy of automotive clearcoats – I. Experimental methods and mechanics, Polym. Degrad. Stab. 60 (97) (1998) 291–299, URL http://www.sciencedirect.com/science/article/pii/S0141391097000815.

[18] M. Kanerva, J. Jokinen, E. Sarlin, O. Saarela, Crack propagation under mode II dominance at stainless steel-epoxy interfaces with residual stresses and microscale roughness, Int. J. Solids Struct. 50 (20–21) (2013) 3399–3405, http://dx.doi.org/10.1016/j.ijsolstr.2013.06.008.

[19] W. Loh, A. Crocombe, M. Abdel Wahab, I. Ashcroft, Environmental degradation of the interfacial fracture energy in an adhesively bonded joint, Eng. Fract. Mech. 69 (18) (2002) 2113–2128, http://dx.doi.org/10.1016/S0013-7944(02)00004-8, URL http://linkinghub.elsevier.com/retrieve/pii/S0013794402000048.

[20] J. Elambasseril, R.N. Ibrahim, Validity requirements of circumferentially notched tensile specimens for the determination of the interfacial fracture toughness of coatings, Composites B 43 (5) (2012) 2415–2422, http://dx.doi.org/10.1016/j.compositesb.2011.11.038.

[21] M.A. Sutton, J.J. Orteu, H. Schreier, Image Correlation for Shape, Motion and Deformation Measurements, Springer US, 2021, http://dx.doi.org/10.1007/978-0-387-78747-3.

[22] F. Hild, S. Roux, Digital image correlation: From displacement measurement to identification of elastic properties — A review, Strain 42 (2006) 69–80.

[23] F. Hild, S. Roux, Comparison of local and global approaches to digital image correlation, Exp. Mech. 52 (2012) 1503–1519, http://dx.doi.org/10.1007/s11340-012-9603-7.

[24] B. Pan, K. Qian, H. Xie, A. Asundi, Two-dimensional digital image correlation for in-plane displacement and strain measurement: A review, Meas. Sci. Technol. 20 (6) (2009) 062001, http://dx.doi.org/10.1088/0957-0233/20/6/062001.

[25] Dassault systemes, 2017, Abaqus 2017 Documentation, User manual.

[26] Z. Zou, S.R. Reid, S. Li, P.D. Soden, Modelling interlaminar and intralaminar damage in filament-wound pipes under quasi-static indentation, J. Compos. Mater. 36 (4) (2002) 477–499, http://dx.doi.org/10.1177/0021998302036004539.

[27] M. Kanerva, E. Sarlin, O. Saarela, Variation in mode II dominated interface fracture of stainless steel-epoxy bonds. Part 1: Mechanical testing, Eng. Fract. Mech. 99 (2013) 147–158, http://dx.doi.org/10.1016/j.engfracmech.2012.12.002.

[28] Solvay, Solvay specialty polymers, Torlon PAI, design guide (2015), 2015, http://www.solvay.com.

[29] D. Raabe, M. Sachtleber, H. Weiland, G. Scheele, Z. Zhao, Grain-scale micromechanics of polycrystal surfaces during plastic straining, Acta Mater. 51 (6) (2003) 1539–1560, http://dx.doi.org/10.1016/S1359-6454(02)00557-8.

PUBLICATION IV

A concept for defining the mixed-mode behaviour of tough epoxy film adhesives by single specimen design

J. Jokinen, O. Orell, M. Wallin and M. Kanerva

Journal of Adhesion Science and Technology 34, 18 (2020) pp. 1982–1999
https://doi.org/10.1080/01694243.2020.1746606

This is an accepted manuscript version for an article.

A concept for defining the mixed-mode behaviour of tough epoxy film adhesives by single specimen design

Jokinen, J[a,1], Orell, O[a], Wallin, M[b], Kanerva, M[a]

[a]*Tampere University, Materials Science and Environmental Engineering, PO Box 589, FI-33101 Tampere, Finland*
[b]*Patria Aviation, Lentokonetehtaantie 3, FI-35600 Halli, Finland*

Abstract

Fracture modes I and II interact in mixed-mode loading conditions, and the interaction is typically taken into account using a mixed-mode fracture criterion. In this work, a concept for defining the criterion is developed through an experimental-numerical simulation analysis. The mixed-mode behaviour for the criterion is tested and analysed with a single specimen design. The design of the specimen simplifies the measurement when complex test arrangements and preparations for various specimen geometries are excluded in practice. Here, the mixed-mode fracture behaviour of the specimen is analysed in detail using digital image correlation (DIC). The DIC data is used in collaboration with a finite element–based crack onset analysis, including the virtual crack closure technique, in order to consider the typical simplifications and their effects on the mixed-mode criterion. As a benchmark case, the fracture criterion is determined for an epoxy film adhesive FM 300-2 using the developed approach. The developed approach was shown to be feasible and effective for defining the mixed-mode fracture criterion. The determined Power law criterion's exponents were below unity, which points out that the common (presumed) exponent values in the current literature are actually unconservative.

[1] Corresponding author.

Email address: Jarno.Jokinen@tuni.fi (Jokinen, J)

Keywords: adhesive, mixed-mode testing, epoxy, virtual crack closure technique, digital image correlation

1. Introduction

Adhesively bonded joints are typically designed to carry shear loads. This type of pure single-mode loading can be computationally analysed by comparing the energy release rate (ERR) – provided by the selected numerical analysis – to the critical ERR provided by the experiments. A pure single-mode loading is scarce in real applications, where joints will also meet peeling loads, e.g., loads that typically exist at the edges of the joints. The actual loading in the adhesive layer is a combination of both peeling and shearing loads. The interaction of mode I and II can cause failure to occur when total ERR is less than critical value of either modes [1]. Shearing and peeling fracture modes have an interaction which is taken into account by using an adjusted mixed-mode fracture criterion. Several mixed-mode fracture criteria have been developed [2, 3, 4]. One of the most typical fracture criteria is the power law. The power law is typically formulated using only two fracture modes (I and II). The power law is commonly implemented in the commercial finite element (FE) codes, such as Abaqus [5]. The power law criterion can be extracted in the following form:

$$\left(\frac{G_I}{G_{IC}}\right)^{\alpha} + \left(\frac{G_{II}}{G_{IIC}}\right)^{\beta} = 1 \qquad (1)$$

where G_I and G_{II} are the ERRs evaluated in the analysis of the joint and G_{IC} and G_{IIC} are critical ERRs determined for the adhesive (layer). The parameters α and β are the fitting parameters.

The mixed-mode criterion is an equation which is fitted based on experimental results. The experimental methods for describing pure single fracture modes (I and II) have been developed and are essentially standard. A test using a double cantilever beam (DCB) specimen is the standard test method for mode I testing [6]. The methods for mode II testing include end-notched flexure (ENF), an end-loaded split (ELS),tapered end notched flexure (TENF) and end loaded shear joint (ELSJ) [7]. Standardised methods do not exist for fracture mode III.

The determination of the criterion (fitting) parameters requires experiments describing the mixed-mode behaviour. The mixed-mode testing for composite delamination is typically performed using mixed-mode bending (MMB) apparatus [8]. The MMB apparatus allows changing the mixed-mode ratio between modes I and II. Currently, no mixed-mode standard exists for adhesive testing. Various mixed-mode test specimens have been used for adhesives in the current literature and they include: an asymmetric tapered DCB specimen [9], a fixed-ratio mixed mode (FRMM) specimen [10], a mixed-mode flexure (MMF) specimen [10], an Arcan-type specimen [11, 12] and a single leg bending (SLB) specimen [13]. The different mixed-mode specimens in a loaded condition are visualised in Fig. 1 for clarity.

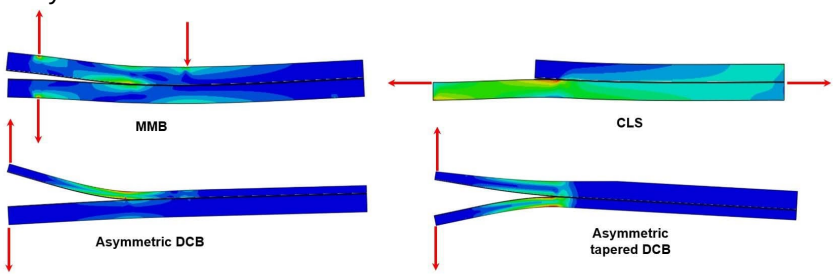

Figure 1: Different mixed-mode specimens in a typical loading condition. The colour range illustrates the estimative load intensity (von Mises).

In this work, a concept for defining the mixed-mode behaviour by using a single-specimen design, mainly based on SLB geometry, is developed. The test method is based on a simple three-point bending test setup, instead of using complex testing apparatus. The developed concept is applied for defining the mixed-mode fracture criterion for a structural, highly toughened epoxy film adhesive (FM 300-2 by Cytec). In addition to the mixed-mode testing, mode II (ENF) tests were performed for the selected adhesive. The mode I (DCB) results for the joints (FM 300-2) have been published in our previous work [14] and are the reference for the mode I results.

In addition, the mixed-mode deformation at the crack is studied in detail using the digital image correlation (DIC) method. The deformation is studied in terms of peel and shear strains. Strains are widely used for defining the sustainability limits of adhesive in the design of intact joints. The adhesive properties are typically defined under pure shear with a thick-adherend lap

shear (TALS) specimen. The target of applying the DIC was to verify the mixed-mode condition and provide an estimate for the maximum strains near the crack. The post-processing of test results via the ERR basis are performed with the virtual crack closure technique (VCCT), and a comparison of the adhesive behaviour amidst the crack tip is performed on a micro-meso length scale. The DIC results are compared with the numerical results for defining the representativeness of the DIC and the post-processing method.

2. Materials and methods

2.1. Materials and test specimens

ENF and SLB test specimens were prepared for the testing of this study. The materials of the specimens were identical for all of the specimen series. The specimen adherends were machined out from an aluminium alloy plate (Alumec 89, Uddeholm). The nominal thickness of the aluminium plate was 15 mm and 15.7 mm for ENF and SLB specimens respectively. The Young's modulus of 71 GPa and Poisson's ratio of 0.3 were used in all of the analyses for the aluminium. The epoxy film adhesive FM 300-2 (Cytec) was used in all of the specimens and the properties were estimated using the work carried out by Ishai et al. [15], who studied the adhesive FM 300 (Cytec). The values of 2.45 GPa and 0.38 were used for the Young's modulus and the Poisson's ratio respectively. Jokinen et al. [14] defined that the fracture toughness value of G_{Ic} = 1820 J/m^2 for the adhesive FM 300-2 should be used when determining the fracture criterion.

The dimensions of the test specimens are shown in Figs. 2–3. The average widths of the SLB and ENF specimens were 20.10 mm and 16.94 mm (measured) respectively. The average adhesive thickness of the ENF, SLBa and SLBb specimens were 0.71 mm, 0.40 mm and 0.67 mm respectively. Both specimens were fabricated using two adhesive plies, and the pre-existing crack was applied between the adhesive plies, as shown in Figs. 2–3. The adhesive thickness of the prepared SLBa specimens was determined to be lower than the other specimens. The manufacturing process was identical for all the specimens but the scatter in the processing devices and practical preparations resulted in 27 % deviation in the actual value of adhesive thickness (average SLBa thickness 0.4 mm and average SLB thickness 0.67 mm). The average pre-crack lengths of the ENF, SLBa and SLBb specimens were 107.88 mm, 24.63 mm and 29.48 mm respectively. The geometry for SLBa and SLBb specimens are the same, but the loading direction is opposite.

The pre-treatment of the adhesive bonding was performed using Sol-Gel handling [16], and finally, the adhesive was cured in an oven (120 °C) under a vacuum bag. The bonding was performed by joining larger plates, which were water-jet cut to the final specimen width after curing. Two identical test series of SLB specimens were formed, which are referred to as SLBa and SLBb later in this study.

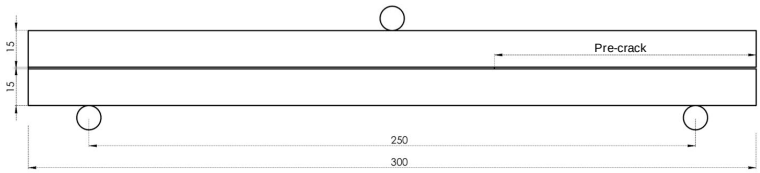

Figure 2: ENF specimen testing and the dimensions applied in this study.

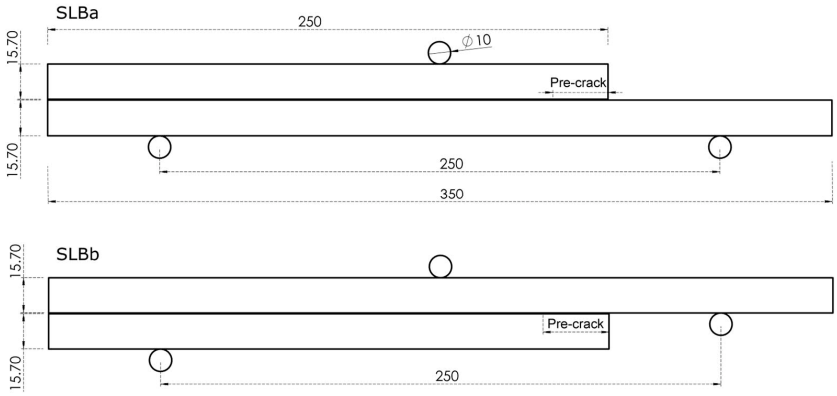

Figure 3: SLBa and SLBb specimen testing and the dimensions applied for the tests in this study.

2.2. Experimental testing

The ENF testing was performed using a universal testing machine (Dartec, 100 kN) with the three-point bending setup. The displacement in the specimen middle point was measured using an auxiliary displacement transducer (WA-T 20 mm, HBM). The SLB tests were performed with a

universal testing machine (5967, Instron, 30 kN). The tests of SLBa and SLBb were carried out with the three-point bending jig with the support and loading cylinders having a diameter of 10 mm. For the SLBb test, the support jig was modified for maintaining the horizontal orientation of the specimen. The difference between the tests are shown in Fig. 3. The crosshead displacement rate was 2 mm/min and the test programme for the SLBa and SLBb tests consisted of a constant loading and unloading steps corresponding to 4 mm and 3 mm midpoint deflection respectively. The load and the crosshead displacement data were collected with the integrated software (BlueHill 3, Instron). The strain at the bottom surface of the SLB specimen (below the loading cylinder) was measured using a foil strain gauge (5 mm gage length by Kyowa [Japan]) connected to Labview SignalExpress software (National Instruments). The SLBa test arrangement is presented in Fig. 4.

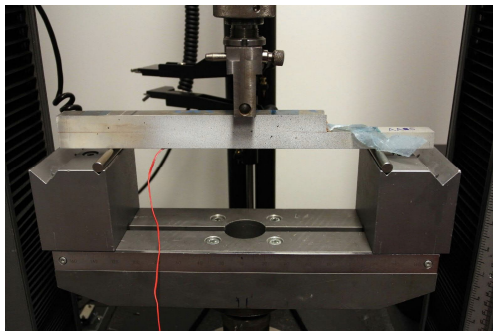

Figure 4: The SLBa testing set-up including the three point bend pins and a specimen with a strain gauge. The specimen is also provided with a speckle pattern for DIC.

2.3. DIC and the determination of adhesive deformations

In a typical DIC technique, the studied surface is divided into small facets (i.e. subsets) whose movements are then tracked from image to image. A subset needs to have enough unique features to be distinguished from other subsets, which is normally accomplished by applying some random speckle pattern on the surface. The precision and spatial resolution of the DIC analysis largely depend on the used subset and step sizes. The position of the centre point of each subset can be determined, and the density of the computed points is controlled by the step size. Finally, a full displacement

field can be determined, from which further strain fields can be calculated. [17]

In heterogeneous structures, such as the ones consisting of materials with very different mechanical properties, high spatial resolution is often needed in order to be able to measure the deformation gradients accurately. In many cases, by decreasing the subset size, the spatial resolution can be increased but, simultaneously, the precision of the quantity of interest (e.g. the displacement or strain) will decrease and vice versa. The maximum spatial gradient that the DIC system can resolve depends on, amongst other things, the image scale offered by the test set-up (or the final pixel-to-mm ratio), the speckle size of the used pattern, and the subset and step sizes when carrying out the analysis. [18, 19]

Here, the three-dimensional DIC technique was used to determine the full-field displacements and strains during the SLB tests. The system consisted of two 5 Mpix cameras (Imager E-Lite, LaVision), with the objectives having the focal length of 50 mm, and synchronized LED flashes, controlled with Davis 8.4 software (LaVision). The recording rate was 2 Hz. The scale factor with the used test configurations ranged between 22–25 pix/mm. The correlation analysis was performed using subset and step sizes of 25 pix and 7 pix respectively. The subset in the performed analysis corresponded approximately a 1 mm x 1 mm square in the test coordination, resulting in the applied DIC setup not directly offering a spatial resolution that was high enough for the detailed quantitative analysis of the deformations measured in the thin adhesive layer (t<0.7 mm) of the specimens.

However to overcome this, the shear and opening deformations of the bond line were determined with the following approach. It is assumed that the adherend behaviour is purely elastic during the given loading (Section 2.2), where the normals of the neutral axis of the specimen remain normals in the deformed state. First, the displacement vectors at the adherends of the loaded specimen are determined along the length of the sample (in the x-direction) at three different distances (here 1, 2 and 10 mm) from the midline of the adhesive layer. The constant n presents the ordinal of the exported DIC displacement vectors where n = 1 equals the location at the pre-crack. A line is fitted using these three points by the least squares method for each x-coordinate location (n). The fitted lines p_n and p_n' are presented in Fig. 5, where the points $\boldsymbol{A_n}$-$\boldsymbol{C_n}$ are the points in the undeformed upper adherend at

the n^{th} location, and the points $\boldsymbol{A'_n}$ - $\boldsymbol{C'_n}$ are then the same points in the deformed state.

When the location of the adhesive mid-line is known in the x-y plane (the origin at the pre-crack observed in the DIC images), the length of the vector $\boldsymbol{O_n}$ can be expressed as

$$\|\boldsymbol{O_n}\| = \|\boldsymbol{P_n}\| = L_0 \tag{2}$$

During the loading of the specimen, the compressive and shear strains in the metal adherend, near the epoxy adhesive, remain small and it is assumed that L_0 remains constant throughout the test. In the deformed state, the location of the point $\boldsymbol{Q'_n}$ is then given as:

$$\boldsymbol{Q'_n} = \boldsymbol{C'_n} + \boldsymbol{P_n} \tag{3}$$

where vector $\boldsymbol{P_n}$ is parallel to line p'_n.

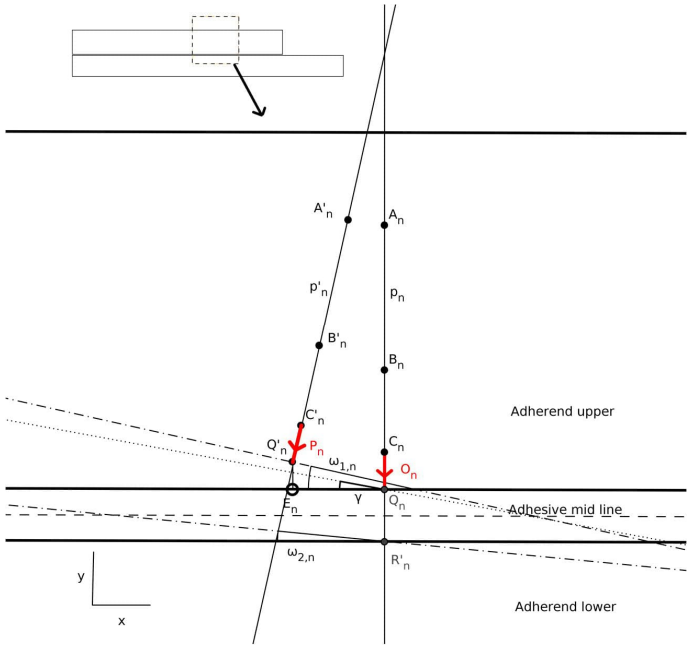

Figure 5: An illustration of a deformed specimen and the control/reference points used in the DIC data analysis.

A similar procedure is then performed for the lower adherend to determine $\boldsymbol{R'_n}$ or the location of the contact point between the lower adherend and the adhesive. Finally, the deformed adherend–adhesive contact points are obtained throughout the region of interest along the x-axis for each n.

During loading, the adherends rotate to angles $\omega_{1,n}$ and $\omega_{2,n}$ Thus, for a thin adhesive layer its mid-line rotation can be defined with:

$$\alpha = (\omega_{1,n} + \omega_{2,n})/2. \tag{4}$$

Taking the rigid body rotations into account, as described in detail by Hogberg et al. [20], we can determine the shear (v) and opening (w) deformations of the adhesive bond line in a (x,y) coordinate system with the known rotation:

$$v = v_0 \cos\alpha + (w_0 + t)\sin\alpha\,, \tag{5}$$

$$w = (w_0 + t)\cos\alpha - v_0 \sin\alpha - t \tag{6}$$

where $v_0 = \|\boldsymbol{E_n Q_n}\|$, $w_0 = \|\boldsymbol{Q'_n E_n}\|$ and $t = \|\boldsymbol{Q_n R'_n}\|$.

Finally, the engineering shear strain (γ_{xy}) and opening (ε_{yy}) strains over the whole adhesive bond line and from each DIC image are calculated as follows:

$$\gamma_{xy} = v/t \tag{7}$$

and

$$\varepsilon_{yy} = w/t \tag{8}$$

2.4. FE analysis and VCCT

FE models representing SLBa, SLBb and ENF specimens were created using Abaqus/Standard 2017 (Dassault Systemes). The adhesive layers were included in addition to the aluminium adherends of the specimens. Adhesive and adherend parts were joined using the tie constraint. This allowed the usage of dissimilar meshes between the adhesive and the adherend. The applied FE models were modelled using 3D solid elements. The elements were C3D8R and C3D8I for the adherend and adhesive parts respectively. The typical element dimension in the adherend and adhesive parts were 2.5 mm and 0.35 mm respectively. Typical element size was constant throughout the adhesive and adherend and no mesh grading was applied. ENF and SLBa element meshes are shown in Fig. 6. The SLBb mesh was practically similar

than SLBa excluding difference in adhesive element thickness. The VCCT was used for analysing the ERR in all of the tested specimens. The VCCT was originally developed by Kanninen and Rybicki [21] and is based on Irwin's crack closure integral. The VCCT has been used in the analysis of various bonded joints [22, 23, 24]. The VCCT evaluates the momentary ERR using the reaction force at the crack tip and the separation of displacements next to the crack tip. The ERR for mode II can be extracted from the equation:

$$G_{II} = \frac{F\delta u}{2B\delta a}, \tag{9}$$

where F is the (nodal) reaction force, δu is the separation, and B and δa are the width and the element length respectively. The VCCT evaluates other fracture modes in a similar way. The interface required by the VCCT was modelled at the midline of the adhesive part, which also equals the 'cohesive' debond surface (which is between two adhesive film plies in reality).

Boundary conditions of ENF and SLBa are presented in Figure 6. All three models had boundary conditions in two locations. These locations presented supporting boundary conditions at the specimen bottom (Figs. 2 and 3). The boundary conditions were defined using partition lines for the whole width of the model. The boundary condition (the precrack side) allowed the translation in the longitudinal direction of the specimen while others were restricted. Another supporting boundary condition had all translations restricted. The loading was attached to the nodal line at the longitudinal middle of the specimen to the opposite side the boundary conditions. The loading presenting the experimental average force was divided into nodal points using the concentrated force in the FE analysis.

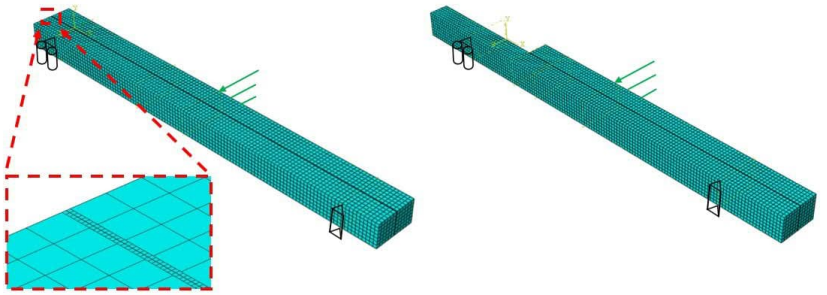

Figure 6: ENF and SLBa specimen models with the applied FE mesh and boundary conditions.

3. Results

3.1. Fracture test results

The post-test fracture surfaces for the SLBa and SLBb specimens are shown in Fig. 7. The fracture type in all the specimens was cohesive. The force-displacement curves of the ENF, SLBa and SLBb experiments are shown in Figs. 8, 9 and 10. The curves show a common trend. The curves first reach a peak value, which is followed by a force drop caused by the crack onset and propagation. The force growth continues soon after the drop. The unloading curve of one specimen in the SLBa testing and for all of the ENF specimens was not recorded.

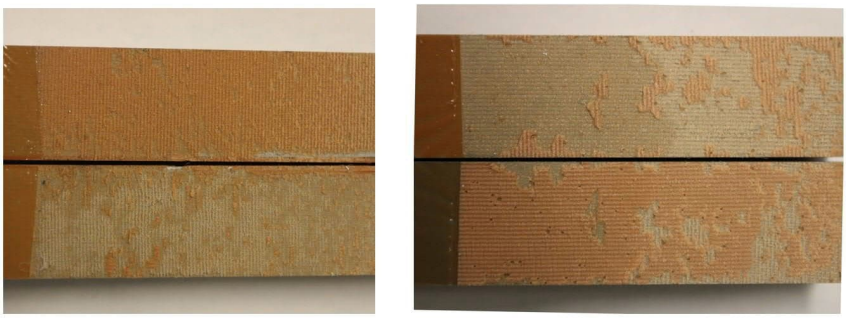

Figure 7: Fracture surface fractography of SLBa (left) and SLBb (right) specimens after testing.

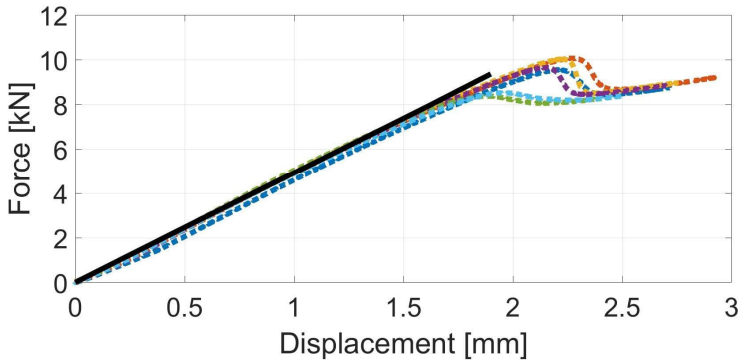

Figure 8: ENF force-displacement curves, based on the experimental tests (the dotted line) and FE analysis (the solid line).

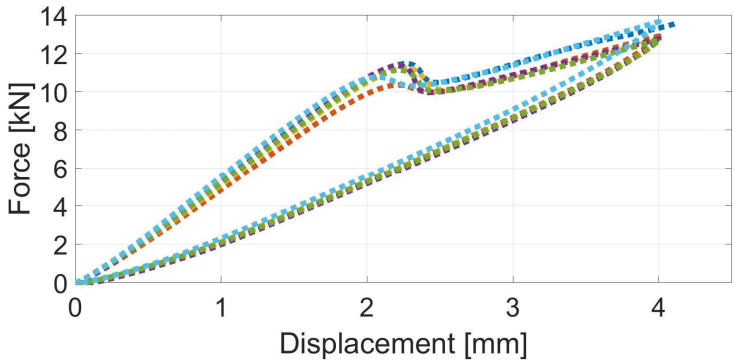

Figure 9: The SLBa force-displacement curves from the experimental tests.

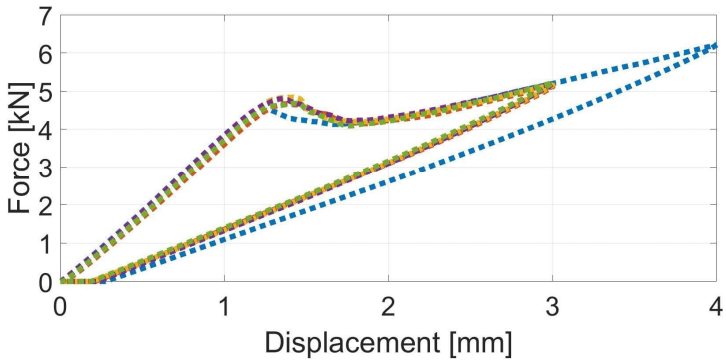

Figure 10: SLBb force-displacement curves from the experimental tests.

A strain gauge was located in the middle point in the tension side of the SLBa and SLBb specimens. The SLBa and SLBb related force-strain curves are shown in Figs. 11 and 12. The specimen 2 strain gauge was observed to have broken and the strain could not be read (SLBa testing). All the curves remain essentially linear up to the peak load.

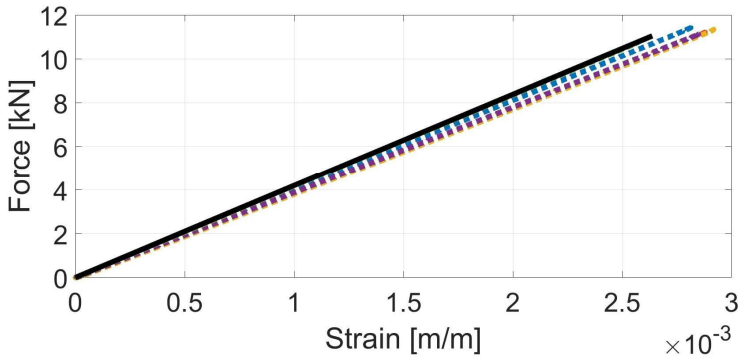

Figure 11: SLBa experimental force-strain curves (the dotted line) and FE analysis maxima (the solid line).

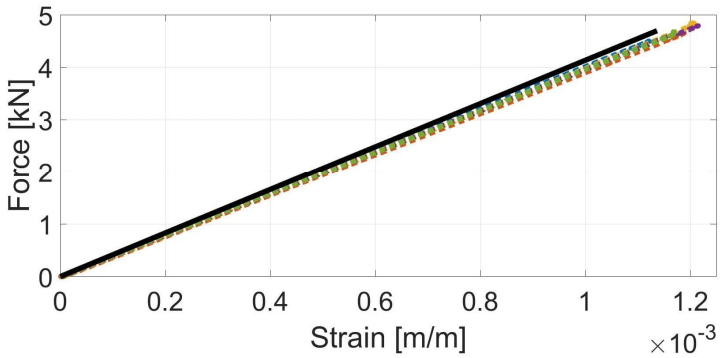

Figure 12: SLBb experimental force-strain curves (the dotted line) and FE analysis force-strain curves (the solid line).

The average experimental peak load before the drop applied in the FE analysis are presented in Table 1. These force values were used in the ERR analysis per each test. The response of the FE analysis model was compared to the experimental force-displacement curves of the ENF testing and the force-strain curves of the SLBa and SLBb experiments. These VCCT results are shown in Figs. 8, 11 and 12. The comparison between the FE and experimental curves shows a good correlation in terms of the specimen

stiffness. The FE provides slightly stiffer behaviour than the experimental curves due to the negligible non-linearities during the experiments.

Table 1: The average experimental peak load applied in the FE analysis per test series.

	SLBa	SLBb	ENF
Peak load before the drop [N]	11,045 ± 419	4,696 ± 134	9,362 ± 739

3.2. Mixed-mode specimens DIC analysis

Figs. 13a and 13b show the full-field strain maps of the vertical strains (ε_{yy}) (opening or compressive) and Figs. 14a and 14b show the shear strains (ε_{xy}) for typical SLBa and SLBb specimens right before the initiation of the crack propagation. In the SLBa test, a small compressive strain is generated at the tip of the upper adherend specimen due to the slightly different curvatures of the adherends around the pre-crack area (when the specimen was loaded). The upper adherend's free end thus acts as a local constraint during bending, also causing slight opening-type (mode I) deformation in the crack-tip locus in addition to dominant mode II loading in the SLBa. In the SLBb tests, the strain distributions are more symmetrical, as seen in Figs. 13b and 14b.

a)

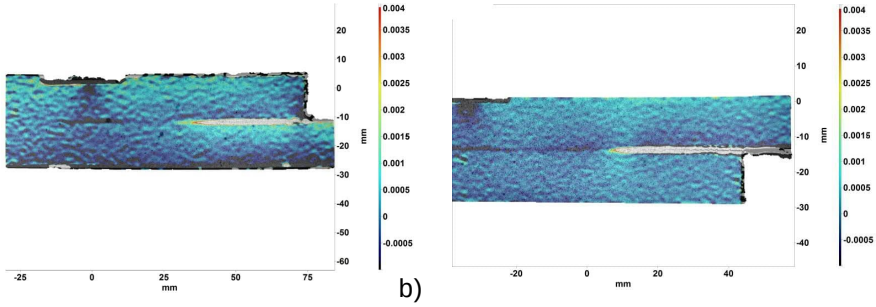

b)

Figure 13: The strain (ε_{yy}) on (a) an SLBa specimen at 57 s (10.4 kN) and (b) an SLBb specimen at 35 s (4.2 kN).

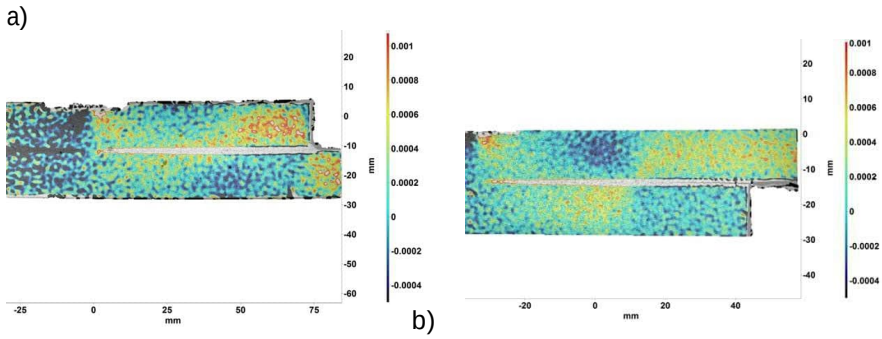

Figure 14: The strain (ε_{xy}) on (a) an SLBa specimen at 57 s (10.4 kN) and (b) an SLBb specimen at 35 s (4.2 kN).

The shear and opening deformations of the selected median specimens, calculated by Eqs. 5 and 6, are presented at the time of the crack propagation onset along the adhesive layer in Fig. 15. Although, in the SLBa-type test, there is a significant amount of opening deformation, the shear deformation is the dominating deformation mode throughout the bond line. In the SLBb-type test, it is seen that, near the crack tip (< 5 mm), the opening deformation exceeds the shear deformation. It is also seen that, in this test type, the opening of the adhesive bond changes into a small compressive deformation at an approximately 11 mm distance from the crack tip.

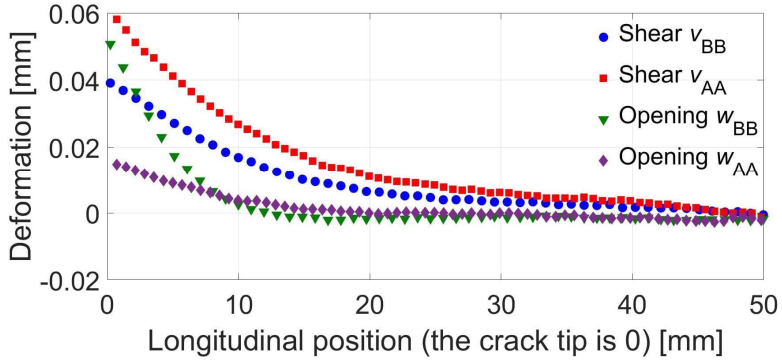

Figure 15: Experimental shear and opening deformations in the adhesive layer in the SLBa and SLBb specimens.

The resolved shear and opening strains determined with Eqs. 8 are shown in Figs. 16 and 17. The figures also include the strains provided by the FE analysis, which are needed for an accurate ERR determination. The comparison of the DIC- and FE-based shear strains of the adhesive shows good correlation. However, the comparison of the opening strain indicates significant difference between the two methods. The DIC provided greater values when compared to the FE analysis. The fracture surface revealed that the release film used to prepare the pre-crack (thickness: 20 µm) had wrinkled during the specimen manufacturing. An optical profilometer image of an SLBa specimen (Fig. 18) shows the waviness of the pre-crack area to have a peak-to-peak amplitude of approximately 100 µm. The small scale sliding of the adherends free ends during bending with the observed wavy surface topography causes some local constraint for the system. This, at least partly, can explain the difference between the experiments and the simulation because in FE the pre-crack surfaces are assumed to be smooth and sliding relative to each other without any surface asperities hindering the process.

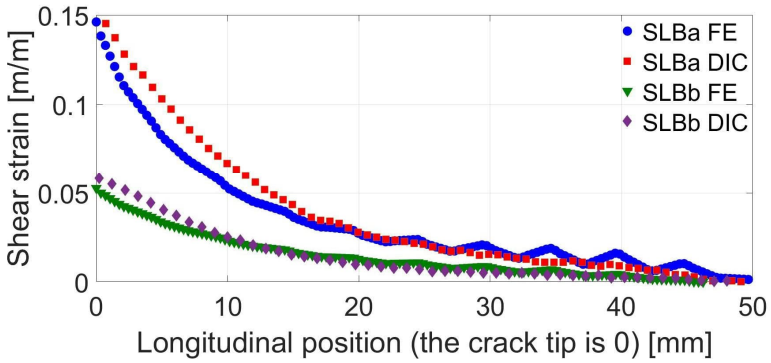

Figure 16: Shear strain in the adhesive layer in the SLBa and SLBb specimens at crack onset.

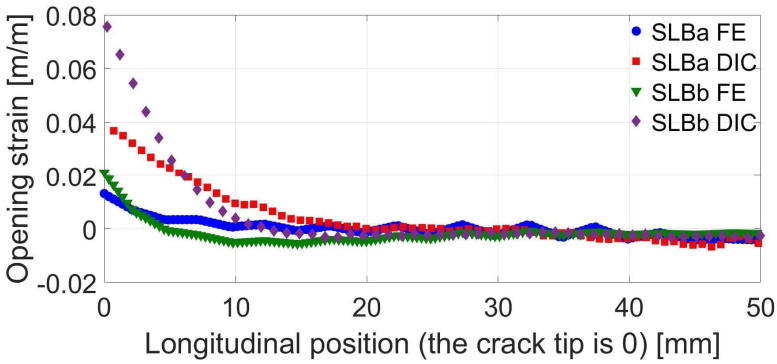

Figure 17: Opening strain in the adhesive in the SLBa and SLBb specimens at crack onset.

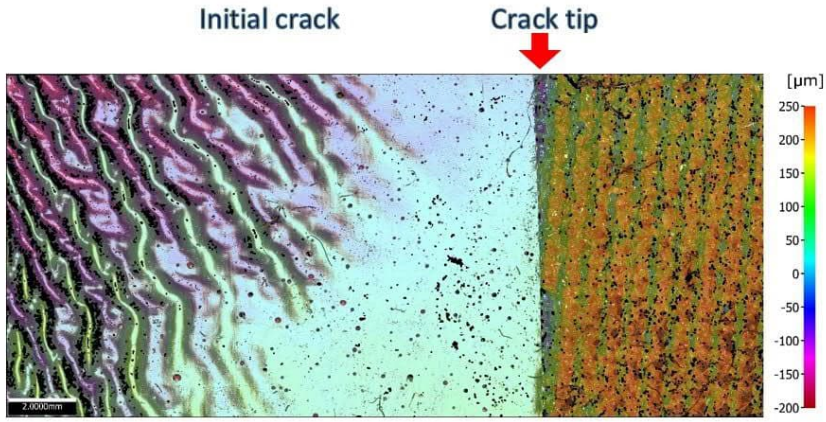

Figure 18: Surface topography measured by using a profilometer close to the pre-crack tip of an SLBa specimen.

3.3. Mixed-mode fracture criterion

The VCCT analyses were performed for all the three specimen types. The VCCT evaluated the ERR distributions at the 3D crack tip, and these results are shown in Fig. 19. Fig. 19 presents the mode I and mode II values for the SLBa and SLBb specimens. Pure mode II is presented for the ENF specimen. The mode II distributions have the highest values at the outer edges of the

specimens in contrast to the fracture mode I. Specimen ERR distributions should be presented with one value when determining the criterion. The middle point (line) value of the distribution was chosen to be representative. This selection basically follows the plane strain assumption, which is typically used in two-dimensional FE analyses. The middle nodal point values are collected into Table 2, which also presents the mode I DCB result [14].

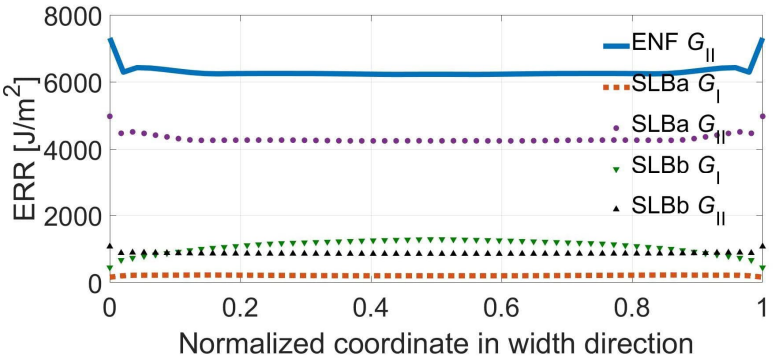

Figure 19: Energy release rate distributions for ENF, SLBa and SLBb specimens and test types.

Table 2: A summary of the fracture test–given ERR values at crack onset.

	DCB	SLBa	SLBb	ENF
G_I [J/m²]	1820	200	1285	0
G_{II} [J/m²]	0	4250	850	6230

Based on the defined ERR values (Table 2), curve fitting for the power law criterion was determined. The least square method fitting was performed using Isight software (Dassault Systemes). Fittings were performed for unequal α and β, and also with equal values ($\alpha = \beta$). The results of the fitting survey are shown in Fig. 20. In addition, the experimental results and the typically used linear criterion is shown (Fig. 20). Based on the results, the power law defined by SLBa and SLBb specimens undoubtedly improves the accuracy of the interaction between pure modes I and II for mixed loadings.

The linear power law is shown to be non-conservative and the difference between these fits is almost 20 percent.

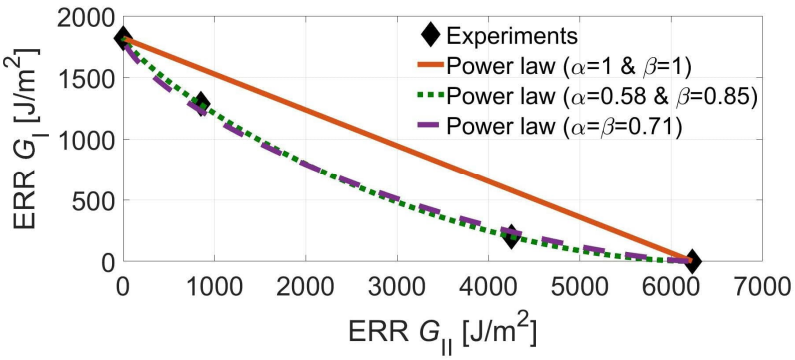

Figure 20: The developed fracture criterions for linear fit and power law (unequal α and β and equal (α=β)).

4. Discussion

The usage of one common specimen design in a single loading condition only provides a single-mode ratio value. More ratios can be achieved when dimensions are modified per specimen design. In this work, two different mixed-mode ratios are achieved using a single specimen design without changing any dimensions of the specimen. The applied specimen geometry is simple from the manufacturing point of view. The specimen is loaded under three-point bending, which does not require the use of a complex testing jig (e.g. as in MMB testing). Basically, the specimen geometry and the induced loading are relatively similar to the ENF specimen testing.

The established testing method in the composite laminate mixed-mode delamination testing is the MMB [8]. The MMB includes a complex loading jig where the ratio between modes can be varied – this being an advantage. The fracture processes of structural joints are typically much more ductile than a composite interlaminar fracture. This results in having thicker adherends with which to avoid adherend plastic deformation. Elastic adherend deformation is typically required for standard material properties to be evaluated. The increase in the specimen size, in turn, requires higher loading, which should be taken into account when designing the loading jig. For that

reason, the adhesive mixed-mode testing should aim for test with simpler specimens and testing fixture [25].

The target of the testing was also to define the fracture criterion for FM 300-2. Tenchev and Falzon [26] stated that power law exponents are typically between 1 and 2. Donough et al. [27] applied FM 300-2K in experiments and an analysis of a single lap joint and skin-doubler joints. They used a quadratic power law criterion in their analysis. Kim et al. [28] used an exponent value of 1 when analysing scarf joints under in-plane loading and impact. In the current literature, both Donough et al. [25] and Kim et al. [26] presumed the order of the criterion, i.e. did not find the value of exponent based on experimental data. Based on literature, power law exponents are mainly assumed to have value of 1 or 2. The exponent values determined in this study were less than 1. This means that the typical assumptions used in the literature do not provide conservative results under mixed-mode conditions for the current adhesive. The usage of the exponent value of 2 makes the situation even less conservative.

The maximum shear strains determined by DIC were roughly 0.15 and 0.05 in the SLBa and SLBb specimens respectively. The material data sheet of FM 300-2K [29] provides 0.093 and 0.544 for knee and ultimate strains (knee of the curve stands for significant change in slope of stress-strain curve). Duong and Wang provided the values 0.083 and 0.3 for elastic and maximum shear strains [30]. Here, the maximum measured strains in the SLBa specimens are close to the linear and knee strains found from literature. However, there is a difference when compared to the ultimate shear strains. It can be assumed that, very near the existing crack tip, the strains are higher, but this cannot be detected by the utilised DIC method due to restricted spatial resolution. Generally, the stress-strain behaviour of adhesive shear properties is studied using the TALS specimen. The shear deformation in these specimens are distributed more smoothly than in the SLB specimens in this study. Of course, this also minimises the mode I fracturing at the crack tip, which was not the target of the SLBa testing.

5. Conclusion

In this work, an alternative concept for defining the adhesive mixed-mode criterion is developed. The approach relies on a simple mixed-mode specimen design (SLBa, SLBb) that is loaded under the three-point bending condition. The specimen usage provides two different mode ratios. For a

complete criterion, DCB and ENF tests are typically performed alongside each other – as they are in this work. The fracture criterion for the epoxy film adhesive FM 300-2 was defined with this approach. The power law criterion exponents' values were determined to be 0.58 and 0.85 for modes I and II respectively and 0.71 when having equal exponents for both modes. The new criterion provides lower values under mode-mixity conditions compared to the typically used criterion with linear exponents.

Here, DIC was applied for the mixed-mode testing in order to understand the precise mixed-mode loading of the adhesive. Because the DIC was not able to directly determine strain distributions at the adhesive bond line (thickness 0.4–0.67 mm), the DIC output was post-processed using adherend reference points for determining (shear) strains in the adhesive. The enhanced DIC analysis revealed the opening strains in the SLBb specimen and in the SLBa specimen. The comparison of strain components amidst the crack tip showed that the opening strains (defined by FE and DIC) differ significantly while the shear strains had good correlation.

6. Acknowledgements

This work was funded by the financial support of the Finnish Defence Forces Logistics Command. The technical support offered by the CSC–IT Center for Science Ltd (Finland) is gratefully appreciated.

7. References

[1] D. A. Dillard, H. K. Singh, D. J. Pohlit, J. M. Starbuck, Observations of decreased fracture toughness for mixed mode fracture testing of adhesively bonded joints, Journal of Adhesion Science and Technology, 23 (2009), 1515-1530

[2] M. L. Benzeggagh, M. Kenane, Measurement of mixed-mode delamination fracture toughness of unidirectional glass/epoxy composites with mixed-mode bending apparatus, Composite Science and Technology 56 (1988) 439–449.

[3] J. R. Reeder, An evaluation of mixed-mode delamination failure criteria, NASA Technical Memorandum 104210, 1992.

[4] R. L. Ramkumar, Performance of a quantitative study of instabilityrelated delamination growth, NASA Contractor Report 166046, 1983.

[5] Dassault Systemes, Abaqus 2017 Documentation, User manual, 2017.

[6] ISO 25217, Adhesives – Determination of the mode 1 adhesive fracture energy of structural adhesive joints using double cantilever beam and tapered double cantilever beam specimens, International Organization for Standardization, 2009.

[7] S. Marzi, O. Hesebeck, M. Brede, F. Kleiner, An end-loaded shear joint (ELSJ) specimen to measure the critical energy release rate in mode II of tough, structural adhesive joints, Journal of Adhesion Science and Technology, 23 (2009), 1883-1891

[8] ASTM D6671, Standard Test Method for Mixed Mode I-Mode II Interlaminar Fracture Toughness of Unidirectional Fiber Reinforced Polymer Matrix Composites, American Society for Testing and Materials, ASTM, 2006.

[9] S. Park, D. A. Dillard, Development of a simple mixed-mode fracture test and the resulting fracture energy envelope for an adhesive bond, International Journal of Fracture 148 (2007) 261–271.

[10] B. R. K. Blackman, A. J. Kinloch, F. S. Rodriguez-Sanchez, W. S. Teo, The fracture behaviour of adhesively-bonded composite joints: Effects of rate of test and mode of loading, International Journal of Solids and Structures 49 (2012) 1434–1452.

[11] H. L. J. Pang, C. W. Seetoh, A compact mixed mode (CMM) fracture specimen for adhesive bonded joints, Engineering Fracture Mechanics 57 (1997) 57–65.

[12] T. N. Chakherlou, S. R. Hakim, A. Mohammadpour, H. N. Maleki, A. B. Aghdam, Experimental and numerical investigations of crack face adhesive bonding effect on the mixed-mode fracture strength of PMMA, Journal of Adhesion Science and Technology, 30 (2016), 2236-2256

[13] M. V. Fernandez, M. F. S. F. de Moura, L. F. M. da Silva, T. Marques, Mixed-mode I + II fatigue/fracture characterization of composite bonded joints

using the Single-Leg Bending test, Composites Part A: Applied Science and Manufacturing 44 (2013) 63–69.

[14] J. Jokinen, M. Wallin, O. Saarela, Applicability of VCCT in mode I loading of yielding adhesively bonded joints – A case study, International Journal of Adhesion and Adhesives 62 (2015) 85–91.

[15] O. Ishai, H. Rosenthal, N. Sela, E. Drukker, Effect of selective adhesive interleaving on interlaminar fracture toughness of graphite/epoxy composite laminates, Composites 19 (1) (1988) 49–54.

[16] J. Aakkula, J. Jokinen, O. Saarela, S. Tervakangas, Testing and modelling of DIARC plasma coated elastic-plastic steel wedge specimens, International Journal of Adhesion and Adhesives 68 (2016) 219–228.

[17] E. M. C. Jones, M. A. E. Iadicola, A Good Practices Guide for Digital Image Correlation, International Digital Image Correlation Society, DOI:10.32720/idics/gpg.ed1, 2018.

[18] M. Bornert, F. Bremand, P. Doumalin, J.-C. Dupre, M. Fazzini, M. Grediac, F. Hild, S. Mistou, J. Molimard, J.-J. Orteu, L. Robert, Y. Surrel, P. Vacher, B. Wattrisse, Assessment of Digital Image Correlation Measurement Errors: Methodology and Results, Experimental Mechanics 49 (2009) 353–370.

[19] M. Rossi, P. Lava, F. Pierron, D. Debruyne, M. Sasso, Effect of DIC Spatial Resolution, Noise and Interpolation Error on Identification Results with the VFM, Strain 51 (2015) 206–222.

[20] J. L. Högberg, B. F. Sørensen, U. Stigh, Constitutive behaviour of mixed mode loaded adhesive layer, International Journal of Solids and Structures 44 (2007) 8335–8354.

[21] E. F. Rybicki, M. F. Kanninen, A finite element calculation of stress intensity factors by a modified crack closure integral, Engineering Fracture Mechanics 9 (4) (1977) 931–938.

[22] G. Marannano, L. Mistretta, A. Cirello, S. Pasta, Crack growth analysis at adhesive-adherent interface in bonded joints under mixed mode I/II, Engineering Fracture Mechanics 75 (2008) 5122–5133.

[23] R. K. Behera, S. K. Parida, R. R. Das, Effect of the aspect ratio of the pre-existing rectangular adhesion failure on the structural integrity of the adhesively bonded single lap joint, Journal of Adhesion and Technology, 33 (2019), 2093-2111

[24] J. Jokinen, M. Kanerva, M. Wallin, O. Saarela, The simulation of a double cantilever beam test using the virtual crack closure technique with the cohesive zone modelling, International Journal of Adhesion and Adhesives 88 (2019) 50–58.

[25] G. G. Tracy, P. Feraboli, K. T. Kedward, A new mixed mode test for carbon/epoxy composite systems, Composites: Part A 34 (2003) 1125–1131.

[26] R. T. Tenchev, B. G. Falzon, Experimental and numerical study of debonding in composite adhesive joints, 16th International Conference on Composite Materials, Kyoto, Japan, 2007.

[27] M. Donough, A. Gunnion, A. Orifici, C. Wang, Critical assessment of failure criteria for adhesively bonded composite repair design, Proceedings of the 28th Congress of the Aeronautical Sciences, Brisbane, Australia, 2012.

[28] M. K. Kim, D. J. Elder, C. H. Wang, S. Feih, Interaction of laminate damage and adhesive disbonding in composite scarf joints subjected to combined in-plane loading and impact, Composite Structures 94 (2012) 945–953.

[29] FM 300-2 film adhesive, Technical data sheet, Cytec Engineered Materials, 2011.

[30] C. N. Duong, C. H. Wang, Composite repair Theory and design, Elsevier, 2007.

PUBLICATION V

Use of DIC in the characterisation of mode II crack propagation in adhesive fatigue testing

O. Orell, J. Jokinen, M. Kanerva

International Journal of Adhesion & Adhesives 122 (2023) 103332
https://doi.org/10.1016/j.ijadhadh.2023.103332

Publication is licensed under a Creative Commons Attribution 4.0 International License CC-BY

International Journal of Adhesion & Adhesives 122 (2023) 103332

Contents lists available at ScienceDirect

International Journal of Adhesion and Adhesives

journal homepage: www.elsevier.com/locate/ijadhadh

Use of DIC in the characterisation of mode II crack propagation in adhesive fatigue testing

Olli Orell *, Jarno Jokinen, Mikko Kanerva

Tampere University, Materials Science and Environmental Engineering, PO Box 589, FI-33101, Tampere, Finland

ARTICLE INFO

Keywords:
Adhesive
Fatigue
Digital image correlation
Mode II
End-notched flexure

ABSTRACT

Adhesively bonded joints are used in many applications which are dynamically loaded. Thus, excellent fatigue properties of adhesives, especially under fracture mode II, are required. The fracture mode II testing of adhesive is challenging, where the observation of the crack length is complicated. Accordingly, compliance-based effective crack length definitions avoiding direct observation have been used instead. The experimental crack monitoring method using digital image correlation (DIC) is studied in this work. The DIC-based monitoring is compared to the compliance-based method in defining the crack length. The developed DIC-based method is useful to study, especially, the microcracked adhesive region ahead of the distinct open crack tip.

1. Introduction

A significant amount of research has been conducted to understand failure in adhesively bonded joints. Static fracture testing has already taken steps towards standardisation. The testing of fracture mode I has already been standardised [1], and the mode II-related standard is being processed. Typically, static mode II testing has been performed using the method of end-notched flexure (ENF) [2], four-point end-notched flexure (4ENF), or the end-loaded split (ELS) [3]. The specimen types have differences in fracture surface friction and stability of crack propagation. Recently, the focus of research has been on the method development for fatigue. The testing for fatigue has mainly been performed using the ENF and ELS specimens.

Fatigue testing of joints is generally more complex than the corresponding quasi-static tests. One of the main challenges in the fatigue testing of adhesives, especially in mode II loaded joints, is the measurement of the crack length. Typically, the experimental methods are based on visual observation of the open crack and using magnifying tools, e.g. microscopes [4]. The visual observation interpretation depends on the observer when the test is performed manually. The manual observation becomes even less attractive when low load levels are used and the testing time is increased. Other techniques not dependent on visual observation are developed, e.g. crack gauges [5]. Clip gauges have been used to determine the crack length in single-lap shear tests [6] and double cantilever beam (DCB) tests [4]. In addition, distributed optical fibre sensors have been used to characterise crack propagation in fatigue testing with step-lap specimens [7].

Generally, the physical crack propagation in mode I testing is defined as the opening of the debonded interface. However, existing plastic deformation adjacent to the crack tip complicates the definition of the precise crack length. The damage related to the plastic-deformed crack tip might result in several micro-crack tips or smear the crack tip beyond the technique used for observation [8]. On the other hand, the crack propagation in mode II testing is even more challenging compared to mode I testing [9]. The mode II crack propagation is seen as a relative sliding of the originally united components in the debonded interface. Several studies have excluded the experimental determination of the crack length in mode II testing. Crack monitoring has been considered overly labour-intensive and inaccurate [10]. The adhesive properties, such as plasticity, strain hardening and relaxation, add complexity [11,12]. The challenges of the crack length have mainly been overcome by developing numerical post-processing methods using beam theory, specimen compliance and equivalent crack-based methodologies [8,10,11,13]. The equivalent crack length analytical approaches have been developed, including the fracture process zone (FPZ), which considers the plasticisation and micro-straining [8] at the crack tip regime.

This paper studies a novel approach to characterise crack propagation using digital image correlation (DIC). The DIC is an optical contactless measuring technique to study surface displacements. The method is already an established tool and is used in various applications, which include material testing [14], component testing [15], particle movement measurements [16] and fracture characteristics [17]. The

* Corresponding author.
E-mail address: olli.orell@tuni.fi (O. Orell).

https://doi.org/10.1016/j.ijadhadh.2023.103332
Received 28 June 2022; Received in revised form 16 December 2022; Accepted 23 January 2023
Available online 4 February 2023
0143-7496/© 2023 The Authors. Published by Elsevier Ltd. This is an open access article under the CC BY license (http://creativecommons.org/licenses/by/4.0/).

DIC can monitor even tiny details when using an optical setup that can produce high magnification. Here, we have used the DIC-based crack monitoring technique for mode II testing for fatigue by using an ENF-type specimen. However, typically 20–30 mm of crack propagation is observed in ENF fatigue specimens during a single test requiring a relatively large field of view from the used setup. For that reason, the DIC could not be focused locally, only on the crack tip in the adhesive. Instead, the cracked adhesive region was studied by post-processing the determined displacement fields of the adherends similar to the previous work by Jokinen et al. [18]. The crack growth of the epoxy film adhesive FM 300-2, used to join aluminium alloy adherends, was studied under three different load levels. The DIC results were compared to the compliance-based method and the indications by penetrating fluid study. The main target of the work was to study the applicability of the developed crack monitoring method based on the DIC measurements of the adherend deformation.

2. Materials and methods

2.1. Specimen

The ENF specimens in this work consisted of aluminium alloy (Alumec 89, Uddeholm) adherends and the studied adhesive. The adhesive was epoxy film adhesive FM 300-2 by Solvay, which includes a thermoplastic polyester knit carrier. The original aluminium plates were bonded using two adhesive film layers, and the pre-existing crack between the layers was made using PTFE film (thickness 20 μm). The initial crack length (a_0) was 0.66 L, where L corresponds to half of the support span (125 mm). The film-bonded plates were vacuum bagged and finally cured at 120 °C. The fabricated joined plates were water jet cut to 15 mm wide specimens with dimensions as depicted in Fig. 1.

2.2. Mechanical testing

The experimental test setup is presented in Fig. 2. A servo-hydraulic universal testing machine (Instron, 8800) with a 100 kN load sensor was used to induce the cyclic loading. First, a quasi-static ENF test at a test rate of 5 mm/min was carried out. Then, force-controlled fatigue tests at three different loading levels were performed. The maximum load in the static ENF test was 9674 N, and the fatigue tests were then carried out using a load level of 50%, 60% and 70% of the static maximum force (Fig. 3). The slight nonlinearity in the load-displacement curve prior to the load maxima is presumably due to the initiation of the plasticised region's formation at the pre-crack tip. Three specimens were tested per loading case. The applied R-ratio was 0.1, which was used to avoid total load removal because it is known to decrease the specimen's movement in the test jig. The loading spectrum (waveform) consisted of a repeating series of 16 sinusoidal cycles at the frequency of 4 Hz followed by a 1-s static hold at the maximum force (Fig. 3), which was first screened to be suitable parameter spectrum in terms of the performance of the used measurement devices. It should be noted that the spectrum must have the short hold at the maximum load at selected cycle intervals, otherwise the type of cycling can be chosen freely.

2.3. Fracture surface characterisation

The fatigue tests were run until the crack in the adhesive layer had visually propagated near the central loading pin. After the fatigue tests, the adherends were manually torn apart, and the fracture surfaces were studied visually. For two of the fatigue tests, the loading was stopped after the visually-observed crack had propagated several millimetres. The cracked area of the specimens was studied using a penetrating fluid (MR® 68NF, MR® Chemie GmbH, Germany). The penetrating fluid was applied by spraying it over the same surface of the specimen observed during the fatigue test (for crack propagation). The excess penetrating fluid was wiped off after 10 min, and the developer fluid was sprayed on the surface. The adherends were torn apart, and the developer fluid was sprayed onto the revealed fracture surfaces. Finally, the fracture surfaces were studied using the optical profilometer (Alicona InfiniteFocus G5, Bruker).

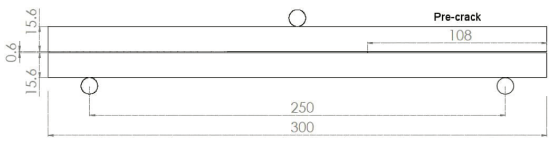

Fig. 1. The ENF specimen's dimensions (in mm) in this study.

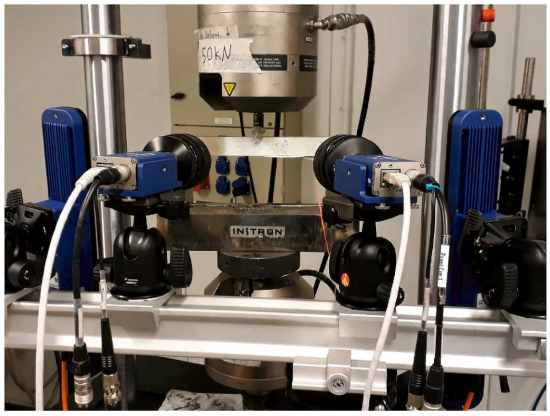

Fig. 2. The experimental test setup in this work.

2.4. Equivalent crack length concept

The crack length during the tests was determined using the equivalent crack length-based theorem [19–21]. In the theorem, instead of trying to detect the visible changes in the crack length (a), the effective equivalent crack length (a_e) is used to characterise the crack propagation. The equivalent crack length is calculated utilising the changes in the specimen compliance as the crack propagates. The equivalent crack takes, by theory, into account not only the distinct observable visual crack length but also considers the effect of the FPZ ahead of the distinct crack tip. The FPZ, in the vicinity of the crack tip, is difficult to observe visually, but it affects the material's mechanical performance. Thus, FPZ also affects the compliance of the specimen that is being measured. The equivalent crack length was determined using the Compliance-Based Beam Method (CBBM) [22] as

$$a_e = a + \Delta a_{FPZ} = \left[\frac{C_{corr}}{C_{0corr}}a_0^3 + \frac{2}{3}\left(\frac{C_{corr}}{C_{0corr}} - 1\right)L^3\right]^{1/3} \quad (1)$$

where

$$C_{corr} = C - \frac{3L}{10Gbh} \text{ and } C_{0corr} = C_0 - \frac{3L}{10Gbh} \quad (2)$$

In the above equations, C and C_0 denote the current and initial (i.e. pre-crack state) compliances of the specimen determined from the load and mid-point deflection data. a_0 is the initial crack length, L is the span length of the specimen, and G, b and h are the shear modulus, the width, and the height of the single adherend, respectively. When using the CBBM, a_e is evaluated purely from the load-deflection data, excluding the need to measure any exact crack length.

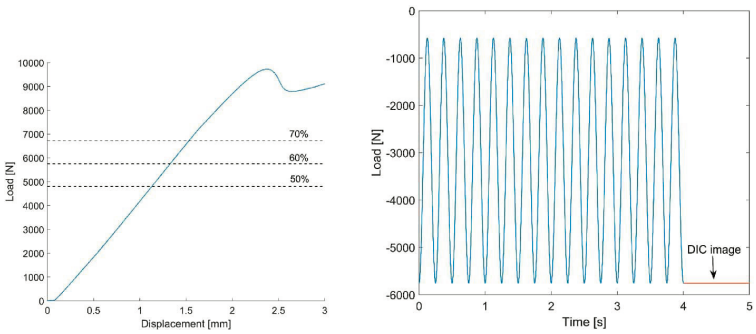

Fig. 3. a) The maximum compression loads used in the sinusoidal loading applied in fatigue testing based on the load-displacement curve of the quasi-static ENF test. b) The repeating unit of the loading spectrum for the 60% loading case.

2.5. Digital image correlation

A three-dimensional DIC setup was used to study the adherends' deformation in a specified (surface) area between the central loading pin and the initial pre-crack. The DIC method is based on tracking the movement of small facets (subsets) to which the studied digitised surface images are divided [23]. The locations of the identified subsets are tracked from image to image using so-called correlation algorithms. From the result, the full-field displacement vectors of the studied surface can be calculated. The resulting full-field data can finally be derived into the desired quantity of interests, such as strains or velocity.

Each subset must have a unique pattern to be distinguishable from the other identified subsets. In order to accomplish this, a thin random black and white pattern was applied over the selected ENF specimen's surface using matt paints and foam rollers. The 3D DIC system consisted of two 5 MP cameras with 50 mm objectives (using an aperture of F11) and pulsed LED flashes. The recording rate was 0.2 Hz, and the image exposure time was synchronised with the test machinery so that an image pair with the two cameras were taken at every static hold step at the maximum load and throughout the fatigue test (see Fig. 3). The calibrated setup resulted in a scale factor of 0.0236 mm/px. The DIC analysis with the images was carried out using Davis 10.0.5 software (Lavision, Germany). The matching criterion was the zero-normalised sum of squared difference (ZNSSD), and affine shape functions were allowed for the subsets. A 6th-order spline was used as the interpolation method. The subset and step sizes were screened first to achieve good spatial resolution and, simultaneously, to keep the noise at a reasonable level. Finally, 35 px and 11 px values were used in the analysis.

2.6. Post-processing of DIC data for crack length

The specified area of interest was selected to cover the area between the central loading pin and the pre-crack tip, i.e. the region where the crack can propagate during a test. The 3D DIC provides the full displacement and strain fields over this area. However, due to the large field-of-view and the resulting mm-to-pixel scale factor, the DIC setup and the analysis parameters yielded a larger virtual strain gauge size (VSG) (57 px or 1.34 mm) than the thickness of the adhesive layer. In other words, the spatial resolution of the applied setup was too low to measure the actual strain values directly (in a reliable manner) in the adhesive. A small VSG size, close to the used thickness of the adhesive layer, could have been achieved by decreasing the subset and step sizes during the analysis. However, it is challenging to ensure that the strong deformation gradients at the adhesive-adherend interfaces, and the damaged adhesive region in front of the distinct crack would not have specimen-wise effects on the derived DIC-based strain values in the specimen. Also, decreasing the subset size will result increased noise in the derived strain. Because an automated and objective method for monitoring the crack propagation was aimed, as presented schematically in Fig. 4, the direct method to derive the crack tip position basing on the DIC-based strain field was not considered feasible.

Fig. 5a depicts the patterned surface of an ENF specimen, which shows the pre-crack location and the approximate location of the instantaneous crack tip in a fatigue test. Visually defining the exact crack tip location is difficult, if not impossible. This is especially true in mode II dominant tests, although the applied thin white paint over the specimen surface makes the visual detection slightly easier (than without any paint). Instead of studying the computed strains directly in the adhesive layer, the developed crack tip detection method is based on measuring the local displacement vectors of both adherends (upper and lower) near the adhesive layer. More precisely, the displacement vectors of the two adherends are derived along two lines (of data collection) defined by an equal distance from the adhesive layer's centre line (here 1 mm), as presented in Fig. 5a. A recent study used a similar technique to determine the shear and opening strains of the adhesive layer under a mixed-mode loading [18].

The method of defining the crack tip location is illustrated in Fig. 5b. Fig. 5b shows the displacement in the y-direction (vertical) for the upper and lower adherends after the first block of the repeating cycles of the test (i.e. initial), and after 3000 cycles. A video presenting the adherends' displacement over a single fatigue test is found in the Supplementary data. The separation ($\Delta d = d_{upper} - d_{lower}$) between the displacements of the upper and lower adherends is determined along the whole adhesive line (inside the specified area of DIC measurement). In the beginning of a test, the initial pre-crack tip location can be visually observed (confirmed). The separation in the adherends' deformation at the pre-crack location, under the initial hold at the maximum force after the first block of cycles, is used as the definite threshold value representing the crack position. This threshold is used to determine the DIC-based crack length or, in other words, the position of the DIC-based equivalent crack tip location.

A MATLAB script was written to find, from each curve, the 'horizontal' location (x), where the same Δd is observed as at the pre-crack tip at the start of the test (hold at the load maxima). Both the separation of sliding (x-direction) and opening (y-direction) deformations, as the basis for the crack tip detection, were studied. It should be noted that the curvature of the specimen was not taken into account here. Still, its effect on the determined displacements at the adherends' surfaces (in the specified region) can be considered negligible due to the large radius of the specimen curvature.

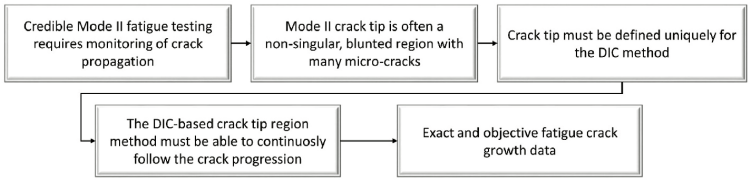

Fig. 4. The targets and requirements in steps to determine crack growth with a DIC concept.

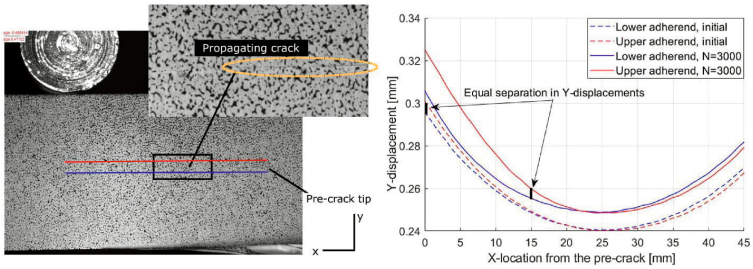

Fig. 5. a) A propagating crack during a fatigue test (the specimen with a DIC pattern). The red and blue lines show the data collection along which the adherend's displacement for further DIC analysis is exported. b) The principle for the method is to determine the instantaneous crack location from the adherend's (opening) displacement. The 'initial' refers to the measured status at the first hold in the load maxima (i.e. cycles = N = 16).

3. Results and discussion

3.1. Fracture surfaces and penetrating fluid experiments

The fatigue tests were continued until the crack, by visual observation, propagated right below the central loading pin. All the specimens, the glued adherends, were torn apart after testing, and the fracture surfaces were optically studied. Representative fracture surfaces for three different fatigue load levels are shown in Fig. 6. In addition to the tested specimens, a fracture surface after a quasi-static ENF test is shown for comparison.

The pre-crack was formed between two layers of film adhesive during the specimen fabrication. The fracture surfaces indicate that the crack propagated closer to the upper adherend (surface), as observed similarly in other studies [24]. In most of the specimens, the crack found its way from the adhesive layer's centre line towards the upper

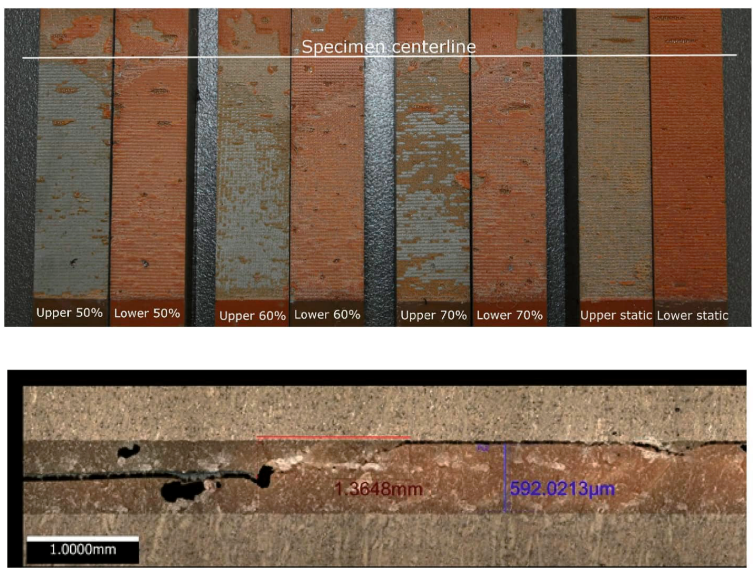

Fig. 6. (Above) The fracture surfaces of the fatigue-tested specimens (load levels of 50%, 60%, 70%) and a quasi-static tested ENF specimen. (Below) An optical image is taken from a cross-section of a tested specimen (50%). The red bar presents the approximate distance (1.365 mm) from the pre-crack tip to the stable crack path point near the upper adherend. The blue line presents the thickness of the adhesive layer (0.592 mm).

adherend's surface just after a few millimetres of propagation (Fig. 6). Although the fracture propagated very near the upper adherend, the failure mode is still cohesive for every test based on adhesive residue.

Two fatigue tests at the load level of 60% were stopped before the visually detected crack propagation below the central loading pin. The first test was stopped after 1500 cycles, and the second after 2000 cycles. These specimens were studied using the penetrating fluid method, and the analysis images are shown in Fig. 7. The pre-crack tip is located on the right-hand side of the image, and the crack has propagated to the left. The fracture surfaces of the specimens can be divided into three regions: 1) the white region on the left, 2) the pink-tinted region in the middle, and 3) the dark purple region on the right. The white colour indicates the fracture surface where the penetrating fluid had not migrated, i.e. where the adhesive had been entirely intact when the penetrating liquid was applied. The dark purple colour indicates the region where the penetrating liquid had flown readily, i.e. there was a distinct crack. In the pink-tinted region, the assumption is that the amount of the penetrating liquid had been significantly lower than the location of the distinct crack with the well-penetrating liquid. However, as some liquid had penetrated through the specimen in the width direction (from one surface and up to the opposite surface), there must have been continuous cracks (or micro tunnels) throughout the adhesive layer in the width direction of the specimen. The lengths determined based on the colour categories are presented in Table 1. The observed non-uniformity of the pink-tinted region, in the width direction of the specimens, is presumed to have formed due to fabrication-based voids in the adhesive layer.

3.2. Results based on the compliance-based approach

When the crack propagates, it results in a decrease in the bending stiffness of the ENF specimen. Thus, crack propagation increases the specimen's measured compliance. As the tests here were performed with the force-controlled movement, the deflection of a specimen increases with the crack propagating. An example of the change in the mid-point-related deflection (measured at the point of maximum force per cycle) is shown in Fig. 8a. The equivalent crack length curves for different load levels, determined by using the compliance measurements and Eq. (1), are depicted in Fig. 8b. The tests were stopped intentionally when the crack was visually estimated to be propagated near the central loading pin.

In general, the shape of the curves remains similar, and the decrease in load level shifts the equivalent crack length towards a higher cycle count. The specimen-wise scatter in the crack propagation behaviour increases with the decreased load level. The curves show that, for approximately the first 5 mm, the value of a_e propagates with a highly nonlinear growth rate. After this regime, the crack propagates at a steadier rate until a_e reaches approximately 22–25 mm. Basically, this crack (length) shows the point where the compression—caused by the central loading pin—starts to cause compressive normal stress at the adhesive. This behaviour has been explained to hinder self-similar crack growth [10]. The compression in the loading direction can also be seen in Fig. 5b, where the deformation curves of the adherends, determined using the DIC-based displacements, are shown. The normal stress at the adhesive changes from small tensile stress to compressive stress at a distance of approximately 22 mm from the pre-crack. In addition, this location is near the point of the ultimate valley of the deformed shape of the specimen under bending.

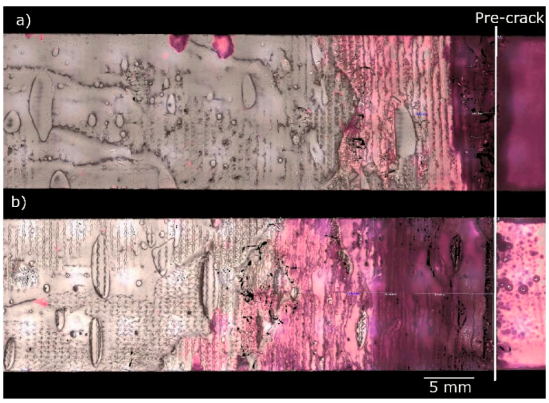

Fig. 7. The fracture surface of a fatigue test specimen after the adherends have been torn apart (60% load level) and after the application of penetrating fluid. Two examples are shown: a test stopped after a) 1500 cycles, and a test stopped after b) 2000 cycles.

Table 1
The crack lengths determined with different methods for the specimens stopped after 1500 and 2000 loading cycles.

Specimen	Penetrating fluid, purple (crack) area [mm]	Penetrating fluid, pink-tinted (microcracked) area [mm]	Effective crack length a_e [mm]	DIC, opening-based [mm]	DIC, shear-based [mm]
Loading 60%, 1500 cycles	4–5	17	3.5	19	7
Loading 60%, 2000 cycles	11–13	22–32	10	30	21

3.3. Results based on the DIC-based approach

Fig. 9 shows the progression of the determined separations (Δd) determined from the opening and shear deformation data (i.e. in y- and x-directions of the adherends) along the adhesive line during a fatigue test. The black dots in Fig. 9 present the points for a proceeding test, where Δd (either opening or shear direction) having the defined threshold value representing the crack tip is observed. To sum up, this data presents the location maps where the deformation state at the adherends (over a test) is similar to the initial condition (at the vicinity of the pre-crack location).

At the beginning of a test, the opening-related Δd is naturally very small. Still, as the test proceeds, a more prominent separation is formed, and the curves' shape changes. Fig. 9b shows the procedure results but determined from the shear deformation (namely based on the displacements in the x-direction).

3.4. Sensitivity of the DIC-based approach

Fig. 10 depicts the determined crack propagation using the opening and shear data versus the cycle count for a median specimen (60% load level). It is interesting to see the effect of the threshold on the detected crack length, which was used to define the original crack tip. The separation value (Δd) for the pre-crack location, after the first repeating loading cycle ('Initial' point), is the reference against which the accumulating data is analysed in the method. The crack-defining threshold can technically be freely selected. The results show that the method, when based on the shear separation, is highly sensitive to the used threshold value. However, the effect is much less for the crack length by the opening-based data.

The normal strain (in the y-direction, matching the loading direction) in the aluminium adherend is negligible during the bending of the ENF specimen in this study. Therefore, the measured displacement separations (Δd values) in the y-direction due to the progressing crack in

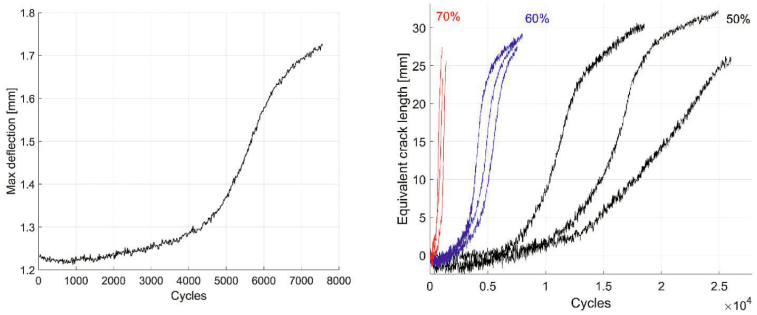

Fig. 8. a) An example for the maximum deflection data of the specimen's (60% load level) middle point versus the cycle count. b) The equivalent crack length (a_e) for different load levels.

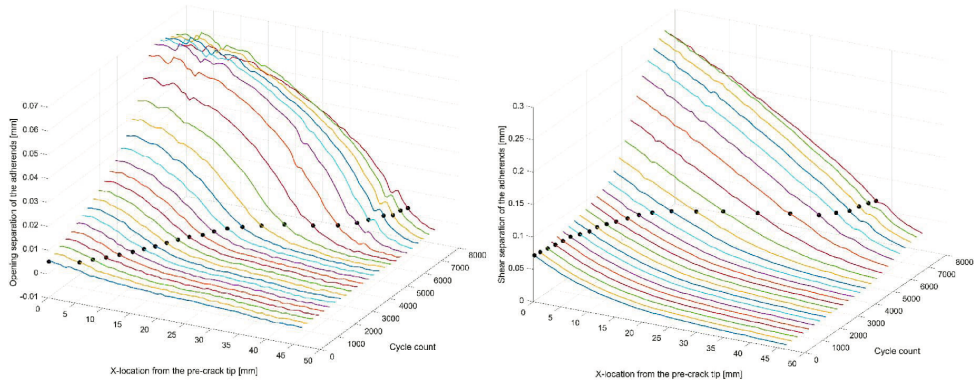

Fig. 9. Displacement separation curves along the adhesive (line) as a function of cycle count (60% load level). The black dots present the location of the instantaneous equivalent crack tip defined based on the initial separation threshold based on a) opening and b) shear displacement.

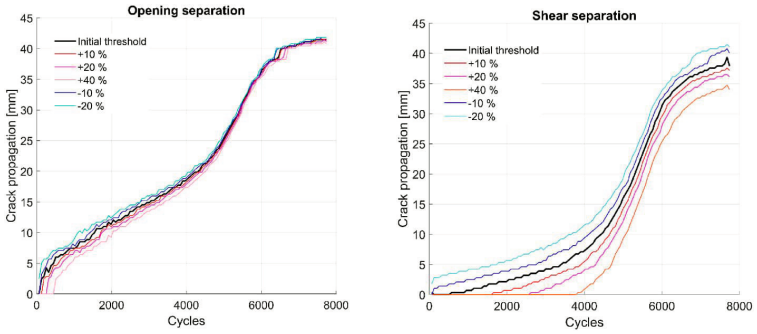

Fig. 10. Crack propagation curves and the effect of the crack-defining threshold when using a) the opening data; b) the shear data (60% load level).

the adhesive originate practically only due to the changes in the adhesive layer. Thus, the exact (y-) distance of the extracted displacement vectors at the adherends (distance from the adhesive centre line) has an insignificant effect on the DIC-based method when using the opening data. This is illustrated in Fig. 11, where the crack propagation length, obtained using the adherend deformations extracted at two different (y-) distances (1 mm and 3 mm), are shown. Again, the shear data-based results show a high sensitivity for the selected distance.

The minimum distance where the adherend displacements can be derived is significantly affected by the parameters used in the DIC analysis and, especially, by the subset size. Basically, the distance must be more than half of the adhesive thickness plus half of the subset size (here 0.71 mm). When this condition is fulfilled, the local displacement information for the DIC analysis is obtained only on (pixels of) the aluminium adherend outside the adhesive-adherend interface (affine deformations assumed).

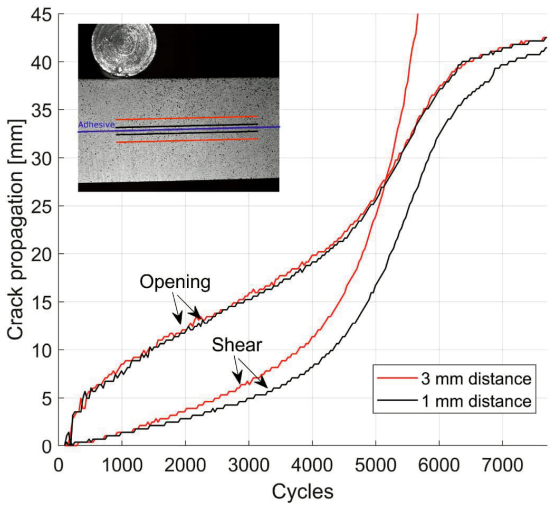

Fig. 11. The effect of the selected extraction distance, measured from the adhesive layer's centre line, on the crack propagation. The effect is shown for data related to opening and shear deformation.

3.5. Comparison of the approaches to detect the crack length

The crack lengths determined using the two approaches for a typical (median) test specimen (at 60% load level) are shown in Fig. 12. The trend of all the curves is similar, resembling an S-curve. In these S-curves, a clear increase in the crack propagation rate is detected after the first essentially linear propagation phase. However, the crack propagation curves between the DIC and CBBM approaches still differ significantly.

Although challenging, by careful pure visual observation of the recorded (camera) images, the position of the crack tip or, at least, the plasticised adhesive can be manually estimated at the painted specimen surface. This basically forms a third method of determining the crack length. By comparing the methods, the visual observation of the crack matches best with the DIC-based method using the opening displacement data. On the other hand, the shear displacement-based DIC method matches quite accurately with the CBBM results. The CBBM shows the shortest determined crack length.

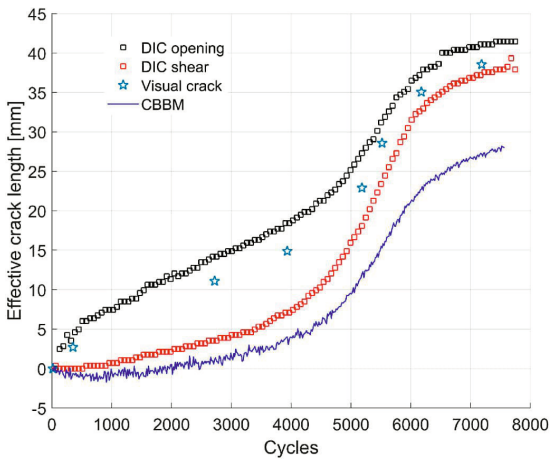

Fig. 12. Comparison of the crack propagation (length) determined with three different methods.

The crack lengths of the tests stopped after 1500 and 2000 cycles, determined with the different methods, are shown in Table 1. It can be seen that the CBBM results in comparable values with the values obtained via the analysis of penetrating fluid. More specifically, the data matches the dark purple region in Fig. 7. The opening data-based DIC resulted in comparable values with the pink-tinted region. The crack lengths detected with the different techniques for the specimen loaded for 2000 cycles are illustrated in Fig. 13, together with optical microscopy images. The distinct crack, close to the upper adherend (seen in close-up 2), is visible approximately to the same point (distance) as given by the compliance-based equivalent crack length (point B). The region between this point (point B) and the point given by the length result of the opening data-based DIC method (point E) shows a clear repeating, inclined cracking pattern in adhesive. Basically, this region also corresponds to the pink-tinted region observed using the penetrating fluid.

According to the results, the developed opening-based DIC method reveals thus the region of the adhesive, in which permanent damages in the adhesive have occurred due to the cycled loading. On the other hand, the length of the distinct, continuously open crack can be estimated well with the CBBM. The shear-based DIC method seem to correlate with the CBBM, but the method is highly sensitive on the analysis parameters hindering its use. The considered methods to monitor the progressing crack in fatigue loaded ENF test are summed up in Fig. 14.

3.6. Remarks on the DIC-based opening separation

The opening (between adherends) in an ENF test is not intuitive when pure mode II loading is considered. However, small 'opening' deformations have been documented originating from the phenomena due to the micro-cracked and segmented adhesive [25], and the roughness of the fracture surfaces [21]. Basically, non-zero damage (preceding the crack tip) and Poisson's ratio less than 0.5 of the adhesive will also have to open the stiff adherends after cracking. The opening deformations observed by DIC can also partly be explained by contact surface roughness when there is no perfect match in the contact of the adherend surfaces encountering shear-induced sliding. The ENF specimen has a pre-existing crack tip made by a release film strip. Based on our observations, it is pretty typical that the fabricated pre-crack plane has some waviness. The waviness is formed due to the unbalanced shrinking of the (PTFE) release film during the adhesive curing process. This waviness at the specimen end region can clearly be detected after tearing apart the adherends, as depicted in Fig. 15. It should be noted here that the opening by the waviness balances out when the

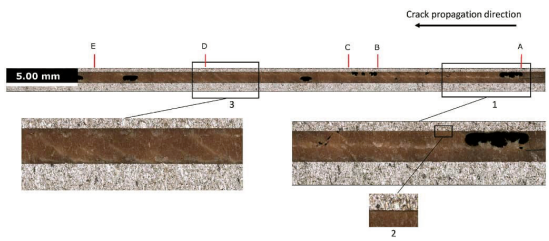

Fig. 13. An optical image of the adhesive layer after the fatigue-tested specimen showing various locations for the detected crack (lengths) with different methods. The loading level was 60%, and the test was stopped after 2000 cycles. A = pre-crack location, B = effective crack length, C = crack with penetrating fluid and purple colour, D = the minimum length of 'FPZ' with penetrating fluid creating a pink-tinted region and E = crack length with DIC opening-based data.

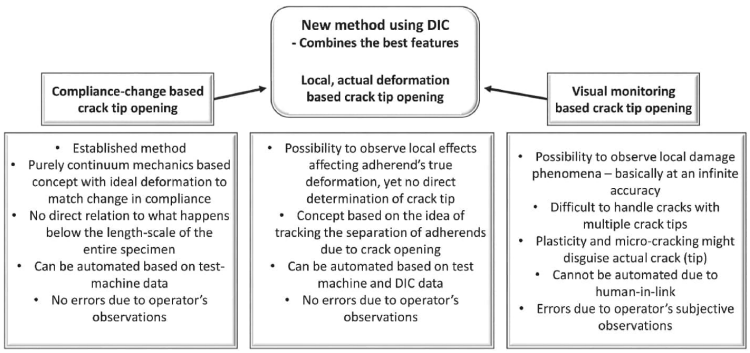

Fig. 14. Summary of the compared methods for the crack tip monitoring in ENF fatigue test.

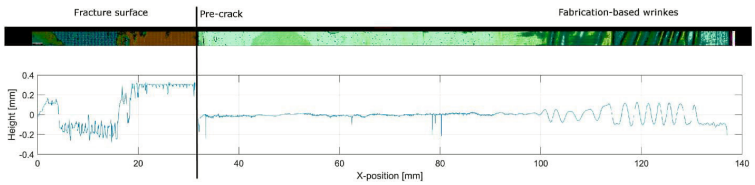

Fig. 15. A profilometer image of a lower adherend's portion of the fracture surface (top) and the line contour shows the height profile (bottom). The right-hand edge is the specimen end, and the crack has propagated to the left from the pre-crack.

crack-defining threshold is selected specimen-wise in each test.

3.7. Formation of the fracture process zone (FPZ)

The FPZ is the established designation to define the non-negligible region ahead of the distinct crack tip where the material has already undergone softening damage. The damage can happen by different means, including plastic deformation, microcracking, crack-branching, microvoid formation and possible fibre bridging [22,26,27].

The results of this study revealed that extensive microcracking was prominent in the adhesive layer after testing (the inclined cracks in Fig. 13). The woven carrier is a feature of the adhesive film product that can increase the likeliness of microcracking. It is suggested here that the interfaces between the filaments of the polyester carrier and epoxy are prone to microvoids. In practice, microcracking and damage function as the desired toughening mechanism and also increases the size of the FPZ.

The microcracked region was visually detected here during and after the tests. However, accurate length measurement for FPZ is ambitious. The penetrating fluid indicated a rather distinct region between the open crack (purple colour) and the undamaged region. It is suggested here that this region (the pink-tinted region) is the microcracked region.

Due to the FPZ, unambiguous detection of any 'true' crack length is practically impossible [3]. Eventually, this fact complicates the analysis of the ENF tests since the size of the FPZ affects the resolved fracture energy. The effective crack length (a_e) determined with the CBBM includes, by theory, also the FPZ because the derivation of a_e bases on the measured (real) changes in the flexural rigidity of the ENF specimen (including the FPZ) [22,28].

3.8. Separated adherend zone (SAZ)

The DIC-based method presented here analyses crack propagation according to the measured adherends' separation. The determined (crack) length for opening data, i.e. the separated adherend zone (SAZ), shall be distinguished from the CBBM results with the FPZ. From the mechanical point of view, the SAZ, depending on the threshold and for the ENF specimen, makes the separation of the adherends more prominent whenever damage or plastic deformation of adhesive occurs. With the current formulation, the SAZ does not distinguish if the separation is due to the propagation of any 'true' crack or the expanded plasticised or damaged region in the adhesive layer. The penetrating fluid, however, indicated a good correlation between the length with the microcracked region and the SAZ.

Fig. 16a depicts the effective crack length curves (60% load level) determined by the CBBM and DIC-based methods. The difference between the two methods is presented in Fig. 16b. The result suggests that the SAZ begins to develop first. It is presumed to originate due to the plastic deformation and microcracking of adhesive ahead of the originally blunt pre-crack tip (i.e. nucleation). However, this first phase does not affect the measured compliance (within experimental scatter) nor the effective crack length a_e by the CBBM. When the SAZ reaches 11 mm, the effective crack length determined by the CBBM increases, this increase is assumed to originate due to the formation of a coalesced crack in the adhesive (near the upper adherend surface in this study). Thereafter, the FPZ and the SAZ increase at different rates. The difference curve (Fig. 16b) indicates that the length of the SAZ (in front of the FPZ) increases as the test proceeds. This indicates that the length of the deformed adhesive (its zone ahead of the crack) is not exactly stable, but increases as the crack propagates during an ENF test.

In Fig. 16b, a clear change in the curve is observed at 4000 cycles, which equals the SAZ and FPZ lengths of 24 mm and 6 mm, respectively. The distance of 24 mm is also the location of the valley point in the deformed shape of the ENF specimen because of the unsymmetrical deformation due to the pre-crack (Fig. 5). Around this valley point, the value of normal strain in the loading direction in the adhesive layer changes from tensile strain to compressive strain. The observation indicates that when the microcracked adhesive region propagates and reaches the valley point of the bent specimen, the slope of the crack propagation rate determined by either of the methods significantly

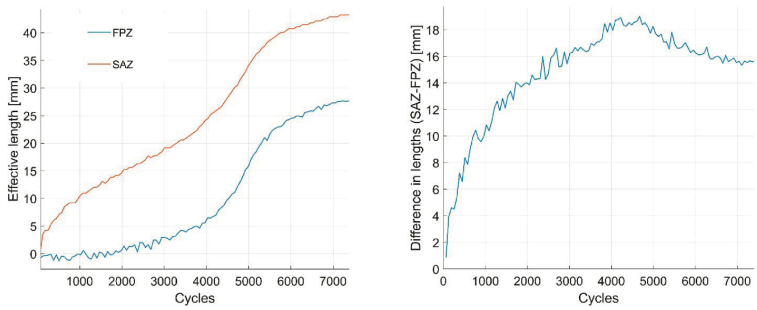

Fig. 16. a) Determined effective crack lengths with the FPZ (by the CBBM) and SAZ (by the DIC-based adherend opening). b) The difference between the CBBM and the SAZ-crack lengths.

increases. The behaviour was similar in all the tests with different load levels. Therefore, the development of the damaged or plasticised adhesive region tends to affect the crack propagation rate of the 'distinct' crack determined by the CBBM.

4. Conclusion

The work focused on characterising crack propagation in FM 300-2 epoxy adhesive film under fatigue loading using the ENF specimen. The crack propagation in the ENF test is shown as sliding at the debonded interface when there is mode II loading. The sliding is exceptionally challenging to observe visually. Moreover, the precise crack length definition is not unambitious due to the damaged large region ahead of the distinct crack. In this work, the applicability of a DIC-based approach is developed and analysed in detail. Instead of aiming to detect the distinctly visible crack, the new approach uses the adherends' deformation to define the damaged region in the adhesive by studying the introduced specimen's separated adhesive zone (SAZ). The applicability of both opening (vertical) and shear (horizontal) deformation of the adherends was considered. The reference results were provided with the established CBBM method. In addition to the developed approach and the CBBM, penetrating fluid measurements were performed to study the developed crack in the adhesive layer.

Based on this work, the following conclusions can be made:

- The DIC measurements indicated small opening deformation between the adherends of the ENF specimen. The observation was used in defining the damaged adhesive region in the specimen.
- The crack monitoring was achieved with the established SAZ-defined crack tip.
- The DIC-based method estimates a larger crack length than the CBBM.
- The penetrating fluid measurements indicated two different regions at the specimen fracture surface. The intensively penetrated region agreed with the CBBM results and was verified as the distinct crack length. The less penetrated region agreed well with the DIC method with the opening data and is suggested to denote the damaged microcracked adhesive in ahead of an open crack tip.
- The length of the microcracked region ahead of the distinct crack increases as a fatigue test proceeds. However, it does not obviously affect the compliance of the bent ENF specimen. On the other hand, its size was eventually observed to affect the propagation rate of the distinct crack in fatigue-loaded ENF specimens.

Declaration of competing interest

The authors declare that they have no known competing financial interests or personal relationships that could have appeared to influence the work reported in this paper.

Data availability

Data will be made available on request.

Acknowledgements

This work was funded by the financial support of the Finnish Defence Forces Logistics Command.

Appendix A. Supplementary data

Supplementary data to this article can be found online at https://doi.org/10.1016/j.ijadhadh.2023.103332.

References

[1] ISO 25217:2009. Determination of the mode 1 adhesive fracture energy of structural adhesive joints using double cantilever beam and tapered double cantilever beam specimens. Int. Organ. Stand. 2009;1:1–24.
[2] Floros IS, Tserpes KI, Löbel T. Mode-I, mode-II and mixed-mode I+II fracture behavior of composite bonded joints: experimental characterization and numerical simulation. Compos B Eng 2015;78:459–68. https://doi.org/10.1016/j.compositesb.2015.04.006.
[3] Blackman BRK, Kinloch AJ, Paraschi M. The determination of the mode II adhesive fracture resistance, GIIC, of structural adhesive joints: an effective crack length approach. Eng Fract Mech 2005;72:877–97. https://doi.org/10.1016/j.engfracmech.2004.08.007.
[4] Bernasconi A, Beretta S, Moroni F, Pirondi A. A study on fatigue crack propagation in thick composite adhesively bonded joints. In: 18th Eur. Conf. Fract. Fract. Mater. Struct. From micro to macro scale; 2010. p. 1–8.
[5] Madhusudhana KS, Narasimhan R. Experimental and numerical investigations of mixed mode crack growth resistance of a ductile adhesive joint. Eng Fract Mech 2002;69:865–83. https://doi.org/10.1016/S0013-7944(01)00110-2.
[6] Krenk S, Jonsson J, Hansen LP. Fatigue analysis and testing of adhesive joints. Eng Fract Mech 1996;53:859–72.
[7] Wong L, Chowdhury N, Wang J, Chiu WK, Kodikara J. Fatigue damage monitoring of a composite step lap joint using distributed optical fibre sensors. Materials 2016;9. https://doi.org/10.3390/ma9050374.
[8] Chaves FJP, da Silva LFM, de Moura MFSF, Dillard DA, Esteves VHC. Fracture mechanics tests in adhesively bonded joints: a literature review. J Adhes 2014;90:955–92. https://doi.org/10.1080/00218464.2013.859075.
[9] Blackman BRK, Brunner AJ, Williams JG. Mode II fracture testing of composites: a new look at an old problem. Eng Fract Mech 2006;73:2443–55. https://doi.org/10.1016/j.engfracmech.2006.05.022.
[10] Fernández MV, De Moura MFSF, Da Silva LFM, Marques AT. Characterization of composite bonded joints under pure mode II fatigue loading. Compos Struct 2013;95:222–6. https://doi.org/10.1016/j.compstruct.2012.07.031.
[11] de Moura MFSF, Gonçalves JPM, Fernandez MV. Fatigue/fracture characterization of composite bonded joints under mode I, mode II and mixed-mode I | II. Compos Struct 2016;139:62–7. https://doi.org/10.1016/j.compstruct.2015.11.073.
[12] Olajide SO. Progress on investigation on damage analysis in bonded polymer composites under fatigue. Int J Fatig 2017;96:224–36. https://doi.org/10.1016/j.ijfatigue.2016.12.016.
[13] Pérez-Galmés M, Renart J, Sarrado C, Brunner AJ, Rodríguez-Bellido A. Towards a consensus on mode II adhesive fracture testing: experimental study. Theor Appl Fract Mech 2018;98:210–9. https://doi.org/10.1016/j.tafmec.2018.09.014.

[14] Orell O, Vuorinen J, Jokinen J, Kettunen H, Hytönen P, Turunen J, Kanerva M. Characterization of elastic constants of anisotropic composites in compression using digital image correlation. Compos Struct 2018;185. https://doi.org/10.1016/j.compstruct.2017.11.008.
[15] Janeliukstis R, Chen X. Review of digital image correlation application to large-scale composite structure testing. Compos Struct 2021;271:114143. https://doi.org/10.1016/j.compstruct.2021.114143.
[16] Ghaednia H, Cermik O, Marghitu DB, Kardel K. Collision measurements using digital image correlation techniques. Int J Mech Sci 2017;131–132:836–46. https://doi.org/10.1016/j.ijmecsci.2017.07.025.
[17] Sun G, Liu X, Zheng G, Gong Z, Li Q. On fracture characteristics of adhesive joints with dissimilar materials – an experimental study using digital image correlation (DIC) technique. Compos Struct 2018;201:1056–75. https://doi.org/10.1016/j.compstruct.2018.06.018.
[18] Jokinen J, Orell O, Wallin M, Kanerva M. A concept for defining the mixed-mode behaviour of tough epoxy film adhesives by single specimen design. J Adhes Sci Technol 2020:1–18. https://doi.org/10.1080/01694243.2020.1746606.
[19] De Moura MFSF, Gonçalves JPM, Chousal JAG, Campilho RDSG. Cohesive and continuum mixed-mode damage models applied to the simulation of the mechanical behaviour of bonded joints. Int J Adhesion Adhes 2008;28:419–26. https://doi.org/10.1016/j.ijadhadh.2008.04.004.
[20] de Moura MFSF, de Morais AB. Equivalent crack based analyses of ENF and ELS tests. Eng Fract Mech 2008;75:2584–96. https://doi.org/10.1016/j.engfracmech.2007.03.005.
[21] Yoshihara H, Ohta M. Measurement of mode II fracture toughness of wood by the end-notched flexure test. J Wood Sci 2000;46:273–8. https://doi.org/10.1007/BF00766216.
[22] de Moura MFSF, Silva MAL, de Morais AB, Morais JJL. Equivalent crack based mode II fracture characterization of wood. Eng Fract Mech 2006;73:978–93. https://doi.org/10.1016/j.engfracmech.2006.01.004.
[23] Jones MA, Iadicola EMC. A good practices guide for digital image correlation. Int. Digit. Image Correl. Soc. 2018;94. https://doi.org/10.32720/idics/gpg.ed1.
[24] Dessureault M, Spelt JK. Observations of fatigue crack initiation and propagation in an epoxy adhesive. Int J Adhesion Adhes 1997;17:183–95. https://doi.org/10.1016/s0143-7496(96)00044-9.
[25] Leone FA, Girolamo D, Dávila CG. Progressive damage analysis of bonded composite joints. 2012. NASA/TM-2012-217790).
[26] Majano-Majano A, Lara-Bocanegra AJ, Xavier J, Morais J. Experimental evaluation of mode II fracture properties of Eucalyptus globulus L. Materials 2020;13:1–13. https://doi.org/10.3390/ma13030745.
[27] Arrese A, Insausti N, Mujika F, Perez-Galmés M, Renart J. A novel experimental procedure to determine the cohesive law in ENF tests. Compos Sci Technol 2019;170:42–50. https://doi.org/10.1016/j.compscitech.2018.11.031.
[28] de Moura MFSF, Campilho RDSG, Gonçalves JPM. Pure mode II fracture characterization of composite bonded joints. Int J Solid Struct 2009;46:1589–95. https://doi.org/10.1016/j.ijsolstr.2008.12.001.